UNIVERSIDAD DE GRANADA

Tesis doctoral
Abril 2014

Accurate Photometry and Photometric Redshifts for Cosmological Surveys.

[PhD THESIS]

Alberto Molino Benito
Instituto de Astrofísica de Andalucía - CSIC

Tesis por memoria
presentada en la Universidad de Granada
para optar al grado de Doctor en Física y Matemáticas

Director de tesis:
Narciso Benítez Lozano

Abril, 2014

Editor: Editorial de la Universidad de Granada
Autor: Alberto Molino Benito
D.L.: GR 1889-2014
ISBN: 978-84-9083-069-7

"Es <u>tan</u> grande, que se te escapa..."

- A mi abuelo Florencio, cuando me hablaba del Universo siendo yo un niño. -

Derechos de autor

El doctorando Alberto Molino Benito y el director de la tesis el Doctor Narciso Benítez Lozano, garantizamos al firmar esta tesis doctoral, que el trabajo ha sido realizado por el doctorando bajo la dirección del director de la tesis y hasta donde nuestro conocimiento alcanza, en la realización del trabajo, se han respetado los derechos de los autores al ser citados, cuando se han utilizado sus resultados o publicaciones.

Granada, a 25 de Febrero de 2014

Director de la tesis

Fdo.: Narciso Benítez Lozano

Doctorando

Fdo.: Alberto Molino Benito

D. Narciso Benítez Lozano, Científico Investigador del Instituto de Astrofísica de Andalucía, del Consejo Superior de Investigaciones Científicas (IAA-CSIC),

CERTIFICA:

que la presente tesis: ***"Accurate Photometry and Photometric Redshifts for Cosmological Surveys"*** ha sido realizada en el Instituto de Astrofísica de Andalucía, del Consejo Superior de Investigaciones Científicas (IAA-CSIC), por Don Alberto Molino Benito bajo su dirección y que constituye su Tesis Doctoral para optar al grado de Doctor en Física y Matemáticas.

Granada, 25 de Febrero de 2014

D. Narciso Benítez Lozano

Fdo.:

Agradecimientos

I specially want to express my deep respect and gratitude to my advisor Txitxo Benitez, for his guidance during these years of intensive work at the IAA-CSIC. He has been and will be my mentor. Throughout all this period, he provided me with good teaching and good scientific criticism, encouragement and self-confidence. He provided me the opportunity to visit the Johns Hopkins University and get involved in the CLASH survey, an invaluable experience to me. Almost seven years of hard work, good company, enliven trips with selected classic music, invaluable hints about how to invest in stock market and great relaxing barbecue moments at his house. It has been an honor to be your "alumnus". Likewise, my gratitude to Mariano Moles for giving me the opportunity of joining the ALHAMBRA survey project and do my PhD at the IAA-CSIC with Txitxo. For his good advices and for keep counting on me for the incoming future.

A mis padres, Eduardo y María, por su apoyo incondicional durante tantos años, creyendo en mí y en mi sueño de dedicarme a trabajar en astrofísica. Por comprender y aceptar mis decisiones. Por haberme hecho sentir siempre tan cerca de casa, a pesar de la distancia. A mi padre por sus incondicionales visitas allí donde yo estuviera. Reencuentros que tanto aliento me han proporcionado. Por estar conmigo aquel inolvidable primer día de trabajo en Granada, para iniciar un largo viaje que ahora termina. Por tus conversaciones, por nuestros "spritzs" en Venecia, por tus propinillas, por tu generosidad, por tu sinceridad, por tu amistad, por saber hacerme sentir siempre alguien importante, por ser una fuente de admiración. A mi madre por sus incansables llamadas los fines de semana. Por su paciencia de vernos cuando yo lo diga. Por todos esos abrazos con los que siempre me recibe en Mendez Álvaro, por nuestras entrañables conversaciones en aeropuertos y estaciones, por nuestras cenas y desayunos en Chantada, intentando entender la Vida y el Mundo.

A Laura, mi pequeña. De alguna forma, ella estará siempre presente entre los renglones de este manuscrito. Esta tesis ha sido posible gracias a su generosidad durante todos estos años. Por haber luchado por nosotros con los ojos vendados. Por haber renunciado tantas veces a ella misma, por mi y mi trabajo. Por haber sido mi compañera y mi amante incondicional. Por saber escucharme, saber calmarme y hacerme sentir una persona espacial. Por haberme devuelto tantas sonrisas a cambio de tantas caras serias. Por sus lágrimas cuando me he marchado de viaje. Por venir a buscarme y sacarme del estudio con besos. Por nuestros paseos. Por lo inmensamente feliz que he sido estos años viviendo a su lado en Granada. Por ser ella, sin lugar a dudas, el descubrimiento más fascinante de esta tesis.

A mi amigo Juan, por su inagotable paciencia y admiración conmigo. Durante estos años tan difíciles para mi, nunca me ha faltado un buen consejo, una regañina, una llamada ó un mensaje a tiempo, para recordárme quién era yo, aquello por lo que estaba luchando, de dónde venía y, sobretodo, a no perder de vista mi camino. La Vida es un aprendizaje. Caminar, tropezar, reflexionar, sonreír, y

continuar. Él lo sabe bien. Sin lugar a dudas, estos siete años lejos de él, de Madrid, de nuestros viajes y de nuestros fines de semana, me han enseñado a conocerle desde la distancia, a comprender lo mucho que le admiro y, sobre todo, a cuantificar las páginas en blanco que su amistad dejarían en mi historia si no pudiera contar con él. Seguiremos apuntando a las estrellas. A Vanessa por crecer conmigo durante estos siete años en los que tantos cambios hemos vivido. Por no dejarme atrás y apostar por nuestra amistad aún cuando le haya desatendido precisamente cuando más me necesitabas. Por interesarse por mis amores. Por aguantar tantos años de "chapa" científica y seguir interesándose solo porque sabe que es importante para mi. Por quererme tanto.

A mi amigo Kike, por estar siempre ahí cuando le he necesitado. Por sus innumerables visitas a Granada los fines de semana, haciendo ínfimos los cuatro cientos kilómetros que me separaban de Madrid. Por haber sido él quien me llevara a Granada el día que firmaba el contrato en el CSIC. Sin lugar a dudas, un evento memorable para mi. Por ayudarme con las mudanzas. Nunca olvidaré aquella tarde en IKEA con Laura, con él, las albóndigas y aquella furgoneta de alquiler. Por haber llevado a Laura hasta Nueva York para que pudiéramos vernos unos días. Por haber cuidado de ella. Por abrirme su corazón y confiarme sus secretos. Por recibirme en Madrid siempre con una sonrisa y un gran abrazo. Por saber cómo hacerme sentir especial con sus preguntas y sus cumplidos. Por seguir ahí después de todos estos años.

A mis hermanos Eduardo y Javier, por su paciencia al haber estado yo tan ausente en algunos momentos. Por sus visitas a Granada, que hicieron de esta casa de alquiler, un reflejo de nuestro hogar en Madrid. Por las cervezas filosóficas. Por abrirme sus corazones haciéndome sentir cerca, aún estando lejos. Porque su cariño y admiración me ayudan a seguir luchando.

A Fabio per essere stato la cosa più importante che ho trovato a Granada. Per essere stato il mio amico ed la mia famiglia. Per la tua sincerità, per la tua sensibilità, per tutti i nostri momenti filosofici, per tutte le bottiglie di Ribera del Duero che ne abbiamo bevuto insieme, per quell'estate colle "motrileñas", per i primi giorni al "arcoiris", per tutte le volte che abbiamo lottato sul mondo, la politica e la Dark Matter. Per essere stato un fratello per me. Alessandra, grazie per tutti i momenti speciali che ne abbiamo vissuto insieme.

A mi estimado amigo Fernando Buitrago. Por sus incondicionales llamadas al despacho, preocupándose por mi y mi trabajo. Por confiarme sus inquietudes, por haberse convertido en el gran científico que hoy admiro, por su honestidad, por su sinceridad, por ser un luchador que me inspira, por conservarnos a sus amigos, aún viviendo lejos de casa.

A mis compañeros del IAA y Granada. En especial a Yolanda con quien tuve el placer de compartir paseos y cenas durante aquel "Baltimore-experience". Por su siempre puntual sonrisa, sus generosas palabras de apoyo, por considerarme su amigo y por hacerme sentir alguien importante. A Begoña por las sonrisas que intercambiamos en el trabajo, ella sentada en su mesa y yo desde el umbral de la puerta de su despacho, sonrisas que hacieron los días en el trabajo un poquito más llevaderos. Por su energía, por su apoyo, por sus buenos consejos. A Vasiliki por su cariño hacia nosotros. A Gabriella per essere così speciale, ribelle e sensibile colla vita. A William por su ayuda y disponibilidad. A Cesar por brindarme su amistad. A Pedro y a Miriam por su cariño todos estos años, por su amistad,

por tantos buenos momentos, por cuidar de Laura mientras yo terminaba la tesis. A Alba por estar ahí siempre que la necesité, aunque el tiempo nos haya distanciado en ocasiones. Por el cariño con el que siempre me han mirado sus ojos. A los compañeros y compañeras del proyecto ALHAMBRA por su ayuda y buenos consejos. Especial mención a Emilio Alfaro con quien disfruté numerosas veces hablado de ciencia en su despacho. A la gente del CEFCA por su apoyo. En especial a Carlos L.S., Jesús V. y Alessandro E. por hacerme sentir uno más dentro de esa gran familia científica. A Javier Cáceres por compartir conmigo la emoción del PIIISA. A Victor Briones por hacernos las 80 camisetas de ALHAMBRA. A Leandro, un amico speciale che ho conosciuto all'inizio di Granada ma che purtroppo il tempo ci ha allontanato. Grazie comunque per tutti quel momenti inolvidabili.

To Holland Ford for hosting me at the JHU during the summers of July 2010 & 2011. I'm grateful for the time I spent with you, talking about life, books and showing me Maryland from the skies. To Marc Postman for giving me the opportunity of get involved in the CLASH survey, for his patience and his advises. To Dan, Elinor and Doron for the time we spent together in Baltimore. To Tiffany, Matt and Azalee for your generosity and humanity. For making me feel like at home when I was thousands of miles away from Spain.

Finally, to John Noble (Walter Bishop), Edward J. Olmos (Commander Adama) and Bryan Cranston (Walter White) for all the unforgettable moments I frenetically experienced watching those marvelous episodes.

Summary

Due to the finite speed of light, which imposes any physical event to not instantaneously propagate though space-time, the history of the universe can be traced back. This very fact makes possible to observe the universe as it was in other epochs and so understand the physical processes that, millions of years ago, dictated the distribution, formation and evolution of the galaxies we observe today. Just by looking at increasingly distant sources in the universe. The expansion of the universe stretches the electromagnetic radiation emitted by extragalactic sources while traveling through the space-time. This quantifiable effect, commonly known as cosmological $redshift$, has become a widely-accepted indicator to measure cosmological distances, and so understand when (in terms of the cosmic time) the light that we register today in our observatories departed originally from the galaxies. Interpreting this spectral $shifting$ as a physical distance certainly requires the support of a theoretical framework. The theory of General Relativity (or theory of gravity) has played a fundamental role in describing the present-day universe since gravity is the only fundamental force acting at larges scales. As briefly introduced in Chap. 1, this theory successfully explains the expansion history of the universe in terms of the energy-mass content and the geometry of the space-time, through the evolution of the scale factor.

During the last decades, cosmology, the science of the universe as a whole, has experienced a tremendous progress. Today, the Lambda-Cold-Dark-Matter (ΛCDM) scenario is widely accepted as the standard model of cosmology describing not only the evolution of the universe but also the different constituents that may have populated it over most its cosmic time. The different ingredients and their proportions are expressed through the cosmological parameters, which represents the real physical quantities that can be retrieved by observations. Fortunately, the combination of multiple studies (such as the Cosmic Microwave Background Radiation (CMB), the Dark Matter content and distribution on Massive Galaxy Clusters, the Dark Energy equation of state via distant Supernovae, the re-ionization epoch examining high-z QSO spectra, the Big Bang nucleosynthesis of the primordial abundances of light elements, the galaxy formation and evolution or the large scale structure (LSST) of galaxies, among others) has made possible that most cosmological parameters are known to a few percent accuracy now. One of the reasons why modern cosmology has achieved a solid world-model is due to the carefully designed observational programs that have systematically surveyed the universe, scanning the whole electromagnetic range. From the largest to shortest wavelengths. From the coolest and quietest to the most dynamical and energetic universe. During chapter 2, the role of redshift surveys is briefly introduced, along with a small discussion regarding the advantages and drawbacks of different methodologies inferring the galaxy redshifts.

The main research activities of this PhD thesis have been focused on the acquisition of accurate photometric redshift catalogues for two cosmological surveys. i.e., to simultaneously interpret and deal with all the complexity derived from the analysis of the astronomical images. As several times discussed

during the manuscript, to perform complete, unbiased, homogeneous and reliable measurements for the observed galaxies is a delicate task. Spite of the fact that the two projects involved in this work shared exactly the same methodology for the estimation of the galaxy redshifts, it was (at certain points) impractical to freely applicate the same analytical tools from one dataset to another. The kind of problems associated to each survey made the design of the pipelines quite complex, rather than a repetitive task. Thanks to my participation in both ALHAMBRA (Moles07) and CLASH (Postman12) survey, my research work offered me the chance to handle images as much from ground-based observatories (CAHA & SUBARU) as from space-based telescopes (*HST* & *Spitzer*). This situation served me as an useful training to comprehend the kind of analytical difficulties one may face when combining the information gathered from different instruments or telescopes.

As discussed through Chapter 3, to retrieve the current scientific catalogues in ALHAMBRA, a long list of processes had to be addressed. In order to compute a reliable PSF-corrected multi-band photometry, we used (and updated) the *ColorPro* software (Coe et al. 06, Molino et al. 2014) to meet the specification of the survey. As required by the software, it was necessary to generate PSF-models per each individual image, carefully selecting hundredths of well-isolated and good photometric stars to assure the fidelity of the final models. A new approach to generate broad-band images, as a combination of individual bands, was developed and implemented. This served for ALHAMBRA to create synthetic HST/ACS F814W detection images, defining a constant, homogeneous and comparable window for all the ALHAMBRA fields with other projects like the COSMOS-survey. A set of simulations were designed to assure the goodness of *ColorPro* retrieving precise photometry across images with varied PSF. It was proved that the software was indeed able to retrieve precise corrections with a photometric dispersion as low as $\sim$3% for sources as faint as magnitude F814W=23.0. These testing simulations, which had never been reported before, proved the validity of *ColorPro*. A new approach to mask out saturated stars, stellar spikes, ghosts or simply damaged areas through the images was developed and implemented. This step served to improve as much the source detection efficiency as the background subtraction process. To decontaminate extragalactic sources from field stars, a statistical classification method where every detection was classified in terms of the probability of being a star or a galaxy, given its apparent geometry, F814W magnitude, optical F489W-F814W and NIR J-Ks colors was developed and implemented. When this statistical criteria was applied to the final catalogue, it was possible to identify $\sim$20.000 star candidates in the galactic halo. A substantial fraction of time was devoted to deal with the photometric zero-point (PZP) calibrations. Initially calibrated PZP using spectrophotometric stars, were then refined using the colors of the galaxies predicted by photometric redshifts (photo-z). This step served to improve not only the final photo-z accuracy but also to decrease the fraction of catastrophic outliers. Meanwhile, during this thesis it was developed a new methodology capable to internally calibrate the PZP based on photometric redshift estimations for emission-line galaxies. This method solved a major limitation for photometric redshift surveys, since a spectroscopic sample of redshift galaxies was always needed for calibration and verification purposes.

To derive photo-z estimations for the galaxies we relied on a new version of BPZ (Benítez 2000, Benítez 2014, in prep.). Since the redshift probability distribution function p(z) usually becomes

multimodal and completely asymmetric for most faint galaxies, we used of the complete information yielded by the P(z,T|C). When comparing the P(z) derived for the ALHAMBRA-04 field with that for the COSMOS survey, it was observed that both distributions consistently reproduced a double peak at redshifts z$\sim$0.3 and z$\sim$0.9. However, the global P(z) derived averaging the seven ALHAMBRA fields showed a mean redshift $< z >$=0.56 for F814W<22.5 and $< z > = 0.85$ for F814W<25.5, indicating that the COSMOS field had a rather peculiar redshift distribution which mimics a significant redshift density evolution effect. To calibrate and validate the photo-z estimations, a sample of $\sim$7200 galaxies with secure spectroscopic redshifts was compiled. This sample showed the ALHAMBRA photo-z to reach a precision of δz/(1+zs)=1% for galaxies brighter than I<22.5 and δz/(1+zs)=1.4% for 22.5<F814W<24.5. Results that surpassed the theoretical expectations for the survey. Finally, a new methodology to identify potential AGN candidates using BPZ was discovered. When plotting the Odds distribution as a function of F814W magnitude for all galaxies, we found an unexpected locus for bright magnitudes. Very strong broad-emission-line objects, AGNs or even variable sources were populating that locus.

On the other hand, I devoted a large part of this thesis to work on the CLASH survey. Although my contribution to CLASH was original planned to be working on the weak-lensing pipeline, due to the fact that several unexpected problems came up in the *HST* pipeline, when deriving photometric redshifts in the massive galaxy clusters, I had to reschedule my priorities. This issue drew my attention and I made the decision to seriously focus on the problem, start digging deeply into its understanding and eventual solution. Fortunately, the experience previously gathered working in ALHAMBRA served to identify the source of this problem. As fully explained in Chapter 4, an additional background signal from the Brightest Cluster Galaxies (BCGs) and the Intra-Cluster-Light (ICL) was disrupting the galaxy colors as much as to completely deteriorate the photometric redshift estimations. This background signal was typically inhomogeneous, position-dependent, wavelength-dependent and showing small- and large-scale structure, making its treatment a long procedure. Therefore, since this nuisance signal was closely tied to the properties of each cluster, an one-by-one analysis was carried out. By observing the galaxies from the *UDF* through different background conditions, it was possible to quantify the photometric bias induced by this nuisance signal. Particularly, it was proved that the ICL + BCG emission was causing an asymmetric photometric scatter in the original colors as large as two magnitudes for faint galaxies in the reddest filters. Due to the application of a more "aggressive" background subtraction treatment to the images, this photometric bias was partially mitigated letting retrieve colors closer to the originals. Starting from the assumption that photo-z are very sensitive algorithms to the quality of the inputed data, it was proved that they could be used to identify which might be the optimal background configuration per each cluster, and so enhance the CLASH final data products. To overcome the problem of an insufficient spectroscopic redshift sample for photo-z testing, during this PhD thesis a new approach was developed and implemented. Based on the *UDF* photometric catalogue (Coe et al. 2006), and the new BPZ library of galaxy templates, the *UDF* was extended from its 4 original bands to the 16 constituting the CLASH filter system. It was called the UDF-16. The injection of this synthetic dataset within the cluster images, along with a set of simulations extensively sampling the background parameter space, it was possible not only to work out

the most convenient background configuration for each cluster, but also to discovery, model and correct several additional photometric biases. During these simulations, it was warned that the detectability of faint galaxies, within the innermost part of the clusters, was also strongly background-dependent. A potential unnoticiable bias that may cause serious statistical biases if not taken into account, as much in terms of the detectability of high-z (faint) galaxies, as in terms of the completeness factor when deriving luminosity or mass functions.

Same manner as for ALHAMBRA, we relied on *ColorPro* to derive PSF-corrected photometry across filters. Averaged HST/PSF-models were built by combining ∼70 stars visually selected from the 25 clusters. The PSF stability across images was explored, finding that an internal photometric scatter <<1% might be produced by assuming a single PSF-model per image. It was confirmed that the photometric uncertainties reported by *SExtractor* were, by default, highly underestimated. A more realistic approach was adopted and implemented to account for correlations among pixels, where the empirical dependence between the background RMS and the sizes of the photometric apertures was systematically estimated per every image. Meanwhile, when validating the so-corrected photometric uncertainties, it was noticed that *SExtractor* was enormously underestimating the photometric uncertainties for the brightest sources. It came out that *SExtractor* was artificially overestimating the photometric apertures for the brightest (largest) galaxies, something that led to an excessed integrated signal, causing the photometric uncertainties to be unrealistically small. When background-subtracting the images most light from the brightest galaxies was removed, making the magnitudes not optimal for any physical parameter estimation. The possibility of performing an alternative photometry, based on the background-subtracted detection images (to assure the number of detections) but capable to retrieve realistic total magnitudes was explored. Fortunately, it was found that there existed an optimal photometric aperture capable to minimize the photometric differences between originals and background-subtracted images. Meanwhile, accurate upper limits were computed using the empirically estimated photometric uncertainties, demonstrating that trusting the *SExtractor* originally reported uncertainties, photometric upper limits became strongly overestimated. This bias had a direct impact on photometric redshift estimations forcing BPZ to artificially favor higher redshift solutions, and so making the galaxy redshift distributions $n(z)$ to show a "false" peak at z>>2.5. Empirical upper limits made the artificial peaks to vanish, enhancing the foreground-background sample selections. Finally, once BPZ was ran on the so-derived photometry, photo-z were compared to a real sample of ∼160 spectroscopic redshift galaxies. This sample shows an accuracy for the CLASH photo-z better than 3% for the complete sample, 2.5% accuracy for ∼80% of the galaxies and 2.0% accuracy for ∼60%. Results in good agreement with simulations, considering that the first three UVIS/WFC3 filters were not included in the analysis given their scarce signal-to-noise. Fortunately, with the so-enhanced photo-z the Odds parameter was capable to retrieve secure and precise subsamples. This very fact made finally possible for CLASH to retrieve improved mass model estimations than those obtained with the preliminary versions of the photometric redshifts catalogues.

Finally, I devoted a smaller fraction of my time participating in other three scientific groups within the CLASH collaboration: the high-z team, the supernova team (led by Nobel Prize winner Adam Riess) and the weak-lensing team. Whereas the contribution to the latter group also represented

a substantial fraction of my time, it has deliberately not included in this manuscript. It is worth mentioning that during my visits to the JHU, I contributed to the installation and validation of the *ColorPro* and the BPZ softwares, the implementation of the same methodology developed in ALHAMBRA (for the generation of synthetic F814W images) to calibrate the SUBARU images, along with a systematic validation of the photo-z catalogues. An example of the high-level scientific products that came out from the work on this pipeline were published in the ApJ (Umetsu et al., 2012).

My participation in the discovery of (at the time) the first z>9 galaxy in the Universe is briefly narrated in Chapter 5. After performing a tailored photometry for MACS1149-JD in both *HST* and *Spitzer* datasets, an exhaustive photo-z study was carried out in parallel by the BPZ and the LePhare codes. Both analysis shown a remarkable good agreement discarding a low-z interloper as being several times less likely than the high-z solution. The analysis of this galaxy stellar populations made possible to asses, with 95% confidence level, that the galaxy had been formed less than 200 million years after the Big Bang (z ∼14.0). The result of this paper fortunately deserved its publication on Nature (Zheng et al., 2012).

Finally, my participation in the CLASH supernova team represented a three-year long work, where every solid SNIa candidate detected in the *HST* images, was immediately explored by myself in terms of its photometric redshift. As explained in Chapter 6, since the host galaxies were observed as in the HST/ACS parallel fields as in the wide-field SUBARU images, in order to retrieve as much information as possible for these galaxies before computing the photo-z, it was necessary to simultaneously work with both datasets. Whenever the so-derived redshift probability distribution function (P(z)) was compatible with a SNIa, the team decided the viability of triggering a follow-up spectroscopy. Most cases, the photo-z predictions were in remarkable good agreement with the spectroscopic redshift estimations. As a result of this collaboration, the discovery of a sample of 27 SNe in the parallel fields was reported. Of these SNe, ∼13 were classified as SNIa candidates, including four SNIa candidates at redshifts z>1.2. The photo-z estimations for these SNe made possible to measure volumetric SNIa rates to redshift 1.8 and add, for the first time, an upper limit on the SNIa rate in the range 1.8<z<2.4. The results of this work were published in the ApJ (Graur et al., 2014).

Resumen

Gracias al hecho de que la velocidad de la luz es finita, lo cual impide que los sucesos físicos se propaguen instantáneamente por el espacio-tiempo, la historia del universo puede ser reconstruida. Este hecho en si mismo hace posible que podamos observar el universo como fue en otras épocas, y así entender cuáles fueron los procesos físicos que, millones de años atrás, dictaron la distribución, la formación y la evolución de las galaxias que observamos a día de hoy. Tan solo, mirando fuentes astronómicas más y más lejanas. La expansión del universo estira la radiación electromagnética emitida por las fuentes extragalácticas durante su viaje a través del espacio-tiempo. Este efecto, conocido como *corrimiento al rojo cosmológico*, se ha convertido en un popular trazador para infererir distancias cosmológicas y, por lo tanto, poder saber en que época cosmosógica la luz que detectamos en nuestros observatorios salió originalmente de las galaxias. La relación entre "desplazamientos espectrales" y distancias físicas requiere, lógicamente, de un marco teórico que lo soporte. La Teoría de la Relatividad General (o teoría de la gravedad) ha desempe–ado un papel fundamental describiendo el universo actual ya que, la gravedad, es la ́enica fuerza fundamental capaz de actuar a grandes distancias. Como se explica brevemente en el capt́itulo 1, esta teoría ha proporcionado una explicación satisfactoria sobre la historia de la expansión del universo en términos del contenido de masa y energía y la geometría del espacio-tiempo, a través de la evolución del factor de escala.

Durante las últimas décadas, la cosmología o la ciencia de todo el universo, ha experimentado un enorme progreso. A día de hoy, el modelo de Lambda-Cold-Dark-Matter (ΛCDM) es comúnmente aceptado como el modelo estándar de la cosmología, describiendo no solo la evolución del universo sino también los distintos constituyentes que han debido poblar el universo a lo largo de su historia. Los distintos "ingredientes" así como sus proporciones vienen representados por los parámetros cosmosógicos, que son las cantidades físicas que pueden realmente ser medidas mediante observaciones astronómicas. Afortunadamente, la combinación de muy diversos estudios (tales como la radiación cósmica de fondo de microondas (CMB), el contenido y distribución de materia oscura en los cúmulos masivos de galaxias, la ecuación de estado de la energía oscura mediante la detección de distantes supernovas, la época de re-ionización mediante el estudio de los espectros de QSO distantes, la nucleosíntesis primordial mediante el estudio de la abundancia de elementos ligeros, la formación de las primeras galaxias así como su evolución ó la estructura a gran escala del universo, entre otros), ha permitido que los parámetros cosmológicos puedan conocerse con una alta precisión. Una de las razones por las que la cosmologoía moderna ha conseguido desarrollar un modelo teórico sólido ha sido gracias al diseño de programas de observación que, sistemáticamente, han cartografiado el universo. Barriendo todo el espectro electromagnético. Desde las ondas más largas a las más cortas. Desde el universo más frío y tranquilo hasta el más energético. A lo largo del capítulo 2, el papel que han desempeñado los cartografiados se expone brevemente, junto con una pequeña discusión sobre las ventajas e inconvenientes que tienen los distintos métodos adoptados por estos proyectos para medir

el corrimiento al rojo de las galaxias que observan.

La principal actividad investigadora de esta tesis doctoral ha estado centrada en la obtención de catálogos científicos de alta precisión sobre la medida del corrimiento al rojo de las galaxias observadas por dos proyectos de cosmología. Es decir, trabajando en la reducción, análisis e interpretación de las imágenes astronómicas. Como se discute varias veces a lo largo del manuscrito, desarrollar medidas precisas, completas, sin sesgos, homogéneas y sólidas para las galaxias que se observan es, en general, una tarea muy compleja. A pesar de que los dos proyectos cosmológicos que componen el contenido de esta tesis están basados en la misma metodología para la estimación de las distancias de las galaxias, en algunos momentos, resultó impracticable la aplicación de las mismas herramientas analíticas de un proyecto a otro. El tipo de problemas asociados a las observaciones para cada proyecto hizo el dise–o de sus procedimientos de reducción de datos altamente complejo, en lugar ser simplemente un proceso supuestamente repetitivo. Gracias a mi participación en ambos proyectos ALHAMBRA (Moles07) y CLASH (Postman12), durante mi trabajo de investigación tuve la oportunidad de aprender a manejar imágenes astronómicas tanto de observatorios terrestres (CAHA & SUBARU) como espaciales (HST & Spitzer). Este hecho supuso un gran ejercicio donde pude familiarizarme con los problemas típicos asociados con el tratamiento y combinación de imágenes de distinto formato y calidad.

Como se discute a lo largo del capiťulo 3, para poder obtener los actuales catálogos del proyecto ALHAMBRA fue necesario desarrollar un larga lista de procedimientos, los cuales, se resumen a continuación. Para poder calcular una precisa fotometría multibanda corregida de PSF, usamos una versión actualizada del códio *ColorPro* software (Coe et al. 06, Molino et al. 2014). Dado que el código así lo requería, fue necesario generar modelos de PSF para cada una de las imágenes. Para ello, se seleccionaron y combinaron varios cientos de estrellas aisladas y con buena calidad fotométrica a fin de asegurar la fidelidad de los modelos. Un nuevo método para generar imágenes de banda ancha, como combinación de las imágenes individuales, fue desarrollo e implantado durante esta tesis. Este algoritmo sirvió para generar imágenes sintéticas de detección en la banda HST/ACS F814W, definiendo una ventana homogénea, constante y comparable para todos los campos de ALHAMBRA con el proyecto COSMOS. Se diseñaron un conjunto de simulaciones con el objetivo de asegurar la capacidad de *ColorPro* corrigiendo las variaciones de PSF sobre las imágenes con distinto *seeing*. Se encontró que el código fue capaz de proporcionar precisas correcciones, con incertidumbres fotométricas menores de un 3%, para las magnitudes más brillantes de F814W=23AB. Un nuevo proceso de enmascaramiento de estrellas saturadas, spikes, ghosts u otros defectos en las imágentes fue desarrollado e implementado. Este proceso sirvió para mejorar tanto la detección de fuentes como el modelado y substracción del background de las imágenes. Para poder descontaminar las fuentes extragaláctivas de objetos estelares, un método estadístico de clasificación estrella/galaxia basado en la geometría, la magnitud aparente, el color óptico F489W-F814W y el color infrarrojo J-Ks fue desarrollado e implementado. Cuando este método de clasificación fue aplicado a la muestra global de ALHAMBRA, se identificaron unas ∼20.000 fuentes candidatas a ser estrellas del halo galáctivo. Una fracción substancial de tiempo de esta tesis se dedicó a la calibración de los puntos cero fotométricos (PZP). Los PZP fueron refinados usando los colores predichos por los $redshift$ fotométricos (photo-z), mejorando no solo la precisión de los photo-z sino también la fracción de errores catastróficos (*outliers*). Asimismo,

durante esta tesis se desarrolló un método capaz de calibrar los PZP mediante el uso de photo-zs estimados a partir de galaxias con intensas líneas de emisión. Este método sirvió para solucionar uno de los mayores problemas asociados con estos proyectos que necesitan una muestra espectroscópica tanto para la calibración fotométrica como para la validación de los photo-zs.

Para estimar el photo-z de las galaxias observadas, se utilizó el códio BPZ (Benítez 2000). Dado que las funciones de distribución de probabilidad $P(z)$ suelen ser multimodales y asimétricas para las galaxias más débiles, en lugar de utilizar valores puntuales, se decidió utilizar toda la información contenida en la $P(z, T|C)$. La comparación de la $P(z)$ derivada para el campo ALHAMBRA-04 con la de COSMOS, se observó que ambas distribuciones reproducían consistentemente un doble pico para valores de z$\sim$0.3 y z$\sim$0.9. Sin embargo, la distribución $P(z)$ global, procedente de la combinación de todos los campos de ALHAMBRA, mostró un valor de $< z >$=0.56 para magnitudes F814W<22.5 y $< z > = 0.85$ para magnitudes F814W<25.5. Estos resultados indicaron que el campo de COSMOS mostraba una distribución peculiar en redshift, mostrando claros efectos de evolución por efectos de entorno. Para poder calibrar y estimar la precisión de los photo-zs de ALHAMBRA, se conformó una muestra espectroscópica de unas $\sim$7200 galaxias con medidas seguras del redshift. Cuando comparados con dicha muestra, los photo-zs alcanzaron una precisión de δz/(1+zs)=1% para galaxias más brillantes de magnitud I<22.5 y δz/(1+zs)=1.4% para 22.5<F814W<24.5. Los resultados mejoraron las expectativas teóricas estimadas a partir de las simulaciones informáticas. Finalmente, un nuevo método para identificar candidatos potenciales a ser AGNs fue identificado. Al representar la distribución de las ODDs (BPZ) frente a la magnitud F814W para todas las galaxias, se encontró una secuencia inesperada para objetos con magnitudes brillantes. Tras un proceso de validación, se observó que en su mayoría se encontraba conformado por objetos con intensas líneas de emisión, AGNs y fuentes variables.

Por otra parte, durante el transcurso de esta tesis, se dedico una importante fracción de tiempo trabajando en el proyecto CLASH. Aunque mi principal aportación al proyecto estaba enmarcada en la elaboración de la pipeline para el estudio del *weak-lensing*, dados los problemas que surgieron en la pipeline principal con las imágenes de *HST* a la hora de derivar las estimaciones de redshift de las galaxias de los cúmulos masivos. Este asunto llamó mi atención e hizo que me centrara en la comprensión y solución del problema. Afortunadamente, la experiencia acumulada trabajando en el proyecto ALHAMBRA sirvió para rastrear la fuente del problema. Tal y como se explica en el capítulo 4, una señal adicional procedente de la luz intracumular (ICL) más la luz procedente de las galaxias más brillantes (BCG) del cúmulo, hacían que los colores de las galaxias quedaran totalmente afectados, deteriorando las estimaciones de los photo-zs. Esta señal adicional de fondo típicamente inhomogénea, dependiente de la posición en la imagen, dependiente de la longitud de onda y mostrando estructura a pequeña y larga escala, hizo de su tratamiento un proceso largo y complejo. Por lo tanto, esta señal contaminante estuvo íntimamente vinculada a las propiedades de cada cúmulo lo cual supuso un tratamiento cúmulo a cúmulo. Gracias a la observación de las galaxias del UDF a través de diferentes condiciones de background, resultó posible cuantificar el sesgo fotométrico inducido por este efecto. En concreto, se demostró que la señal ICL+BCG estaba induciendo un elevado sesgo asimétrico en los colores originales de las galaxias, especialmente significativo en los filtros más rojos.

Gracias a la aplicación de un tratamiento "agresivo" del background de las imágentes, resultó posible mitigar substancialmente el sesgo, recuperando en gran medida los colores originales de las galaxias. Partiendo de la afirmación de que los photo-zs son algoritmos extremadamente sensibles a la calidad fotométrica de los datos, se provó la hipótesis de utilizar photo-z para identificar una configuración óptima para el tratamiento del background. Para solucionar el problema de no disponer de una muestra espectroscópima abundante para verificar este tratamiento, durante esta tesis se apostó por diseñar una nueva metodología. Basados en el catálogo fotométrico del UDF (Coe et al. 2006) y de la nueva librería de templares de galaxias de BPZ, el UDF fue extendido de sus 4 bandas originales a las 16 que componen el sistema fotométrico de CLASH. Se denominó UDF16. La inyección del UDF16 en los cúmulos de galaxias, junto con un amplio conjunto de simulaciones que muestrearon el espacio de parámetros característicos del background, hizo posible no solamente la identificación de la configuración optima de background para cada cúmulo sino, además, modelar y corregir varios sesgos fotométricos adicionales. Durante el tratamiento de las simulaciones, se advirtió que la detectabilidad de fuentes en las imágentes dependía enormemente de la configuración de background utilizada. Este sesgo, de no ser considerado y corregido, puede inducir sesgos importantes en la detección de galaxias a alto z, así como sesgos a la hora de derivar los efectos de selección de los cúmulos al derivar funciones de luminosidad ó funciones de masas.

De la misma manera que para el caso de ALHAMBRA, también se apostó por *ColorPro* para realizer una fotometría multibanda corregida de PSF. Modelos promediados de PSF para las imágentes del HST fueron elaborates mediante la combinación de $\sim$70 estrellas seleccionadas visualmente de entre los 25 cúmulos. La estabilidad de la PSF a lo largo de la imagen fue explored encontrando que, en el peor de los casos, la utilización de un único model de PSF por imagen, introducía una incertidumbre fotométrica simper inferior al $<<$1%. Durante los análisis realizados, se confirmó cuantitativamente que el código *SExtractor* subestimada sistemáticamente las incertidumbres fotométricas. Un método empírico para medir la relación real entre las apertures fotométricas y la RMS asocial a la señal de background fue desarrollado e implement ado. Tratamiento que mejoró la estimación de las incertidumbres. Asimismo, durante la fase de validación de dichos tratamientos, se advirtió que textitSExtractor subestimaba sistemáticamente las incertidumbres para las fuentes más brilliants. Tras explorer el origen de esta inconsistencia, se encontró que *SExtractor* sobreestimaba las aperturas fotométricas de las galaxias más brillantes (más grandes), causando un exceso de flujo integrado que, a su vez, inducía a una subestimación de las incertidumbres. Dicho efecto se modeló y corrigió, incrementando la calidad de las medidas fotométricas. Dado que la substracción del background en la imágenes eliminaba parte de la luz de las galaxias más brillantes, las magnitudes derivadas de estas imágenes no representaban medidas adecuadas para la obtención de propiedades físicas de las galaxias. Para poder mantener el núero de detecciones fijadas por las imágenes sin background, se estudió la posibilidad de modificar controladamente las aperturas fotométricas hasta el punto de poder verdaderas magnitudes totales, como las que se medirían si las imágentes no se hubieran tratado de background. Afortunadamente, se encontró que existía una apertura óptima para todos los cúmulos que minimizaba las diferencias fotométricas entre las imágenes originales y las imágenes sin background. Se estimaron precisas magnitudes límite mediante la utilización de las medidas emperícas del background. Dichas magnitudes empírisas demostraron que las incertidumbres originales de *SExtractor* conducían a una sobreestima-

ban severa de las magnitudes límite. Dicho efecto tenía un impacto directo en la estimación de los photo-z ya que, al ser valores artificialmente débiles, obligaban a BPZ a favorecer soluciones a más alto redshift. Este efecto podía verse claramente a través de la aparición de un pico artificial en la distribución de redshift $n(z)$ a un z>>2.5. Las magnitudes límite hicieron no solo que dicho pico desapareciera, alojando dichas galaxias a soluciones a bajo z, sino que permitió mejorar la calidad de las selecciones de galaxias delante y detrás del cúmulo. Finalmente, una vez que BPZ se aplicó sobre dicha fotometría mejorada, los photo-z fueron comparados con una muestra espectroscópica real de ∼160 galaxies. Esta muestra mostró que los photo-z alcanzaron una precisión δz/(1+zs)=3% para la muestra completa, δz/(1+zs)=2.5% para el ∼80% de la muestra y un δz/(1+zs)=2% para el ∼60%. Los resultados obtenidos estaban en perfecto acuerdo con las expectativas derivadas de las simulaciones, si se tiene en cuenta que los tres primeros filtros de UVIS/WFC3 no se incluyeron en el análisis dada su poca profundidad fotométrica. Con estos photo-zs mejorados, se observó como el parámetro de las ODDs de BPZ permitía realizar submuestras precisas y seguras. Este hecho permitió reconstruir modelos de materia oscura con una precisión mejorada respecto de los modelos obtenidos usando los catálogos originales.

Asimismo, se dedicó una fracción del tiempo de seta tesis a la participación en otros 3 líneas de trabajo, dentro de la colaboración CLASH: el grupo de galaxies a alto z, el grupo de supernovas y el grupo de weak-lensing. Aunque la contribución a seta último línea de trabajo también representó una fracción substantial de trabajo, ha sido excluida del contenido de seta tesis. Sin embargo, resulta convenient mencionar que durante mis visits a la JHU, contribuí a la instalación y validación de los códigos *ColorPro* y BPZ. Asimismo, implementé la misma metodología desarrollada en ALHAMBRA (para generar las imágenes sintéticas F814W) para calibrar fotométricamente las imágenes de SUBARU, mediante la obtención de las ecuaciones de transformación del sistema de filtros de CLASH al sistema de filtros de SUBARU. Finalmente, se lideró la validación de la calidad de los photo-z de los catálojos de dicha pipeline. Como ejemplo de los resultados obtenidos en este grupo de trabajo, se puede acudir al trabajo de Umetsu et al. (2012) publicado en ApJ.

En el capítulo 5, la participación en el descubrimiento de (la que en su momento fue) la galaxia más lejana del universo (a un z>9) es brevemente discutida. Después de desarrollar una fotometría optimizada para MACS1149-JD tanto en las imágenes de *HST* como en *Spitzer*, un análisis exhaustivo del photo-z se llevó a cabo mediante la utilización simultánea tanto de BPZ como del código LePhare. Ambos análisis mostraron un sólido acuerdo donde la posible solución a bajo z fue descartada al ser varios ordenes de magnitud menos probable. El análisis de sus poblaciones estelares hizo posible la estimación, con un 95% de confidencia, confirmó que la galaxia se había formado antes de los 200 primeros millones de años después del Big Bang (z ∼14.0). El resultado de este trabajo fue publicado en la revista Nature (Zheng et al., 2012).

Finalmente, mi participación en el grupo de supernovas representó tres años de trabajo. Durante ese tiempo estuve encargado de realizar el análisis de cada uno de los candidatos a SNIa en thermanos de su photo-z. Tal y como se explica en el captítulo 6, dado que las galaxias host fueron observadas tanto en los campos paralelos del HST/ACS como en las imágenes de gran campo de SUBARU, para poder obtener el máximo de información posible fue necesaria la utilización y combinación de ambas

bases de datos. En aquellos casos en los que la distribución de probabilidad en redshift $P(z)$ para la galaxia host era compatible con una supernova tipo Ia, se contemplo la viabilidad de hacer un seguimiento espectroscópimo. Como resultado de esta colaboración, se genró una nueva muestra de 27 supernovas (13 de las cuales fueron clasificadas como SNIa), donde cuatro se encontraron a un z>1.2. Las estimaciones de los photo-z para todas estas supernovas hizo posible medir la tasa de SNIa hasta un z∼1.8 y, además, proporcionar el primer upper limit para la tasa de SNIa en el rango de redshift 1.8<z<2.4. El resultado de este trabajo fue publicado en la revista ApJ (Graur et al., 2014).

Index

List of Tables

List of Figures

1

Introduction.

1.1 The mathematization of the Universe.

1.1.1 The Field Equation.

As any other discipline in science, Cosmology requires to be supported by a theoretical framework capable to make precise and quantitative predictions about the history of the universe. For almost a century now, the General Relativity (Einstein, 1916) has remained as the most successful theory explaining the observed Universe as a whole. Since gravity is the only fundamental physical force acting on the large scales, it has been given the name of theory of gravity. By means of the Einstein field equation (1.1), the relation between the mass-energy content in the universe and the geometry of the space-time is posed, as expressed in the following equation:

$$G_{\alpha\beta} = -\frac{8\pi G}{c^4} T_{\alpha\beta} - \Lambda g_{\alpha\beta} \tag{1.1}$$

with $G_{\alpha\beta}$ being the Einstein tensor representing the geometry of space-time, $T_{\alpha\beta}$ the stress-energy tensor representing the mass-energy content, Λ the Cosmological constant and $g_{\alpha\beta}$ the metric tensor. Solving the Einstein field equation renders possible to describe the temporal evolution of the universe. Therefore, one of the fundamental goals in General Relativity has been the finding of the right metric, describing the current universe, along with the identification of the material content (including particles, radiation, fields and zero-point energies) that has contributed to the stress-energy tensor.

1.1.2 The Cosmological Principle.

Although the universe that surround us shows lots of structure on small scales, the Cosmological Principle assumes that, on sufficient large scales, the universe must be spatially homogeneous and isotropic at every time during its history. If the Universe may indeed be isotropic, on the one hand, the non-diagonal components of the stress-energy tensor T may vanish (T_{ij}=0, $\forall$ i$\neq$j), since there will not be any anisotropic or friction terms. In addition, if peculiar velocities of galaxies and galaxy clusters are negligible compared to that of the Hubble flow, their contribution to the tensor might

be null either. i.e., T_{i0}=0. On the other hand, if the Universe is also homogeneous, it may have the same physical properties everywhere (i.e., position independent), meaning that quantitates such as the energy density ρ or the pressure p may only be able to vary as a function of the Cosmological Time. In other words, the isotropy and homogeneity in the universe would make the stress-energy tensor to be equivalent to a perfect fluid with density $\rho(t)$ and pressure $p(t)$ related as follows:

$$T_{\alpha\beta} = (\rho + p)u_\alpha u_\beta + p g_{\alpha\beta} \tag{1.2}$$

with u_α being the quadrivector-velocity which, in absence of peculiar velocities, takes the simple components u_α = (1,0,0,0) with the following matricial expression:

$$[T] = \begin{bmatrix} T_{00} & T_{01} & T_{02} & T_{03} \\ & T_{11} & T_{12} & T_{13} \\ & & T_{22} & T_{23} \\ & & & T_{33} \end{bmatrix} = \begin{bmatrix} -\rho & 0 & 0 & 0 \\ 0 & \mathrm{p} & 0 & 0 \\ 0 & 0 & \mathrm{p} & 0 \\ 0 & 0 & 0 & \mathrm{p} \end{bmatrix} \tag{1.3}$$

1.1.3 The Geometry of space-time

In general relativity events in space-time are labeled by the four coordinates x^α of time and space. Neighboring events $ev1$ and $ev2$ at separation dx^α have an invariant separation ds defined by the linear element:

$$ds^2 = g_{\alpha\beta} dx^\alpha dx^\beta \tag{1.4}$$

From a geometrical point of view, the metric tensor $g_{\alpha\beta}$ can be understood as a function of position in space-time, which univocally defines distances, areas or volumes between two points x^α and x^β, by integrating their differential elements.

$$S = \int_{s_0}^{s_1} ds^2 = \int_{s_0}^{s_1} \sqrt{|g_{\alpha\beta}|} dx^\alpha dx^\beta \tag{1.5}$$

The simplest case of an homogeneous (invariant to translations) and isotropic (invariant to rotations) metric tensor is that given by the (linear) Minkowski form:

$$ds^2 = -(cdt)^2 + (dr)^2 + r^2(d\theta^2 + sin^2\theta d\phi^2) = -(cdt)^2 + dl^2 \tag{1.6}$$

with the following matricial expression:

$$[g] = \begin{bmatrix} g_{00} & g_{01} & g_{02} & g_{03} \\ & g_{11} & g_{12} & g_{13} \\ & & g_{22} & g_{23} \\ & & & g_{33} \end{bmatrix} = \begin{bmatrix} -c^2 & 0 & 0 & 0 \\ 0 & 1 & 0 & 0 \\ 0 & 0 & r^2 & 0 \\ 0 & 0 & 0 & r^2 sin^2\theta \end{bmatrix} \tag{1.7}$$

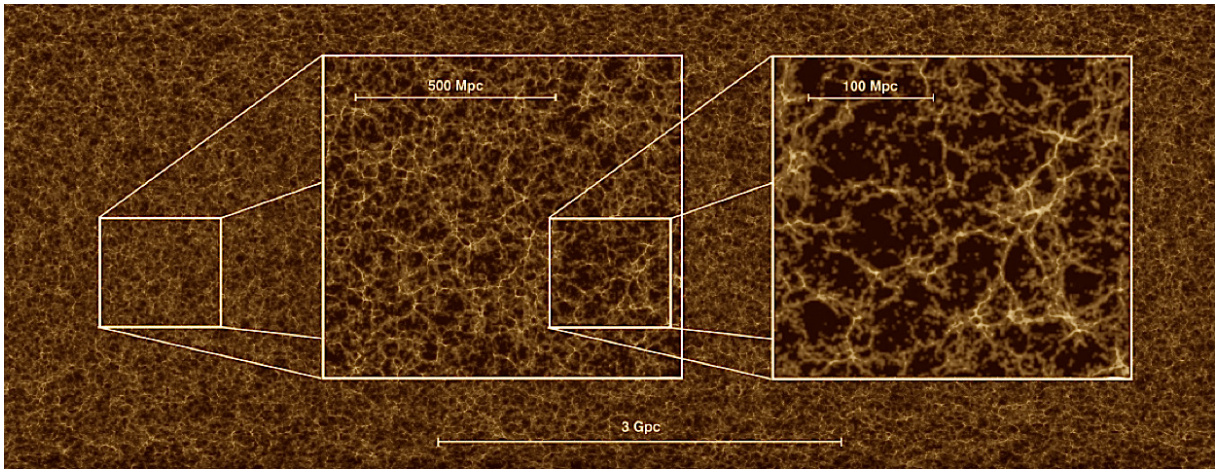

Figure 1.1 Illustration of the Cosmological Principle. Although the nearby universe shows lots of structure, on sufficient large scales might be spatially homogeneous and spatially isotropic at every time during its history.

$$ds^2 = g_{00}dt^2 + g_{11}dr^2 + g_{22}d\theta^2 + g_{33}d\phi^2 \tag{1.8}$$

1.1.4 The Robertson-Walker metric.

Robertson (1935) and Walker (1936) independently showed that the most general description for the field equation was a solution expressed in spherical coordinates, with symmetric and scalable spatial component (a) and an arbitrary curvature (ϵ) . This equation, known as the Robertson-Walker metric, was defined as follows:

$$ds^2 = -(cdt)^2 + a^2(t)((\frac{dr}{\sqrt{1-\epsilon r^2}})^2 + r^2 d\phi^2) \tag{1.9}$$

1.1.5 Distance Measures.

For radial light rays ($d\phi^2 = 0$) that travel on null geodesics (ds^2=0) the metric simplifies and the temporal dependency with the scale factor ($a(t)$) defines different sets of distances in the universe:

1. **Proper and comoving distance**: the comoving distance (D_c) is a fundamental time-independent distance measure in cosmology between two comoving observers. Complementary, the proper distance (D_p) is time-dependent and evolves as the scale factor, even if the radial comoving coordinate r remains constant.

$$D_p = a\int_0^r \frac{dr}{\sqrt{1-\epsilon r^2}} = a\, D_c \quad ;\ where \tag{1.10}$$

$$D_p = \begin{cases} a \times sin(r) & \text{if } \epsilon = +1 \\ a \times r & \text{if } \epsilon = 0 \\ a \times sinh(r) & \text{if } \epsilon = \text{-1} \end{cases}$$

2. **Transverse comoving distance**: The transverse comoving separation of an object with apparent angular size (θ) in the sky is given by:

$$D_{trans} = D_c(\epsilon) \times \theta \tag{1.11}$$

being D_c the aforementioned comoving angular diameter distance. Therefore, transverse comoving distances are ideal to estimate comoving volumes at high redshift.

3. **Angular Diameter distance**: The angular diameter distance relates the physical (instead of the comoving) size of an object to its angular size on the sky. This is given by multiplying the transverse comoving distance by the scale factor as expressed in the following equation:

$$D_{ang} = a \times D_{trans} \tag{1.12}$$

An worth mentioning that D_{ang} does not increase to infinity with redshift. It reaches a maximum (around z $\sim$ 1.5 for ΛCDM model) and then decreases again. Thus, objects of the same physical size appear larger to the observer if they are located at z = 3 compared to z = 1.

4. **Luminosity Distance**: In Euclidean space the flux of an object decreases with the inverse square of the distance. The distances defined above do not obey this rule because space expands during the travel time of the photons and the flux is further diluted. The luminosity distance (D_{lum}) obeys the inverse square law and so is related to the other distance measures in the following way:

$$D_{lum} = \frac{D_{ang}}{a^2} = \frac{D_{trans}}{a} \tag{1.13}$$

1.1.6 The cosmological redshift.

For an isotropic and homogeneous universe, the Robertson-Walker metric explains the observed $redshift$ as a natural consequence of a varying scale factor with time ($a(t)$). The cosmological redshift is so produced by the expansion of the universe itself, which causes the light emitted by distant sources to be redshifted when observed today; i.e., increasing their wavelengths as it does the scale factor.

By means of the definition of the proper motion (eq. 1.10), the apparent motion of a distant source within the space-time can be derived as indicated in the following equation:

$$\dot{D}_p = v_{tot} = \dot{a}D_c + a\dot{D}_c = HD_p + a\dot{D}_c = (v_{geo}) + (v_{kinem}) \tag{1.14}$$

where the first final term (v_{geo}) refers to the *geometrical* redshift or variation of the proper distance, and the second term (v_{kinem}) corresponds to the *kinematic* redshift or variation of the co-moving distance. Therefore, the cosmological redshift can be characterized by the Hubble constant (H), which represents the expansion rate of the universe in terms of the scale factor at any time:

$$H = \frac{\dot{a}}{a} = H(t) \tag{1.15}$$

Since the scale factor is time-dependent, the Hubble constant will eventually take different values for each cosmic epoch. Rearranging terms in the equation 1.10 and considering a constant comoving distance ($\dot{D}_c$=0) among two time intervals t_0 & t, it is easy to see that:

$$\frac{a_0}{a} = \frac{t_0}{t} = \frac{\nu}{\nu_0} = \frac{\lambda_0}{\lambda} = 1 + z \tag{1.16}$$

This equation, relating the observed redshift z with the scale factor a, is of great significance for cosmology since for most extragalactic sources the $redshift$ is the only information about the distant that can be retrieved.

1.1.7 The Friedman Equations

Once the Robertson-Walker metric (for an isotropic and homogeneous universe) and the stress-energy tensor (for a perfect fluid) are defined, the Einstein field equation leads two a set of two non-lineal, second-order equations, known as the Friedman equations, which express the macroscopic evolution of the Universe in terms of the temporal variation of the scale factor $a(t)$. These equations are sumarized as follows:

$$\frac{\ddot{a}}{a} = -\frac{4\pi G}{3}(\sum_i \rho_i + 3\,p_i) + \frac{\Lambda}{3} \tag{1.17}$$

$$\left(\frac{\dot{a}}{a}\right)^2 = \frac{8\pi G}{3}\sum_i \rho_i - \frac{\epsilon}{a^2} + \frac{\Lambda}{3} \tag{1.18}$$

where G is the Newton's gravitational constant, p_i and ρ_i represent the pressure and energy density contribution for the i^{th} constituent, ϵ represents the effect of the curvature and Λ the cosmological constant [1]. Whereas the first equation corresponds to the balance of forces, the second equation corresponds to the conservation of energys in the universe. The signs on these equations indicates the physical impact of the different constituents. Whereas the "-" sign indicates contraction effect the "+" sign indicates repulsion effect.

[1] For simplicity in the notation, the speed of light was normalized to $c = 1$.

1.1.8 The equation of state

In order to derive theoretical predictions of the temporal evolution of the scale factor from equations 1.17 and 1.18, the equation of state (EOS) is required relating pressure to density, for the various components that are contributing to the total energy density. This way, the Fridmann equations can be combined to yield the adiabatic equation:

$$\dot{\rho} = -3\left(\sum_i \rho_i + p_i\right)\frac{\dot{a}}{a} \tag{1.19}$$

Assuming interactions among different constituents of a cosmic fluid to not exist, the total pressure p can be defined as the sum of partial p_i pressures and the total energy density ρ as the sum of the energy densities ρ_i. So, different constituents (matter, radiation, dark energy,...) will define different equations of state. Therefore, the evolution of the expansion rate will come parameterized by the dominant equation of state (ω^i) at any cosmic time:

$$p = \omega\rho \quad \Longrightarrow \quad \dot{\rho} = -3\left(\sum_i \rho_i(1+\omega^i)\right)\frac{\dot{a}}{a} \tag{1.20}$$

Integrating out the equation 1.19, the evolution of the energy density (ρ) as a function of the scale factor (a) and the dominant equation of the state (ω) can be easily derived:

$$\int_\rho^{\rho_o}\frac{\dot{\rho}}{\rho} = -3\,(1+\omega)\int_a^{a_0}\frac{\dot{a}}{a} \quad \Longrightarrow \quad \left(\frac{\rho}{\rho_o}\right) = \left(\frac{a}{a_o}\right)^{-3(1+\omega)} \tag{1.21}$$

For the three components which have dominated the EOS at different times, the dependence between the energy density and the scale factor can be described as follows:

- **Matter**: $\Longrightarrow \quad w = 0 \quad \Longrightarrow \quad p_m = 0 \quad \Longrightarrow \quad \rho_m \propto a^{-3}$
- **Radiation**: $\Longrightarrow \quad w = 1/3 \quad \Longrightarrow \quad p_r = \rho_r\, c^2/3 \quad \Longrightarrow \quad \rho_r \propto a^{-4}$
- **Dark Energy**: $\Longrightarrow \quad w = \text{-}1 \quad \Longrightarrow \quad \rho_\Lambda = \text{const} \quad \Longrightarrow \quad p_\Lambda = \text{-}\rho_\Lambda$

1.1.9 The mean energy density.

Based on the what has been posed before, it is customarily to express the evolution of the scale factor in the second Friedman equation (1.18) as a function of all possible energy densities:

$$\left(\frac{\dot{a}}{a}\right)^2 = \frac{8\pi G}{3}(\rho_m + \rho_r + \rho_\epsilon + \rho_\Lambda) \tag{1.22}$$

where ρ_m represents the mean mass density of non-relativistic matter (mainly baryons and non-baryonic dark matter), ρ_m the mean mass density of radiation and relativistic particles (mainly low

mass neutrinos), ρ_ϵ the effect of the curvature of space and ρ_Λ the value of the dark energy. Being the last two terms expressed as follows:

$$\rho_\epsilon = -\frac{3\epsilon}{8\pi G a^2} \tag{1.23}$$

$$\rho_\Lambda = \frac{\Lambda}{8\pi G} \tag{1.24}$$

In the special case of an Universe without curvature (ϵ=0), it is defined the *critical density* (ρ_c) which may separate eternally expanding world models from those that may re-collapse eventually in the future.

$$\rho_c = \frac{3H^2}{8\pi G} \quad \Longleftrightarrow \quad \rho_{c,0} = \frac{3H_0^2}{8\pi G} \quad (if \;\; t = t_0) \tag{1.25}$$

Finally, the dimensionless energy density parameters are expressed in terms of the normalized $\rho_{c,0}$, which represents just the amount of energy density required to make current universe perfectly flat. These parameters are derived as follows:

$$\Omega \equiv \frac{\rho}{\rho_c} = \sum_i \frac{\rho_i}{\rho_c} = \sum_i \Omega_i = (\Omega_m + \Omega_r + \Omega_\Lambda) \tag{1.26}$$

1.1.10 The Hubble Constant

The Hubble constant (H) is one of the fundamental parameters in cosmology. As a result of the combination of the equations (1.17, 1.18 & 1.21), this equation globally relates the expansion rate of the universe with the energy density parameters, the dominant EOS, the scale factor or the redshift:

$$H = \left(\frac{\dot{a}}{a}\right) = H_o \sqrt{\sum_i \Omega_{io} \left(\frac{a_0}{a}\right)^{3(1+\omega_i)}} = H_o \sqrt{\sum_i \Omega_{io}(1+z)^{3(1+\omega_i)}} \tag{1.27}$$

where its present value, represented as H_0, takes the value of ∼65 Km/s/Mpc.

1.1.11 Age of the Universe

It worth noting that different energy densities, taking place at different cosmological epochs, will not only dictate the evolution of the scale factor (a) but also determine the age of the universe (t). This inter-dependence is described as follows:

$$t = \int_0^t dt = \int_0^a \frac{da}{aH} = \int_0^a \frac{da}{aH_o \sqrt{\sum_i \Omega_{io} \left(\frac{a_o}{a}\right)^{3(1+\omega_i)}}} \tag{1.28}$$

or as a function of the cosmological redshift z:

$$t = \int_0^t dt = \int_z^\infty \frac{dz}{H\,(1+z)} = \int_z^\infty \frac{dz}{H_o(1+z)\sqrt{\sum_i \Omega_{io}(1+z)^{3(1+\omega_i)}}} \tag{1.29}$$

Once again, considering just the most representative EOS, the age of the universe can be expressed as a function of the scale factor as follows:

- **Matter**: $\Longrightarrow \quad w = 0 \quad \Longrightarrow \quad a \propto t^{2/3}$
- **Radiation**: $\Longrightarrow \quad w = 1/3 \quad \Longrightarrow \quad a \propto t^{1/2}$
- **Dark Energy**: $\Longrightarrow \quad w = \text{-}1 \quad \Longrightarrow \quad a \propto \exp\left(\sqrt{\frac{8\pi G}{3}}\rho\, t\right)$

1.1.12 The Deceleration parameter

To characterize whether the current expansion of the universe is decelerating ($\ddot{a} < 0$) or accelerating ($\ddot{a} > 0$), it is defined the *decelerated parameter*. This parameter, which represents the temporal variation of the expansion rate of the universe, can be expressed as a function of the Hubble constant (left hand-side) or as a function of the dimensionless energy density parameters (right hand-side), such as indicate the following equations:

$$q = -\frac{\ddot{a}}{a}\frac{1}{H^2} \quad \Longleftrightarrow \quad q = \frac{1}{2}(\sum_i \Omega_i + 3\omega^i\Omega_i) \tag{1.30}$$

Recent studies suggest that the universe is currently undergoing an accelerated expansion ($q_0 < 0$) meaning that the contribution to the energy density given by the cosmological constant ω_Λ has to differ significantly from zero. A complete list with the *decelerated parameters* for all possible world-models, is included in the Appendix A.2.

2

Observational Cosmology

Cosmological observations are difficult in general, simply because the majority of the Universe (and with it most of the sources it contains) is very far away from us. Distant sources are very dim. This explains why our knowledge of the Universe runs in parallel with the development of the large telescopes and sensitive detectors. The most important aspect of cosmological observations is the finite speed of light, which renders possible to look back into the past. The finite speed of light, in an euclidean space, implies that we can only observe points in space-time for which $|r| = c \times \delta t$ ($\delta t \equiv$ time interval). The set of points in space-time which satisfy this condition are called our *observable Universe*. This strong observational restriction implies that our ambition to observe (and study) the entire Universe is unfeasible. Only if the Universe turns out to have an essential "simple" structure, we will eventually be able to mind it, by means of the combination of accurate astronomical observations and precise theoretical modeling.

As introduced in Chapter 1, the standard cosmological model is based on the assumption that, on sufficiently large scales, the Universe must be homogeneous and isotropic (Cosmological Principle). This principle states that the general statistical properties[1] of the Universe should not depend on the (arbitrarily) selected line-of-sight, and so there is not obvious reasons about why the inferred properties of our *observable* Universe could not be extended to those $un-observable$ regions of the Universe. Likewise, throughout Appendix A, the most relevant events that occurred in the Universe over time are briefly listed and explained. This compilation-model of the Universe (the ΛCDM) not only provides cosmologist with precise explanations about the physical processes that governed the evolution of the Universe, but also yields a set of observables (the cosmological parameters) which serve to eventually validate/reject the theoretical model itself.

Therefore, the scope of observational cosmology is to design (and carry out) amples set of accurate observations, to derive and constrain the values of the different cosmological parameters. Fortunately, nowadays there exist more than one independent estimate for each cosmological parameter, making its determination highly redundant. This very aspect is considerably more important than the precise

[1] such as the matter and radiation power spectra, the mean energy density, CMB temperature, space-time curvature, abundance of primordial elements, ...

values of the parameters themselves, because it provides a test for the consistency of the cosmological model.

Nowadays, there are two pillars upon which modern cosmology is fundamentally based: the cosmic microwave background (CMB) radiation and the large-scale structure (LSS) of matter. On the one hand, the analysis of the CMB anisotropy power spectrum[2] has yield precise information about the physical conditions governing the early-Universe (when radiation and matter were still coupled), along with very restrictive values for (almost) all of the cosmological parameters. On the other hand, the study of the LSST of galaxies and the abundances of gravitationally bounded structures (such as clusters or super-clusters), provides valuable information to estimate the energy density content and the physical mechanisms dominating the contemporary-Universe. Even though only the spatial distribution of visible (baryonic) matter can be observed, assuming that the galaxy distribution traces (approximately) the underlying distribution of dark matter, the power spectrum of the matter density fluctuations can also be retrieved[3]. Understanding how the co-moving density of matter has evolved (and clustered) as a function of redshift, can be used to validate the cosmological model since these global evolutionary trends, are mainly dictated by the cosmological parameters Λ and Ω_m.

2.1 The Redshift Surveys

Due the the lack of references in the sky, our view of the Universe (and so the information we can register in an astronomical image) results in an artificial 2D projection, where all astronomical sources collapse over the celestial sphere. To be able to empirically retrieve (upon others) physical properties such as the Power Spectrum of Density Fluctuations, the distribution or the evolution of matter in the Universe, it becomes absolutely necessary to calculate which are the distances to all the astronomical sources that we can observe. i.e., to retrieve the 3D cosmological depth. Whenever this information becomes available, it renders possible to put the galaxies in order according to their distances and so, as mentioned before, to infer in which cosmological epoch the light we are receiving today was originally emitted by the sources.

During the last decades, the advent of wide-field and high sensitive imaging detectors (CCDs), the fiber multi-object spectrographs (FMOS), the new generation of 8-10m telescopes and the development of automatic pipelines capable to accurately infer distances from thousands to millions of distant galaxies in a reasonable amount of time, has prompted the emergence (or planning) of many different observational programs. All these redshift surveys, briefly summarized in the Appendix B, have made possible to progressively increase the number of known galaxies at different cosmic times and so unveil the large scale structure of the universe.

[2]The outstanding improvement in the knowledge of the properties of the CMB radiation has been possible thanks to the different generations of space missions (COBE (Bennett et al.,1992), WMAP (Jungman et al.,1996) and Planck (Planck Collaboration, 2011)) which have progressively increased the sensitivity and the angular resolution of the observations.

[3]The connection between dark matter and galaxies is parametrized by the so-called *linear bias factor b*, defined as the ratio of the relative overdensities of galaxies to dark matter.

2.2 Measuring the cosmological redshift.

As introduced in Chapter 1 (Section 1.1.6), there exist two well-differentiated physical processes that cause light emitted from distant galaxies to be redshifted. On the one hand, the *kinematic* redshift (z_{kin}) corresponds to a variation in the energy frequency emitted by a source due to its proper motion (Doppler effect). On the other hand, the *cosmological* (or *geometric*) redshift (z_{cos}) corresponds to a variation in the energy frequency caused by the recessional velocity of a galaxy, consequence of being (both galaxy and radiation) embedded on an expanding Universe. As explained in Section 1.16, the quantification of a galaxy redshift serves to infer for how long the radiation has been traveling through space-time. Through this work, since we will face the study of distant sources in the Universe, whenever it is refered to a galaxy "redshift", it may be interpreted as a galaxy "cosmological redshift".

When attending to the methodology utilized to derive the galaxy redshifts, cosmological surveys may be split in two main families: the spectroscopic and the photometric surveys.

2.2.1 Spectroscopic surveys.

On the one hand, the spectroscopic approach yields a direct measurement of every source spectrum. The analysis of the spectrum provides direct information not only on the spectral redshift but also on the chemical content (the spectral-type) of the source. Although this kind of approach may look ideal for redshift estimations, it also shows several limitations.

- *Observational threshold.* Spectroscopic samples are typically limited to the brightest sources (I∼24 mag) since the investment in time required to gather high signal-to-noise spectra (and so properly differentiate spectral features) is enormous. This fact introduces a selection function (so-called *Malmquist* bias), favoring the detection of intrinsically brightest objects at every redshift range. An effect which becomes specially significant for distant sources, since brightest objects are typically the rarer or least representative in the Universe.

- *Completeness factor.* Even with the last generation of fiber multi-object spectrographs (FMOS), there is a maximum number of fibers that can be simultaneously allocated on the plate per exposure. Apart from the fact that it sets a timing in the observational process to cover a complete field, this minimum physical separation among fibers introduces another bias in the selection function (*crowding* effect). This effect becomes specially significant for the study of crowded fields, such as star or galaxy clusters.

- Additionally, spectroscopic samples demand photometric catalogues for identification and target selection purposes[4]. This means that spectroscopic samples have to rely on existing databases or to incorporate new observations which represents an additional time-factor.

[4]For surveys which target objects of specific interest, the multi-color data is used to preselect galaxies for spectroscopic observations. One of the most evident examples would be the study of z>3 Lyman-break galaxies by means of the Drop-out technique

2.2.2 Photometric surveys.

On the other hand, the photometric approach utilizes multi-wavelength observations to derive low resolution spectra. By analyzing the global photometric information, this technic provides redshift samples in a quick and (almost) inexpensive way. With the availability of wide-field photometric detectors (CCDs), this kind of approach is capable of observing much *deeper* samples of astronomical sources (I∼28 AB mag) for an *enormous* amount of sources in a relatively small fraction of time. Therefore, this photometric approach makes possible the analysis of objects which would be too faint for conventional spectroscopy, and so extends the cosmological studies to even earlier epochs.

Likewise, this technic is not free of inconveniences, being the most relevant the ones list below.

- Being an inverse problem, the indirect estimation of a galaxy redshift based on their colors make it strongly depend on: 1. the quality of the data (in terms of the signal-to-noise) or the wavelength coverage. Since the spectral features evolve with redshift, a non ideal observational window may lead to complicated selection functions or to unavoidable degeneracies in the color-z space
- Typically, it provides low resolution spectra for the observed sources (so-called photo-spectra). Even though during the last decade the number of photometric filters involved has increased considerably (from 4 to 60), in all cases they provide a much poorer vision of the Spectral Energy Distribution (SED) of the sources. The detection of important emission lines requires the usage of medium/narrow-band filters.
- In general, this approach is strongly dependent on the wavelength coverage. Since the spectral features evolve with redshift, a non ideal observational window may lead to complicated selection functions or to unavoidable degeneracies in the color-z space.
- Although it has been proven the high efficiency of this technics when using large set of filters (specially narrow-band filters) to retrieve the z, its typical accuracy rapidly decreases as it does the photometric signal-to-noise.

2.3 Photometric Redshifts.

Multi-band photometry can provide (very) low resolution spectra and so be used to derive redshift samples of galaxies and other extragalactic sources. As explained in Yee (1998), the idea of using broad band photometry to estimate the redshifts of the galaxies was suggested as early as 35 years ago by Baum (1963). He obtained photoelectric photometry of early-type galaxies in distant galaxy clusters using 9 bands. He estimated the redshift of the clusters by comparing the spectral energy distributions (SEDs) with those from galaxies in the Virgo Cluster, using primarily the position of the 4000Åbreak in early-type galaxies. Later on, Loh & Spillar (1986), used CCD photometry in 6 filters and obtained redshifts by fitting galaxy SEDs of various morphological types, and attempted to determine ω via galaxy number density as a function of redshift. However, many of the early efforts were hampered by the lack of high quality wide-field digital data, and the difficulties of obtaining a significant and convincing set of verification redshifts.

More recently, with the advent of more efficient and much bigger (arrays of) CCD detectors, it has become feasible to obtain deep multi-color photometry of a large sample of galaxies (up to hundred of thousands) in a quick and efficient manner. The publicly available HDF-N data in 1995 instigated a major revival of interest in photometric redshifts. The very deep images in 4 bands provided an excellent data set for applying the technique to unprecedented depth and redshift, allowing to study galaxy evolution over 90% of the age of the Universe. In addition, it encouraged the development of other scientific fields as the galaxy luminosity function (SubbaRao et al. 1996, Mobasher et al. 1996, Gwyn & Hartwick 1996, Sawicki, Lin & Yee 1997), luminosity density (Connolly et al. 1997, Madau 1998) and the projected spatial correlation function (Connolly et al. 1998, Miralles & Pelló 1998) among other.

Only in the last decades, several thousands scientific publications using HST data have been published carrying out many different photometric redshift analysis. The potential of this technique on galaxy evolution and formation analysis has been beat recently with the discovery of the most distant galaxies known in the Universe (Bouwens et al. 2012, Zheng et al. 2012, Bradley et al. 2013, Coe et al. 2013, Bouwens et al. 2013).

The photometric redshift technics may be (mainly) split into two big families:

2.3.1 Empirical Training-set methods.

The empirical training-set methods (Connolly et al. 1995, Brunner et al. 1997, Wang et al. 1998, Wang et al. 1999, Firth et al. 2003, Vanzella et al. 2004, Collister et al. 2004, Hsieh et al. 2005, Wadadekar 2005, Way et al. 2006, Wang et al. 2007, Wang et al. 2008, Li et al. 2008, Wang et al. 2008a, Ball et al. 2008, Wang et al. 2008b, Wolf 2009, Way et al. 2009, Budavári 2009, Zhang et al. 2009, Freeman et al. 2009, Wang et al. 2010a, Wang et al. 2010b, Carliles et al. 2010, Gerdes et al. 2010, Bonfield et al. 2010, Way 2011, Abdalla et al. 2011, Laurino et al. 2011), aims at obtaining an optimal fit between the photometric and the redshift measurements, and uses this fit to predict the redshift of objects with only photometric data. It means that these methods require a training set of data in which both the photometry and the redshift are available. Although these methods have the advantage of being empirical, and hence are not dependent on having an exact knowledge of the SEDs of galaxies (including evolutionary models or extinction laws), obtaining a proper and sufficiently large training sets is very often expensive observationally.

It is worth noting that one demerit of this kind of approach, comes from the necessity of having a previous knowledge of an ample set of galaxy redshifts. This fact automatically sets all the observational limitations from the spectroscopy to the photometric samples. In other words, it is unreliable when used for objects at fainter magnitudes than the training set. In addition, this condition makes unfeasible the application of this kind of approach to any full-sky deep photometric surveys. Furthermore, extrapolating the fit to galaxies with magnitudes or redshifts outside the ranges (to other regions in the sky or different datasets) must be done with great caution, since it will produce additional unknown uncertainties.

2.3.2 SED-fitting methods

In the SED fitting methods (Koo 1985, Gwyn & Hartwick 1996, Fernández-Soto et al. 1999, Benítez 2000, Bolzonella et al. 2000, Arnouts et al. 2002, Babbedge et al. 2004, Ilbert et al. 2006, Feldmann et al. 2006, Brammer et al. 2008, Assef et al. 2008, Kotulla & Fritze 2009, Dahlen et al. 2010), photometric redshifts are estimated by comparing observed galaxy fluxes at the ith photometric band, f_i^{obs}, with those expected from a spectral library of templates f_i^{temp}, integrated through the filter transmission curves. The analysis, which relies on a χ^2 minimization criteria, runs over a previously defined template-redshift space. In other words, this approach assign photometric redshifts to an object by finding the template and redshift that best reproduce the observed flux. The so-computed merit function of the fitting residuals can be expressed as:

$$\chi^2 = \sum_{i=1}^{N} \frac{[f_i^{obs} - a f_i^{temp}(z,T)]^2}{\sigma_i^2} \tag{2.1}$$

where N is the number of photometric passbands (filters), σ_i refers to the observational uncertainties in the ith band, and a indicates the scale factor which is chosen in such a way as to minimize χ^2 for each template, as follows:

$$a = \sum_{i=1}^{N} \frac{f_i^{obs} f_i^{temp}(z,T)}{\sigma_i^2} \Big/ \sum_{i=1}^{N} \frac{f_i^{temp}(z,T)^2}{\sigma_i^2} \tag{2.2}$$

It is worth noting that this approach, not only provides the most likely redshift for the observe galaxy but also its best spectral template, supplying additional information regarding the galaxy stellar content, age, activity, chemical enrichments, etc. Since template-fitting methods do not need a previous knowledge about the z, they are preferred when exploring new regimes since their extrapolation is trivial.

One of the key issues in this kind of methodologies is the proper selection of the spectral library, where it has to be decided whether it is more convenient to rely on an empirically- or synthetically-derived set of templates. On the one hand, empirical libraries (Coleman et al. 1980) take advantage of using directly the SED information from real nearby galaxies (spanning the whole range of Hubble morphological types (E, Sbc, Scd and Irr)). However, since at earlier cosmological epochs, evolution could play a substantial role (in changing both morphological and spectrophotometric properties of distant galaxies), the simple extrapolation of galaxy properties from the local Universe to higher redshift, it is not straightforward since there is no solid evidences supporting it. On the other hand, synthetic models do take into account the evolution based on the current state of the Stellar Population Physics. These templates have inherent uncertainties due to uncertainties in the stellar evolution physics (specially latest and fastest stages) along with the uncertainties in the stellar spectral libraries (specially in the UV wavelengths).

3

The Cosmic Evolution.

One of the major topics in Cosmology is the comprehension of the *cosmic evolution*, which can be defined as the variation of a given property with redshift once the physical dispersion of that property (the *cosmic variance*), has been taken into account. In other words, the *cosmic evolution* faces the study of how individual objects, families or even structures (voids, clusters or filaments) at different epochs have evolved their properties with the elapse of cosmic time, i.e., as a function of the cosmological redshift. Given the inhomogeneity of the observed Universe up to scales of several tens of Mpc, the study of *cosmic evolution* implies the analysis of large numbers of similar objects and to sample large enough physical volumes, to capture not only representative averaged properties of the Universe (smoothing out local inhomogeneities), but also to quantify their variance.

Meanwhile, to gather meaningful cosmological samples it is necessary to combine both wide area and depth observations. To properly map out the structures of the Universe and follow its content and properties with redshift, the observations have to satisfy a continuous spectral coverage and good enough spectral-resolution, to avoid complex selection functions when inferring the redshift and the spectral-type identification.

3.1 The ALHAMBRA survey.

The ALHAMBRA (Advance Large Homogeneous Area Medium Band Redshift Astronomical) survey (Moles et al. 2008) has been optimized to detect and measure precise and reliable photometric redshifts for a large population of galaxies over 8 different fields. As it was shown in Benítez et al. (2009b), although counterintuitive, broadband photometric surveys can be significantly shallower, in terms of photometric redshift depth, than well designed, medium band imaging. ALHAMBRA uses a especially designed filter system (see also Aparicio-Villegas et al. 2010) which covers the whole optical range (3500Åto 9700Å) with 20 contiguous, equal-width, non overlapping, medium-band filters along with the standard JHKs near-infrared bands, aiming at covering a total area of 4 $\deg^2$ on the sky separated in 8 non-contiguous regions (Figure 3.1).

The ALHAMBRA-Survey will allow the determination of the global content of the Universe in

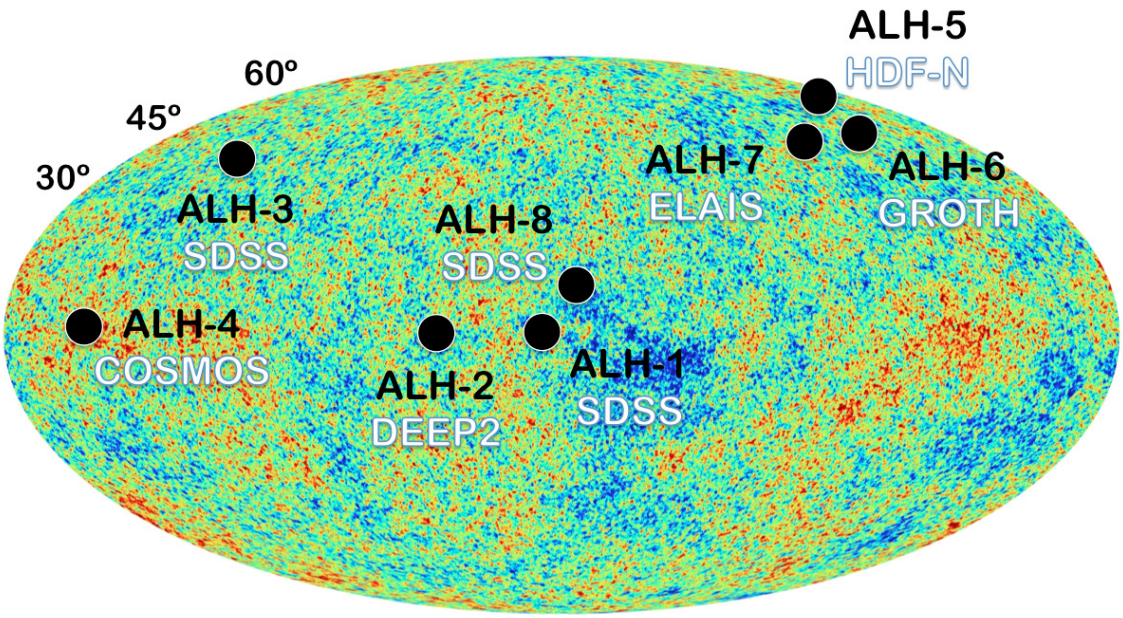

Figure 3.1 The figure shows the different fields observed by the ALHAMBRA survey along with their correspondence with other existing surveys. The mean galactic coordinates are specified in Table 3.1.

representative volumes at every z-value, and to follow its change with z.

The sample covered by the ALHAMBRA observations, covers an important fraction of the observational gap between the observed CMB anisotropies and the clustering of galaxies, approaching the interesting epochs for galaxy and structure formation.

3.2 The ALHAMBRA fields.

As explained in Moles et al. 2008, the ALHAMBRA fields were specifically selected to maximize the observability throughout the year, trying to get as wide a range of RA as possible. This fact increases the feasibility of in short time scales, since the observations had to be systematically repeated for every filter in the photometric system. Meanwhile, the ALHAMBRA fields had to satisfy several additional criteria, such as a low intergalactic extinction (Fig.3.2), no (or few) known bright sources (to avoid saturation issues), high galactic latitude and having partial overlap with other existing surveys and/or other wavelengths. Recalling that the main goal of the ALHAMBRA survey is to probe Cosmic Evolution, it is necessary to cover cosmological meaningful volumes at all redshifts for which a large area coverage and good depth are required. Meanwhile, to beat down the problem of the cosmic variance, (sampling independent volumes), ALHAMBRA defined eight different well-separated areas of the sky where to carry out its observations. These fields are specified in table 3.1.

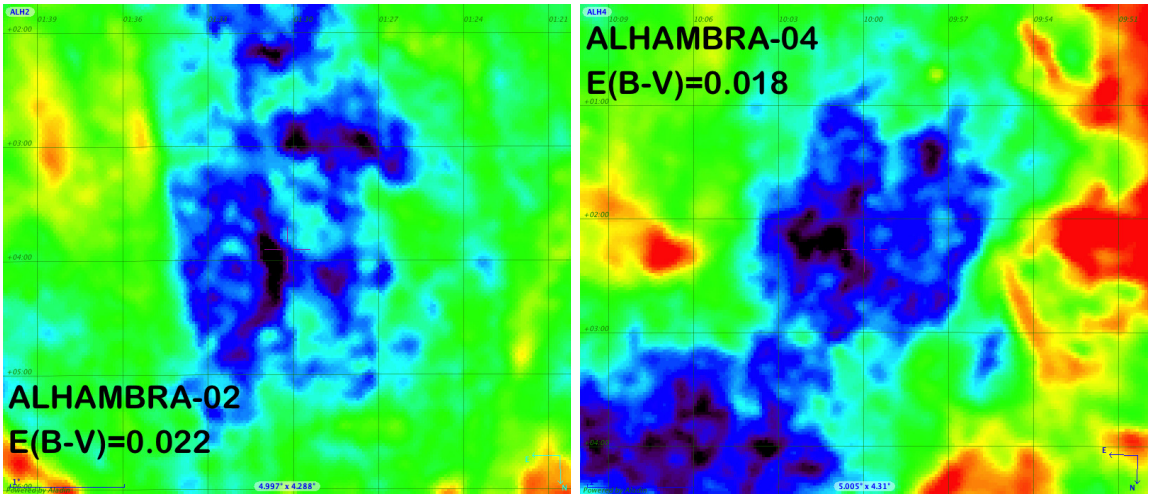

Figure 3.2 As explained in Moles et al. 2008, the ALHAMBRA fields were specifically selected to satisfy several observational criteria such as having a low intergalactic extinction. The figure shows an example of the logarithmic Galactic dust reddening content (for the line of sight) of two fields in ALHAMBRA (ALH2 & ALH4). The emission intensity is color-coded in the figure where the largest emission corresponds to the reddest colors and the lowest emissions to the bluest ones. Reddening estimates came from Schlegel et al. (1998), combining results of IRAS and COBE/DIRBE satellites.

3.3 Observations

The ALHAMBRA survey has imaged a total area of 4.0 deg^2 among eight separated regions of the sky during a seven-year period (2005-2012). Observations were carried out on the 3.5m telescope on the Calar Alto Observatory (CAHA, Spain) making use of the two wide-field imagers in the optical (LAICA, Large Area Imager for Calar Alta) and in the NIR (Omega-2000), both installed at the Prime Focus. The ALHAMBRA fields have been observed whenever the conditions were optimal (seeing<1.6", airmass<1.8), up to reach a total exposure time of ∼700hrs (∼32 hrs of on-target). The integration time for individual CCDs was split into ∼27.8 hrs for medium-band filters and ∼4.2 hrs for broad-band Near Infrared (NIR) filters, as explained in Cristobal-Hornillos et al. 2013, (in prep.).

Although ALHAMBRA-01 has already been observed, its analysis has not been included in this paper due to issues with its primary photometric calibration at the time. For a detailed description of the NIR observations, we refer the reader to Cristóbal-Hornillos et al. (2009). The description of the optical observations will be available in Cristobal-Hornillos et al. 2013 (in prep.).

3.4 Data Reduction

In order to homogenize the data sets from both imagers, NIR images from the OMEGA-2000 detector were converted from their original pixel size, 0.45 "/pix, to 0.221 "/pix to match the pixel size of the LAICA images. This way every detection was referred to the same pixel in either 4096×4096 pixels final images. As explained in Cristóbal-Hornillos et al. (2009), individual images from each run have been dark current corrected, flat fielded and sky subtracted. Bad pixels, cosmic rays, linear patterns and ghost images have also been masked out. Processed images have been finally combined using

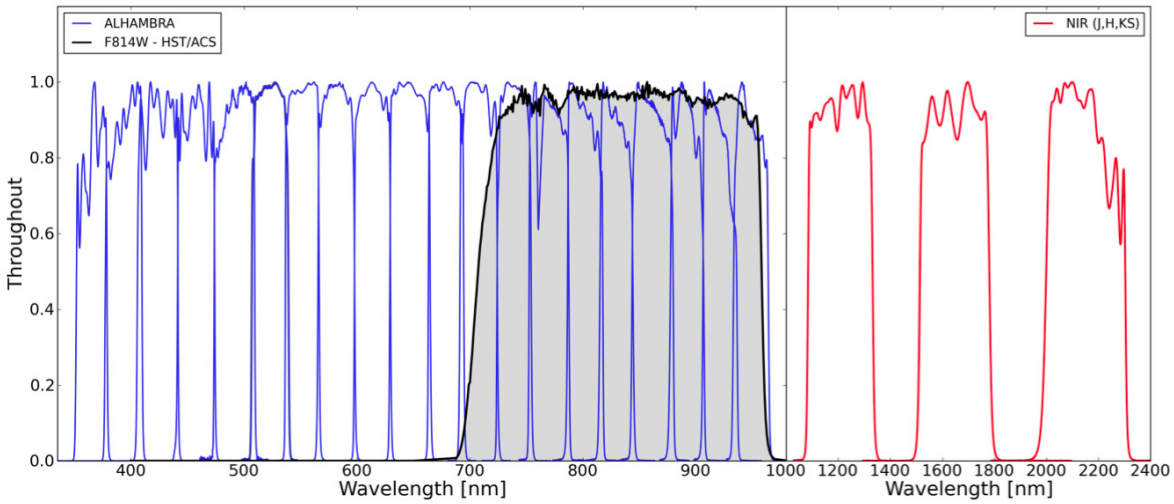

Figure 3.3 The ALHAMBRA survey filter set. On the left-hand side, solid blue lines represent the Optical filter system composed by 20 contiguous, equal-width, non overlapping, medium-band (∼300Å) filters. The solid black line corresponds to the synthetic F814W filter used to define a constant observational window across fields. On the right-hand side, solid red lines represent the standard $JHKs$ near-infrared broad bands. All transmission curves are normalized to its maximum value.

Table 3.1 The ALHAMBRA survey selected fields.

Field Name	Overlapping Survey	RA (J2000)	DEC (J2000)	Area/Eff [deg^2]	Number Images	Detected Sources	Density [#/deg^2]
ALH1	—	00 29 46.0	+05 25 30	0.50 / —	—	—	—
ALH2	DEEP2	01 30 16.0	+04 15 40	0.50 / 0.45	8	67.791	77.144
ALH3	SDSS	09 16 20.0	+46 02 20	0.50 / 0.47	8	68.015	75.000
ALH4	COSMOS	10 00 00.0	+02 05 11	0.25 / 0.23	4	38.464	93.261
ALH5	HDF-N	12 35 00.0	+61 57 00	0.25 / 0.24	4	42.618	82.300
ALH6	GROTH	14 16 38.0	+52 24 50	0.50 / 0.47	8	66.906	77.740
ALH7	ELAIS-N1	16 12 10.0	+54 30 15	0.50 / 0.47	8	79.453	82.185
ALH8	SDSS	23 45 50.0	+15 35 05	0.50 / 0.46	8	75.109	82.452
				3.00 / 2.79	48	438.356	<81.440>

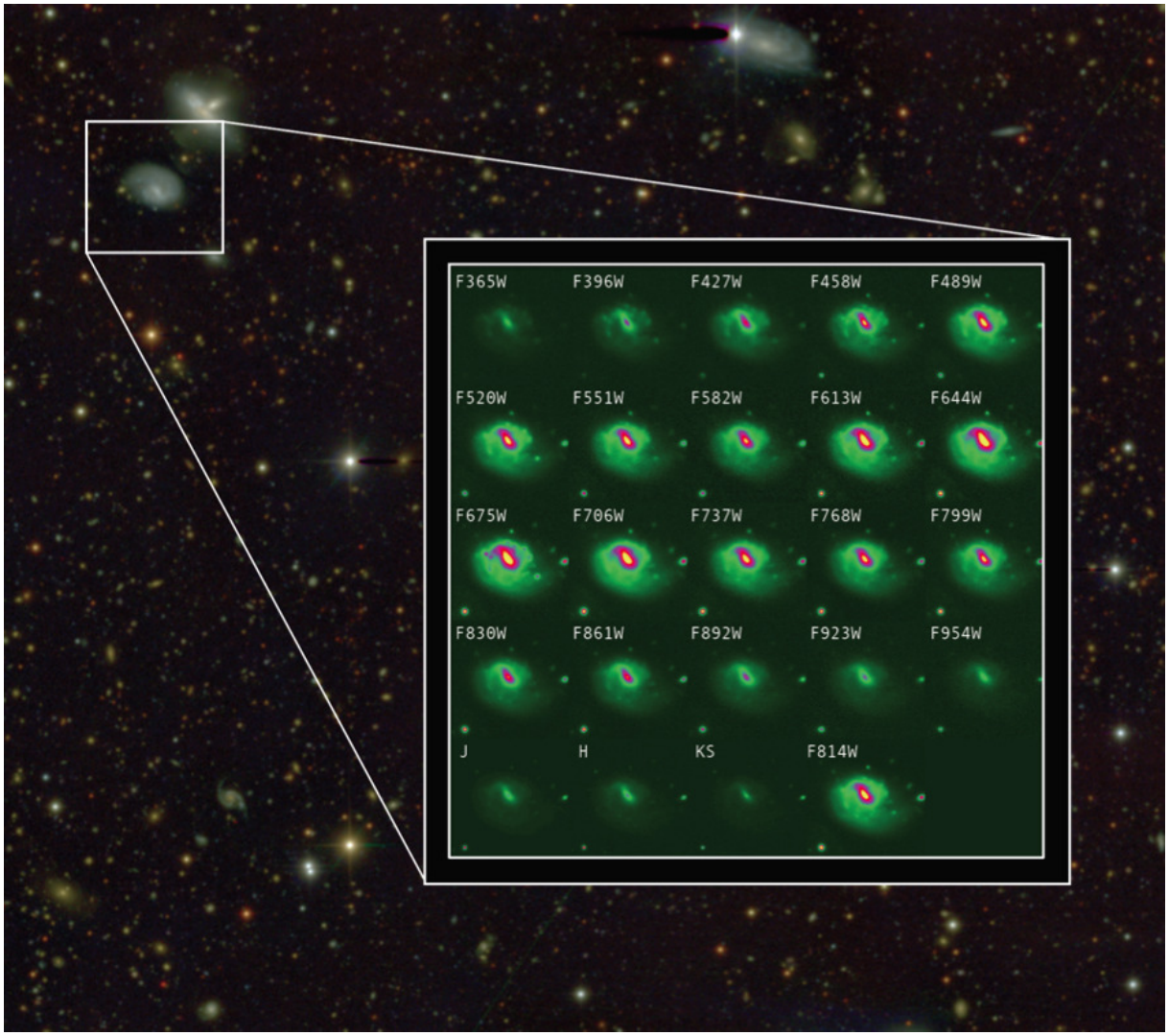

Figure 3.4 The ALHAMBRA survey. The figures shows an example about how a galaxy looks like when observed through the ALHAMBRA filter system. While the optical range is spanned horizontally from top to bottom and left to right, the last row corresponds to the J, H and Ks NIR filters along with the synthetic F814W detection image. The background color image was generated using the *Trilogy* software (www-int.stsci.edu/~dcoe/trilogy/Intro.html).

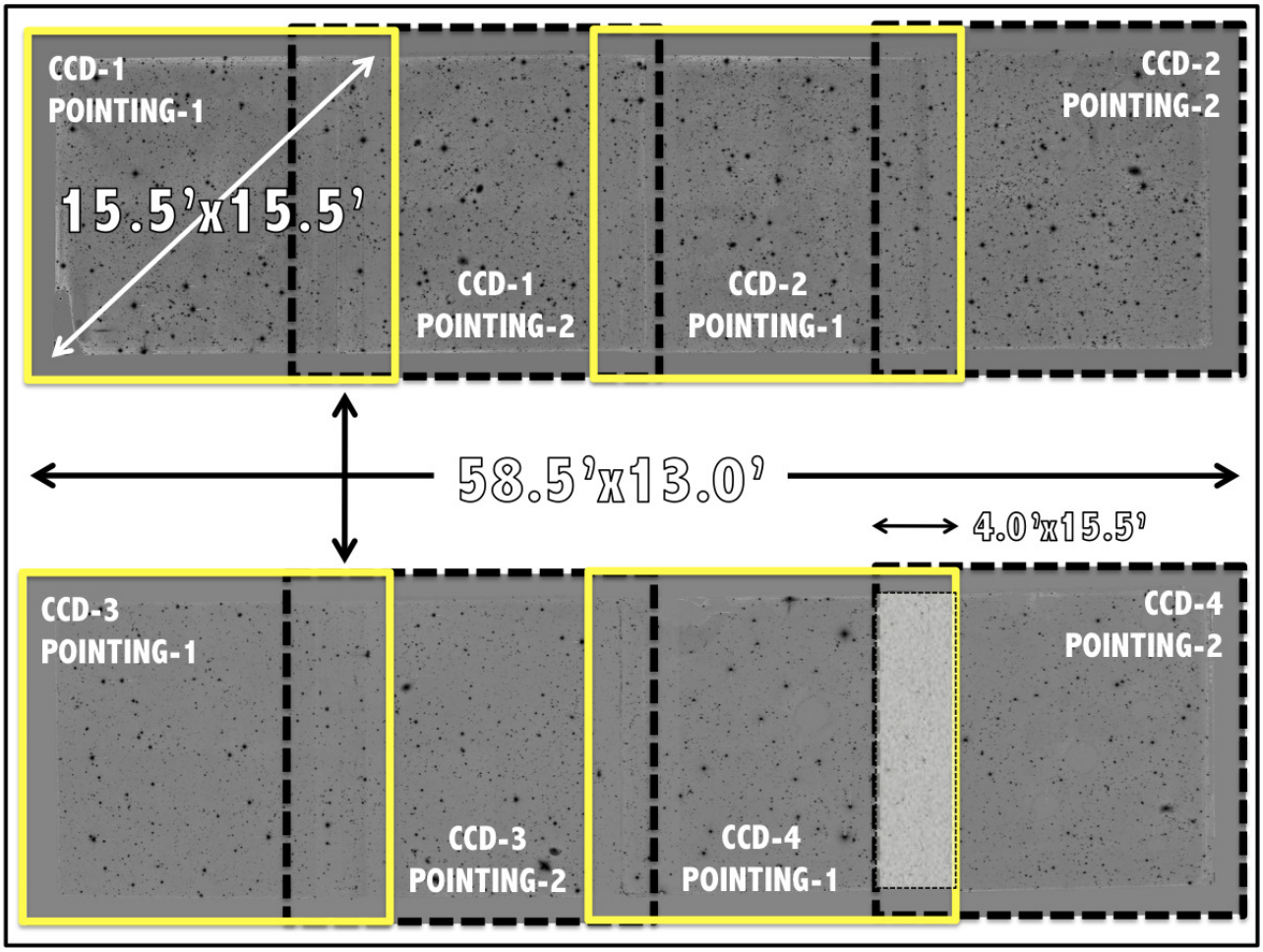

Figure 3.5 Pointing layout for the ALHAMBRA fields. Given the geometrical configuration of the optical imager LAICA, each pointing is composed by four CCDs (as marked with the yellow squares) with an internal gap of ∼13.0'. The combination of two contiguous pointing yields a final layout composed by two strips of 58.5'x15.5' (comprising four individual CCDs) with a separation of ∼13.0'. Contiguous CCDs within each strip show a maximum overlap of 4.0'x15.5'.

SWARP (Bertin et al. 2002) software where applied geometrical distortions have been incorporated in WCS headers.

The total 2.8 deg^2 included in this work are divided in 7 non-contiguous regions of the sky (as summarized in Table 3.1), split in non-overlapping strips composed by 4 individual CCDs, as schematically illustrated in 3.5. Each one of the 48 CCDs represents the minimum area (15.5'×15.5') covered by all the 23 individual filters. To quantify the survey effective area (Section 3.12), FLAG images have been created where pixels not satisfying an established photometry quality criteria have been flagged. Meanwhile both RMS-map and WEIGHT-maps have been generated accounting for the level of photometric uncertainties present across individual images.

3.5 Filter set

As it has been shown in Wolf et al. (2001a) and in Benítez et al. (2009b), once the instrumental setup and exposure time are fixed, the filter set has a powerful effect on the photo-z performance. Table B.1 summarises a small list of different photometric filter systems and their photometric redshift accuracy. The ALHAMBRA survey designed its own photometric system (Benítez et al. 2009b) optimizing both photometric depth and accurate measurements for both Spectral Energy Distribution (SED) and photometric redshift identifications for as many galaxies as possible, along with the detectability of relatively faint emission lines (Moles et al. 2008, Bongiovanni et al. 2010, Matute et al. 2012, Matute et al. 2013). As seen in Fig. 3.3 the system encompasses an optical window ranging from 3500-9700Ådiscretized in 20 constant-width (∼300Å), non overlapping filters with a NIR window given by the standard Johnson NIR bands J, H and Ks. Including both Optical + NIR observations serves to break the so-called color-redshift degeneracies, reducing the fraction of catastrophic outliers and increasing the ALHAMBRA photometric redshift depth. In Fig. 3.4 we show an example about how a galaxy looks like when observed through the ALHAMBRA survey filter system. The main properties for each individual filter are summarized in Table 3.2.

3.6 Primary photometric zeropoint calibration.

Taking advantage of the overlapping areas between ALHAMBRA and the Sloan Digital Sky Survey (SDSS, York et al. 2000), a set of transformation equations among both (optical) photometric systems was initially derived based on a collection of primary standard stars from the Next Generation Spectral Library (HST/STIS NGSL, Gregg et al. 2004), as explained in Aparicio-Villegas et al. (2010).

An exhaustive identification of good photometric stars in the ALHAMBRA fields has been carried out in such a way that only the stars with available SDSS/DR7 photometry were kept. Then, transformation equations from the SDSS/DR7 data are used to obtain the Alhambra photometry in each band for the stellar objects. Photometric zeropoints for optical images have been finally determined as the mean difference between instrumental magnitudes (from transformation equations) and synthetic magnitudes (from the transformation equations) yielding an internal error no larger than a few hundredths of a magnitude for stars in each CCD and filter combination. For an in-depth discussion of the

Table 3.2 Summary of the multiwavelength filter set for ALHAMBRA. The FWHM, the exposure time and the limiting magnitude (measured on 3" diameter aperture) correspond to the average value among the 48 CCDs.

CAMERA	FILTER	λ_{eff} [Å]	FWHM [Å]	$\langle t_{exp} \rangle$ [sec]	$\langle m_{lim}^{(3")} \rangle$ (5-σ)
Optical					
LAICA	F365W	365	279	3918	23.7
LAICA	F396W	396	330	2896	23.8
LAICA	F427W	427	342	2774	23.8
LAICA	F458W	458	332	3079	23.8
LAICA	F489W	489	356	2904	24.2
LAICA	F520W	520	326	2664	24.1
LAICA	F551W	551	297	2687	23.7
LAICA	F582W	582	324	2936	23.8
LAICA	F613W	613	320	2940	23.9
LAICA	F644W	644	357	4043	23.8
LAICA	F675W	675	314	4575	23.5
LAICA	F706W	706	332	5668	23.7
LAICA	F737W	737	304	7095	23.5
LAICA	F768W	768	354	8824	23.5
LAICA	F799W	799	312	8992	23.2
LAICA	F830W	830	296	11436	23.2
LAICA	F861W	861	369	10505	22.9
LAICA	F892W	892	303	9044	22.5
LAICA	F923W	923	308	6338	22.1
LAICA	F954W	954	319	5620	21.5
NIR					
OMEGA	J	1216	2163	5169	22.6
OMEGA	H	1655	2191	5055	21.9
OMEGA	Ks	2146	2412	5050	21.4
Detection					
SYNTH	F814W	845	2366	73522	24.5

calibration of the ALHAMBRA optical photometric system we refer the reader to Cristóbal-Hornillos et al. 2013 (in prep.).

The ALHAMBRA survey has also made use of the spatial overlapping with the 2MASS catalogue (Cutri et al. 2003) to calibrate its NIR images. As explained in Cristóbal-Hornillos et al. (2009) several tens of common point-like sources with high S/N were selected to compute photometric zeropoint offsets with uncertainties of $\sim$0.03 mag. We will discuss the procedure to refine the photometric zeropoints calibrations via SED-fitting techniques in Section XXXX, in the context of the uncertainties reached by the photometric redshifts.

3.7 Multi-wavelength Photometry

As it was throughly described in Coe et al. (2005), measuring multicolor photometry in images with different PSFs is not trivial. To perform good quality multi-color photometry, it is necessary to sample the same physical region of the galaxy and to take into account the smearing produced by different PSFs as seen in Fig. 3.6. We show the distribution of PSFs in the ALHAMBRA survey in Fig. 3.7, separating among Optical, NIR & synthetic F814W detection images, compressing values from 0.7" to 1.6".

A popular way to proceed is carrying out a PSF-homogenization smoothing the whole dataset to the worst seeing condition, making all images look as they had been taken under the same PSF condition (Loh & Spillar 1986, Labbé et al. 2003, Capak et al. 2007). Even though this methodology immediately defines consistent apertures, the general degradation also implies to sacrifice the quality of the best observations down to the level of the worst. Here we have used *ColorPro* (Coe et al. 2006) which accurately corrects for PSF effects without degrading image quality; Laidler et al. 2007; De Santis et al. 2007; Kuijken 2008; Wolf et al. 2008 have also developed similar approaches.

To improve the photometric depth and homogeneity, we relied on deep synthetic F814W images (section 3.9) which are ideal for photometric aperture definitions (given its enhanced S/N) and for galaxy morphology estimations.

3.7.1 PSF-Matched Aperture-Corrected photometry.

ColorPro derives accurate PSF-corrected photometry without degrading high quality images. Initially the software defines every photometric aperture based on the selected detection image. Then it estimates how much encircled flux a galaxy might have missed as a consequence of its PSF by degrading the selected photometry-frame image up to smear other PSF-conditions. The differences in flux measured before and after the degradation are stored and reapplied PSF-correcting magnitudes, as they had all been observed under the same PSF condition. When this procedure runs over the whole dataset, output magnitudes can be easily compared yielding robust photometric colors.

By construction *ColorPro* assumes the selected photometry-frame to have the narrowest PSF and so consistently derive corrections among images. Although desirable, this situation is not always feasible. In the ALHAMBRA survey synthetic we chose F814W images (Section 3.9) for both source

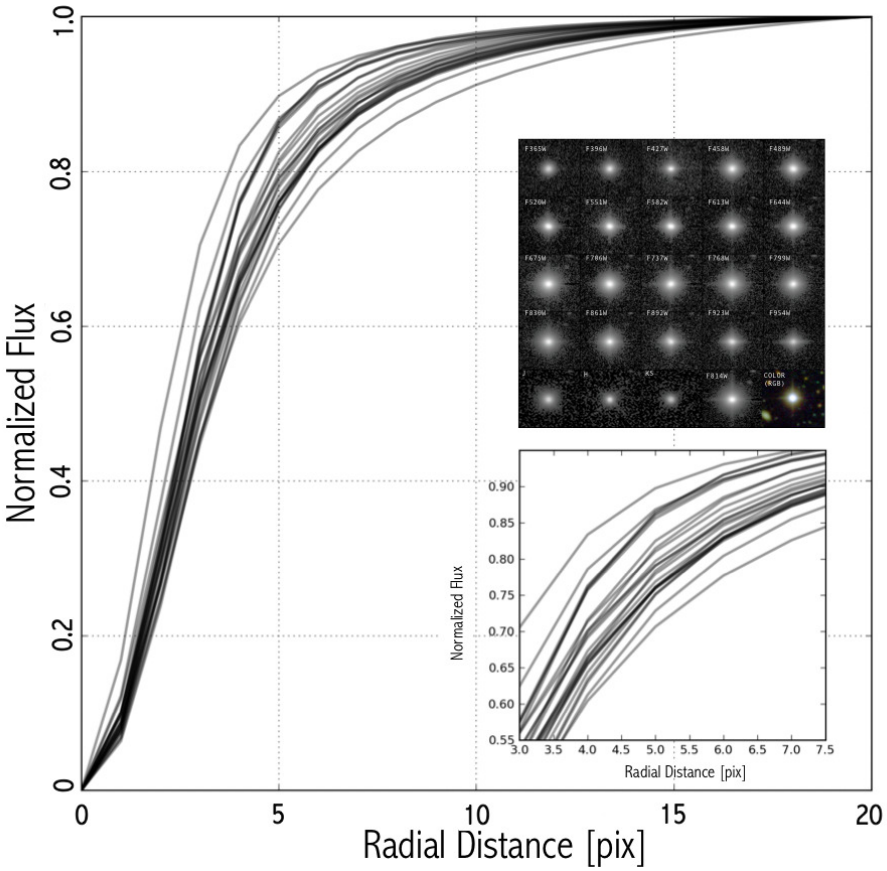

Figure 3.6 Seeing variability across photometric bands. For a single star, solid black lines represent the scatter in the normalized stellar growth curve as a consequence of the varied PSF across filters (insetted top panel). This effect makes the amount of enclosed flux within a fixed aperture to artificially vary, affecting the estimation of accurate photometric colors.

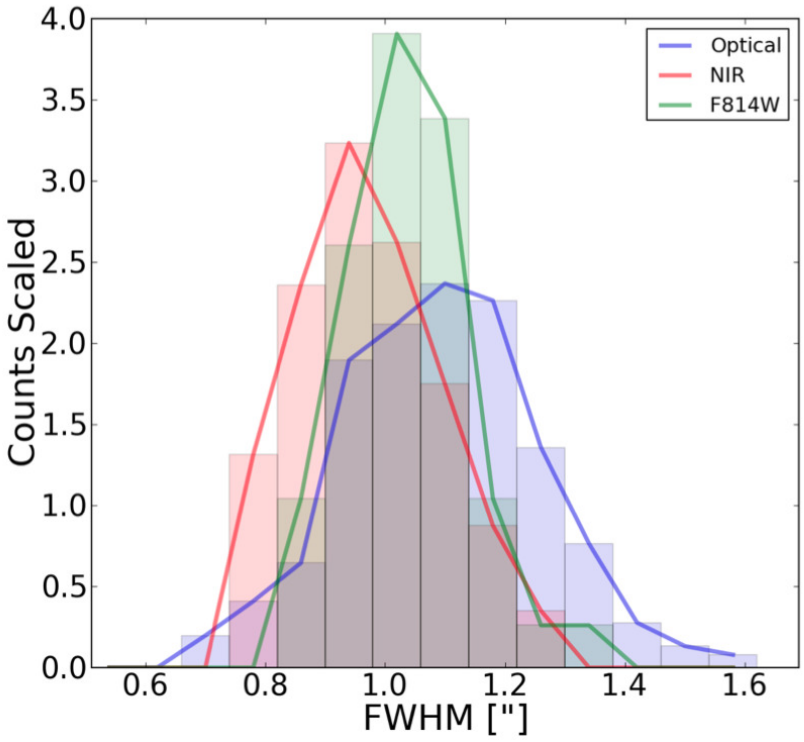

Figure 3.7 Distribution of *seeing* conditions for the ALHAMBRA fields. The figure shows the distribution of PSFs (measured as the FWHM in arcsec) for Optical images (blue), NIR (red) and synthetic F814W detection images (green). Whereas the complete dataset compresses values from 0.7" to 1.6", the Optical images have a mean $< FWHM >\sim$1.1", the NIR images a $< FWHM >\sim$0.9" and synthetic F814W detection images a $< FWHM >\sim$1.0".

detection (as detection image) and PSF-corrections (as photometry-frame). However sometimes individual filters had a sharper PSF than synthetic F814W images meaning that *ColorPro* was not going to account for those "opposite" differences. To get rid of this situation, we updated the software to automatically degrade those images to match synthetic F814W detection image PSF. To do so we relied on the package PSFMATCH from IRAF (Image Reduction and Analysis Facility). This happened in only few percent of the cases.

`SExtractor` (Bertin & Arnouts 1996) ISOphotal apertures produce the most robust colors for faint objects (Benítez et al. 2004) while `SExtractor` AUTO apertures provide better estimations of galaxy total magnitudes. To encompass the usefulness of both measurements, *ColorPro* defines a photometric transformation which provides both `SExtractor` ISOphotal colors and total magnitudes.

Total magnitudes are defined as:

$$M_i = M_i^{ISO} + (M_{det}^{AUTO} - M_{det,i}^{ISO}) \tag{3.1}$$

while the first term corresponds to the standard `SExtractor` ISOphotal magnitude for sources detected on the ith-band, the second term incorporates the PSF-correction (by applying the photometric differences when degrading the detection image (M_{det}) to the ith-PSFs condition ($M_{det,i}$)). Hence, the second term extends `SExtractor` ISOphotal magnitudes into total magnitudes.

Meanwhile ISOphotal colors are derived as:

$$M_j = M_j^{ISO} + (M_{det}^{AUTO} - M_{det,j}^{ISO}) \tag{3.2}$$

$$M_i - M_j = M_i^{ISO} - M_j^{ISO} + (M_{det,j}^{ISO} - M_{det,i}^{ISO}) \tag{3.3}$$

where resulting $M_i - M_j$ colors are just the combination of their `SExtractor` ISOphotal magnitudes plus a second term including their relative PSF-corrections. As expected, those cases with equal PSF the second term might be cancelled out providing colors directly from the `SExtractor` ISOphotal magnitudes. For a more detailed explanation, we refer the reader to Coe et al. (2006).

3.7.2 PSF models

As required by *ColorPro*, it was necessary to generate PSF models for each individual image. We used the package *DAOPHOT* from IRAF (Stetson 1987) which uses an hybrid method to compute PSF models. First, it fits the stars central region by using an analytical function (Gaussian, Lorentzian, Moffat or Penny). Second, the outermost parts (regions connected with the background) are empirical fitted point by point, returning typical residuals between stars and models around $\sim 3\%$.

We initially ran `SExtractor` on each image using a very high threshold ($\sim 100 \times \sigma_{Background}$) to detect only very bright sources. We kept detections classified by `SExtractor` as point-like sources and with $CLASS\_STAR > 0.9$. When plotting the magnitude vs the FWHM for those selected objects, we find they are located in the region of the brightest and most compact sources (Section 3.14.1). To avoid both the very bright sources (mostly saturated stars) and the very faint ones (possibly misclassified

galaxies), we selected detections with magnitudes in between 16<m<22.5, yielding a final sample of several hundred of stars per image.

Afterwards, we visually rejected stars with contaminating neighbors and generated mosaic-like images (Fig. 3.8). These images dramatically decreased the computational time required by *DAOPHOT* to model the PSF. Finally the PSF models were normalized in flux.

Among the different analytical models considered by *DAOPHOT*, the most recurrent one was the Penny2 profile. This model consists of a Gaussian-like function but with Lorentzian wings, indicating that photometric uncertainties could not be exactly Gaussian. Although typical residuals for PSF models from CCD1, CCD2 and CCD4 are around 3%, CCD3 shows a different behavior with systematically larger residuals of 5-10%. This different behavior was probably due to the differences in the efficiency of this detector (CCD3), which was not science grade and significantly worse than CCD1, CCD2 and CCD4 (Cristobal-Hornillos et al. 2013, in prep.).

3.7.3 PSF Model verification.

We systematically verified each PSF model. First we compared its FWHM with the registered seeing (from the image header) and with the mean FWHM value for the stars used to derive the model. The observed scatter among PSFs does not exceed 3-5%, ensuring that stars and models are well in agreement.

Then the PSF stability among CCDs was also checked out. As introduced in Section 3.4, given the spatial configuration of the LAICA optical system, the four CCDs simultaneously imaged (almost) the same part of the sky under same atmospheric conditions and passbands. This fact made it possible to perform statistical comparisons among detectors. Once again we observed good agreements among CCD1, CCD2 and CCD4 but a larger deviation for CCD3 close to a 5-10%.

Finally we studied the radial PSF variability across images to ascertain the usage of a single PSF model per image. We defined a new reference system linking every detection (from each CCD) to the center of the telescope's focal plane. In Fig. 3.10 we show the dependence of the FWHM as a function of the radial distance for ∼20.000 stars, finding a variation smaller than 5%.

3.8 Simulations.

We designed a set of simulations to test the accuracy of *ColorPro* retrieving precise photometry, across images with varied PSF. The main idea was to degrade a better resolution image to the typical condition of ALHAMBRA (in terms of PSF and background noise) and run *ColorPro* on it expecting to retrieve null colors (equal magnitudes) for a sample of galaxies when observed under different PSFs.

We created a mosaic image by rearranging four HST/ACS F814W images from the COSMOS-survey (Scoville et al. 2007) that overlap the ALHAMBRA fields. We rescaled the mosaic to the ALHAMBRA pixel size (from the ACS 0.065 "/pix to the LAICA 0.221 "/pix), convolved with ∼200 PSFs randomly drawn from our models and reapplied background noise using typical values for the ALHAMBRA fields (empirically measured as explained in Section 3.15). An example of the simulated

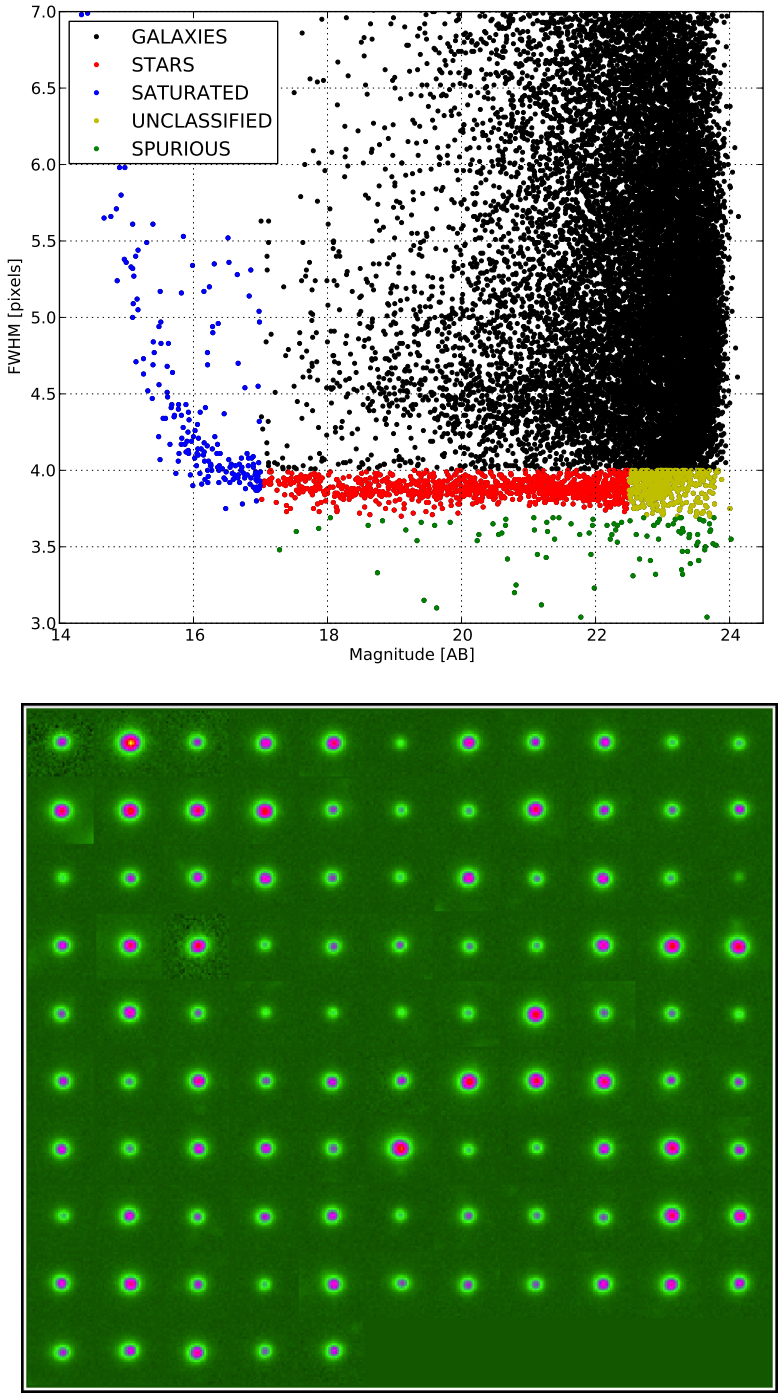

Figure 3.8 Several hundred of non saturated and well-isolated stars were interactively selected across every single image, in order to derive a representative PSF models. We initially ran `SExtractor` on each individual image and then we plot the magnitude vs the FWHM for the extracted sources. We selected those detections located within the red region where the brightest and most compact sources are expected to be located. To avoid potentially saturated stars (blue circles) and possibly misclassified galaxies due to their very faint magnitude (yellow circles), we selected detections with magnitudes in between 16<m<22.5, yielding a final sample of several hundred of stars per image. Finally, we visually rejected stars with contaminating neighbors and generated mosaic-like images. These selections not only served to ascertain the fidelity of the resulting PSFs but also to dramatically reduce the computational time required to generate the models.

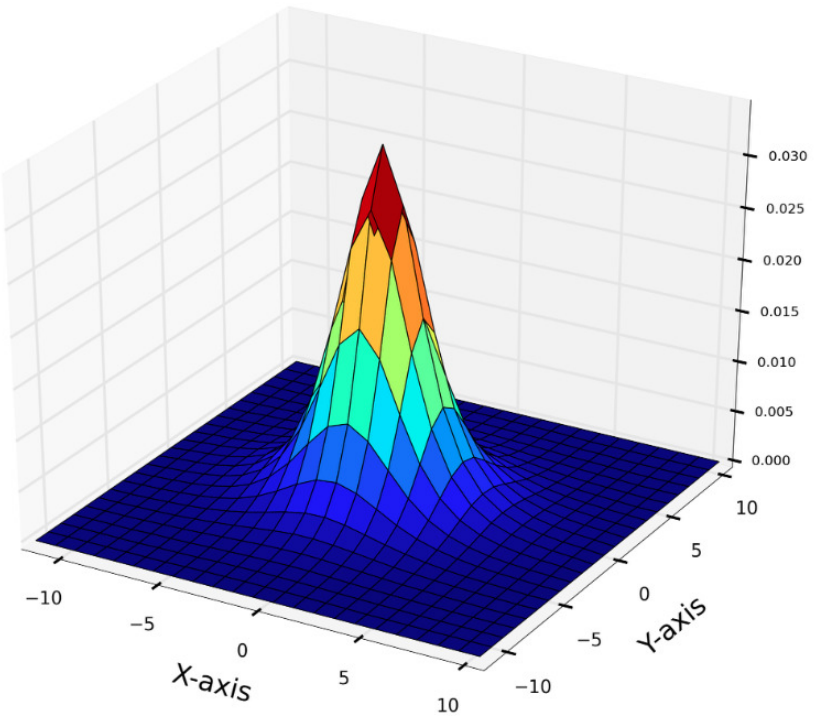

Figure 3.9 We used the package *DAOPHOT* from IRAF (Stetson 1987) to compute PSF models. These selections not only served to ascertain the fidelity of the resulting PSFs but also to dramatically reduce the computational time required by *DAOPHOT* to generate the models. Among the different analytical models considered by *DAOPHOT*, the most recurrent one was the Penny2 profile. This model consists of a Gaussian-like function but with Lorentzian wings, indicating that photometric uncertainties could not be exactly Gaussian.

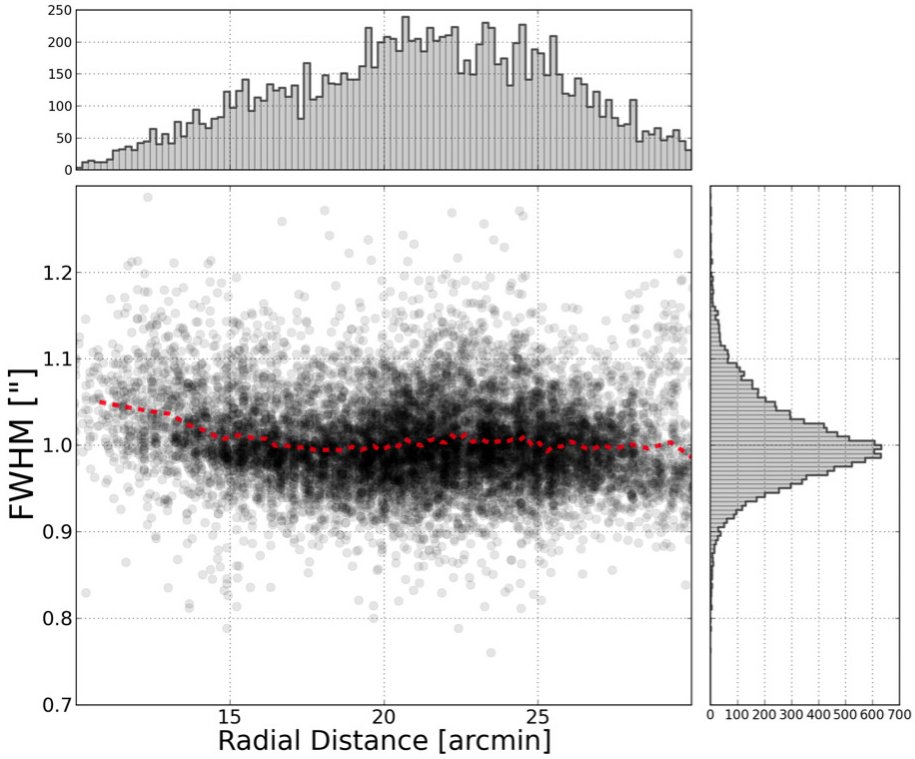

Figure 3.10 Radial PSF variability across images. The figure shows the radial dependence of the PSF (expressed in arcsec and referred to the primary mirror telescope) for the compilation of stars used to derive the PSF models. The mean value of the distribution (dashed red line) has a scatter smaller than 5% enabling the usage of a single PSF model per image.

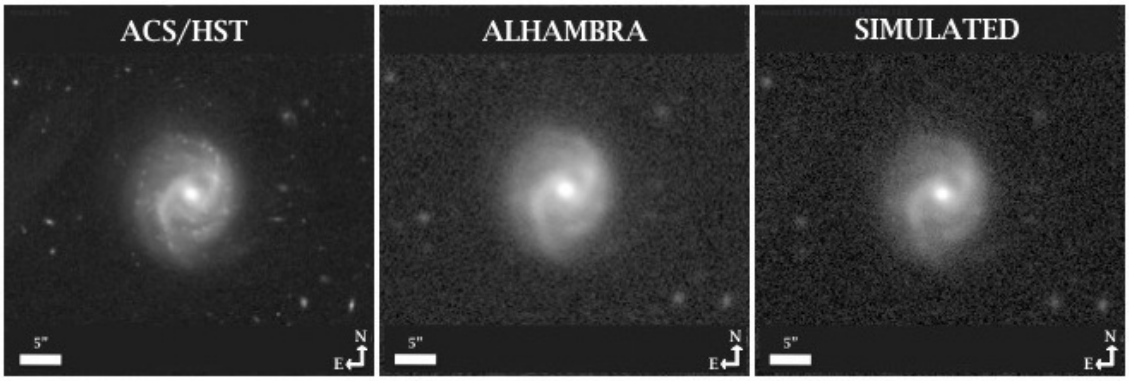

Figure 3.11 Example of the simulated dataset reproducing the typical observational conditions of the ALHAMBRA images (section 3.8). From left to right, it is shown a galaxy as observed in the ACS/HST image, in the ALHAMBRA synthetic F814W detection image and in the rescaled + PSF degraded + background reapplied ACS/HST image.

images is shown in Fig. 3.11 which compares the ACS/HST image of a galaxy (left panel) with the ALHAMBRA image (middle panel) and the simulated image (right panel).

3.8.1 Reliability.

We ran *ColorPro* on the new set of ∼200 mosaics, using the same configuration used for the ALHAMBRA images. We excluded all the detections with photometric problems reported by `SExtractor` (*`SExtractor_Flag`*>1) to eliminate several ghosts and other artifacts (trails) within the original images.

We found that the simulated colors showed a dispersion of $\sigma\sim0.03$ for sources brighter than magnitude F814W=23.0 and a $\sigma<0.05$ for sources with magnitudes in between 23<F814W<24, with negligible biases, as seen in the top panel of Fig. 3.12. The result is in agreement with the expected uncertainties arising from the photometric noise, showing that *ColorPro* is capable to perform accurate PSF-corrections for the ALHAMBRA-like data.

3.8.2 Completeness.

We studied the expected photometric completeness for the ALHAMBRA fields given by the quality of its images in terms of PSF and background level. For this purpose, we used the previous simulations to derive the statistical probability of detecting a sample of faint galaxies when observed through the typical ALHAMBRA observational conditions. In the bottom panel of Fig. 3.12 we show the expected fraction of missed galaxies per magnitude range and square degree. The result indicates that ALHAMBRA is photometrically complete down to a magnitude of F814W∼24. For fainter magnitudes, the number of detections decreases rapidly with a percentage of missed galaxies with magnitude F814W>25 of ∼40%.

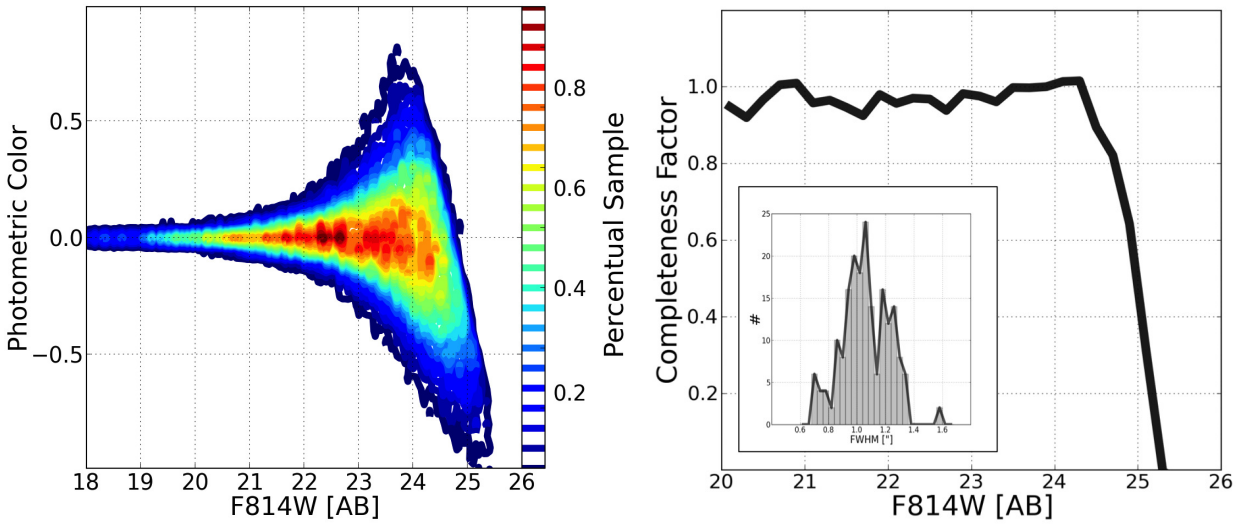

Figure 3.12 PSF-corrected photometry verifications. We designed a set of simulations (Section 3.8) to estimate both the reliability of ColorPro deriving PSF-corrected photometry and the expected completeness in our images. Top panel shows how ColorPro successfully retrieved null colors (same magnitudes) across simulated images, with a dispersion below 3% for magnitudes brighter than F814W=23.0 and 5% for magnitudes in between 23<F814W<24. Bottom panel shows the expected completeness as a function of F814W magnitude.

3.9 Synthetic F814W detection images.

The process of object detection is one of the key ingredients in the production of any astronomical catalogue. In photometric surveys it is a common practice to stack good quality images in order to generate the deepest possible detection images. To define a constant and homogeneous window for all ALHAMBRA fields, we generated synthetic F814W images as the combination of individual bands. To properly calculate the color transformations we used a population of galaxies with typical redshift, magnitude and spectral-type and solved the system of equations generated when estimating the correspondence between synthetic magnitudes among the different filters (eq. 3.4). As the number of equations (given by the number of galaxies Ng) was substantially larger than the number of degrees of freedom (coefficients), the final equation yielded a dispersion smaller than 1%.

The system of equations among filters for the Ng galaxies is defined as follows:

$$F814W = < F814W_{i=1,Ng} > = \sum_{j=1}^{Nf} a_{i,j} \times m_{i,j} \tag{3.4}$$

An example of the so-derived synthetic F814W images is shown in Fig. 3.13.

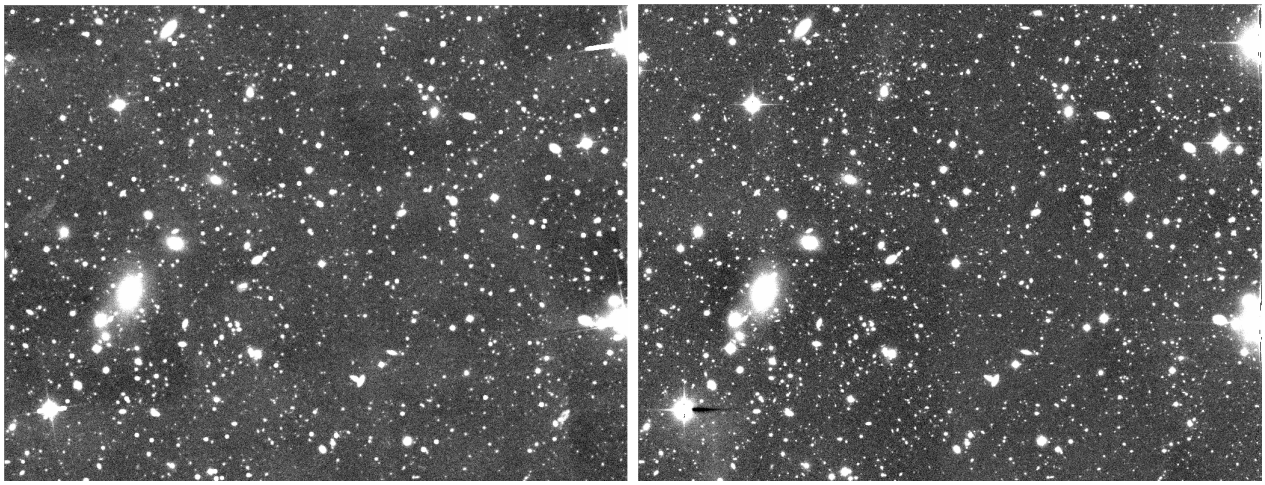

Figure 3.13 Example of the synthetic F814W images derived for the ALHAMBRA fields. Left panel shows how the original HST/ACS F814W image looks like after been scaled to the ALHAMBRA pixel size, convolved with the ALHAMBRA PSF and photometric noise reapplied. Right panel shows the synthetic ALHAMBRA F814W detection image.

$$
\begin{gathered}
F814W = \\
0.105 \times \mathbf{F706W} + 0.178 \times \mathbf{F737W} + 0.179 \times \mathbf{F768W} + \\
+0.142 \times \mathbf{F799W} + 0.115 \times \mathbf{F830W} + 0.119 \times \mathbf{F861W} + \\
+0.073 \times \mathbf{F892W} + 0.049 \times \mathbf{F923W} + 0.040 \times \mathbf{F954W}
\end{gathered} \tag{5}
$$

Given that the typical error in the individual bands is 2-3%, total zeropoint error in the F814W image is very small, providing high homogeneity. To verify the calibration of the synthetic F814W images, we performed a photometric comparison with the COSMOS field. To reproduce the same photometric measurements as in Ilbert et al. (2009), we ran `SExtractor` using fixed circular apertures of 3". We retrieved ∼10800 common sources with ALHAMBRA comprising magnitudes from 19<F814W<25.5. The photometric comparison is shown in Fig. 3.14.

We did not observe photometric zeropoint offsets or trends with magnitude down to magnitudes F814W<23.5. For sources fainter than F814W=24.0 an increasing offset on the magnitudes is observed as a consequence of the rapidly decreasing S/N for the ALHAMBRA detections. In an effort to extend the accuracy of the ALHAMBRA photometric measurements, we derived a magnitude-dependent correction to make ALHAMBRA magnitudes reproduce the COSMOS estimations for fixed apertures of 3". These corrected magnitudes are included in the final catalogues are explained in the appendix C.1.

As a separated test, we ran `SExtractor` on both ACS/F814W and synthetic ALHAMBRA/F814W images separately with the same `SExtractor` configuration. This analysis provided a characterization of the differences in the retrieved detections among both images. For detection magnitudes 19<F814W<23.5 only few tens of sources per CCD were missing from the synthetic ALHAMBRA/F814W images. Detections fainter than magnitudes F814W=23.5 showed a increasing distri-

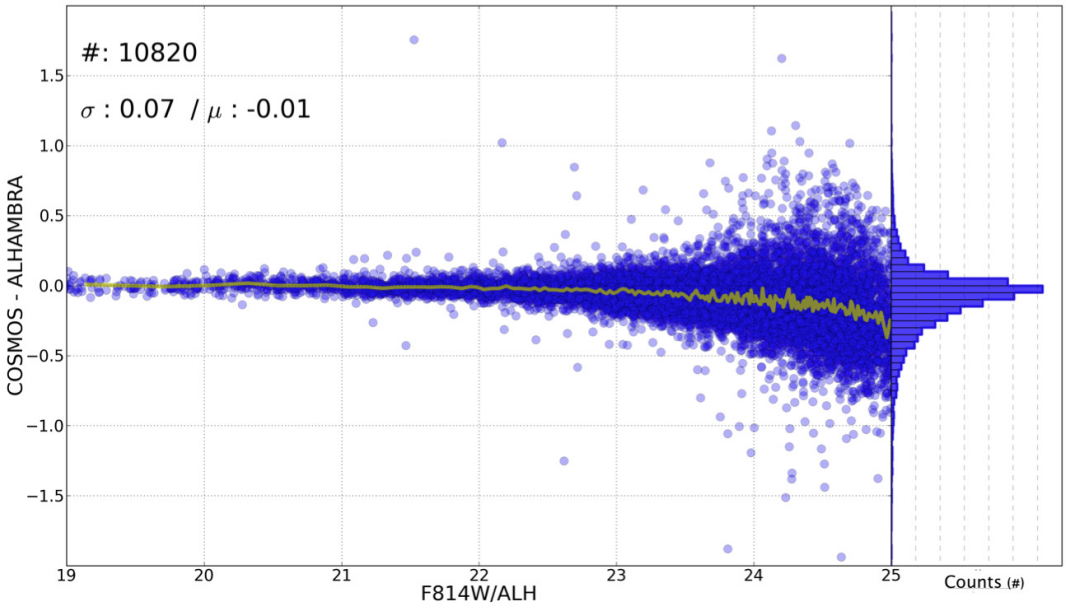

Figure 3.14 Photometric comparison between the F814W/COSMOS and the synthetic ALHAMBRA/F814W images. In order to reproduce the same photometric measurements as done by Ilbert et al (2009), we ran `SExtractor` on the synthetic ALHAMBRA/F814W images using fixed circular apertures of 3". Selecting a common sample of ∼10800 detections between ALHAMBRA and COSMOS, we did not find neither photometric zeropoint offsets nor significant bias for detections with magnitudes 19<F814W<23. For sources fainter than F814W=23.0, an increasingly dependence on the magnitude is observed as a consequence of the rapidly decreasing S/N for the ALHAMBRA detections. To make the ALHAMBRA detections to reproduce the COSMOS magnitudes for fixed apertures of 3", we derived a magnitude-dependent correction which is included in the final catalogues.

bution of undetected sources peaking at a magnitude F814W∼25.5where ALHAMBRA is beyond its photometric completeness limit.

3.10 Masks.

In order to improve the source detection efficiency, we masked every saturated star, stellar spike, ghost and damaged area. Initially we ran `SExtractor` on each synthetic F814W detection image with a special configuration to detect just very bright and extended sources. We visually checked the extracted sources to exclude any possible nearby galaxy. Then we convolved the resulting `SExtractor` segmentation maps with a Gaussian function to broaden the previously defined apertures and so remove residual contributions from stellar halos. We repeated the same procedure on the inverse image to deal with negative extended regions generated by saturated stars. We combined both positive and negative segmentation maps, defining the total region to be masked out. Finally, we replaced all flagged pixels with background noise to minimize the variation of the image RMS. An example of the masking procedure for a saturated star is shown in Fig. 3.15.

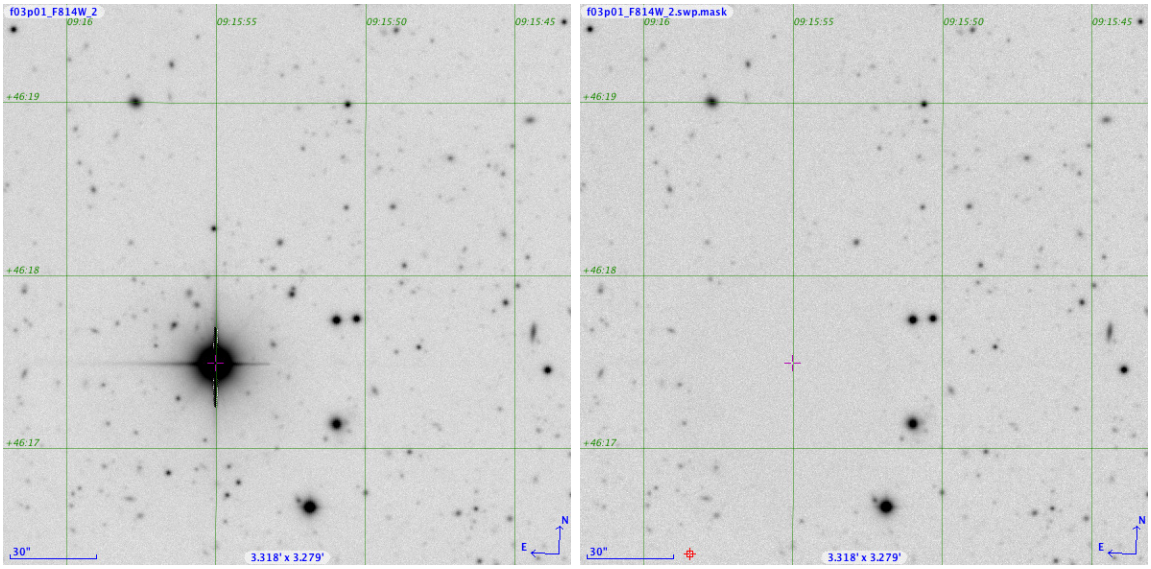

Figure 3.15 In order to improve both the photometric depth and the photometric measurements, F814W detection images were masked out purging saturated stars, spikes, ghosts, negative areas or other artifacts from the images. Figure shows an example about how a saturated star from the original image (left panel) disappears after replacing all its pixels with background signal (right panel).

3.11 SExtractor configuration.

Assuming an expected variability in terms of PSF (and therefore in photometric depth) among the F814W detection images, we explored the optimal `SExtractor` configuration which maximizes the number of real detections. For non crowded fields, the most relevant parameters are the minimum number of contiguous pixels $DETECT\_MINAREA$ and the threshold that the signal has to exceed to be considered a real detection $DETECT\_THRESHOLD$.

As the background should in principle have a symmetric structure in Gaussian limit, a similar amount of spurious detections are expected to be retrieved on both sides of the image. Based on this idea, we initially fixed the $DETECT\_MINAREA$ as twice the image FWHM. Then we studied the lowest threshold that reported the maximum fraction of real detections. We ran `SExtractor` on the direct image and on the inverse image, hence retrieving the relative fraction of fake over real detections per threshold interval. Finally we chose the threshold value that reported no more than 3% of spurious detections, as illustrated in Fig. 3.16. In the Appendix C.2, we show an example of the typical configuration used to perform source detections.

3.12 Flag Images.

In order to be able to quantify the survey effective area, we generated $FLAG$ images for each individual CCD where all problematic pixels were set to 0. As the effective exposure time rapidly decreases when approaching to image edges, we defined homogeneous areas where all sources were adequately exposed (non necessarily detected) in all the 23 bands. We normalized individual weight maps to the

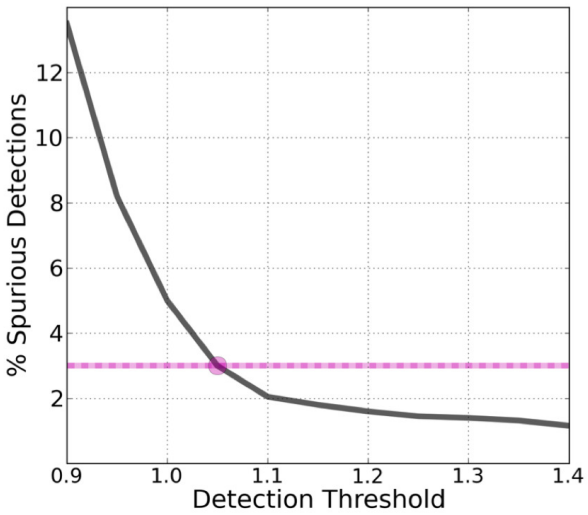

Figure 3.16 Detection threshold. We studied the lowest `SExtractor` detection threshold that reported the maximum number of real detections. We initially fixed the $DETECT\_MINAREA$ as twice the image FWHMW and then ran `SExtractor` twice (once on the direct and once on the inverse image) retrieving the fraction of fake over real detections as a function of $DETECT\_THRESHOLD$. We set the threshold to the value that reported no more than 3% of spurious detections.

maximum exposure time and then flagged the regions with a relative exposure time below the 60% (mostly composed by the image edges).

Meanwhile, these images incorporated the stellar mask information (Section 3.10) as masked regions were replaced by background noise, so provide no detections and artificially varying the expected density of galaxies per unit of area. We combined and stored the information from both criteria in the flag images. Therefore we computed the effective area for each F814W detection image as the direct conversion of the total number of non-flagged pixels into deg^2, as shown in Table C.4. Including all the forty-eight F814W detection images we find a the total surveyed area of 2.79 deg^2.

3.13 RMS Images.

As the effective exposure time on an image is position-dependent, detected sources on the edges usually have shorter exposures than sources on the center, therefore generating gradients in the S/N. From a source-detection point of view, as synthetic F814W images were generated as the combination of many filters, occasional inhomogeneities registered on individual WEIGHT maps became averaged out. On the contrary, for individual filters (especially for the case of NIR images) we found occasional inhomogeneities across the images (Cristóbal-Hornillos 2013, prep.), artificially biasing the expected photometric depth.

To help disentangle whether a galaxy may be missed in a given filter as a consequence of its intrinsic luminosity (below the detection threshold) or due to an insufficient photometric depth, we used the WEIGHT maps (Cristóbal-Hornillos 2013, prep.) to generate a new set of inverseRMS images

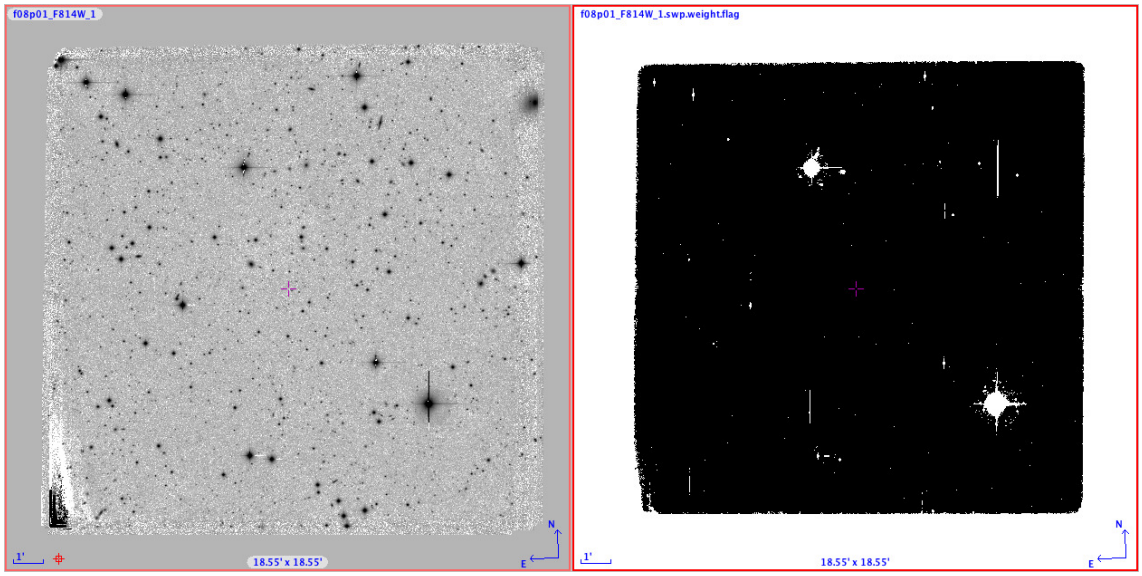

Figure 3.17 In order to be able to quantify the survey effective area, we generated $FLAG$ images for each individual CCD where all problematic pixels were set to 0. These images incorporated well-defined homogeneous areas where all sources were adequately exposed in all the 23 bands, along with the stellar mask information (since masked regions were replaced by background noise). Left panel: it shows the original F814W detection image (before any masking process), where saturated stars and other sort of artifact are clearly visible. Right panel: it shows in white color all the final flagged pixels (set to 0), excluded for the following analysis.

and define two additional photometric Flags. So, we defined the inverseRMS images by applying the following expression to the WEIGHT images:

$$1/RMS = \sqrt{Weight} \tag{3.5}$$

Hence, the $irms\_OPT\_Flag$ and the $irms\_NIR\_Flag$ Flags indicates to the number of individual bands a detection had a signal in its inverseRMS below the 80%, relative to the maximum value. Therefore, galaxies with large values in these photometric flags (indicating a large fraction of filters photometrically flagged) may provide unreliable photometric redshift estimations.

3.14 Star/galaxy separation.

The star/galaxy classification is a necessary step for accurate extragalactic surveys. Stars as real point-like sources (PLS) are observed as the most compact objects in an astronomical image. However, as detections get fainter (decreasing its S/N) the photometric noise makes progressively difficult differentiating the real morphologies of objects.

We followed a statistical approach to perform star/galaxy separation. We assigned a probability to every detection given its apparent geometry, F814W magnitude, optical F489W - F814W and NIR J-Ks colors. For each variable we derived the corresponding probability distribution function (PDF) based on the typical distribution of stars and galaxies. Therefore, every detection is classified in terms

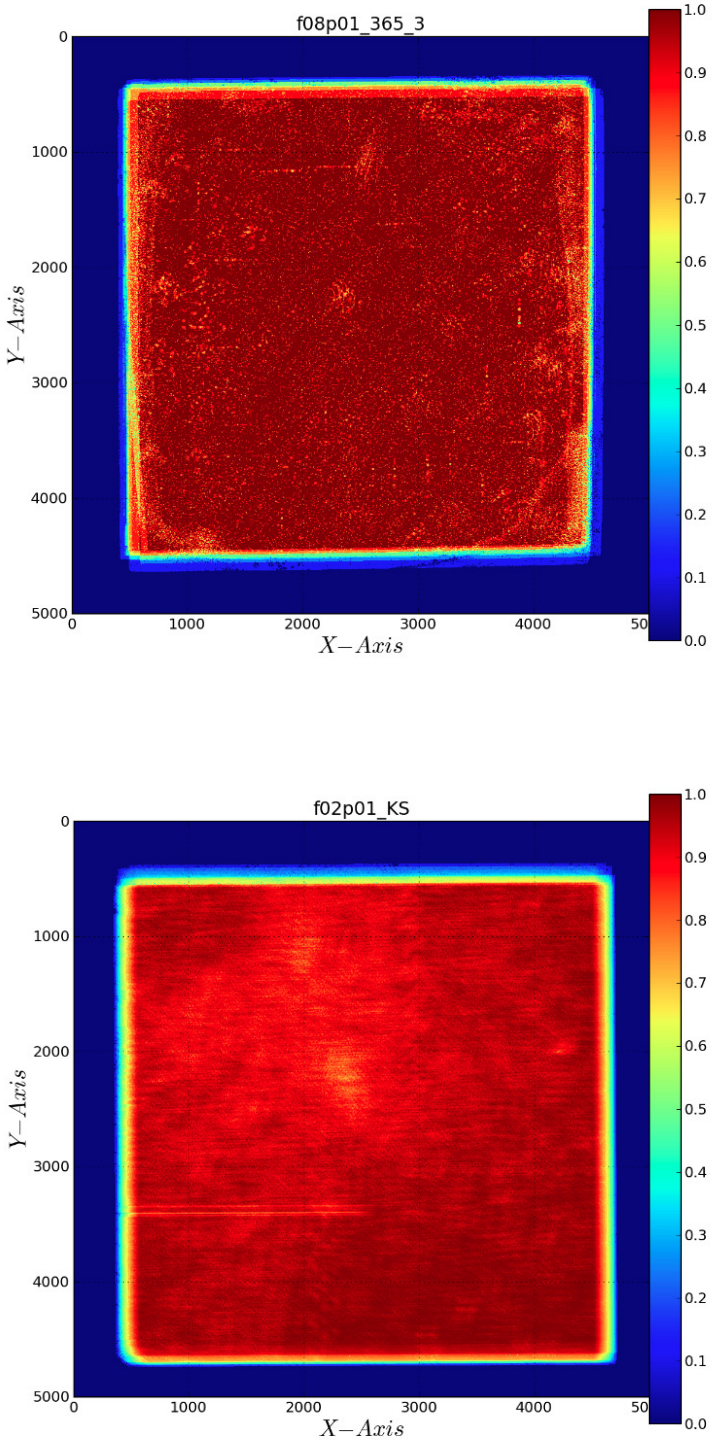

Figure 3.18 As the effective exposure time on an image is occasionally inhomogeneous (position-dependent), detected sources on the edges usually have shorter exposures than sources on the center. To properly characterize both the photometric depth and the photometric uncertainties, it was necessary to generate RMS images for every individual science image. Top and bottom figures illustrate how the effective exposure time can be homogeneously spread over the image generating gradients in the S/N.

of the probability of being a star or a galaxy, as follows:

$$P_{Star} = P_{Star}^{FWHM} \times P_{Star}^{F814W} \times P_{Star}^{Opt} \times P_{Star}^{NIR} \tag{3.6}$$

$$P_{Gal} = P_{Gal}^{FWHM} \times P_{Gal}^{F814W} \times P_{Gal}^{Opt} \times P_{Gal}^{NIR} \tag{3.7}$$

$$where \quad P = P_{Star} + P_{Gal} = 1 \tag{3.8}$$

Final probabilities are stored on the statistical variable *Stellar_Flag* included in the catalogues. The derivation of the four independent PDFs is now explained.

3.14.1 Geometry and Magnitude.

We used the COSMOS HST/ACS images to explore the star/galaxy selection algorithms, since they are considerably deeper and with a obviously much narrower PSF than the ALHAMBRA dataset.

We ran `SExtractor` twice, first on the ACS/F814W images and then on the ALHAMBRA/F814W images in single image-mode, representing the detected sources in a FWHM vs F814W magnitude diagram as shown in Fig.3.19. We selected detections classified as PLS in the ACS/F814W images and used them to match up the ALHAMBRA/F814W detections. Likewise, sources brighter than F814W=22.5 classified as PLS on the ACS/F814W images were equally classified as PLS on the ALHAMBRA/F814W (open red circles). However, detections fainter than F814W=22.5 classified as PLS on the ACS/F814W showed progressively larger FWHM values on the ALHAMBRA/F814W. This result sets the ALHAMBRA survey geometrical resolution limit, usable to identify real PLS based on its apparent geometry, to sources brighter than F814W=22.5.

Additionally we investigated the nature of the faint detections appearing as PLS in the ALHAMBRA/F814W images but clearly not belonging to the ACS/F814W PLS sample (green dots). We proceeded reversely by selecting faint F814W>22.5 PLS in ALHAMBRA and matching them to the ACS/F814W detections. The result showed that those detections were actually very faint extended sources appearing as PLS in the ALHAMBRA/F814W images, where the innermost part was barely detected above the detection threshold due to its low S/N.

3.14.2 Photometric colors.

A popular approach to separate stars from galaxies is based on their spectral differences (Daddi et al. 2004). By combining two photometric colors (one in the optical, one in the NIR) is possible to identify two separated regions where stars and galaxies are typically located, as shown in the left panel of Fig. 3.20. We initially defined a color-color space generating an optical color as F489W-F814W and a NIR color as *J-Ks* and then, we studied how deep in magnitude this photometric technique worked well when considering the level of photometric uncertainties in the ALHAMBRA images.

In order to generate a control sample, we assumed that real PLS (as classified by ACS/F814W

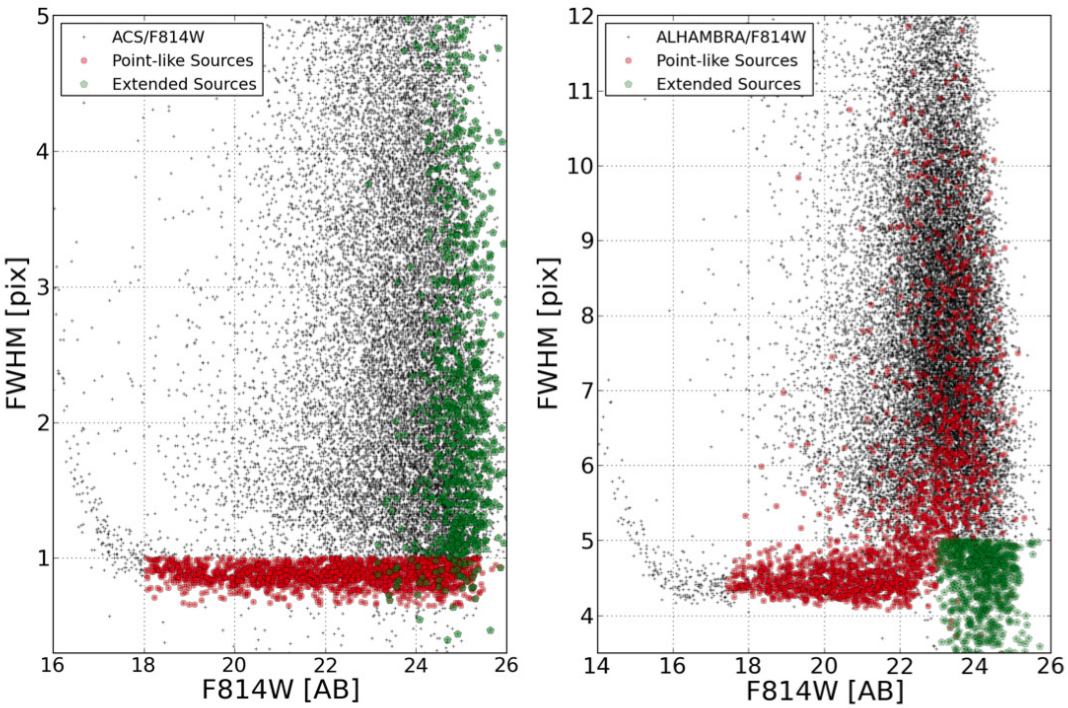

Figure 3.19 Geometrical distortions. We studied the shape degradation of point-like sources observed in our fields as a function of the apparent magnitude. We used the ACS/F814W images from COSMOS to selected real point-like sources (narrowest FWHM) within the ALHAMBRA fields and so understand how these sources might look like when observed under the ALHAMBRA PSF conditions. As seeing in the figure, detections classified as point-like sources on the ACS/F814W images (red circles) brighter than F814W=22.5 were equally classified as point-like sources on the ALHAMBRA/F814W images. However, point-like sources on the ACS/F814W with magnitudes fainter than F814W=22.5 showed an increasingly FWHM when observed on the ALHAMBRA/F814W images. This fact indicates the existence of a strong dependency between the accurate geometrical information retrievable from the images and the apparent magnitudes of the detections. Meanwhile we proceeded inversely selecting detections classified as point-like sources in the ALHAMBRA images with magnitudes fainter than F814W=22.5 (green circles) and therefore with narrower FWHM that real point-like sources. When observed on the ACS/F814W images, these sources were mostly composed for too faint and extended galaxies where the innermost part was barely detected above the detection threshold due to its low S/N.

images) were all "stars" whereas well extended sources (ES) were assumed to be "galaxies". Considering the resolution of the ACS/HST images and the magnitude range involved in this analysis, the so-derived sample of stars/galaxies represented a good approximation as the expected fraction of misclassified galaxies was actually negligible.

We tested the reliability of this methodology by gradually decreasing the S/N of the sample. Initially we selected only sources with very high S/N (F814W<19) as shown on the left-hand side of Fig. 3.20. However, as sources get fainter (F814W<23, on the righ-hand side) the discrimination among the two classes becomes progressively complicated with ES falling into the initially defined stellar locus and PLS into the galactic Locus.

3.14.3 Stellar flag

Finally, we used the retrieved information from the star/galaxy geometry, F814W magnitude, optical and NIR colors to derive empirical PDFs as shown in Fig. 3.21. Therefore we assigned a statistical classification to every detection given its observed information. Considering the level of both photometric and geometric uncertainties when deriving the PDFs, we excluded from the classification all detections fainter than magnitudes F814W>22.5 assigning them a $Stellar\_Flag$ value = 0.5.

We tested the goodness of this statistical classification by comparing the density of selected stars per unit of area. We used the *Trilegal* software (Girardi 2002, 2005) to estimate the expected fraction of stars in the ALHAMBRA fields according to the imaged area, the galactic position and the limiting magnitude. As seen in Fig. 3.22, we find a good agreement when comparing the statistically derived stellar sample to the *Trilegal* prediction. We observed the ALHAMBRA data to best fit the Trilegal estimations when selection as stars all detections with $Stellar\_Flag$>0.7

As shown in the right panel of Fig 3.22, when applying this statistical criteria, we observe that stars dominate the sample down to a magnitude F814W<19. For fainter magnitudes the fraction of stars from galaxies rapidly declines with a contribution of ∼10% for magnitudes F814W=22.5. As indicated in the insetted panel, if we extrapolate the so-derived stellar number counts, the expected contamination for unclassified stars with magnitudes fainter than F814W>22.5 becomes negligible, with a contribution of stars of ∼1% for magnitudes F814W=23.5. We retrieve an averaged stellar density in the galactic halo of ∼7000 stars per deg^2 (∼450 stars per CCD) for sources brighter than F814W=22.5.

3.15 Photometric errors

Image processing (dithering, degradation, stacking, registration, imperfect background subtraction,...) introduces correlations between neighboring pixels making the background noise in images different from a Poissonian distribution. If these effects are not properly taken into account, it can lead to a severe underestimation of the real photometric uncertainties and hence, critically affecting not only the photometric depth estimations (the survey photometric limiting magnitude) but also to the photometric redshift accuracy. Therefore photometric errors have been empirically estimated

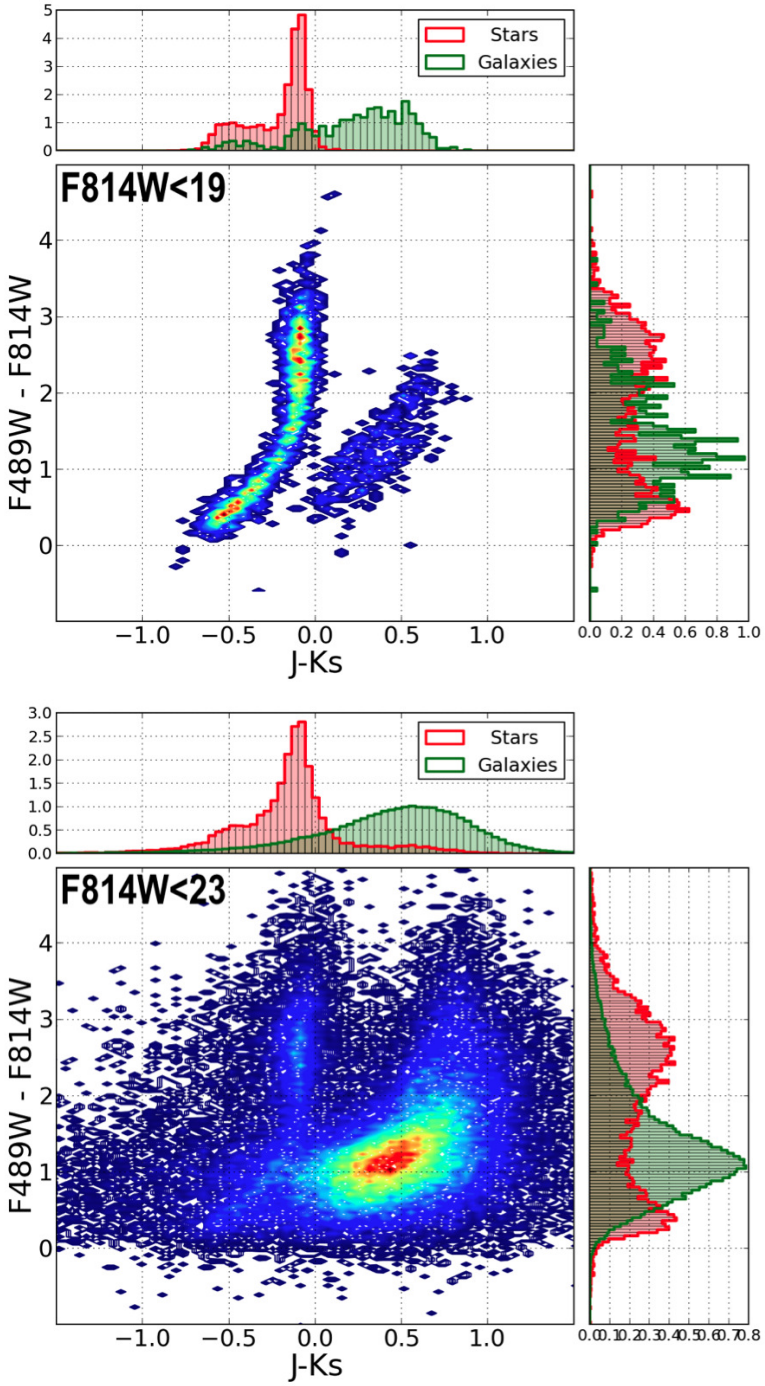

Figure 3.20 Effect of the photometric uncertainties when discriminating between stars and galaxies. We investigated the possibility of using color-color diagrams to separate stars from galaxies and explored the impact of large photometric uncertainties on it. In order to generate a control sample, we assumed sources classified as point-like sources by the ACS/F814W images to be *stars* and well extended sources to be *galaxies*. Considering the resolution of ACS/F814w images and the magnitude ranges involved, the expected fraction of wrong classified galaxies was actually negligible. As seen in the figure, we defined an optical color as F489W-F814W and a NIR color as *J-Ks*. Whereas for high S/N detections this diagram clearly separated stars from galaxies (left panel), as the S/N declines the photometric uncertainties made the contamination among samples impractical (right panel). Therefore, we decided to apply this methodology only to detections with magnitudes brighter than F814W=22.5

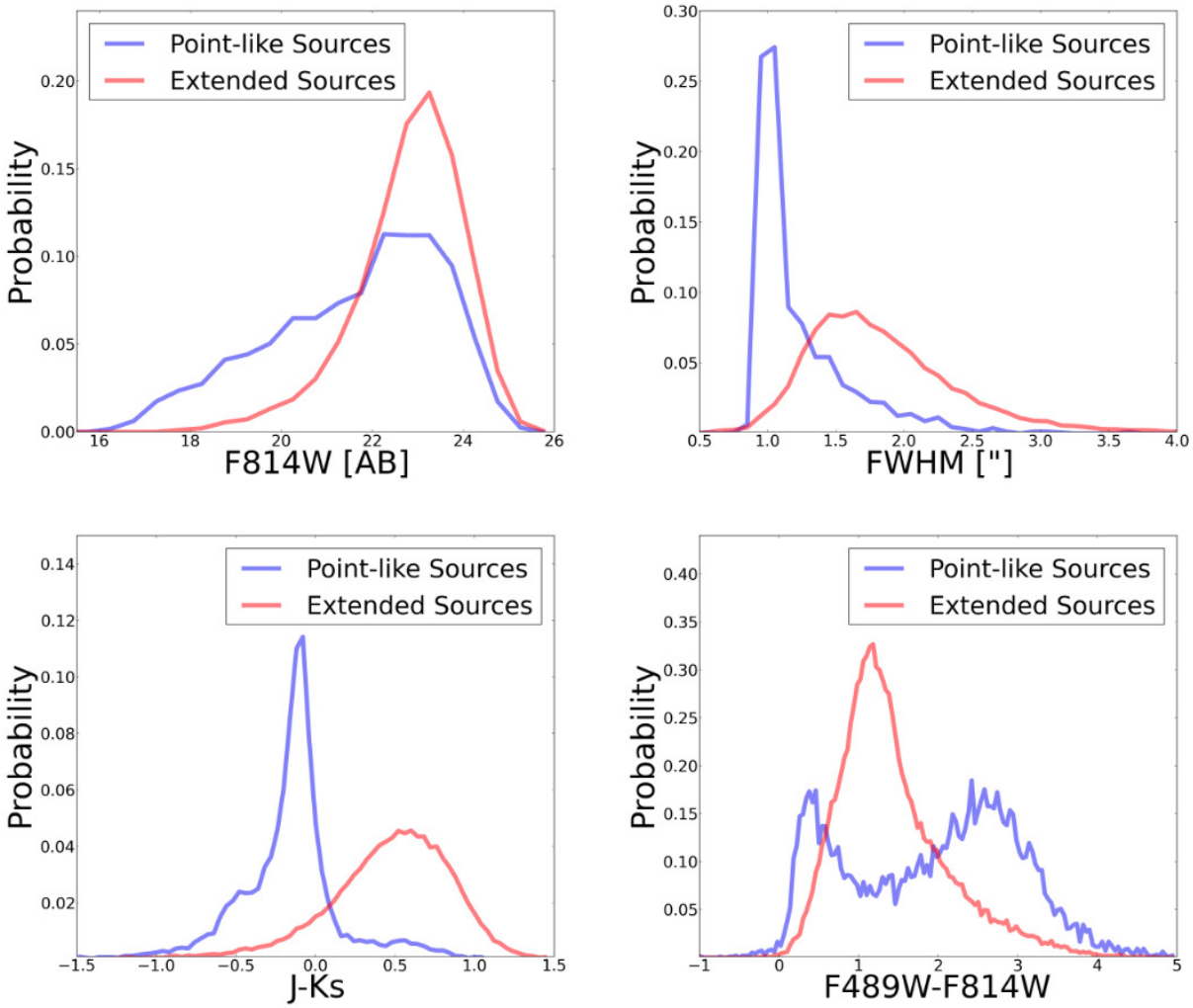

Figure 3.21 Star/galaxy PDFs. The figure shows the four Probability Distribution Functions derived for a control sample of stars and galaxies selected from the ACS/F814W images. From left to right and top to bottom, the distribution of stars (blue line) and galaxies (red line) as a function of the apparent magnitude F814W, the apparent FWHM, the NIR and Optical colors are shown. These PDFs were used to estimate the probability of a detection to be a star or a galaxy as explained in Section 3.14.3.

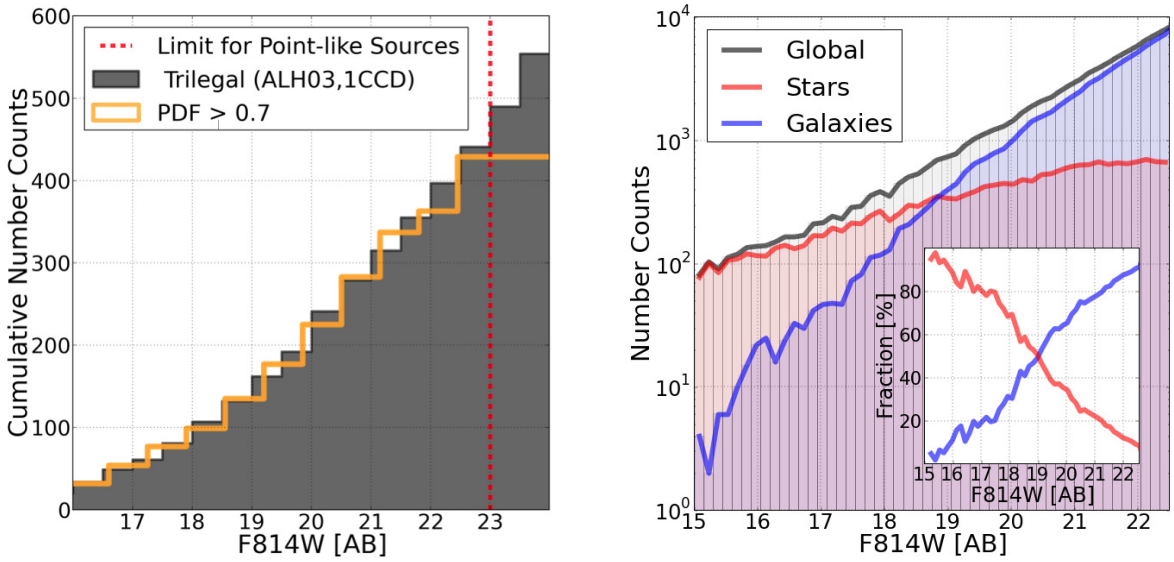

Figure 3.22 Star number counts. For each field in ALHAMBRA, we compared the number of detections classified as stars based on our statistical criteria (solid yellow line) with that provided by the *Trilegal* software (solid grey histogram), as seen in the left panel. The figure shows an example for a single CCD in the ALHAMBRA-03. We retrieved the best matching among samples when selecting as stars detections with *Stellar_Flag* >0.7. When applying this statistical criteria to the whole catalogue (right panel), we observe stars to dominate the sample down to a magnitude F814W<19. For fainter magnitudes, the fraction of stars from galaxies rapidly declines with a contribution of ∼1% for magnitudes F814W=22.5. As indicated in the insetted panel, if we extrapolate the so-derived stellar number counts, the expected contamination for unclassified stars with magnitudes fainter than F814W>22.5 becomes negligible, with a contribution of stars of ∼1% for magnitudes F814W=23.5. When the analysis is extended to the complete catalogue, we retrieved an averaged stellar density in the galactic halo of ∼7000 stars per deg^2 (∼450 stars per CCD), for sources brighter than F814W=22.5.

(following a similar approach as described in Casertano et al. 2000, Labbé et al. (2003), Benítez et al. 2004, Gawiser et al. (2006) and Quadri et al. (2007) to correct for the two main effects.

As explained in Section 3.7.1, *ColorPro* was updated to automatically degrade every image with a narrower PSF than the detection image. In addition the original NIR images (from OMEGA-2000) were also rescaled to the LAICA pixel size (Cristóbal-Hornillos et al. 2013, in prep.). Both procedures dramatically alter the properties of their original background distributions. Moreover, when deriving photometric uncertainties, `SExtractor` always assumes the image background to follow a perfect Poisson distribution. This clearly underestimates the noise, as we will see below.

Now we will describe the procedure to derive the empirical photometric uncertainties for each individual image. Initially, we define the separation among real detections and the background signal using the `SExtractor` segmentation map derived from its corresponding detection image F814W. Every pixel related to a detection is automatically excluded from the analysis. Over the remaining area, we thrown ∼50.000 apertures directly on the images measuring both the enclosed signal and the RMS. The procedure was repeated iteratively spanning a range of apertures between 1-250 pixels. In the meantime, as photometric uncertainties depend on the image total exposure time (which is not necessarily homogeneous), it was necessary to retrieve this information from its corresponding weight maps.

The methodology served to properly estimate the empirical dependence between any galaxy photometric aperture and its RMS. In Fig. 3.23 we show an example of the typical measured background distribution when drawing one pixel apertures. The red line corresponds to the best gaussian fit to the data.

As expected, the ALHAMBRA images are accurately described by a Poisson distribution on small scales. However as apertures become larger, a second term starts dominating the distribution indicating the presence of large-scale correlations among pixels. In this case, the background distribution is described by the relation:

$$\sigma(A) = \frac{\sigma_1 \sqrt{N}(C_1 + C_2\sqrt{N})}{\sqrt{w_N}} \tag{3.9}$$

where coefficient C_1 indicates the Poisson contribution dominating on small scales, C_2 the contribution on large scales, w_N the corresponding percent weight (from WEIGHT map) and σ_1 the background distribution measured for one pixel apertures.

The relevance of this sort of corrections can be appreciated in Fig. 3.24 where the differences between a Poisson-based treatment (solid red line) and an empirically estimated (solid black line) are shown. Whereas the left panel indicates the dependence of the expected RMS as a function of aperture size $\sqrt{N}$, the right panel shows the re-estimated mean photometric uncertainties as a function of magnitude.

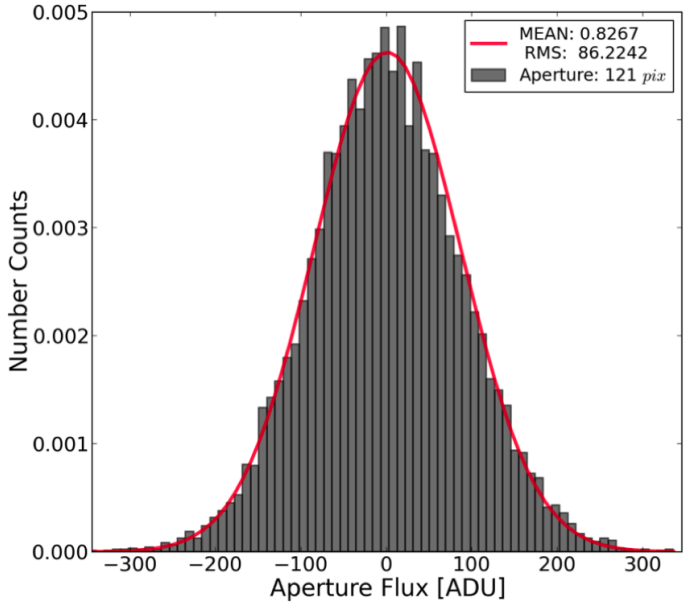

Figure 3.23 The figures shows an example of the empirically measured background distribution for 121-pixel apertures after drawing ∼50.000 apertures on blank regions. To properly estimate the empirical dependence between photometric apertures and the RMS, the procedure was repeated spanning a range of apertures between 1-250 pixels, so fully covering the expected sizes for the ALHAMBRA detections.

3.15.1 Photometric verfication.

As already mentioned in Section **??**, taking the advantage that the optical system LAICA was composed by four CCDs which simultaneously imaging (almost) the same portion of the the sky under the same atmospheric conditions and passband, it was possible to undertake statistical comparisons among contiguous CCDs.

We performed a systematic comparison between the number of detected sources per magnitude range. As illustrated in the Fig. 3.25, the results from the four CCDs were highly consistent for magnitudes F814W<24, where ALHAMBRA is photometrically complete. For fainter magnitudes CCD3 showed a decrease in the number of detections, probably due to its poorer efficiency. Meanwhile, we compared the photometric uncertainties between CCDs. Whereas CCD1, CCD2 and CCD4 showed a good agreement, the CCD3 differed from the general trend showing larger photometric uncertainties.

Finally, we did not observe any horizontal shifts among curves indicating no photometric bias at first order. This is illustrated in the right panel of Fig. 3.25.

3.16 BPZ: Bayesian Photometric Redshifts.

BPZ (Benítez 2000) is a SED-fitting method optimized to compute accurate photometric redshifts. Unlike most similar codes, BPZ introduces the use of a Bayesian inference where a maximum likelihood

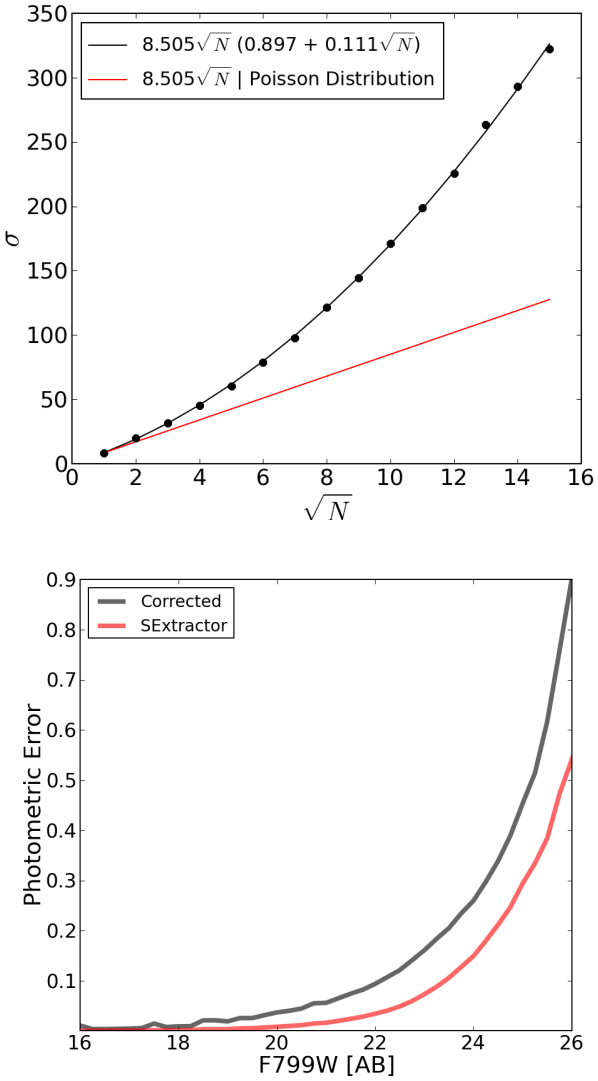

Figure 3.24 Photometric uncertainties. The figure shows the differences between the photometric uncertainties yielded by `SExtractor` (solid red line) assuming that the background follows a Poisson distribution and those empirically estimated (solid black line) using the methodology described in Section 3.15. Left panel illustrates how the dependence between the RMS and the aperture-size ($\sqrt{N}$) becomes progressively underestimated by `SExtractor` due to the presence of large-scale correlations among pixels introduced during image processing. As described in equation 3.9, whereas the number outside the parenthesis in the legend correspond to the background RMS derived for 1-pixel apertures, the numbers inside correspond to the (Poisson) contribution dominating on small scales and to the contribution on large scales, respectively. The right panel compares the average photometric uncertainties, as a function of magnitude, derived by `SExtractor` (solid red line) and using anempirical approach (solid black line). As expected, `SExtractor` always underestimates the real photometric uncertainties, becoming especially significant for faint magnitudes.

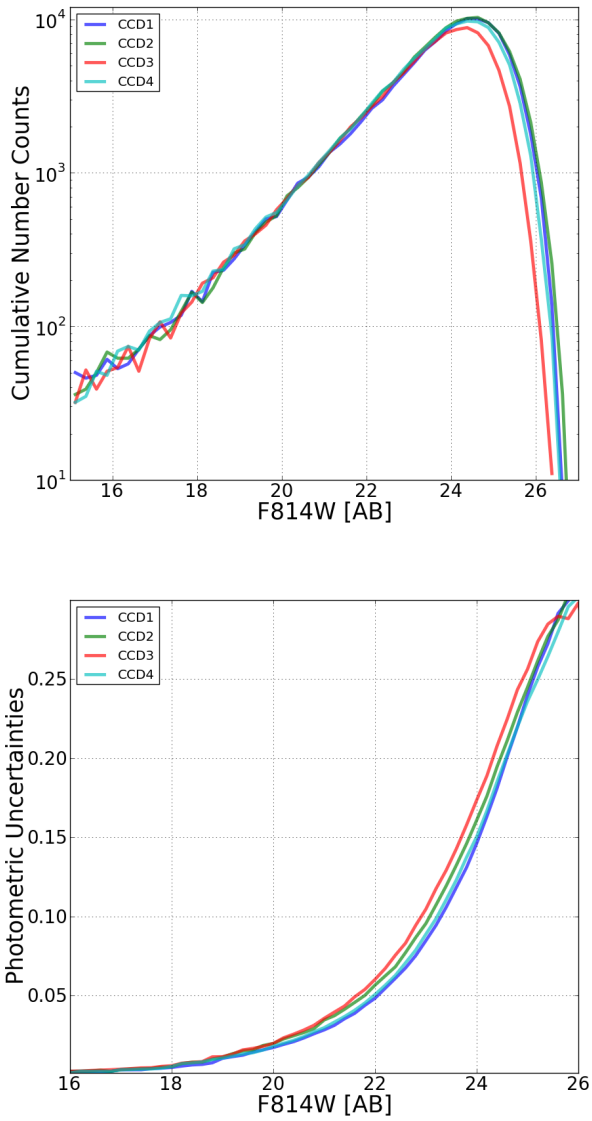

Figure 3.25 Internal photometric verifications. Using the advantage that the LAICA optical system is an array composed by four CCDs imaging simultaneously (almost) the same regions of the sky, under same atmospheric conditions and under same pass-band, we performed internal photometric checks by comparing statistics from different CCDs. As seen on the left panel, on the one hand, we compared number counts per magnitude range. This analysis served to ascertain the homogeneity during the detection process. As expected, whereas CCD1, CCD2 and CCD4 are similar, CCD3 behaved slightly worse with a shallower photometric depth. The absence of bumps or horizontal shifts among CCDs indicates homogeneous detections and no problems of any kind with photometric zeropoint offsets, at first order. On the right panel, on the other hand, we compared the photometric uncertainties as a function of the magnitude for the four CCDs. As expected, CCD3 typically showed larger photometric uncertainties than the other CCDs, confirming its poorer performance.

(resulting from a χ^2 minimization between the observed and predicted colors for a galaxy, among a range of redshifts and templates) is weighted by a prior probability. As the resulting $p(z, T)$ is usually a multimodal distribution (with more than one possible peak given the color-redshift degeneracies) the inclusion of any prior information in the analysis serves to eliminate unrealistic solutions reducing the number of catastrophic outliers. In this work, we used an updated version of the code (BPZ2.0, Benítez et al. 2013, in prep.) which includes several changes with respect to its original version.

The BPZ2.0 uses a new library composed by five SED templates originally drawn from PEGASE (Fioc & Rocca-Volmerange 1997) but then re-calibrated using the FIREWORKS photometry and spectroscopic redshifts (Wuyts et al. 2008) to optimize its performance, i.e., making the templates to have same colors as real galaxies with known redshifts observed with ACS. In addition five GRASIL and one Starburst templates have been added. As seen in the left panel of Fig. 3.26, this new library includes five templates for elliptical galaxies, two for spiral galaxies and four for starburst galaxies along with emission lines and dust extinction. The opacity of the intergalactic medium was applied as described in Madau et al. (1995). An example of the typical spectral-fitting using the ALHAMBRA photometry is shown in the right panel of Fig. 3.26. Meanwhile the inset panel corresponds to the resulting redshift distribution function $p(z)$.

The BPZ2.0 includes a new prior which gives the probability of a galaxy with apparent magnitude m_0 having a certain redshift z and spectral-type T. The prior has been empirically derived for each spectral-type and magnitude by fitting luminosity functions provided by GOODS-MUSIC (Santini et al. 2009), COSMOS (Scoville et al. 2007) and UDF (Coe et al.2006).

In addition, the BPZ2.0 also provides an estimation of the galaxy stellar mass, calculated from the assigned interpolated spectrum of the galaxy by applying the color-M/L ratio relationship established by Taylor et al. (2011) to the BPZ templates. For an in-depth discussion, we refer the reader to Benítez et al. 2013, in prep. We performed two different checks to show the robustness of the BPZ stellar masses. First, when comparing the BPZ stellar masses with the masses measured by Bundy (2006a) on the COSMOS field, we observed that the uncertainties are within the expected by their analysis (of about 0.1 - 0.2 *dex*) with a moderately dependence on the spectral types, as seen in Fig. 3.27. Secondly, we obtained BPZ stellar masses from a semi-analytical simulation (Merson et al. 2013, Ascaso et al. 2013 (in prep.)) and compared them with the input masses after correcting them by the effect of different IMFs (Bernardi et al. 2010). The mean value of the difference is $\sim 0.13 \pm 0.30$ dex which, as before, is consistent with the uncertainties reported (Mitchell et al. 2013), confirming the reliability of the stellar masses estimations.

Along with the most probable redshift and spectral type for each galaxy, BPZ also provides the *Odds* parameter (Benítez 2000). This parameter is a quality indicator which refers to the integral of the redshift probability within a fixed range (0.0125(1+z), in this case) around the main peak of the $p(z)$ distribution. Therefore, the *Odds* parameter is a measurement of the quality/confidence of the photometric redshift estimation. It is worth emphasizing that the *Odds* makes possible to derive high quality samples with very accurate redshifts and a very low rate of catastrophic outliers. We used a redshift resolution of $DZ = 0.001$ from $0.001 < z < 7.0$. In order to fully cover the spectral-type

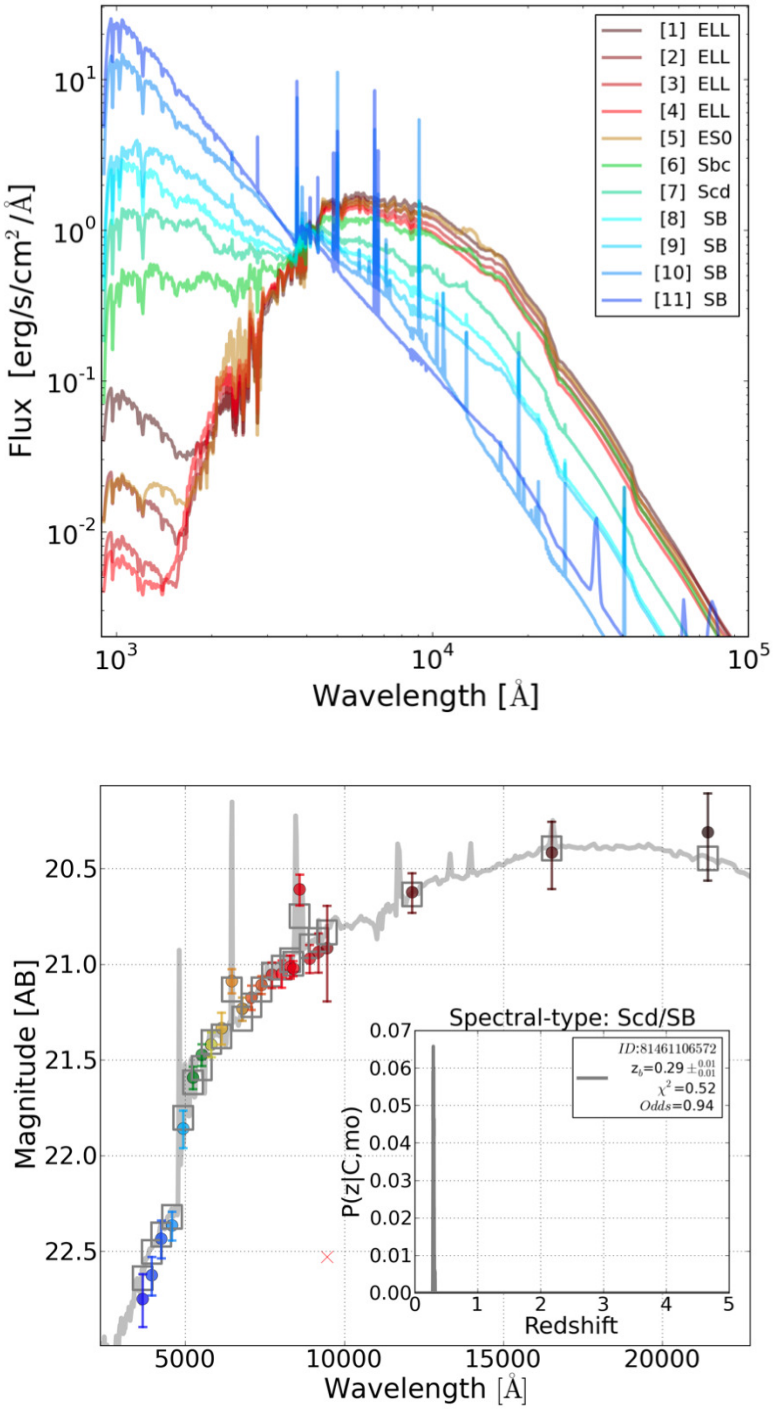

Figure 3.26 The BPZ2.0 new library is composed by five SED templates originally drawn from PEGASE but then re-calibrated using the FIREWORKS photometry and spectroscopic redshifts to optimize its performance. In addition five GRASIL templates and a SB have been added. In the figure we arbitrarily normalized the SEDs to 4000Åfor an easy visualization. The numerical notation for the BPZ templates used in the catalogues is indicated in the legend. The right panel shows an example of the typical spectral-fitting using the ALHAMBRA photometry, where the internal right-corner figure corresponds to its resulting redshift distribution function $p(z)$.

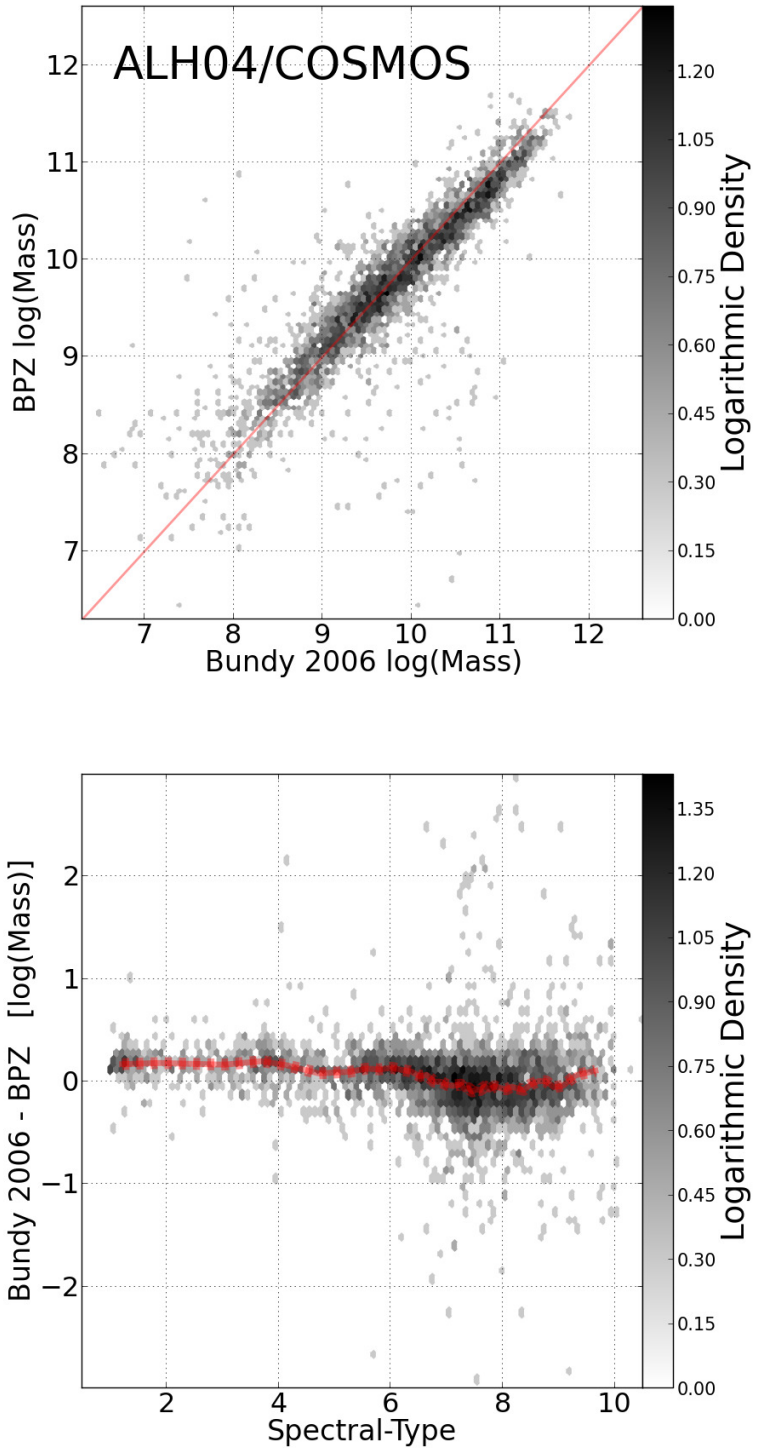

Figure 3.27 The new version of BPZ provides an estimation of the galaxy stellar mass, calculated from the assigned interpolated spectrum, by applying the color-M/L ratio relationship established by Taylor et al. (2011) to the BPZ templates. In the left panel, we show a comparison between the BPZ stellar masses with the masses measured by Bundy (2006a) on a sample of galaxies from the COSMOS field. We observe that the uncertainties (of about 0.1 - 0.2 *dex*) are within those expected by Bundy (2006a). In the right panel, we represent the former comparison as a function of the spectral type. Again, a moderately dependence is observed with uncertainties within 0.1-0.2 *dex*.

space, we used an interpolation factor between templates of 7, i.e. expanded the library of templates by generating seven models in between each of the original eleven models. The redshift confidence interval provided by zb_{min} and zb_{max} corresponds to the 68% of the probability distribution function. Note that, in some cases the probability p(z) can go to 0 within this range.

3.17 Photometric redshift accuracy

The normalized median absolute deviation (NMAD) is known to be a robust measurement of the accuracy reached by a sample of photometric redshifts (Brammer et al. 2008). As photometric redshifts typically show error distributions with extended tails (departing from a pure Gaussian distribution) along with the presence of several outliers, the NMAD estimator becomes more appropriate than the standard deviation as the former is less sensitive to these long tails and to the presence of catastrophic outliers. NMAD is defined as:

$$\sigma_{NMAD} = 1.48 \times median(\frac{|\delta z - median(\delta z)|}{1+z_s}) \tag{3.10}$$

$$and\ \ \delta z = z_b - z_s \tag{3.11}$$

where z_b corresponds to the bayesian photometric redshift and z_s to the spectroscopic redshift. Along with the scatter it is also important to quantify both the presence of any systematic bias μ and the fraction of catastrophic failures when deriving the galaxy redshift. In this work we established two different definitions for catastrophic outliers:

$$\eta_1 = \frac{|\delta z|}{1+z_s} > 0.2 \tag{3.12}$$

$$\eta_2 = \frac{|\delta z|}{1+z_s} > 5 \times \sigma_{NMAD} \tag{3.13}$$

As explained in Section **??**, ALHAMBRA was designed to partially overlap regions observed by other spectroscopic surveys. We compiled a sample of ∼7200 galaxies with spectroscopic redshifts to quantify the expected accuracy for the photometric redshift estimations, imposing two strong criteria. On the one hand, we considered only high quality (secure) spectroscopic redshifts. Although this condition dramatically reduced the amount of available galaxies (and probably slightly biasing the sample to the brightest galaxies) it reduces the contamination and the fraction of spurious outliers (Fernández-Soto 2001). On the other hand, to reduce the amount of mismatched galaxies, we derived accurate astrometric corrections between samples (to avoid any offset) and then established a maximum matching distance of ∼3 pixels (<0.7"), as shown in Fig. 3.28. This maximum separation was manually set for each survey being the distance at which the distribution of matching distances reached its first minimum. As seen in Fig. 3.29, the compiled redshift sample shows a mean redshift $<z_s>\sim0.77$ and a mean magnitude (based on ALHAMBRA photometry) F814W∼22.3. In Table 3.3 the contribution from each survey is specified, indicating the number of selected galaxies, the mean magnitude and redshift.

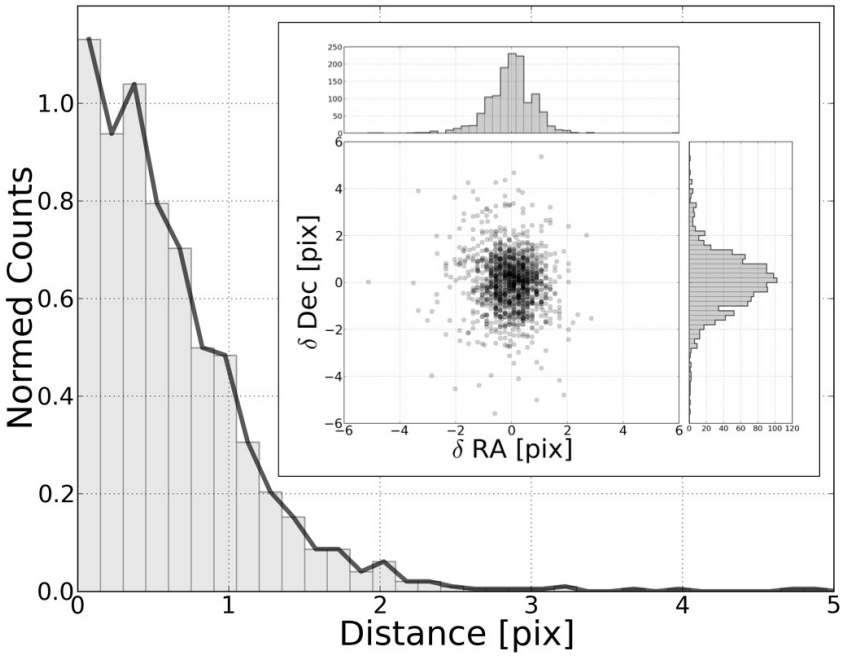

Figure 3.28 Astrometric matching with spectroscopic samples. In order to reduce the fraction of potential mismatched galaxies, we initially performed second-order astrometric corrections between the ALHAMBRA fields and other surveys, to established a maximum distance of ∼3 pixels (<0.7") to match our detections. This maximum separation was manually set for each survey, being the distance at which the radial matching distribution reached its first minimum. As seen in the main panel, ∼60% of the selected spectroscopic sample is well accommodated within a 1-pixel distances. Insetted panel illustrates the astrometric dispersion between ALHAMBRA and the overlapping surveys in terms of δRA (RA^{ALH}-RA^{surv}) and δDec (Dec^{ALH}-Dec^{surv}) in units of pixel.

Table 3.3 Spectroscopic Redshift samples.

#	Survey	Reference	<F814W>	<z>
1269	DEEP-2	Koo et al. 1995	22.64	0.92
1291	COSMOS	Lilly et al. 2009	21.36	0.54
1000	GOODS-N	Cooper et al. 2011	22.75	0.83
2977	GROTH	Demian et al. 2011	22.21	0.70
7237			22.24	0.75

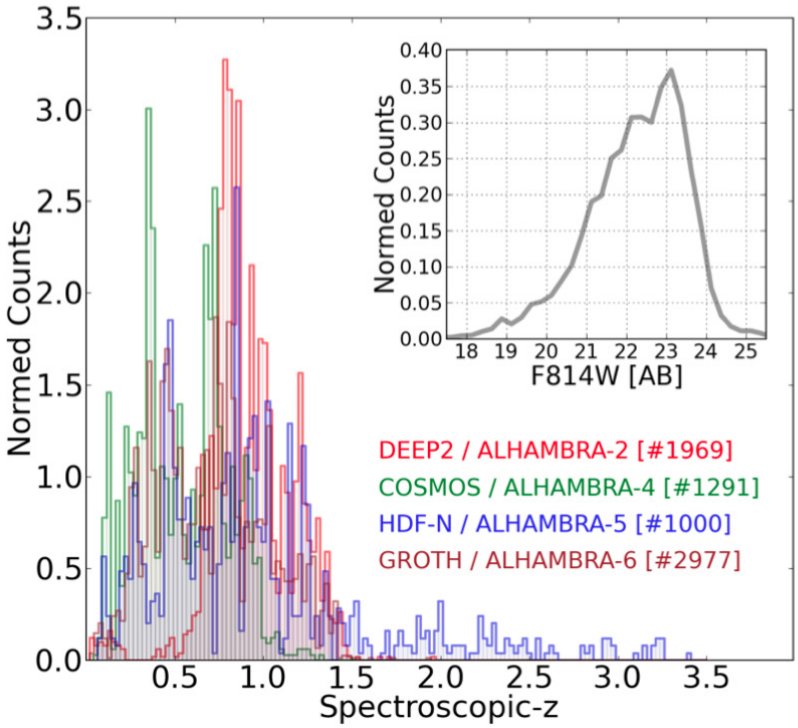

Figure 3.29 Spectroscopic redshift compilation. Given the overlap between the ALHAMBRA fields and other existing spectroscopic surveys, we compiled a sample of ∼7200 galaxies with secure spectroscopic redshifts to quantify the accuracy for our photometric redshifts. Each survey contribution is color-coded (for visualization) as indicated in the legend. As seen in the figure, the compiled redshift sample mostly covering the ALHAMBRA parameter space, showing a redshift range $0< z_s <1.5$ (with a mean redshift $< z_s >\sim 0.77$) and a magnitude range (based on ALHAMBRA photometry) 18<F814W<25 (with a mean magnitude F814W∼22.3).

As seen in Fig. 3.30, when compared with the spectroscopic sample, our photometric redshift estimations show a dispersion $\sigma_z = 0.0106$ for F814W < 22.5 with a fraction of catastrophic outliers $\eta_1 \sim 2.7\%$. For fainter magnitudes F814W < 24.5 the accuracy observed is $\sigma_z = 0.0134$ and the fraction of catastrophic outliers $\eta_1 \sim 4.0\%$. The fraction of catastrophic outliers dramatically decreases when selecting a more restricted sample (excluding X-ray emitters, AGNs or detections observed in only few bands). In addition, the photo-z error and the fraction of catastrophic outliers rapidly decreases as the *Odds* interval increases. We show the expected accuracy for the photometric redshifts as a function of redshift, F814W magnitude and *Odds* range in Fig. 3.31. A more detailed analysis can be found in Table 3.4.

In order to ensure the so-derived $\delta_z/(1+z_s)$ is representative for the spectroscopic sample, the cumulative distribution of sources is represented in Fig. 3.32. We observed that $\sim$64% and $\sim$90% of the photometric redshifts are well fitted within the formal 1σ and 2σ confidence interval, respectively. This indicates that the uncertainties on z_b are realistic.

Applying the same approach as explained in Section 3.15.1, we performed internal photometric redshifts checks to compare our results among contiguous CCDs. As illustrated in Fig. 3.33, the statistical results were consistent between CCDs showing a scatter within the intrinsic variance for the sample observed by each CCD.

3.18 Photometric zeropoint recalibration.

3.18.1 Photometric ZP calibrations using spectroscopic redshifts.

As it was shown in Coe et al. (2006), by comparing the observed colors of galaxies with spectroscopic redshifts against those expected from an empirically defined photo-z library, it is possible to calibrate photometric zeropoints to within a few percentage, similar or better than the accuracy reached by standard, stellar-based calibration techniques. This capability has been included in the BPZ software package from its initial release (Benítez 2000) and has been applied successfully to several datasets (Capak et al. 2008, Hildebrandt, Wolf & Benítez 2008).

To calibrate the ALHAMBRA zeropoints, we followed this procedure for each individual CCD. First, we selected the spectroscopic redshift galaxies detected in all the 24 bands with a S/N>10, and chose the BPZ template which best fit its colors at their redshift. We then calculated the ratios between the fluxes predicted in each band by the templates and those observed; the median ratio, which converted to a magnitude represents the zeropoint offset (ZPO) required to match the observed magnitudes to the expected ones. We then corrected the fluxes by this value and iterated until the process converged and the calculated correction was below 1% in all the filters. Since all these changes are relative by nature, the synthetic F814W images were taken as anchor of the whole system.

Another useful quantity calculated by BPZ is the excess scatter over the expected photometric error, what we call zeropoint error (ZPE). This noise excess can be interpreted as follows. On the one hand, as measurement of the typical mismatch between template and real galaxy colors, averaged over all galaxies observed in that filter. On the other hand, given the flexibility of the template grid,

Table 3.4 Photometric redshift quality vs spectroscopic redshifts and F814W Magnitude.

Spectroscopic Redshift	σ_z (Odds>0.0)	# (%)	η_1 (%)	η_2 (%)	σ_z (Odds>0.5)	# (%)	η_1 (%)	η_2 (%)	σ_z (Odds>0.9)	# (%)	η_1 (%)	η_2 (%)
$0.00 < z < 0.25$	0.0115	10.8	0.4	0.8	0.0086	3.8	0.1	0.2	0.0056	0.3	0.0	0.0
$0.25 < z < 0.50$	0.0101	21.0	0.6	1.5	0.0087	10.5	0.2	0.4	0.0062	1.6	0.0	0.1
$0.50 < z < 0.75$	0.0136	19.6	1.0	2.4	0.0107	11.5	0.3	0.8	0.0061	1.2	0.1	0.1
$0.75 < z < 1.00$	0.0135	21.4	0.7	2.3	0.0104	12.7	0.2	0.7	0.0066	1.4	0.0	0.1
$1.00 < z < 1.25$	0.0171	13.2	0.4	1.3	0.0125	7.0	0.1	0.4	0.0070	0.3	0.0	0.0
$1.25 < z < 1.50$	0.0194	7.2	0.3	0.9	0.0132	2.3	0.1	0.3	—	—	—	—
$1.50 < z < 1.75$	0.0988	3.4	0.1	0.2	0.0567	0.3	0.0	0.0	—	—	—	—
$1.75 < z < 2.00$	0.1078	1.4	0.2	0.4	0.1620	0.0	0.0	0.1	—	—	—	—

Magnitude F814W	σ_z (Odds>0.0)	# (%)	η_1 (%)	η_2 (%)	σ_z (Odds>0.5)	# (%)	η_1 (%)	η_2 (%)	σ_z (Odds>0.9)	# (%)	η_1 (%)	η_2 (%)
$18.0 < m < 19.0$	0.0081	0.8	0.0	0.1	0.0073	0.6	0.0	0.0	0.0055	0.1	0.0	0.0
$19.0 < m < 20.0$	0.0083	2.2	0.1	0.3	0.0077	1.7	0.1	0.1	0.0056	0.3	0.1	0.1
$20.0 < m < 21.0$	0.0095	5.3	0.3	0.7	0.0085	4.1	0.1	0.3	0.0059	0.7	0.0	0.0
$21.0 < m < 22.0$	0.0101	11.9	0.4	1.1	0.0093	9.0	0.2	0.5	0.0058	1.3	0.0	0.0
$22.0 < m < 23.0$	0.0140	26.0	0.7	2.1	0.0111	16.0	0.3	0.9	0.0065	1.5	0.0	0.0
$23.0 < m < 23.5$	0.0182	22.8	0.6	2.1	0.0129	9.4	0.2	0.6	0.0045	0.5	0.0	0.0
$23.5 < m < 24.0$	0.0263	30.7	0.9	2.3	0.0118	7.4	0.2	0.4	0.0038	0.3	0.0	0.0

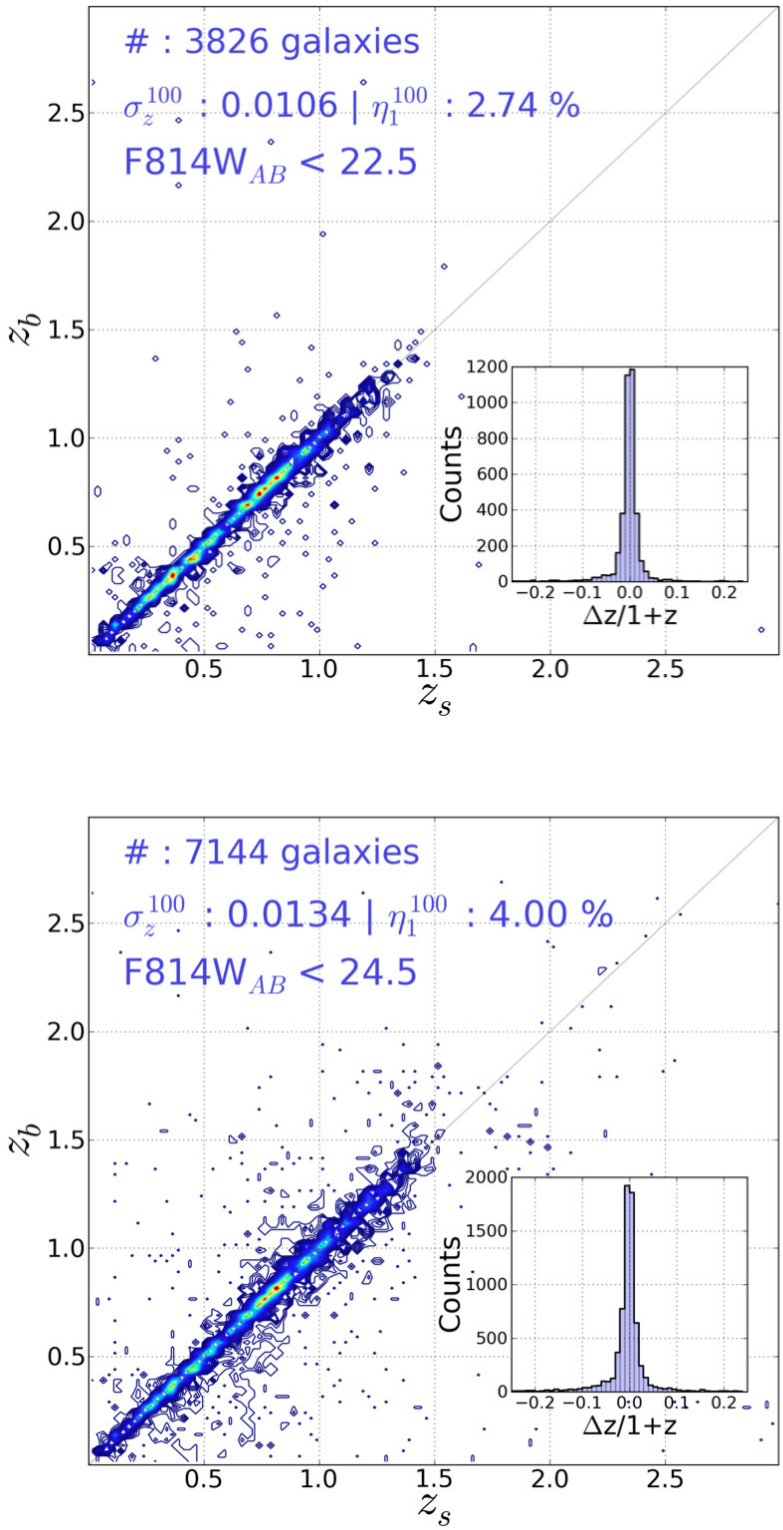

Figure 3.30 Photometric redshift accuracy. The figures show the comparison between the ALHAMBRA photometric redshifts z_b and the spectroscopic redshifts z_s along with the error distribution $\Delta_z/(1+z)$, for two magnitude ranges. While the left panel shows the accuracy obtained for the bright sample (F814W<22.5) with a σ_z<0.0106 and a fraction of catastrophic outliers $\eta_1\sim$2.7%, the right panel shows a σ_z<0.0134 and a fraction of catastrophic outliers $\eta_1\sim$4.0% when including the entire sample. In both cases, the fraction of catastrophic outliers (defined in Section 3.17) dramatically reduces when selecting galaxies with higher *Odds*, as indicated in Table 3.5.

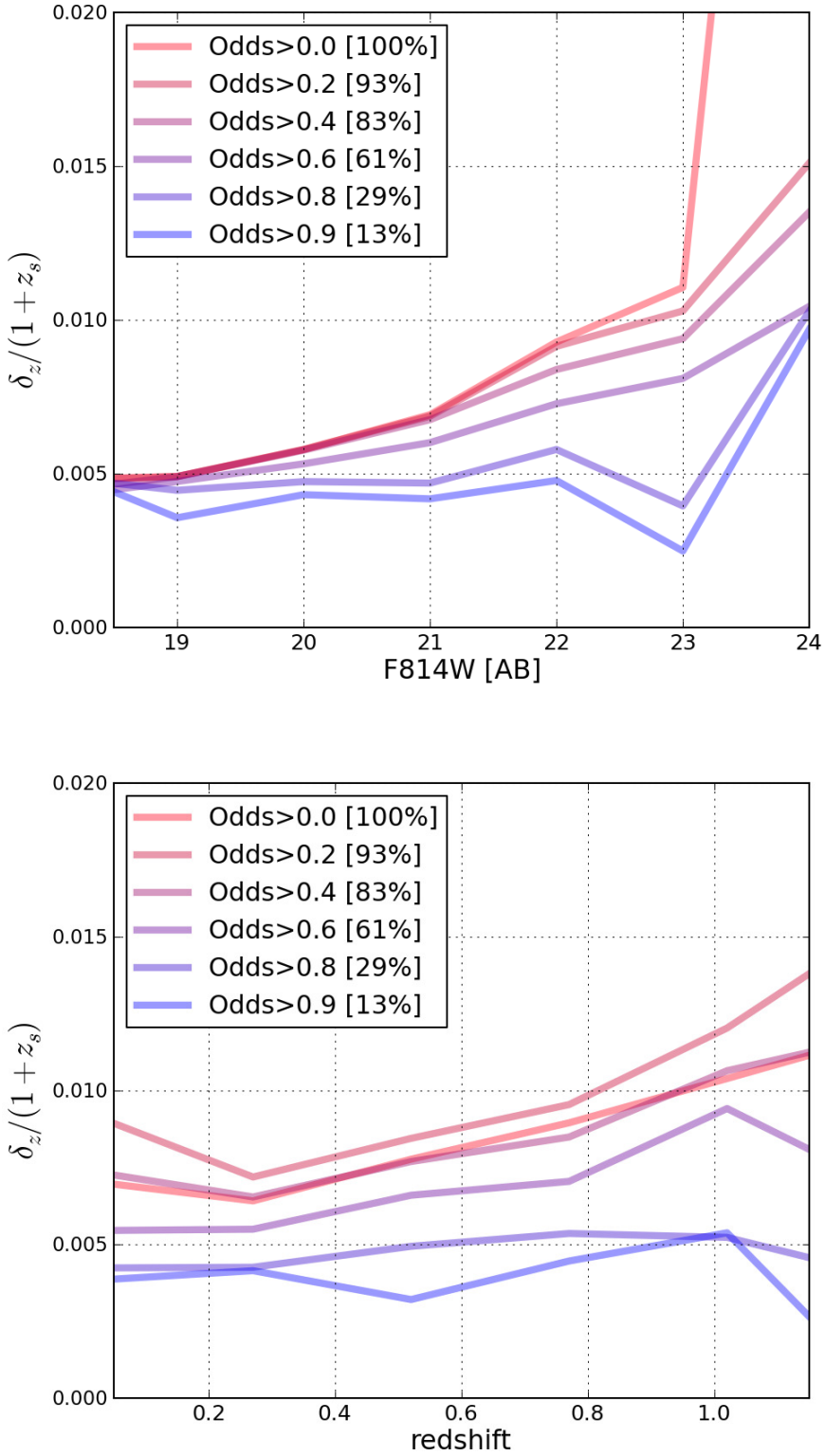

Figure 3.31 Photometric redshift accuracy as a function of apparent magnitude F814W (left panel) and spectroscopic redshift (right panel). We explored the expected accuracy for our photometric redshifts in terms of a specific magnitude range and redshift range applying different *Odds* intervals.

Table 3.5 Photometric redshift accuracy vs Odds, for galaxies with magnitude F814W<24.

Interval	Sample[1] (%)	σ_z	η_1 (%)	η_2 (%)
Odds > 0.00	1.00	0.0137	3.04	8.64
Odds > 0.10	0.91	0.0131	2.56	7.36
Odds > 0.20	0.80	0.0123	2.13	6.01
Odds > 0.30	0.71	0.0116	1.71	5.00
Odds > 0.40	0.61	0.0109	1.46	4.09
Odds > 0.50	0.50	0.0102	1.08	2.89
Odds > 0.60	0.36	0.0093	0.72	1.86
Odds > 0.70	0.24	0.0082	0.51	1.13
Odds > 0.80	0.14	0.0069	0.30	0.57
Odds > 0.90	0.07	0.0062	0.15	0.23
Odds > 0.95	0.03	0.0057	0.08	0.14

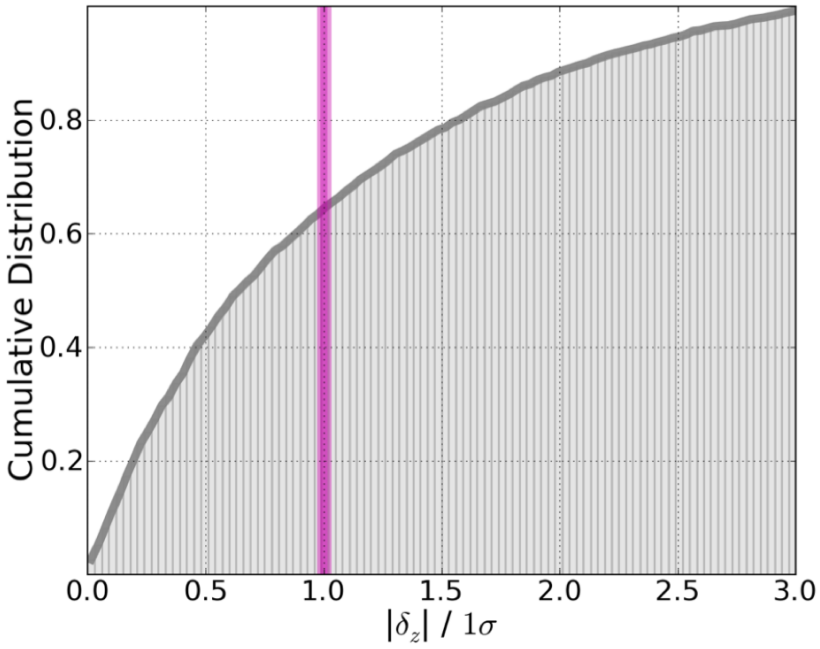

Figure 3.32 Cumulative Distribution of the ratio $|\delta z|/1\sigma$. We observed that ∼64% and ∼90% of the photometric redshifts are well fitted within the formal 1σ (magenta vertical line) and 2σ confidence interval, respectively. This indicates that the photometric redshift uncertainties have been reliably established.

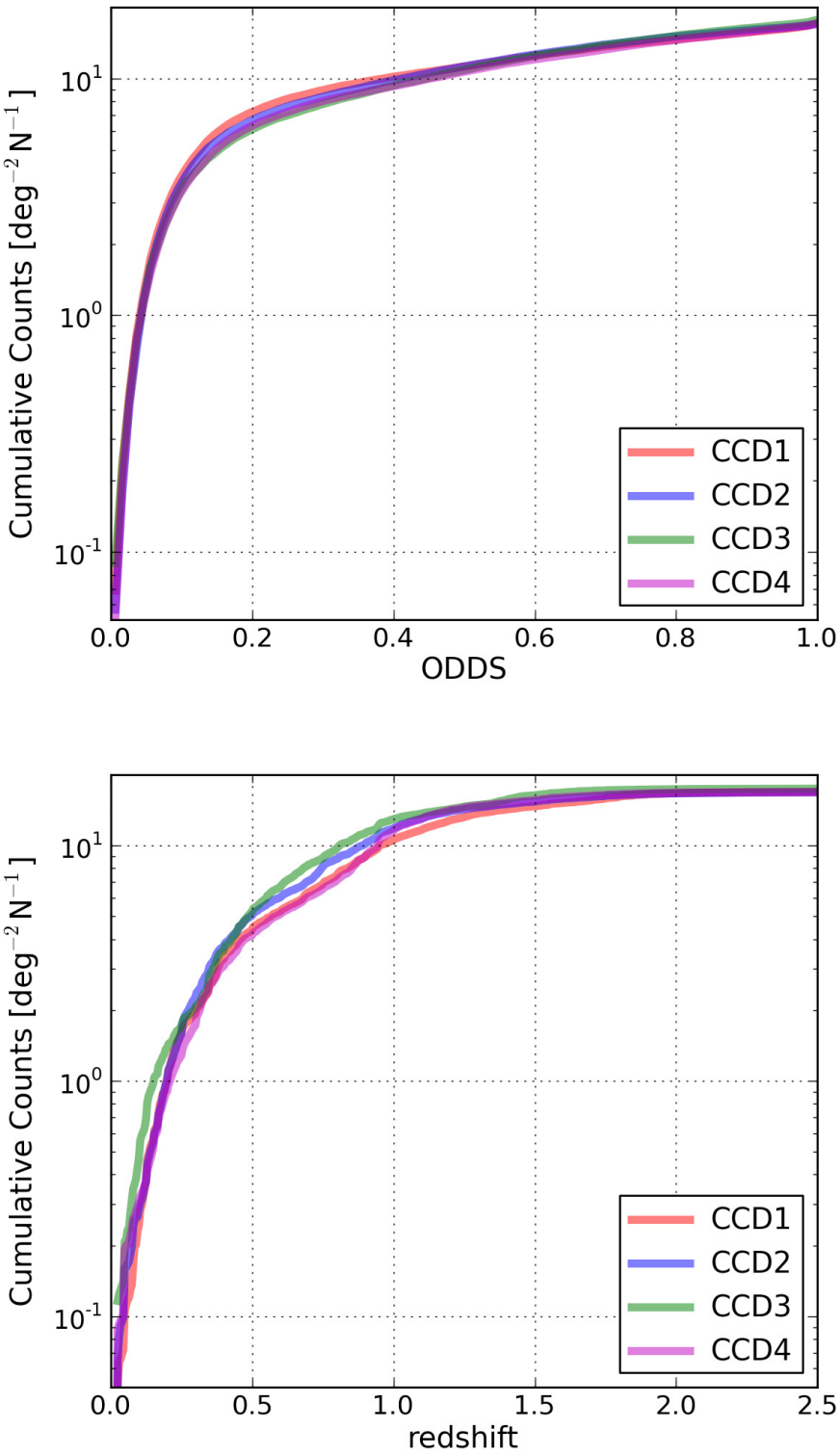

Figure 3.33 Internal photometric redshift checks. Following the same approach as explained in Section 3.15.1, we systematically compared the *Odds* (left panel) and photometric redshift z_b (right panel) distributions among contiguous CCDs. The statistical results were consistent between each other with a scatter within the expected intrinsic variance for the sample imaged by each detector. These test served to ascertain the homogeneity within the different fields.

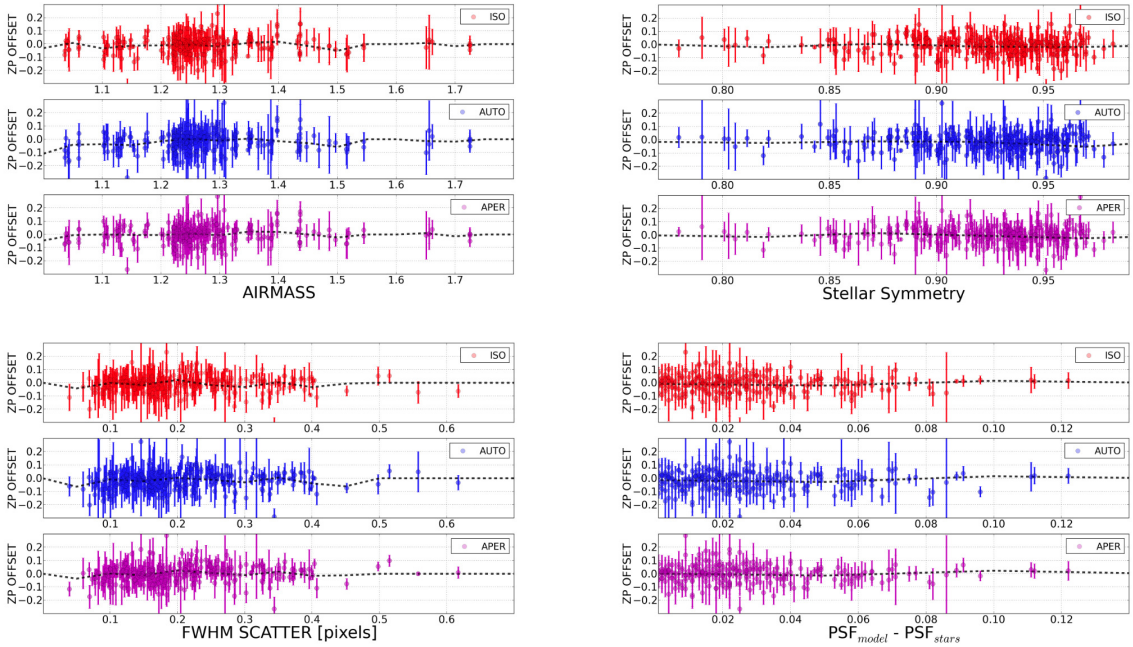

Figure 3.34 Photometric zeropoint validations. We studied the source of the photometric zeropoint corrections (derived using SED-fitting algorithms) by comparing these quantities with several observational variables. Considering the possibility of a systematic effect during the data reduction, we represented globally the corrections for the ∼1100 individual images as a function of the AIRMASS (top left panel), the Stellar Symmetry (top right panel), the FWHM Scatter (bottom left panel) & the differences between PSFs-models and stars (top left panel). The procedure was repeated using three different photometric apertures (`SExtractor`_*ISOphotal* as red circles, `SExtractor`_*AUTO* as blue circles and `SExtractor`_*APER* (3") as magenta circles) to discard any systematic effect due to the galaxy sampling regions. As indicated by the mean value of the distributions (dashed black lines), no clear correlations were observed, with fluctuations smaller than 3% (within the expected photometric uncertainties)

.

a much more consistent explanation with the observations is that we are just observing a systematic error in the measurement of galaxy colors (to be discussed in Benítez (2013, in prep). It is essential to include this factor, in addition to the standard photometric error, to produce photo-z estimates significantly more accurate and robust.

We explored the dependence of the amplitude of these zeropoint corrections on several observational variables. As illustrated in Fig. Fig. 3.34, considering the possibility of a systematic effect during the data reduction, we represented globally the zeropoint corrections for the ∼1100 individual images as a function of the AIRMASS (top left panel), the Stellar Symmetry (top right panel) defined as the ratio of a/b parameters (Table $C.1$), the FWHM Scatter (bottom left panel) & the differences between PSFs-models and stars (top left panel). The procedure was repeated using three different photometric apertures (`SExtractor`$\_ISOphotal$ as red circles, `SExtractor`$\_AUTO$ as blue circles and `SExtractor`$\_APER$ (3") as magenta circles) to discard any systematic effect due to the galaxy sampling regions. As indicated by the mean value of the distributions (dashed black lines), we did not observe any clear correlations, with typical fluctuations smaller than 3% (within the expected photometric uncertainties).

We explored whether zeropoint offsets depended on the magnitude, i.e. whether brighter galaxies (with larger S/N ratio) would show smaller corrections. Then, we split the spectroscopic sample into two equal-sized groups with galaxies brighter and fainter than F814W=22.5. As seen in Fig. 3.35 (blue dots) the corrections derived for both samples are the same, within the typical level of photometric uncertainties. Even though filter F954W showed a clear disagreement among samples, its scatter was as large as ∼0.3 magnitudes indicating other sort of problems perhaps related to the reductions. To look for a dependence on the photometric aperture size, due to some effect related to the PSF corrections we again divided the spectroscopic sample into two equal-sized groups with photometric areas smaller (and larger, respectively) than 125 pixels. As seen in Fig. 3.35 (green dots) differences among samples were always within the photometric scatter. Finally the dependence between redshift range and zeropoint offsets was also considered assuming a possible effect due to evolution in the galaxy populations (since the BPZ templates do not include any evolution). As seen in Fig. 3.35 (magenta dots) the differences obtained from both samples were smaller than 3% and so within the error bars regime. We therefore conclude that the zeropoint offsets do not depend on the photometric treatment and represent real differences between the calibration obtained from traditional color transformations based on stars and the average colors of galaxies as defined by the BPZ template set, which is based on the colors of galaxies observed with HST.

3.18.2 Photometric ZP calibrations using photometric redshifts.

Although ALHAMBRA was designed to overlap with other spectroscopic surveys, only ∼40% of its fields had enough galaxies with spectroscopic redshifts to derive zeropoint corrections, as described above. As discussed in Section 3.18.1 the absence of any clear dependence on the observational parameters made unfeasible any extrapolations among different fields. Given the obvious photometric improvement when applying the zeropoint corrections, this fact created a serious problem of inhomogeneity for all those fields without available spectroscopy.

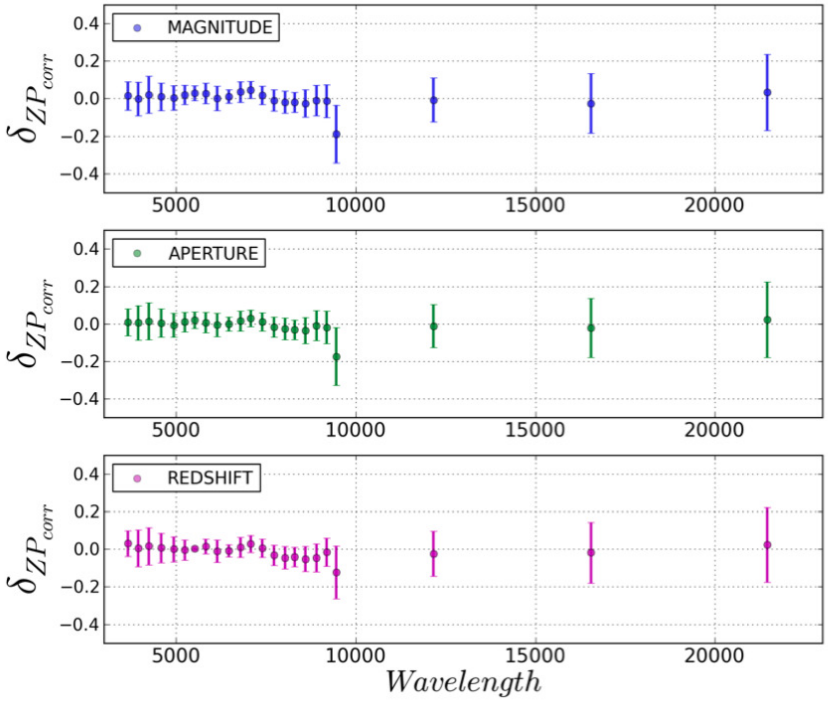

Figure 3.35 Photometric zeropoint validations II. We also studied the robustness of the photometric zeropoint corrections using different samples of galaxies and comparing their outcomes. Therefore, we split the spectroscopic sample in equal-sized groups based on its magnitude (F814W<22.5 & F814W>22.5), aperture size (area<125 pix & area>125 pix) and redshift (z<0.81 & z>0.81) and derived new photometric zeropoint corrections using BPZ. As observed in the figure, for all the three cases, the differences among samples (δ_{ZP}) were always smaller than the internal dispersion given by the error bars. This result ascertains that zeropoint corrections do not depend on any specific redshift range or spectral-type but probably on the inherent differences between the calibrations obtained from traditional color transformations based on stars and the average colors of galaxies as defined by the BPZ template set, calibrated with HST observations.

We realized that the photometric redshifts obtained for emission line galaxies were quite robust to changes in the zeropoint calibration and therefore we could treat those redshifts as spectroscopic for calibration purposes, obtaining an automatic and self-contained zeropoint correction for all our fields. Thus, we ran BPZ on the photometric catalogs with the original, stellar-based zeropoint estimations. Then we selected a sample formed by those galaxies observed in all 24 filters, large S/N (F814W<23.0), good fit to the SED ($Odds \geq 0.9$ and $\chi^2 \leq 1$) and classified by BPZ as late-type galaxies ($tb>7$). We applied the procedure described in Section 3.18.1, using the photometric redshifts as spectroscopic values and iterating until convergence was reached. This is basically equivalent to calibrating the ZP using the slope of the continuum of the ELGs.

In the top panel of Fig. 3.36 we show the photometric redshift accuracy when using three different calibration methods: the original zeropoints (red line), corrections derived from photometric redshifts

(blue line) and corrections from spectroscopic redshifts (green line). The results indicate that the methodology presented here successfully improved the photometric redshifts accuracy almost up to the level provided by the spectroscopic sample, and it also dramatically reduces the fraction of catastrophic outliers. The bottom panel of the Fig. 3.36 shows how the corrections derived with late-type galaxies worked very well for early-type galaxies, showing that the corrections were real and independent of the particular choice of templates in the library. It is worth noting that even if the accuracy reached by this method was always slightly worse than that provided by a real spectroscopic sample, it was always much better than the standard stellar-based calibration. Therefore, we decided to apply this kind of zeropoint calibrations whenever a spectroscopic sample was not available, which significantly improved the overall homogeneity of the ALHAMBRA sample. This kind of calibration, promises to have wide application to future narrow-band surveys such as JPAS (Benítez et al. 2009)

3.19 Photometric Redshift Distributions.

One of the main advantages of ALHAMBRA is that it includes 8 different lines of sight widely separated providing a more realistic estimation of both the typical redshift distribution of galaxies across cosmic time and its inherent variability (cosmic variance).

Considering the probabilistic nature of the photometric redshift estimations, instead of relying on the most likely solution (given by any point estimate) it is desirable to make use of the complete information yielded by the probability distribution functions $P(z, T|C)$ (Benítez 2000, Coe et al. 2006, Mandelbaum et al. 2008; Cunha et al. 2009; Wittman 2009; Bordoloi et al. 2010; Abrahamse et al. 2011; Sheldon et al. 2012). This approach represents a more convenient estimator as the $p(z)$ is not always well represented by a single and symmetric (Gaussian-like) distribution. For most faint galaxies, where the photometric information becomes scarce due to the S/N, redshift probability distributions usually become multimodal and completely asymmetric. In such situations drawing a single value from the distribution represents a clear loss of information or bias. The combination of all $P(z, T|C)$ fully describes the redshift distribution of galaxies indicated by the photometric data.

Therefore, we define the global photometric redshift distribution $P(z)$ as:

$$P(z) = \sum_{i=1}^{N_g} P_i(z) = \sum_{i=1}^{N_g} \left[\frac{\int dT\, p_i(z, T)}{\int dT \int dz p_i(z, T)} \right] \tag{3.14}$$

where $p_i(z, T)$ represents the probability distribution function for the i^{th} galaxy over the redshift range z and spectral-types T.

We also ran BPZ on the photometric catalogue used by Ilbert et al. (2009) to derive the global redshift probability distribution function $P(z)$ for the COSMOS field and so consistently compare it with our results. We initially compared the $P(z)$ derived using the ALHAMBRA-4 data (red line) with the $P(z)$ derived using the COSMOS data (blue line), as seen in the left panel of Fig. 3.37, where both distributions consistently reproduce a double peak at redshifts z$\sim$0.3 and z$\sim$0.9, respectively. However, whereas the ALHAMBRA-4 field shows a mean redshift $\langle z \rangle = 0.60$ for F814W < 22.5 and

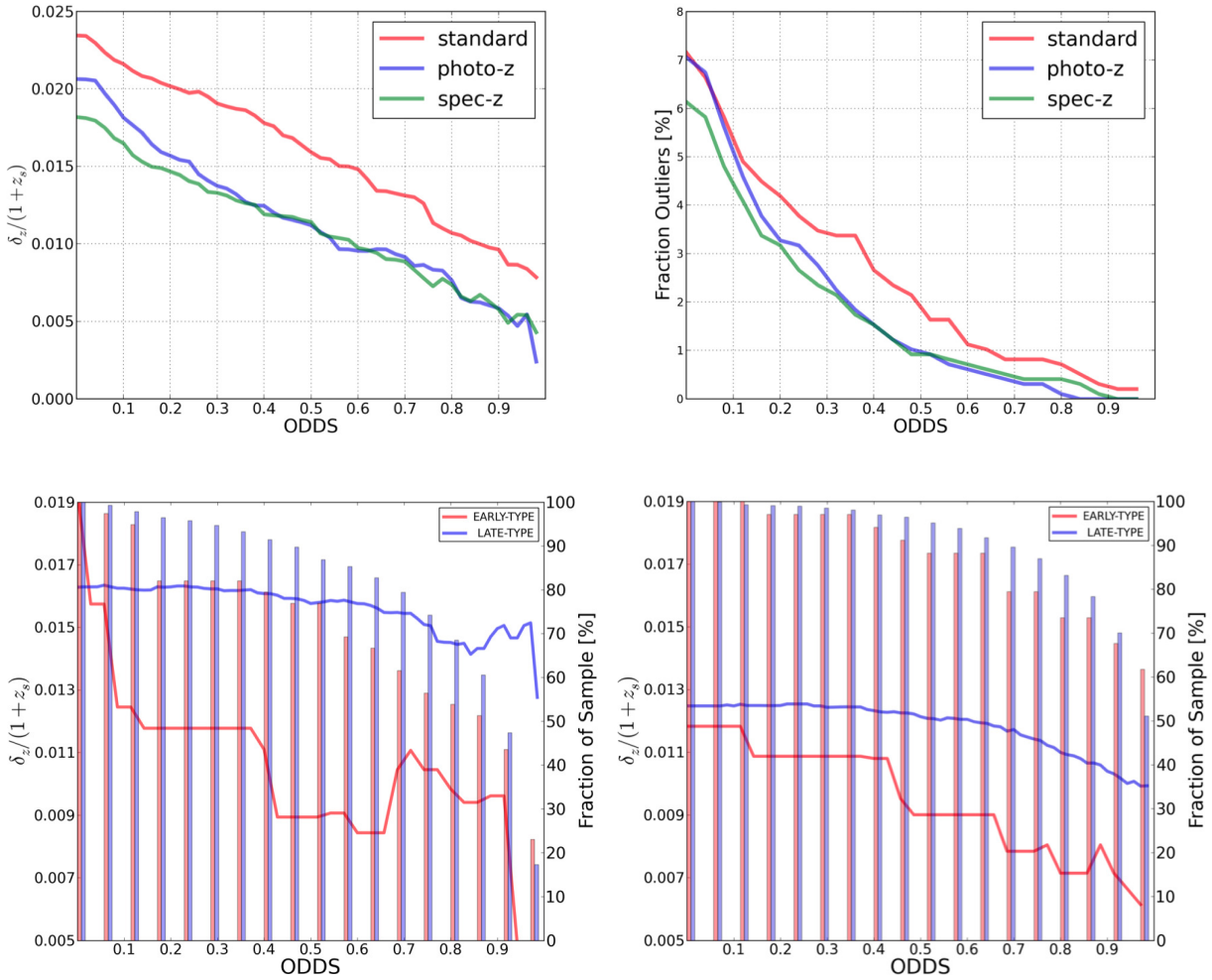

Figure 3.36 Here we show the feasibility of using emission line galaxies to derive photometric zeropoint corrections. To do so, we used the spectroscopic redshift sample to study the performance of our photometric redshifts (in terms of accuracy and fraction of catastrophic outliers) when applying zeropoint corrections derived from three different approaches: using a standard stellar-based method (red line), using photometric redshifts derived from emission line galaxies (blue line) and using a spectroscopic redshift sample (green line). As seen in the top left panel, photometric redshifts using emission line galaxies not only improved the outcomes using the stellar-based method but also increased its final accuracy up to the level of the spectroscopic method for galaxies with secure photometric-redshift (*Odds*>0.3). In addition, the fraction of catastrophic outliers with secure redshift was also significantly reduced as shown in top right panel. Meanwhile, we studied the impact of using emission line galaxies (late-type) to calibrate absorption line galaxies (early-type). We compared the performance of both spectral-types separately before (left bottom panel) and after (bottom right panel) applying the zeropoint corrections. As seen in the bottom panels, not only the accuracy for the late-type galaxies (solid blue line) improved significantly with the corrections but also the early-type galaxies (solid red line). Meanwhile, the fraction of galaxies per *Odds* interval (vertical bars) increased homogeneously among spectral-types, indicating that a larger number of galaxies with secure redshift were found after the calibration.

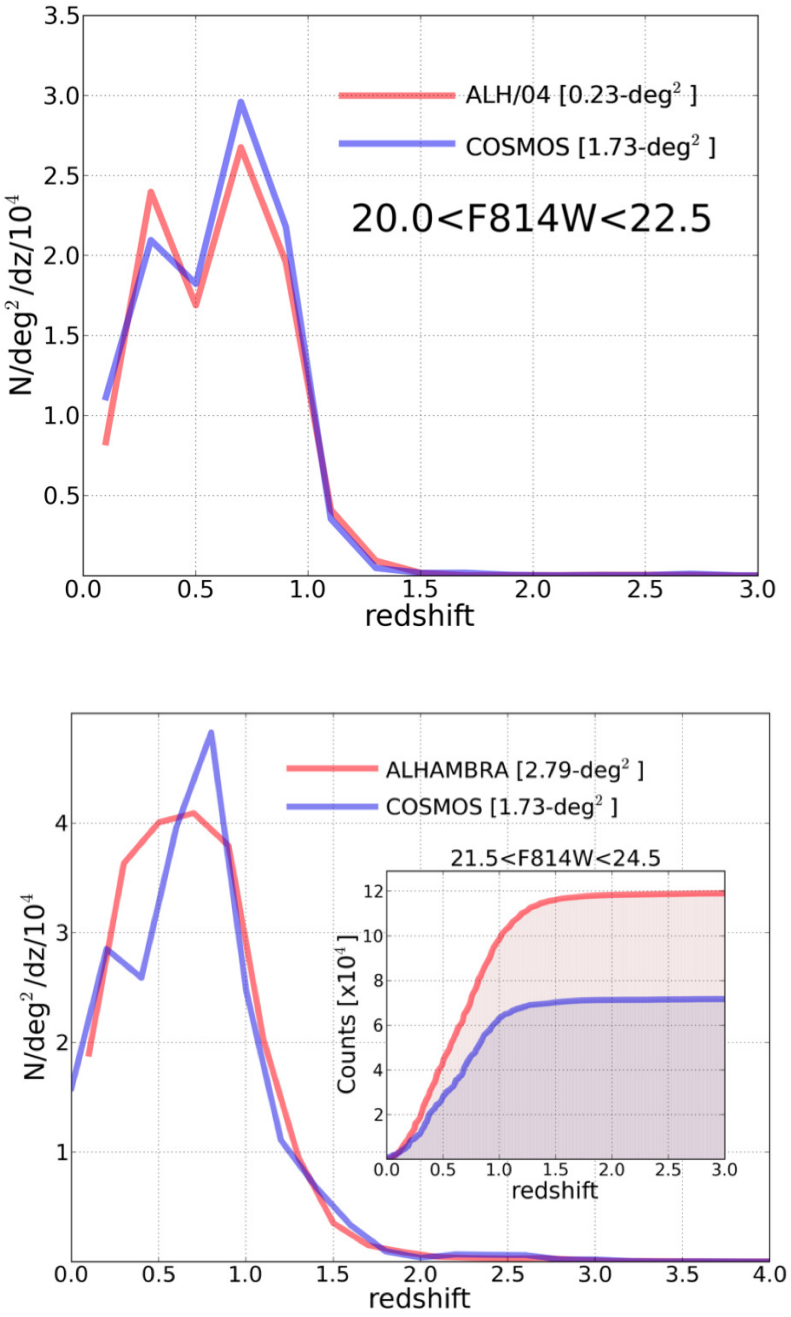

Figure 3.37 Comparison of the redshift probability distribution function $P(z)$ between ALHAMBRA and COSMOS. Considering the probabilistic nature of the photometric redshift estimations, we relied on the complete $P(z)$ to derive the redshift probability distribution functions for each of our fields. In addition, we ran BPZ on the photometric catalogue used by Ilbert et al. (2009) to derive the $P(z)$ for the COSMOS field and so consistently compare its redshift probability distribution with ALHAMBRA. Top: when comparing the $P(z)$ derived from ALHAMBRA-04 (red line) and COSMOS (blue line) both distributions consistently reproduce a double peak at redshifts z$\sim$0.3 and z$\sim$0.9, respectively. However, whereas the ALHAMBRA-4 field shows a mean redshift $\langle z\rangle$=0.60 for F814W<22.5 and $\langle$z$\rangle$=0.87 for F814W<25.5, the COSMOS field shows a mean redshift $\langle z\rangle$=0.66 for F814W<22.5 and $\langle z\rangle$=0.96 for F814W<25.5. Bottom: The global P(z) derived averaging the seven ALHAMBRA fields shows a mean redshift $\langle z\rangle$=0.56 for F814W<22.5 and $\langle z\rangle = 0.85$ for F814W<25.5. This result indicates that the COSMOS field shows a clear over-density with respect to the mean value, indicating that the COSMOS field has a rather peculiar redshift distribution which mimics a significant redshift density evolution effect.

$\langle z \rangle = 0.87$ for F814W < 25.5, the COSMOS field shows a mean redshift $\langle z \rangle = 0.66$ for F814W $<$ 22.5 and $\langle z \rangle = 0.96$ for F814W<25.5, as seen in the right panel of Fig. 3.37. Meanwhile the global photometric redshift distribution derived for all the seven ALHAMBRA fields (excluding stars) shows a mean redshift $\langle z \rangle = 0.56$ for F814W<22.5 and $\langle z \rangle = 0.85$ for F814W < 25.5, as seen in the right panel of Fig. 3.39. This result indicates that as it is known, the COSMOS field shows a clear overdensity with respect to the mean value derived averaging the seven ALHAMBRA fields. In fact, the average galaxy number in COSMOS goes up by a 60% between z=0.4 and z=0.7, whereas no such effect is observed in our average.

To study the evolution of the number counts as a function of the magnitude F814W and redshift, we derived the averaged redshift probability distribution function for the ALHAMBRA fields. As seen in the left panel of Fig. 3.38, the solid red line corresponding to the mean redshift distribution (per bins of 0.5 mags) indicates a clear evolution moving from a $\langle z \rangle \sim 0.2$ for F814W<20.5 to a $\langle z \rangle \sim 0.8$ for F814W>23.0. Inversely, the right panel of Fig. 3.38 shows how the peak of the averaged distribution of galaxies increases as a function of the redshift for different magnitude ranges.

We explored the variance in the redshift-magnitude distribution of galaxies as a function of the absolute B magnitude and the spectral-type. As seen in Fig. 3.40, we split the sample among early-type galaxies (top panel, defined as $1 < T_b < 5$) and late-type galaxies (bottom panel, defined as $7 < T_b < 11$) to compare the resulting distributions among each of the 7 individual ALHAMBRA fields (Ai) + 1 averaged sample (*Global*). As observed from the figure, where the logarithmic density is color-coded, whereas each individual field shows clear and identifiable structures at different redshifts, the global sample shows a much more smooth distribution. In particular, we find that the well-known bimodal distribution in the COSMOS field (A4) is not systematically observed along the other fields. Once again, this result emphasizes the usefulness of the ALHAMBRA sample to measure statistical properties of galaxies.

3.20 Photometric redshift depth.

Due to color/redshift degeneracies, it is possible to have galaxies which are detected at high S/N in many filters but for which no unambiguous redshifts can be derived. One of the main practical ways of characterizing the effective completeness and depth of a photometric redshift catalog is by using the amount of galaxies with *Odds* above a certain threshold, which basically tells us how many galaxies we can expect to have meaningful, unambiguous photometric redshifts (Benítez 2000, Benítez 2009b).

We therefore took into account the *Odds* to carry out a set of analysis and evaluate the completeness and accuracy of our performance. For this work we set the interval to compute the *Odds* parameter to $DZ = 2*0.0125*(1+z)$ since this quantity corresponds to twice the expected sigma. The completeness factor (fraction of galaxies per *Odds* interval) as a function of F814W magnitude is presented in Fig. 3.41.

For sources only detected on its F814W detection image, an upper limit (defined as 1-σ above the background) is provided. These limiting magnitudes represent the deepest magnitudes extractable from an image providing an useful information during SED-fitting analysis. Limiting magnitudes are

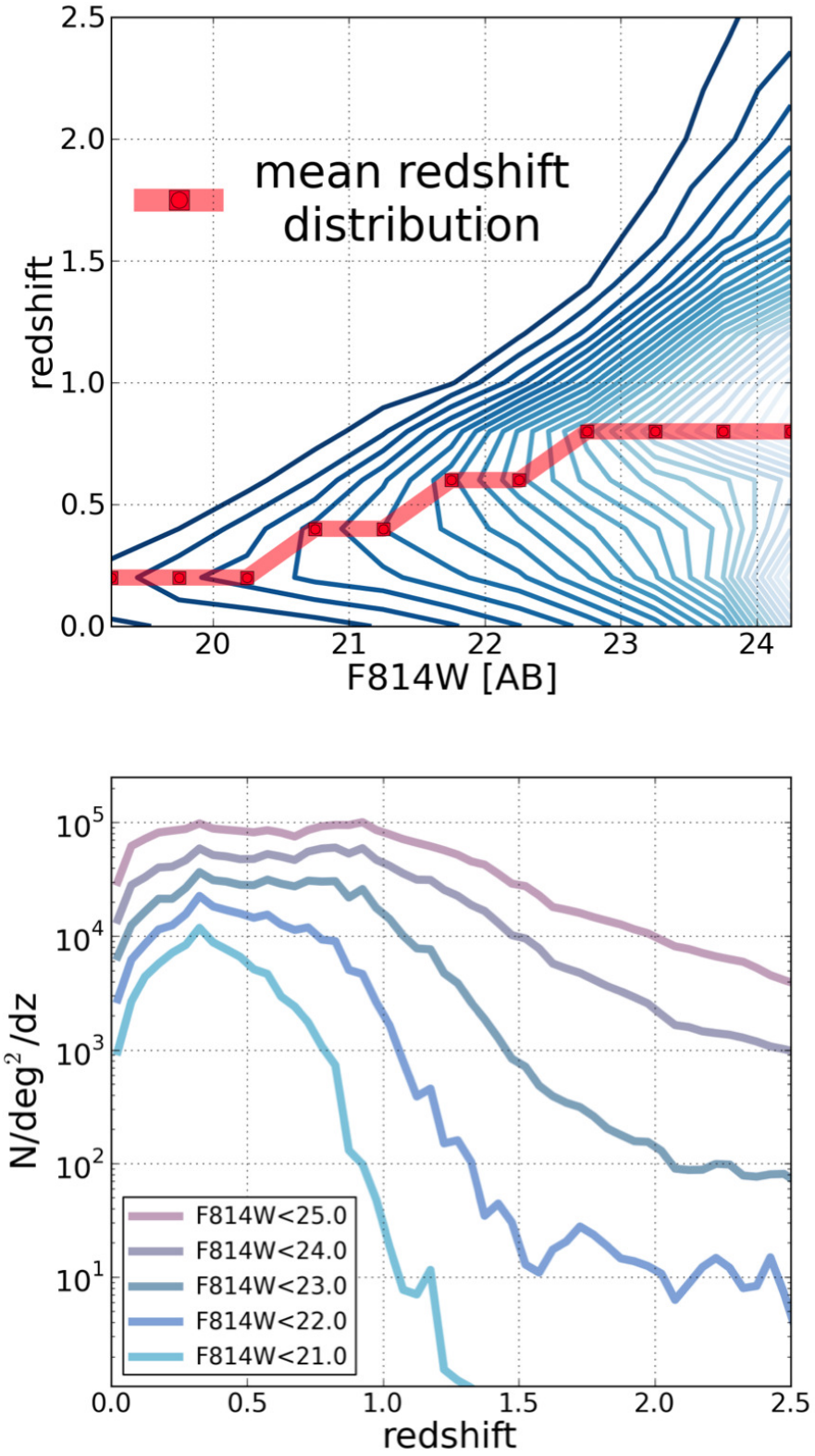

Figure 3.38 Evolution of the redshift distribution. The left panel shows the evolution of the averaged redshift distribution for the ALHAMBRA fields, as a function of the magnitude F814W. The mean redshift distribution (solid red line) indicates a clear evolution moving from a $\langle z \rangle \sim 0.2$ for F814W$<$20.5 to a $\langle z \rangle \sim 0.86$ for F814W$>$23.0. The right panel shows the averaged distribution of galaxies for the ALHAMBRA fields, as a function of the redshift for different ranges in magnitude.

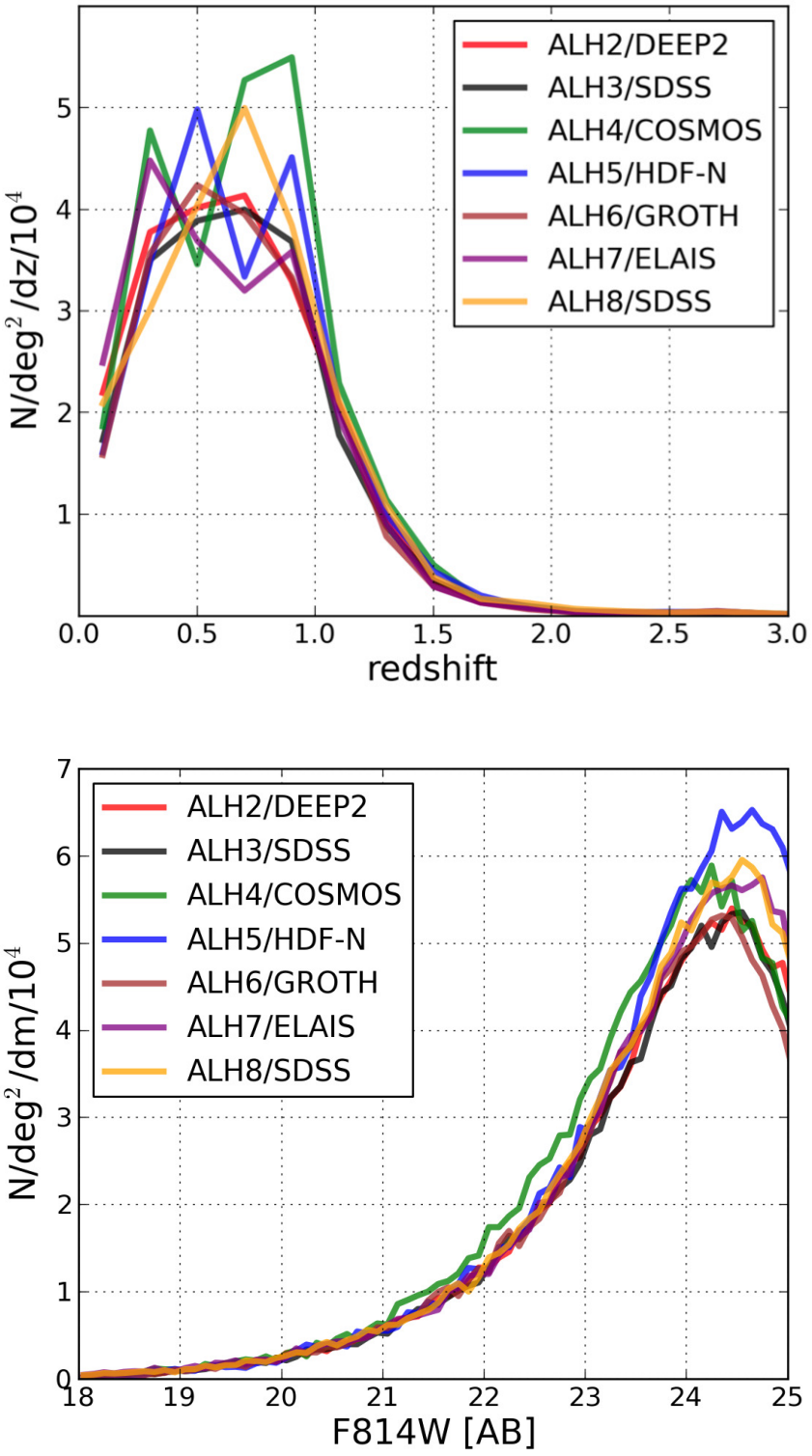

Figure 3.39 Effect of the cosmic variance in the P(z). The left panel shows the redshift probability distribution function $P(z)$ for all the seven ALHAMBRA fields, using a range in magnitudes between 19.0<F814W<23.5. The different ALHAMBRA fields are color-coded as indicated in the legend. Once again the ALHAMBRA-04 field associated with the COSMOS fields (green line) shows a peculiar distribution with a prominent peak at redshift z∼0.86. The right panel shows the cumulative number counts for the seven fields. Again the ALHAMBRA-4 field (green line) shows a clear excess in the number of galaxies detected per magnitude range with respect to the other fields.

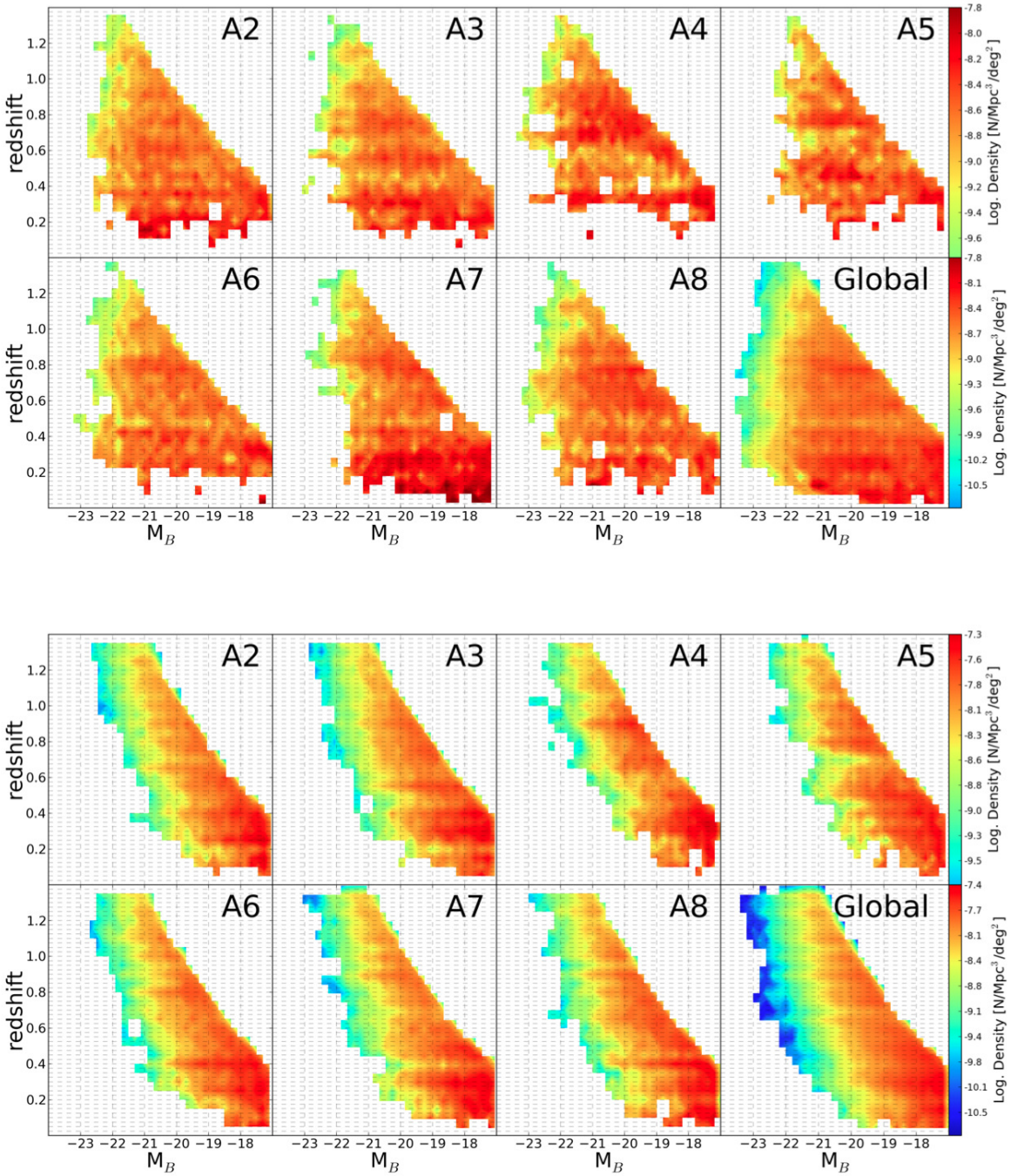

Figure 3.40 Redshift distribution in the rest-frame per ALHAMBRA field. We explored the variance in the redshift-magnitude distribution of galaxies as a function of the absolute B magnitude and the spectral-type. After splitting the sample among early-type galaxies (top panel, defined as $1< T_b <5$) and late-type galaxies (bottom panel, defined as $7< T_b <11$), we compared the resulting distributions among each of the 7 individual ALHAMBRA fields (Ai) + 1 averaged sample (*Global*). As observed from the panels, where the logarithmic density is color-coded, whereas each individual field shows clear and identifiable structures at different redshifts, the global samples show a more smooth distribution. In particular, we find that the well-known bimodal distribution in the COSMOS field (A4) is not systematically observed along the other fields, emphasizing the effects of cosmic variance on galaxy evolution studies.

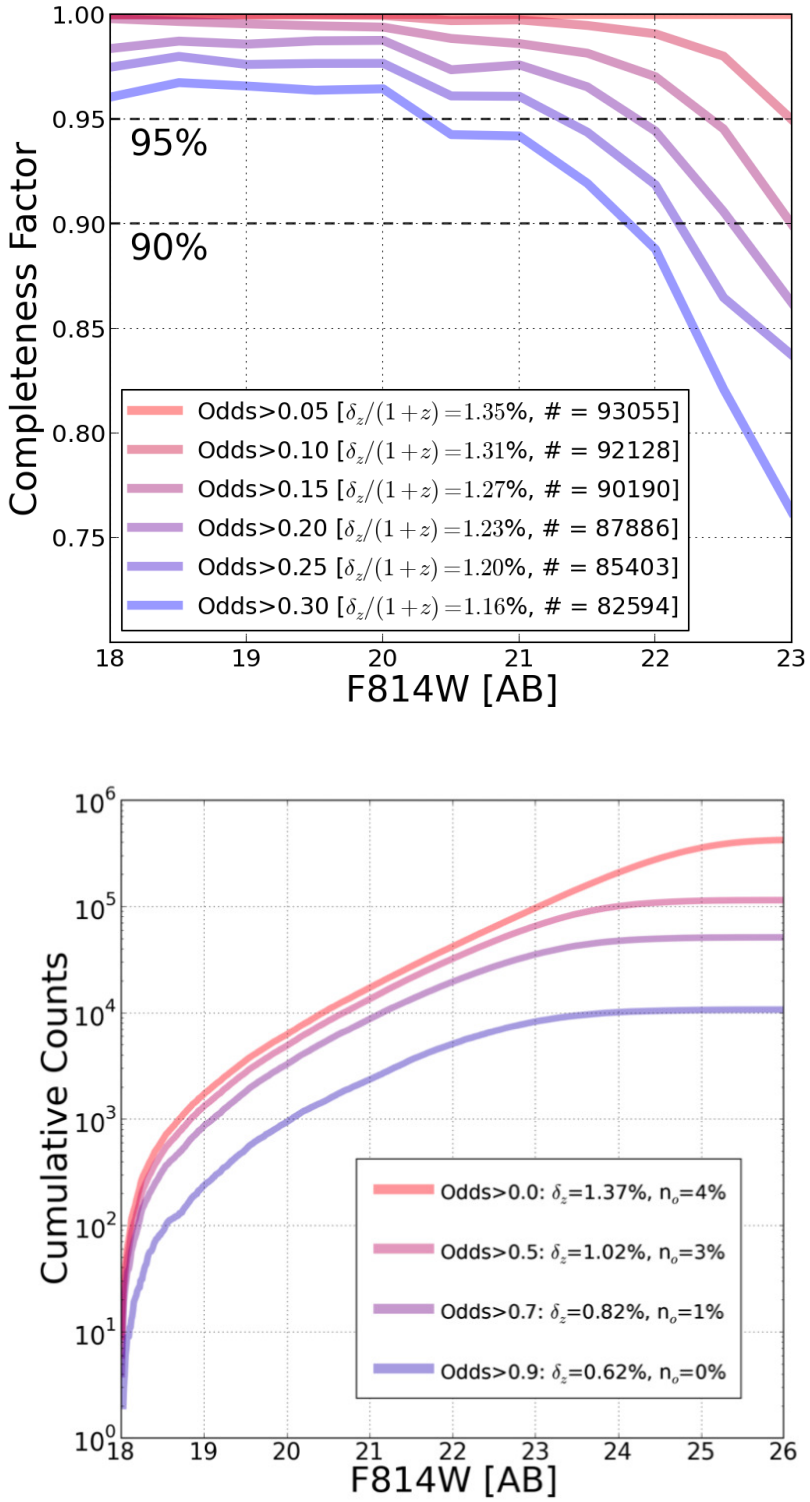

Figure 3.41 Photometric Redshift Depth. In order to characterize the photometric redshift depth for the ALHAMBRA catalogues, we quantified the amount of galaxies per *Odds* interval, which is equivalent to estimate the fraction and distribution of galaxies with a certain photometric redshift accuracy. As seen in the left panel, we explored the expected Completeness Factor as a function of the magnitude F814W and *Odds* interval. The total fraction of galaxies within each interval is specified in the legend. Similarly, the right panel shows the Cumulative distribution of galaxies as a function of the F814W magnitude for different *Odds* intervals. The expected accuracy for the photometric redshifts δ_z and the fraction of catastrophic outliers n_o (according to the spectroscopic sample) is indicated in the legend.

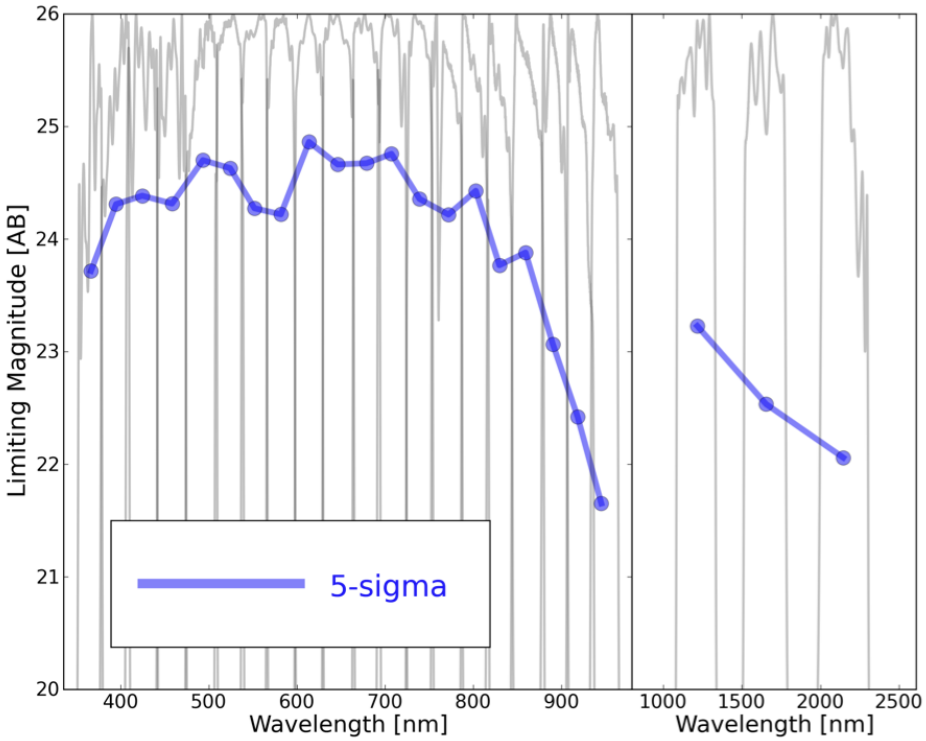

Figure 3.42 Limiting magnitudes. We derived limiting magnitudes for every image, as they represent a very useful piece of information during the SED-fitting procedure. As required by BPZ, we replaced galaxies with measured fluxes equal or lower than the estimation of the background signal by an upper limit defined as 1-σ above the background. Since limiting magnitudes depends on the photometric uncertainties, we computed limiting magnitudes after reestimating empirically the photometric errors. Meanwhile, we calculated the expected limiting magnitude using fixed apertures of 3" and 5-σ, as seen in the figure. These magnitudes correspond to the averaged values for the complete set of images.

applied whenever measured fluxes, inside a fixed aperture, are equal or lower than the estimation of the background signal. Since limiting magnitudes depends directly on photometric errors, we computed limiting magnitudes after reestimating photometric errors, via empirical sigma estimation (Section 3.15). Derived limiting magnitudes for each band can be found within the photometric catalogues. In Fig. 3.42 we represent the averaged 5-σ limiting magnitudes for all the 23 bands using fixed circular apertures of 3".

3.21 Emission-line galaxies

When plotting the *Odds* distribution as a function of F814W magnitude for all galaxies, we find a clear locus at magnitudes in between 18<F814W<23 and 0.0<*Odds*<0.1. When plotting the logarithmic χ^2 distribution over the former *Odds* vs magnitude diagram, it immediately reveals those detections to have the highest χ^2 values and so the worst SED-fitting results to the galaxy templates, as illustrated

in Fig. 3.43.

Detections with unexpected poor χ^2 fitting (given its magnitude) could be due to unreported photometric flaws worsening its SED-fitting performance or to an incomplete library of templates used to fit the data with. After purging the sample for every photometrically flagged detection, remaining galaxies within that locus were classified in two different groups: 1. unresolved stellar pairs (identified as a single detection by `SExtractor`) with clearly asymmetric morphologies (despite their photometric colors) and 2. very strong broad emission-line objects. As mentioned in Section **??**, neither AGN nor QSO templates were included in the BPZ library and therefore these sources might be expected to show poor fits to any BPZ template. As illustrated in left panel of Fig. 3.43, a fraction of $\sim$0.1% active galaxies was found along the ALHAMBRA fields with this technique. Given the high value of χ^2, the resulting photometric redshifts are (in most cases) assigned by the prior probability and so favoring solutions at redshift $z_b \sim 0.4$ with intermediate spectral-types Tb (E0/Scd/Sbc).

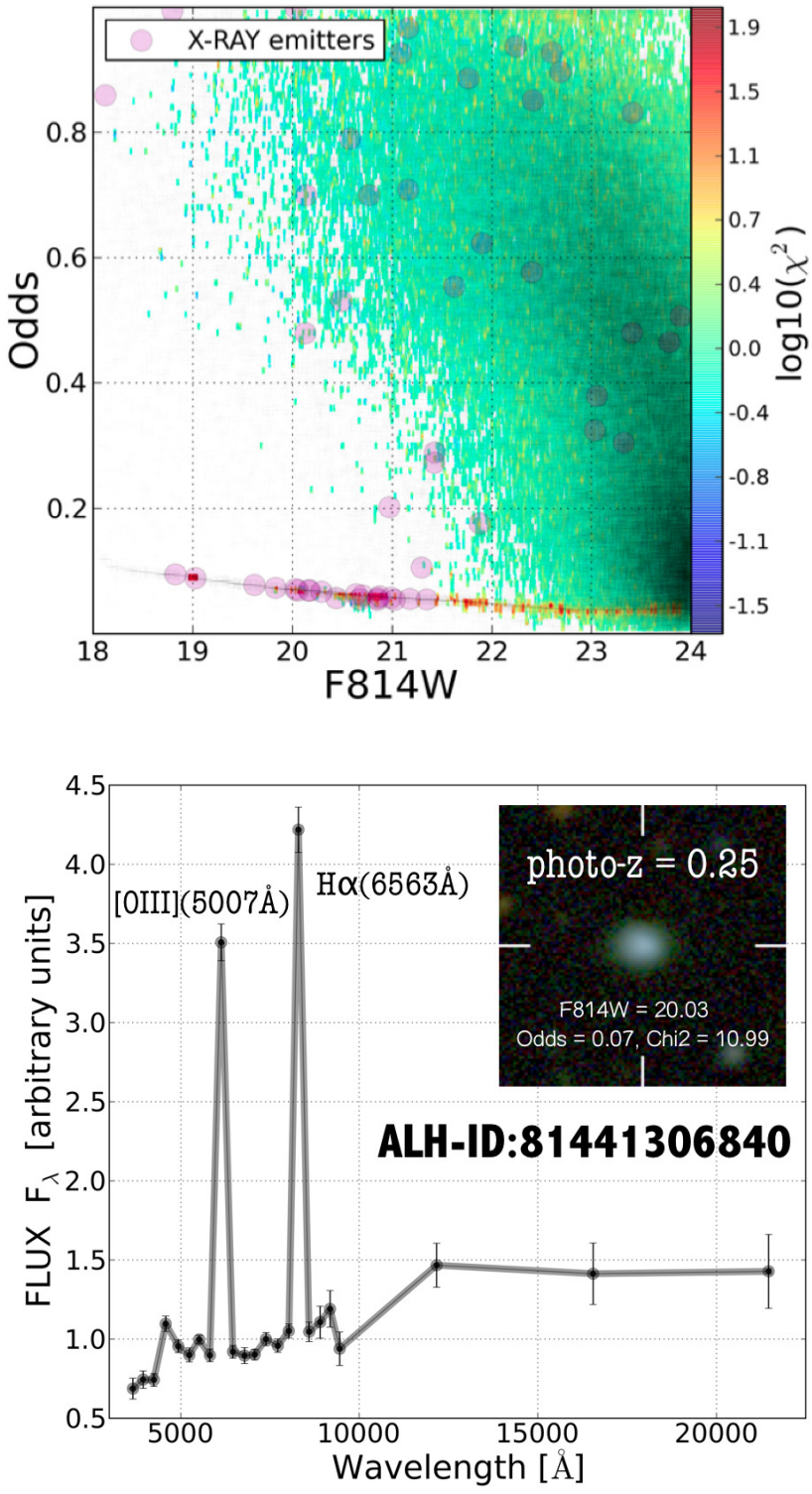

Figure 3.43 Emission-line galaxies identification. The left panel shows the *Odds* distribution as a function of magnitude F814W for the complete catalogue (stars excluded). As expected, there is a clear dependency between the *Odds* and the magnitude, indicating how the photometric redshifts confidence decreases with the S/N. We observed an unexpected locus for magnitudes in between 18<F814W<24 and *Odds* in between 0.0<*Odds*<0.1. When plotting the logarithmic χ^2 distribution, it revealed those detections to have extremely high χ^2 values when SED-fitting the BPZ galaxy templates. We observed that those sources were mostly composed for very strong broad emission-line objects, AGNs and QSOs, galaxy types not included in the BPZ library of templates. The right panel shows an example of an intense emission-line galaxy within that horizontal sequence.

4

Dark Matter

The Universe has proven to be far more intriguing in its composition than we knew it to be even just 14 years ago. It is a "dark" Universe where $\sim 23\%$ of its mass-energy density is made up of weakly interacting (and, as yet, undetected) non-baryonic particles (a.k.a. dark matter) and $\sim 73\%$ is as yet unknown physics (a.k.a. dark energy) that is driving an accelerated expansion of the metric (Riess et al. 1998, Perlmutter et al. 1999, Clowe et al. 2006).

Clusters of galaxies, by virtue of their position at the high end of the cosmic mass power spectrum, provide a powerful way to constrain the frequency of high amplitude perturbations in the primordial density field. As such, they play a direct and fundamental role in testing cosmological models and in constraining the properties of dark matter (DM), providing unique and independent tests of any viable cosmology and structure formation scenario, and possible modifications of the laws of gravity. A key ingredient of such cluster-based cosmological tests is the mass distribution of clusters, both on (sub) Mpc scales and across the range of populations. Accurately determining the relationship between the shape and depth of a halo's gravitational potential and its total mass as a function of redshift provides a fundamental constraint on structure formation theory.

Unfortunately, the best studied clusters to date have also been among the strongest gravitational lenses known. Such lensing-selected clusters are highly biased toward halos with high concentrations, both intrinsically and as projected on the sky due to halo elongation along the line of sight (Hennawi et al. 2007, Oguri & Blandford 2009, Meneghetti et al 2010, Meneghetti et al. 2011). These biases are estimated to lead to systematically higher concentrations by as much as 50% or more. Understanding the true constraints from observed concentration and mass profile measurements on Λ cold dark matter (ΛCDM) structure formation models is one of the important problems that can be tackled with a deep, high angular resolution imaging survey of a significantly larger and more homogeneously selected sample of galaxy clusters.

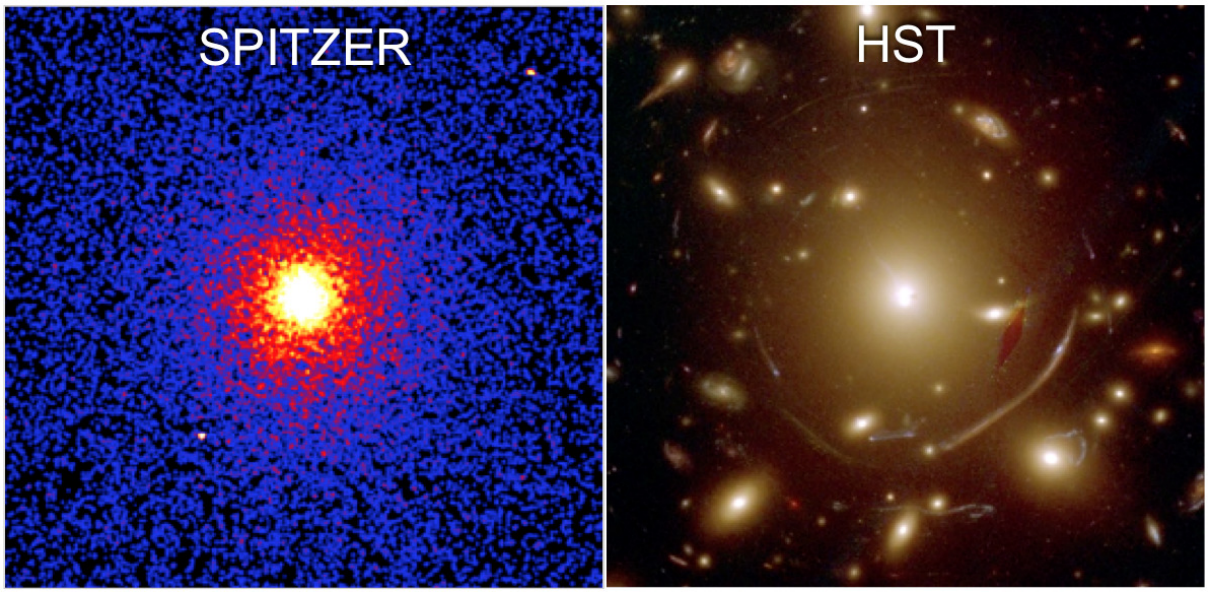

Figure 4.1 The figure shows one of 24 selected cluster (Abell383) for the CLASH survey. Left panel shows the cluster emission as detected by the *Chandra X-ray Observatory*, which exhibits a high degree of dynamical relaxation and a well-defined central surface brightness peaks. Right panel shows the cluster emission as detected by the *HST* Telescope in the Optical range, where by means of its high angular resolution imaging multiple arcs can be easily identified by eye.

4.1 The CLASH survey.

The Cluster Lensing And Supernovae survey with Hubble (CLASH; Postman et al. 2012) is a 524-orbit multi-cycle treasury program to use gravitational lensing properties of 25 galaxy clusters with four main scientific goals: 1. Measure the profiles and substructure of dark matter in galaxy clusters with unprecedented precision and resolution. 2. Detect Type Ia supernovae out to redshifts $z \sim$2.5 to measure the time dependence of the dark energy equation of state and potential evolutionary effects in the supernovae themselves. 3. Detect and characterize some of the most distant galaxies yet discovered at $z >$7. 4. Study the internal structure and evolution of the galaxies in and behind these clusters.

To establish a sample that would be largely free of lensing bias, 20 (out of 25) massive clusters from X-ray-based compilations of dynamically relaxed systems were selected. The clusters were also selected to cover a wide redshift range ($0.18< z <0.90$, with a median z_{mean}=0.40), allowing us to prove the full $c(M, z)$ relations expected from simulations. In addition, these clusters all had $T_x > 5$KeV and exhibit a high degree of dynamical relaxation as evidenced by *Chandra* $X-ray$ *Observatory* images that show well-defined central surface brightness peaks and nearly concentric isophotes.

4.2 The CLASH Filter System.

Redshift estimates for multiply-lensed images are crucial for breaking lensing degeneracies and tightening constraints on mass profiles (Broadhurst et al. (2005), Zitrin et al. (2009), Saha & Read (2009)). However, most of the useful lensed images are much too faint for spectroscopy. Typical lensed source

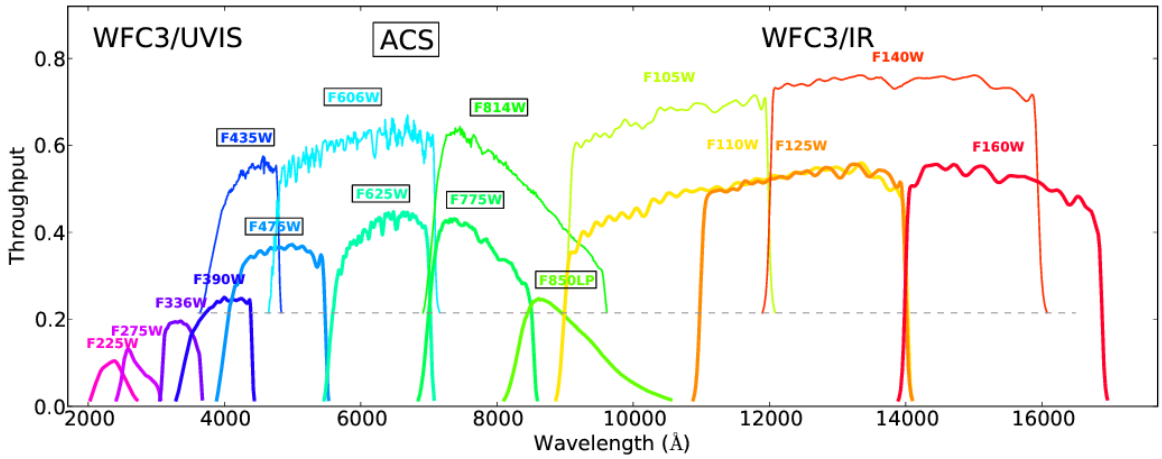

Figure 4.2 Each CLASH cluster was observed in 16 HST filters spanning ∼2.000–17.000$\mathring{A}$ with $WFC3/UVIS$ in the near ultraviolet, ACS in the optical, and $WFC3/IR$ in the NIR. Total throughput curves are plotted for each filter.

magnitudes are $23 < I < 28$, so that only the brightest arcs yield spectroscopic redshifts even when observed with the largest ground-based facilities. With continuous sampling of the broad wavelength range from the NUV to NIR (∼ 2,000–17,000 $\mathring{A}$) that is enabled with $WFC3$ and ACS we can now obtain very accurate photometric redshifts (photo-z's) for most of the lensed objects down to an apparent F775W AB magnitude limit of 26.

For a fixed total observing time, splitting observations into multiple (ideally overlapping) filters significantly improves photo-z precision (Benitez 2009). Simulations were performed to inform our filter selection and estimate our eventual photo-z precision. Galaxy magnitudes, redshifts, and SEDs (spectral energy distributions) were drawn from the UDF (Coe et al. 2006) and "re-observed" with our filter set, adding noise as appropriate given our proposed depths in each filter. Photo-z's were then re-estimated using `BPZ` (Benitez 2000, Benitez 2004,Coe et al 2006). In this simulation, we found that for 16 filters, we may be able to obtain very accurate ($\Delta z \sim 0.02(1+z)$) photo-z's for 80% of objects with F775W mag < 26. Most importantly, we found that we may be able to acquire ∼ 6 times as many reliable photometric redshifts than spectroscopic redshifts for objects at $z > 1$, enabling a very substantial improvement in the number of unique constraints on the DM mass distributions.

4.3 The photometric disruption due to the ICL.

Standard aperture photometry on massive cluster fields does not provide as accurate photometric redshift as expected from field galaxy simulations, where the only source of uncertainty comes from the variable photometric noise. Unlike field samples where galaxies are mostly isolated (apart from pairs, merging or projected neighbors) over an almost flat background, galaxies in massive cluster fields are immersed in a fluctuating background mostly dominated by the brightness of the Brightest Cluster Galaxy (BCG) along with the Intra-Cluster-Light (ICL).

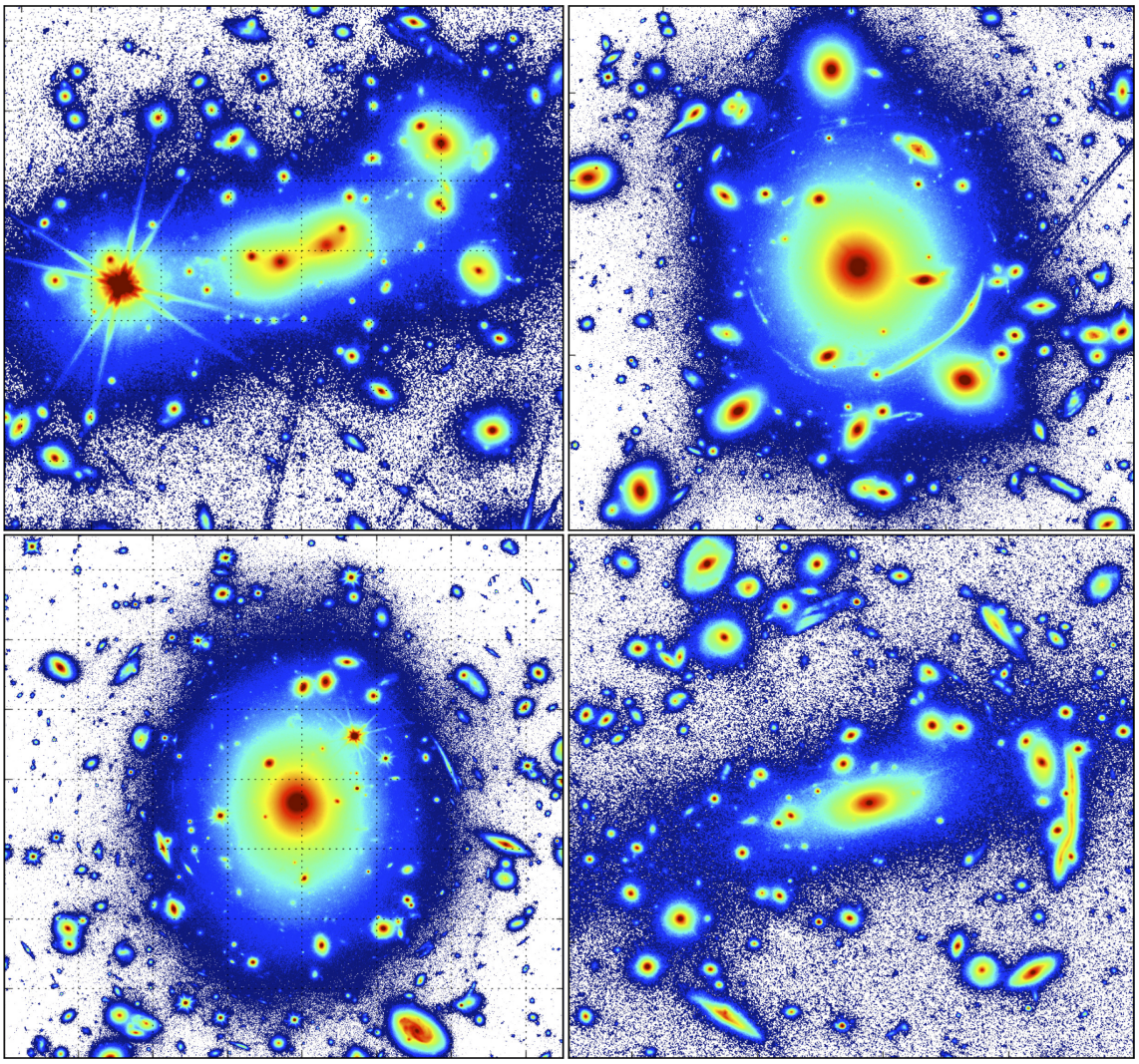

Figure 4.3 The figure shows an example of the typical ICL+Background signal which contaminates the photometric colors of the galaxies. As mentioned in the main body of the text, this signal is both wavelength-dependent (as becomes more significant for the reddest filters) and is spatially-dependent (given by the geometrical distribution of the galaxies within the cluster), as illustrated in the figure. Whereas several clusters corresponds to a rounded-symmetrical structure, others show a much clearer elongated shapes.

From a photometric point of view, when this additional signal (BCG+ICL, hereafter GB) is not properly removed from the images, it disrupts the real color of the galaxies deteriorating the estimation of its photometric redshifts. As discussed later on, in massive cluster fields this signal is so strong that simulations not including this additional uncertainty may overestimate the expected photometric redshift performance. A typical example would be a faint galaxy highly contaminated by a bright neighbor or a bright galaxy with an under/over-estimated magnitude due to an inadequate background subtraction.

In very massive galaxy clusters as those observed by CLASH, since the GB emission is dominating and (typically) inhomogeneous, the background definition and estimation becomes a complicated task. On the one hand, this GB light varies spatially across the image. Depending on the specific cluster configuration, this GB light normally shows both small- and large-scale structures. This fact complicates its modelation as very global background-maps will not account for the rapid variation between galaxies and a too highly resolved background-maps will over-subtract most light from the brightest galaxies. This effect is easily observable when deriving standard photometric zeropoint corrections (based on SED-fitting technics). Instead of observing neat biases with small scatters, it is observed the other way round, large scatters with small biases. As this effect is observable even when selecting same spectral-types, redshift or magnitude ranges (for example, bright cluster members), it proves that equal-type galaxies would require different photometric corrections to match their theoretical colors. Therefore it rules out the hypothesis of SEDs-library incompleteness problems.

4.3.1 Quantification of the photometric bias.

The UDF (Beckwith et al. 2006) represents one of the deepest images ever taken by the HST. Given its very long exposures, it provides the most accurate photometric measurements, with uncertainties as low as 5% for galaxies as faint as magnitude I=28AB.

To explore this GB contaminating effect, we used the galaxies from the UDF to quantify how much their magnitudes may vary if they were observed under different background conditions. To do so, on the one hand, we background-scaled the $UDF/F775W$ image to the level of the CLASH observations, using the `mknoise` routine from IRAF (REFERENCE). This way, the so-generated new image (hereafter *Poisson*) would show how originals magnitudes from the UDF galaxies become noisier when observed in a much shallower image. On the other hand, we combined the $UDF/775W$ image with the CLASH/F160W image from one of the cluster (hereafter $MACS1206$). The so-generated image would serve to quantify how much the magnitudes from the UDF would change when observed through the GB of a massive galaxy cluster.

To properly quantify this effect, we first ran `SExtractor` on the original $UDF/F775W$ image to define the reference magnitudes. Then, we ran `SExtractor` using its double-image mode to perform photometric measurements on the aforementioned two new images. Again, we used the original $UDF/F775W$ image as detection image, to force `SExtractor` to define exactly the same photometric apertures in all the three cases. This approach served to define consistent photometric colors as the difference between original magnitudes (measured for the $UDF/F775W$) and those retrieved from the new images.

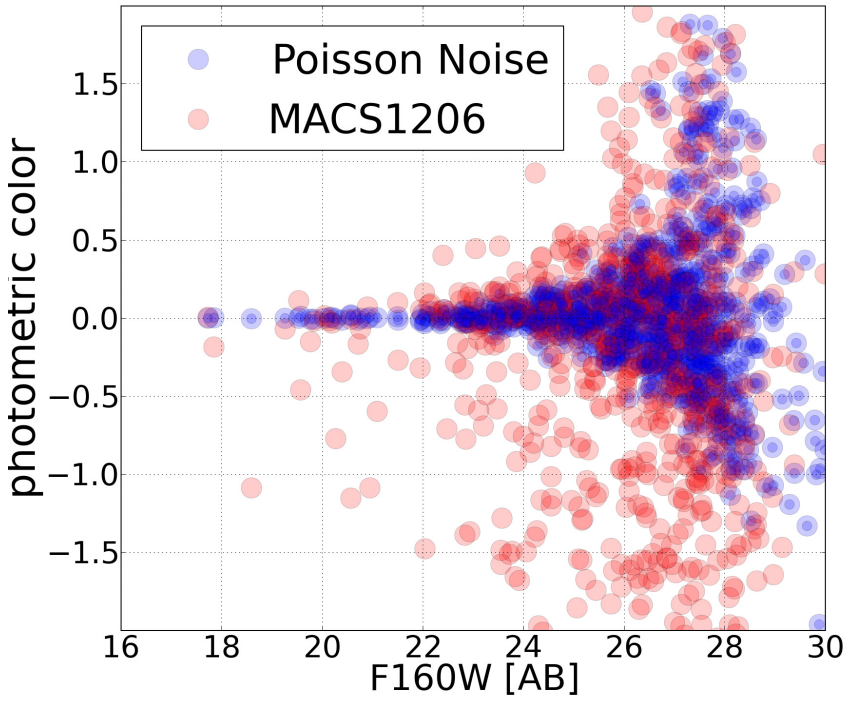

Figure 4.4 Photometric contamination due to the ICL+Background signal. Left panel shows the typical photometric scatter when galaxies from the UDF/F775W are observed through a GC like MACS1206. While the grey histogram represents the variation in the galaxy colors when applying `SExtractor` standard background configurations, solid red line indicates how a more aggressive background configuration subtracts better this nuisance signal retrieving more accurate colors. Right panel shows how the number of retrievable sources from the $UDF/F775W$ increased when using a more detailed background-map, making the source extraction process more homogeneous.

The photometric colors (δ_m) were defined as follows:

$$\delta_m = mag_{UDF}^{before} - mag_{UDF}^{after} \tag{4.1}$$

, where mag_{UDF}^{before} corresponds to the original magnitude and mag_{UDF}^{after} to the magnitude after increasing the background signal.

In Fig. 4.4 we show the so-retrieved distribution of photometric colors as a function of the magnitude. The blue open circles represent the measurements for the *Poisson* image and red open circles to the $MACS1206$. As seen from the figure, whereas for the first case it is obtained a well-behaved symmetric distribution which becomes progressively noisier as the sources get fainter, it is observed an unexpected asymmetric distribution for the second case, indicating a photometric scatter as large as two magnitude for galaxies as faint as 26AB magnitudes.

Therefore, the latter uncertainties, which are dominant for the reddest filters, cannot be explained by means of a gaussian signal and, if not taken properly into account, can lead to a clear degradation of the photometric redshift estimations.

4.3.2 Subtracting the background.

As a consequence of this degrading photometric effect, we wonder wether this effect might be partially mitigated by means of a proper subtraction of this GB light. To do so, we used `SExtractor` since it can automatically compute and subtract a background-map from the input image itself. This way, we defined two different background-configuration files to compare the significance of this subtraction process.

On the one hand, we employed a standard "smoothy" configuration file, which served to globally subtract the main GB contribution from the image. On the other hand, we created a more aggressive configuration file, (highly increasing the mapping resolution), to be able to subtract medium and small-scale variations. With these new configuration files, we ran `SExtractor` again on the $MACS1206$ image using the double image mode strategy, as explained above. We recomputed the new photometric colors (δ_m) and compared their performances. As seen in Fig. 4.5, where the grey histogram corresponds to the colors retrieved when using a standard (low-resolution map) configuration file and the solid red curve corresponds to the colors retrieved when applying a more aggressive (high-resolution map) configuration, the usage of a more convenient background parametrization was capable to significantly improve the overall photometry, making most galaxies to have colors now closer to their originals.

4.3.3 Detectability on Massive Clusters.

As seen in Fig. 4.3, innermost regions of massive clusters are strongly dominated by the BG emission. Most of the times, this signal is so intense that small and faint galaxies can be completely contaminated and so be undetected by `SExtractor`. In other words, we figured out that the fraction of UDF galaxies that could be detected from the $MACS1206$ image, was indeed strongly background-dependent. To visualize this effect, we ran `SExtractor` directly on the $MACS1206$ image using the

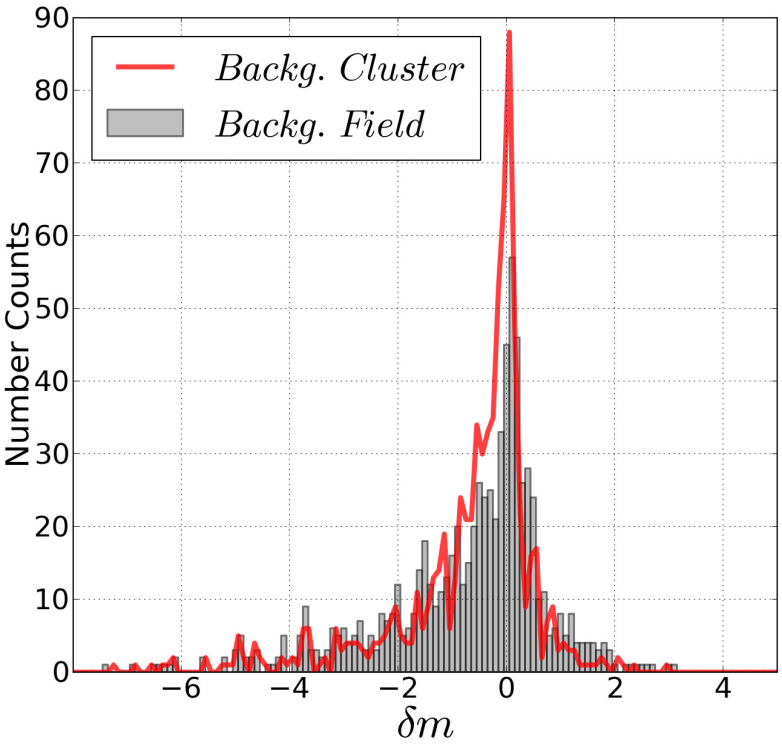

Figure 4.5 Photometric improvement via a more aggressive background subtraction. As seen in the figure, when the grey histogram corresponds to the colors retrieved when using a standard (low-resolution map) configuration file and the solid red curve corresponds to the colors retrieved when applying a more aggressive (high-resolution map) configuration, the usage of a more convenient background parametrization was capable to significantly improve the overall photometry, making most galaxies to have colors now closer to their originals ($\delta_m \sim 0$).

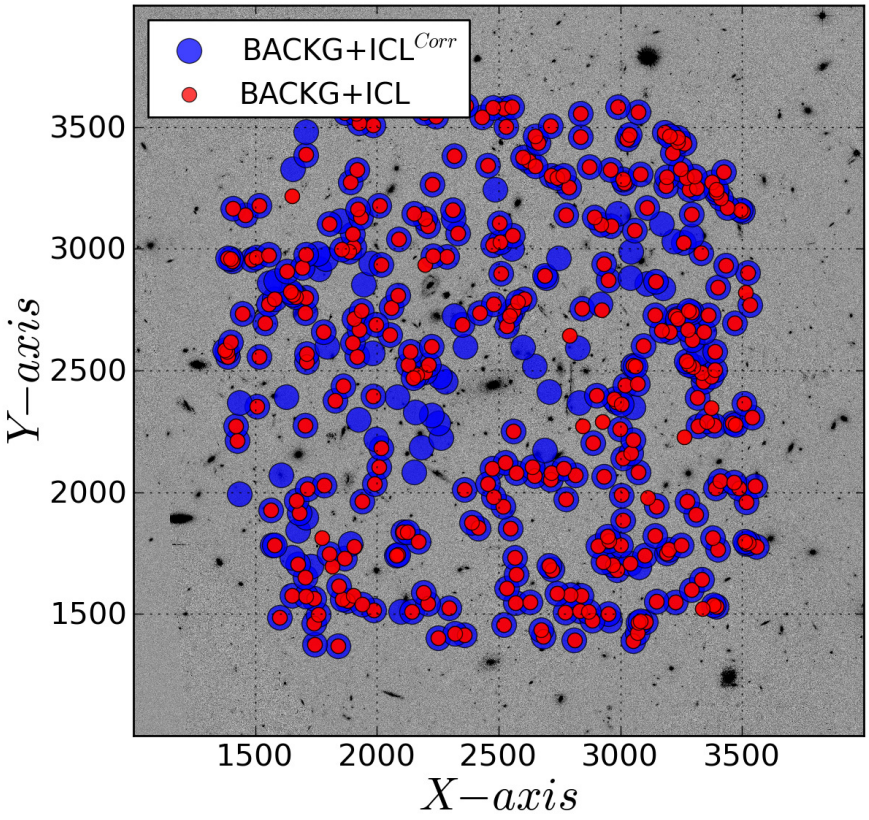

Figure 4.6 The figure shows how the fraction of detected UDF galaxies inside $MACS1206$ image was strongly dependent on the background configuration. To prove it, we ran `SExtractor` directly on the $MACS1206$ image using two different setups. As clearly seen, the fraction of galaxies extracted when using a standard (smooth) background configuration (red circles) was quite smaller than that using a more aggressive configuration (blue circles). This effect emphasizes the potential bias when deriving luminosity functions if this effect is not properly handle.

two different background configurations applied before. The resulting catalogues were then matched out to that from the original $UDF/F775W$ image. As clearly seen in Fig. 4.6, the fraction of galaxies extracted when using the standard configuration file (red circles) was smaller that the fraction of galaxies extracted when using the aggressive one (blue circles). Since a large fraction of (magnified) faint galaxies is expected in these clusters, this effect needs to be seriously considered and treated. Otherwise, estimations such as luminosity functions for high-z galaxies may result biased.

4.3.4 The asymmetric photometric uncertainties.

Once the photometric apertures are defined by a `SExtractor` configuration file (i.e., by its detection parameters), the remaining pixels are automatically assumed to be the image background. For the CLASH clusters, the GB signal is well spread out over several arc-minutes (the complete $HST/WFC3$ camera FoV), and so, is present all over the image. This brings up a new problem since most pixels

classified as background, which contain a large fraction of the GB, will be used for background subtraction purposes. Therefore, the photometry for small galaxies embedded in bright halos may become automatically biased (due to an over-subtraction). In addition, if photometric apertures from large and bright galaxies are not defined with care, it may cause apertures to be substantially smaller than the galaxies real shapes. In other words, light from the galaxies (mainly their wings) could be included when deriving the background corrections. This very fact could make the photometric measurements to be seriously overestimated.

On the other hand, since the GB emission is generated by the cluster members themselves, its intensity becomes strongly wavelength-dependent. To quantify the impact of this effect, we empirically measured the background signal for several CLASH images, following the same methodology described in Molino et al. (2013). Basically, ∼20.000 apertures of different sizes are drawn on blank (background) areas across the image, to empirically describe the correlation between the sizes of photometric apertures and the expected background RMS. As shown in figure 4.7, where the obtained results for two images F606W/ACS & F140W/NIR are presented, the RMS distributions (supposed to be described by a well-described by a Poisson/Gaussian noise) departs from its expected symmetry as a function of wavelength. Whereas for HST/ACS filters this effect was small (but not negligible), for NIR bands it became specially significant causing an evident asymmetric distribution toward positive values. This asymmetric excessed signal cannot be explained by an instrumental background and so, it might correspond to the GB emission which surrounds neighbor galaxies.

Based on all the aforementioned facts, we defined for the ith passband, a galaxy final magnitude as follows:

$$m_i = m_i^o + \delta m_i^{RMS} + \delta m_i^{GB} \tag{4.2}$$

where m_i^o corresponds to the real signal for the galaxy flux, δm_i^{RMS} the additional instrumental background signal (which depends on the total exposure time) and δm_i^{GB} to the (additional) BG contribution from the cluster members.

4.4 Photometric redshifts as background tracers.

From the last section, it was proved that performing accurate photometry on massive cluster galaxies is more complicated than it would be expected. There is an additional source of photometric uncertainty which disrupts the original galaxy colors, ruining the expected photometric redshift performance drawn from simulations. In this sense, as discussed in section 4.3.2, a "tailored" background subtraction can restore (up to a certain extend) the original galaxy colors. Therefore, the effort has to be made on reducing (if not totally eliminating) this additional nuisance term δm_i^{GB} from our photometric estimations (equation 4.2). Starting from the assumptions that photometric redshifts are both 1. very sensitive algorithms to the quality of an inputed data (faulty or offsetted photometry rapidly degrades its accuracy (Coe et al. 2006, Wolf et al. 2008, Ilbert et al. 2009, Molino et al 2013) and 2. mostly exhaustive representing the colors of the galaxies in the Universe (Hildebrandt et al. 2010), we explored the possibility of using photometric redshifts as tracers to identify which background

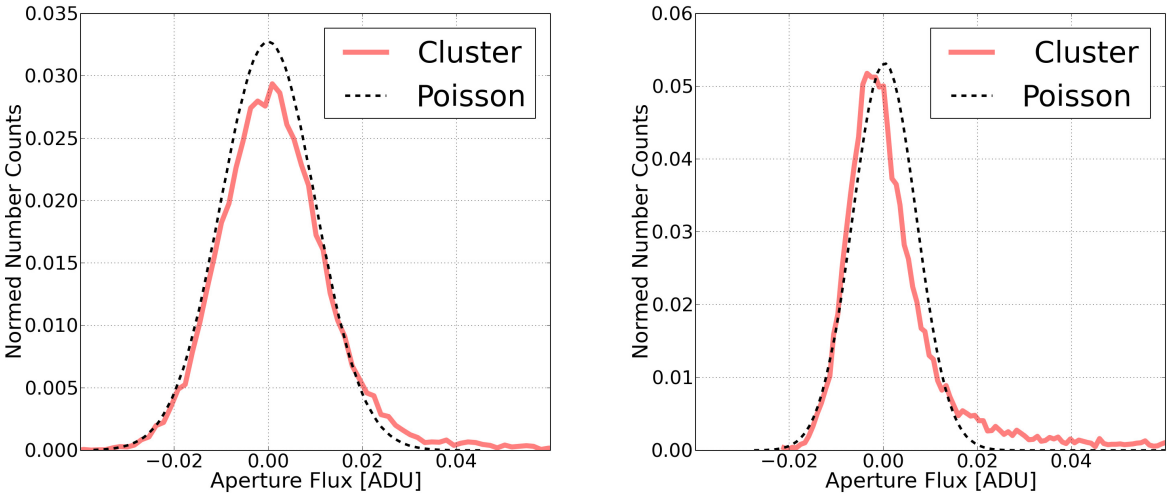

Figure 4.7 We studied the impact of the BG contamination for three different wavelength ranges. To do so, we empirically estimated the RMS signal for $MACS1206$ $ACS/F606W$ (left) and for $WFC3/F160W$ (right) images. Likewise, we compared the effect of an instrumental background signal by adding poisson noise to the $UDF/775W$ image and measuring it empirically in the same manner as done for the other images (dashed lines). As seen in the figure from left to right, whereas for the shortest wavelength (where the emission from cluster members is moderated) the real background distribution (solid red line) reasonable fits the expected poisson distribution (dashed line). However, for longer wavelengths (specially for the NIR bands where the emission becomes maximum) the real background no longer follows a Poisson distribution, showing an asymmetric distribution with positive tails. This (unexpected) asymmetric excessed signal, which cannot be explained by an instrumental background, makes the galaxy colors to vary in such a way that photometric uncertainties cannot longer be described by a gaussian distribution.

configuration (if any) would be able to properly subtract this complex δm_i^{GB} signal, and restore the original galaxy colors.

4.4.1 The UDF-16.

As fully discussed in Molino et al. (2013), photometric redshifts can be very powerful tools for photometric calibration issues. If the redshift values from a sample of observed galaxies are known, statistical analysis between predicted and observed colors can be easily computed (and applied) to enhance the quality of photometric measurements.

The CLASH survey is currently carrying out a 225h follow-up program, at the VLT (PI: Piero Rosati), to gather thousands of spectroscopic redshift per cluster. Unfortunately, since the innermost part of these clusters are $\sim 1'$ radii, the complexity of allocating many fibers in such a small area makes its acquisition very complicated. At the time, only several dozens of galaxies are available (per cluster) for photometric redshift calibration and validation. Considering the importance of having an ample set of redshift galaxies for the background-subtraction testing, we explored the possibility of generating our own sample of synthetic galaxies with known redshifts. Based on the photometric catalogue derived by Coe et al. 2006, we used the new BPZ library of galaxy templates (Molino et al. 2013) to extend the UDF observations from its original 4 bands (F435W, F606W, F775W & F850LP) to the 16 composing the CLASH filter system. The procedure was done as follows:

First, we ran `BPZ` on the PSF-corrected catalogue derived by Coe et al. (2006) to get the most likely redshift and spectral-type for each galaxy in the UDF field [1]. With this information plus the original magnitudes from the $UDF/F775W$ image, we redshifted and flux-scaled the BPZ templates to derive the expected colors for each galaxy in every one of the CLASH filters. In other words, we derived the expected fluxes for each galaxy, on each filter, based on their redshifts and spectral-types. When the fluxes were normalized to the F775W filter, the scaling factors (from that filter to another) were easily achievable. An example of this procedure is illustrated in Fig. 4.9. Essentially it shows how two different spectral-type galaxies are redshifted and convolved with the CLASH filter system (open circles), and normalized to the CLASH/F775W band (black square). Finally, using the so-derived coefficients, we generated a new set of 16 images mimicking the UDF galaxy colors as they were observed through the CLASH filter system. We called this simulated dataset the UDF-16.

It is worthy to emphasize that for the scope we are facing (the background-subtraction testing), it is of not relevance either the galaxy sample is a loyal representation of the real Universe. We are merely interested in having a control sample made of regular colors from typical galaxies at common redshifts, to study the photometric bias caused on the input data for the GB. In other words, since these galaxies will have known redshifts, spectral-types and (input) magnitudes, by injecting the galaxies within the cluster images might be possible to quantify the same sort of photometric biases expected for the real galaxies. Additionally, the UDF-16 sample was not intended to asses estimations about the expected photometric redshift accuracy but just to investigate which background configurations would retrieve (if nay) the input galaxy colors.

[1] We decided not to use directly the estimated photometric redshifts from Coe et al. 2006, since we preferred to apply the new version of BPZ which presents several important updates to the version available on 2006.

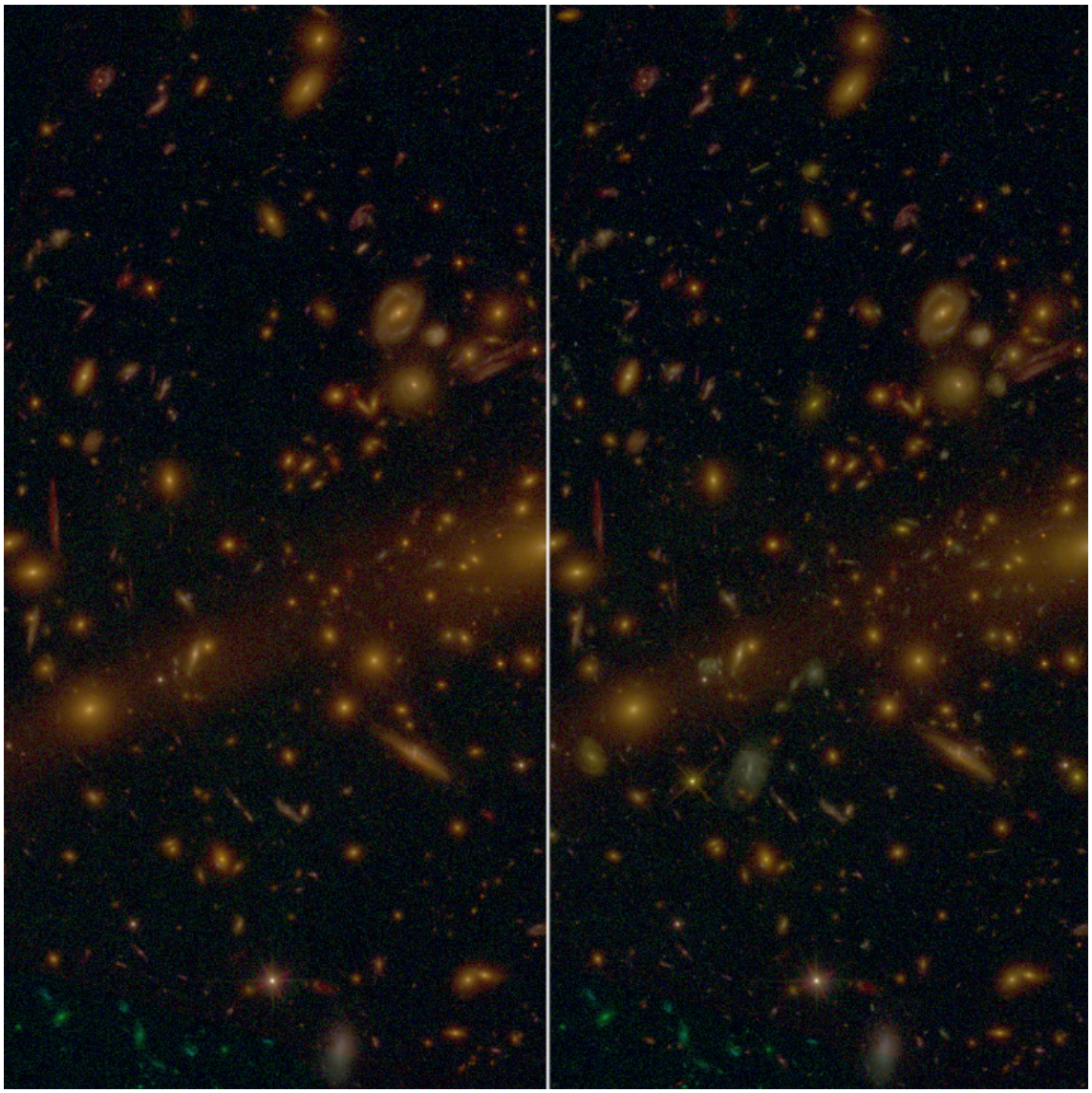

Figure 4.8 Example of the UDF-16. Left: an RGB color image for the original MACS1206 cluster. Right: an RGB color image for the combination of both MACS1206 cluster + the UDF-16. As explained in the main body of the text, given the smallness and faintness of the UDF galaxies, it ensured that injecting those galaxies within the CLASH fields was not going to change the images GB. Precisely the photometric amount under study.

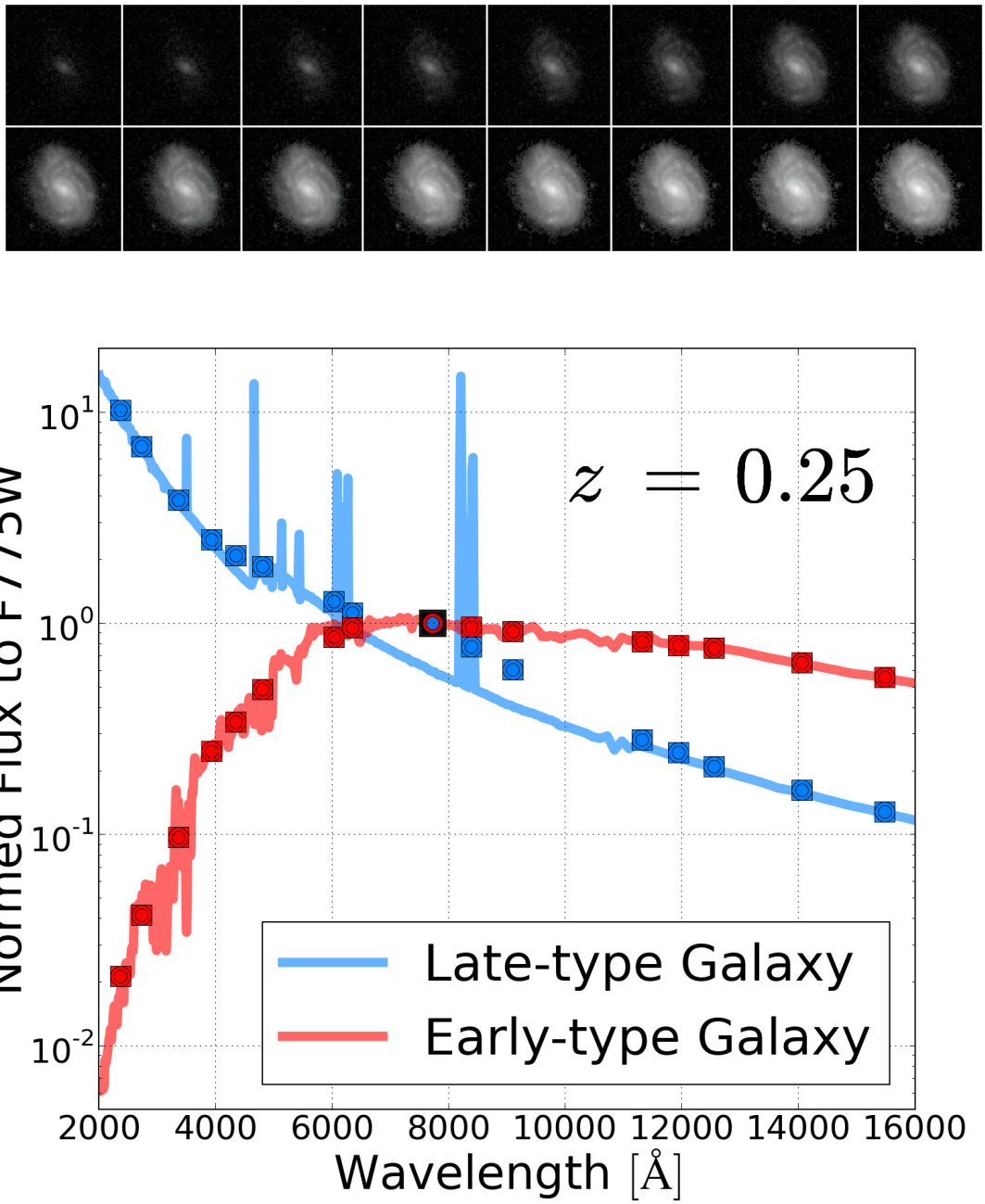

Figure 4.9 We ran initially `BPZ` on the PSF-corrected catalogue derived by Coe et al. (2006) to get the most likely redshift and spectral-type for each galaxy in the *UDF* field. With this information plus the original magnitudes from the *UDF*/*F*775*W* image, we redshifted and flux-scaled the BPZ templates to derive the expected colors for each galaxy in every filter for CLASH. Finally, using the so-derived coefficients, we generated a new set of 16 images mimicking the UDF galaxy colors as they were observed through the CLASH filter system. We called this simulated dataset the UDF-16. The figure shows how two different spectral-type galaxies (solid lines) are redshifted (to a z=0.25) and convolved with the CLASH filter system (open circles), and normalized to the CLASH/F775W band (black square), to derive the scaling factors among filters.

In the meantime, it is worth stressing that the reason of choosing the UDF was double. On the one hand, as mentioned before, since the UDF is one of the deepest fields observed by the *HST*, the uncertainties associated to galaxies as faint as magnitude I∼26AB are (almost) an order of magnitude smaller than those expected for the CLASH observations. Therefore, we can consider the UDF as if they were free-background images. On the other hand, given the smallness and faintness of the UDF galaxies, it ensured that injecting the galaxies within the CLASH fields will not change the images GB. Precisely the photometric amount under study.

4.4.2 The Background Parameter Space.

For the background-subtraction purpose, we relied on `SExtractor` since this software is capable to generate background-maps for any given image. Therefore, we explored all the different configurations for `SExtractor`, finding that the most relevant parameters for this task were the following:

First of all, `SExtractor` allows the user to decide with **BACK_TYPE** whether the background to be subtracted will be a constant value for all the sources ("MANUALLY") or, in the contrary, the user wants `SExtractor` to generate a more detailed background-map ("AUTOMATIC"). While the former configuration could be useful for images with almost flat background distributions, the latter might be the more convenient for complicated background distributions as those founded in massive cluster galaxies.

If the user opts for creating a new background-map, then it becomes necessary to specify what might it be its general properties. On the one hand, **BACK_SIZE** sets the length of the mesh `SExtractor` will split the inputted image. If cells are chosen to have very small lengths, it will produce a too detailed pattern where most light from bright sources will be considered as part of the background, and so underestimating its real magnitudes. In the contrary, if too large lengths are chosen, it will barely account for all small-scaled variations in the image, producing just a rough first-order estimation and so, overestimating the magnitudes of fainter galaxies. Once the configuration is settled, `SExtractor` computes the mean and sigma value for all pixels within each individual cell, setting them all to that constant value afterwards.

Finally, with **BACK_FILTERSIZE** `SExtractor` let the user to apply a median filtering over the constant-valued boxes. The size of this filtering is specified in number of cells and serves to smooth out the final map and rule out large deviations from bright or extended objects.

Once the background-map has already been generated, it is time to decide how it must be applied to the detected sources with **BACKPHOTO_TYPE**. If a non so position-dependent background is expected in the image, `SExtractor` can photometrically correct every source flux by subtracting a GLOBAL (averaged) constant value. In the contrary, if the background is expected to be position-dependent across the image, and so a more accurate measurements are required, a LOCAL background is recomputed. An annulus around each source is defined whose thickness (in pixels) is settled by **BACKPHOTO_THICK**.

In addition, recalling that massive cluster galaxies typically encompasses both very bright and faint galaxies in a small region of the sky, we also considered the usefulness of **CLEAN_PARAMETER**

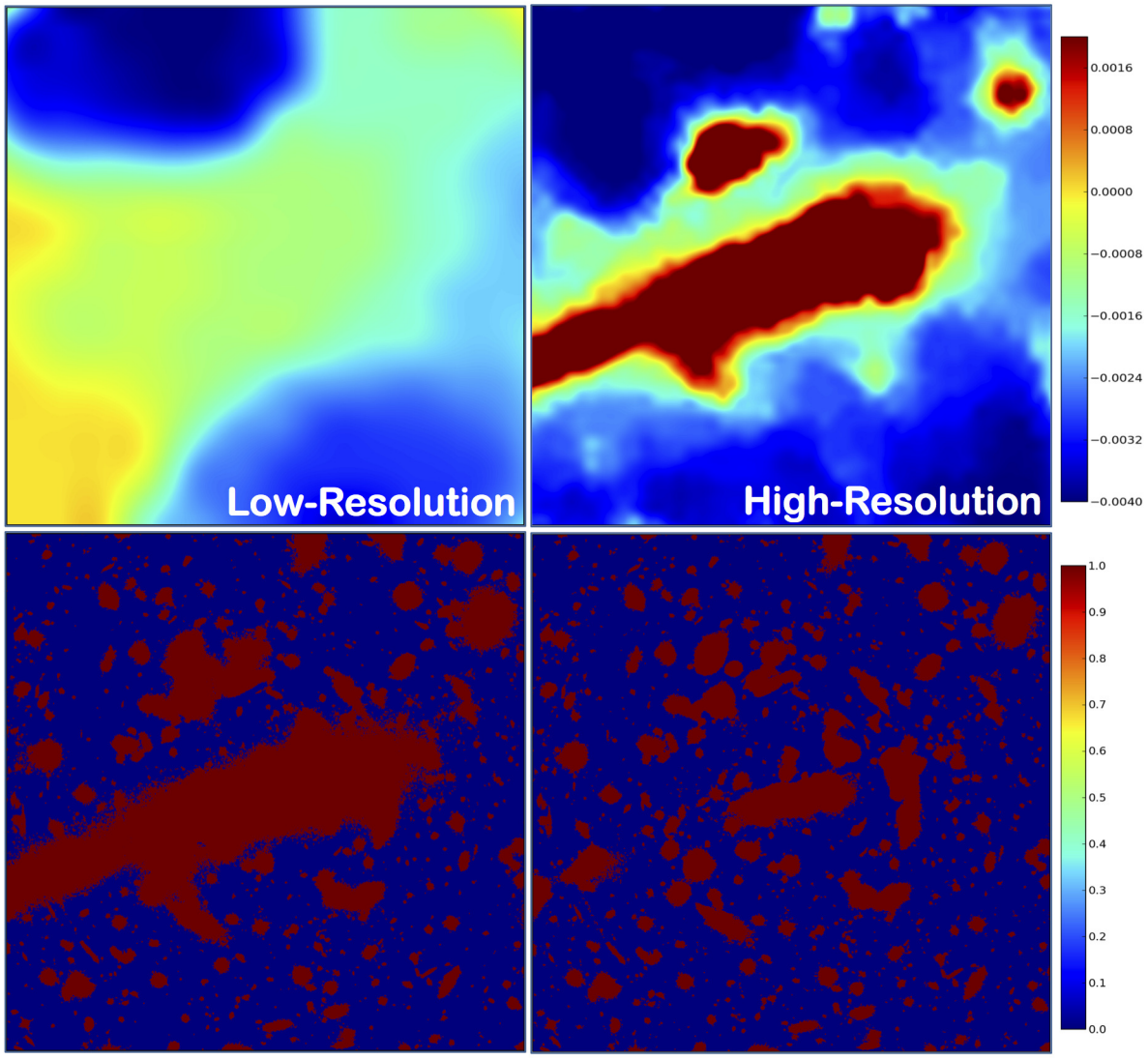

Figure 4.10 The figure illustrates the importance of fully explore the background-space. In the example, there are simultaneously shown either the background-map (top) as its corresponding segmentation-map (bottom) for two opposed configurations. At first glance, it is easy to see how a low-resolution background-map is incapable to properly separate most of the inner galaxies, which appear blended. In the contrary, a high-resolution background-map is capable to identify individual galaxies, and so perform a much cleaner photometry.

Table 4.1 The table shows the different `SExtractor` background variables and their spanned ranges considered during this analysis.

SExtractor Variables	Inputted Values
BACK_TYPE	AUTOMATIC
BACK_SIZE	16, 32, 64, 128, 256
BACK_FILTERSIZE	1, 3, 5, 7, 9, 11
BACKPHOTO_TYPE	LOCAL
BACKPHOTO_THICK	6, 12, 26, 32
CLEAN_PARAMETER	1, 2, 5, 10

on the source detection process. By using this parameter, the user can ask `SExtractor` to double-check whether a source would have been detected if it had not have a close bright neighbor. This way it subtracts the amount of (contaminating) flux coming from its wings by fitting a Moffat profile on the neighbor. In cases like the ones treated in this work, this variable serves to mildly compensate photometrically biased measurements.

An example of the importance of exploring different background configuration is illustrated in Fig. 4.10. In this example, there are simultaneously shown either the background-map (top) as its corresponding segmentation-map (bottom) for two opposed configurations. At first glance, it is easy to see how a low-resolution background-map is incapable to properly separate most of the inner galaxies, which appear blended. In the contrary, a high-resolution background-map is capable to identify individual galaxies, and so perform a much cleaner photometry.

4.4.3 The Optimal Background Configuration.

For each cluster, we start generating the synthetic datasets combining the corresponding 16 CLASH (science) images with those from the UDF-16. Then, on every one of these combined images, we proceed running `SExtractor` using its double-image mode and so generate multi-wavelength catalogues. To make the comparison among configurations much easier, we imposed the $UDF/F775W$ image as a detection image. This assured that only UDF galaxies (within the CLASH clusters) would be detected and measured. Since the inserted galaxies came all from the same (UDF) image, no PSF-corrections were required among bands. The catalogue acquisition process was repeated iteratively, spanning all different background configurations. At the end of this analysis, a total of 480 different photometric catalogues per cluster were performed. Finally, when all catalogues were ready, photometric redshifts were derived running `BPZ`. Finally, it is worth noting that since the ACS/UDF images field-of-view was larger than that of the CLASH/WFC3, it was necessary to imposed an additional selection criteria. To avoid galaxies from the UDF-16 to be located in (external) blank areas within the CLASH images (and so not affected at all by the GB), we restricted the analysis to a small innermost region of $\sim$1' radii.

When looking for the configuration that best retrieved the input photometry, there were several variables that need to be accounted for. On the one, it could be tempting to think that the most

important indicator here will be the standard σ_{NMAD} value, which is usually utilized to quantify the photometric redshift accuracy. Although this variable is indeed valuable, it is totally insensitive to the size of sample utilized for its derivation. As emphasized in Section 4.3.3, the fraction of galaxies that `SExtractor` was able to extracted from the combined images (and so used for these analysis) was strongly background-dependent. Therefore, to be consistent when comparing background configurations, we also considered the amount extracted galaxies used to derive the photometric redshift precision.

On the other hand, there were another two statistical variables which played a vital role here. It is worth recalling that the main motivation for generating the UDF-16 was to own an ample sample of galaxies with known photometric colors and redshifts. Whenever this is the case, BPZ can be run on its $ONLY\_TYPE = YES$-mode redshifting all its templates to match every galaxy redshift. This way, it turns out possible to derive systematic comparisons among predicted and observed colors[2].

These color distributions, which are computed per each passband, are enormously informative. Since the ratio between the observed and expected fluxes is supposed to be very close to $\sim$1 (meaning perfect agreement), mean deviations from unicity are understood as to be photometric biases. That is why, these corrections are typically called zero-point offsets. Likewise, the scatter from these distributions (its FWHM) provides valuable information about the level of agreement (or discrepancy) between expectations and real data. Recalling that real (input) magnitudes were derived from BPZ models (by construction of the UDF16), this variable should serve to identify which configuration minimizes the differences between input and output colors. In other words, the narrower the distribution, the closer the colors. Although it is usually ignored, this zero-point scatter variable (hereafter, $ZP_{scatter}$) represents a very powerful photometry quality indicator.

Combining all the four aforementioned variable, we defined a figure of merit (FoM) as follows:

$$FoM = \frac{N_{galaxies}}{\sigma_{NMAD} \times < ZP_{scatter} > \times \ |1 - < F_{ratio} > |} \tag{4.3}$$

where $N_{galaxies}$ represents the number of extracted galaxies from the image, σ_{NMAD} the scatter of the $\delta_z/(1+z)$ distribution, $< ZP_{scatter} >$ the aforementioned zero-point scatter and $|1 - < F_{ratio} > |$ an estimation of the zero-point offset.

Fig. 4.11 represents the multiple background configurations (black circles) in the so-defined figure-of-merit space, for one cluster. As seen from the plot, there exist not only a tendency towards optimization (from right to left), but also an optimal configuration (red circle) which best meet all the aforementioned conditions. This includes a large fraction of galaxies, with accurate photometric redshifts, small bias and small scatter for the zero-points. The parameters describing the optimal background configuration (for a single cluster) are listed within the legend. The same procedure was applied for all the clusters, where the optimal background-maps were identified.

Once these background-maps were generated, a new set of background-free images was produced.

[2]Fixing the redshift for each galaxy and forcing BPZ to choose the model to best fit the data, makes the number of uncertainties in the analysis to be reduced 1 dimension.

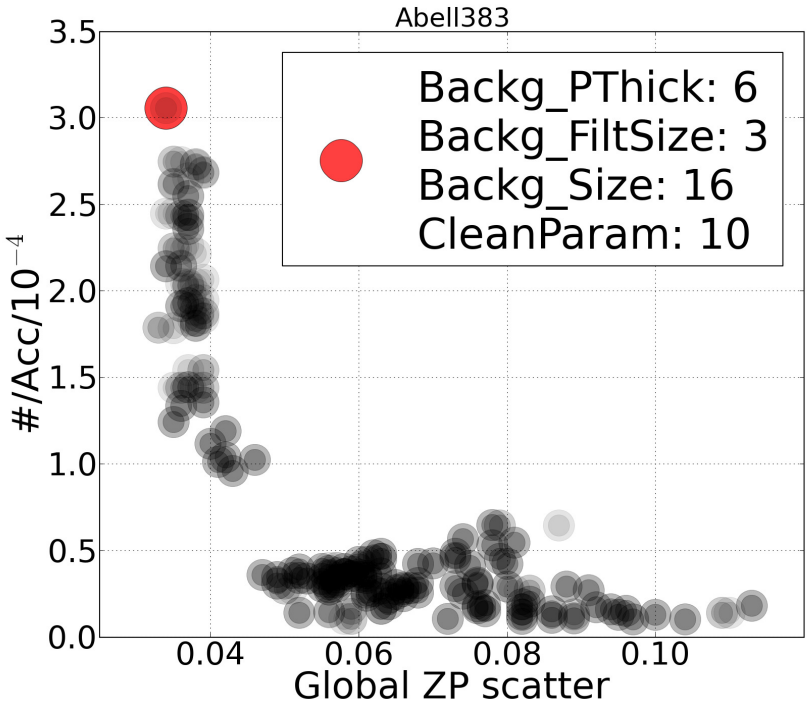

Figure 4.11 The figure represents how the multiple background configurations (black circles) are disposed in the so-defined figure-of-merit space. As seen for the case of the cluster Abell383, there exist not only a tendency towards optimization (from right to left and bottom to top), but also a configuration (red circle) which best meet all the aforementioned conditions. This includes a large fraction of galaxies, with good photometric redshift and a small value for the mean ZP_scatter. The parameters describing the optimal background configuration are specified inside the legend.

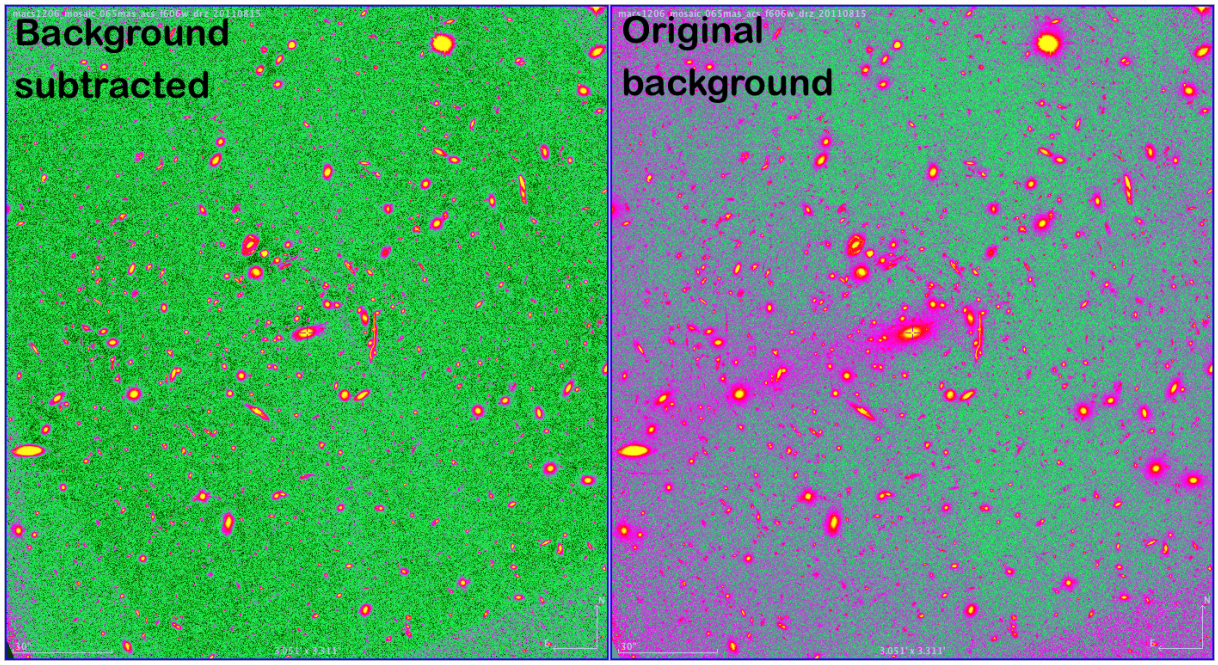

Figure 4.12 The figure shows the result when subtracting the so-derived background-maps to the original images. As can be easily seen, after subtraction (left) the new background distribution appears much flatter than in the original image (right).

As an example of the kind of results obtained with this procedure, the Fig.4.12 shows how the new background distributions appeared now to be much flatter and homogeneous with a larger fraction of well-isolated galaxies across the image.

4.4.4 Photometric Uncertainties.

As stated in Jouvel et al. (2013), when flux uncertainties (taken directly from `SExtractor` output) are compared against those predicted from the *HST* exposure-time calculator, they show a perfect agreement. Unfortunately, this apparent agreement is just caused by a circular argument, since `SExtractor` assumes (as the *HST* calculator does) that the images background can be accurately described by a Poisson distribution. However, it is well-known that `SExtractor` underestimates the photometric uncertainties, due to the fact that science images usually undertake several cosmetic processing (dithering, degradation, stacking, registration, ...), which introduces correlations between neighboring pixels. This correlation makes the background noise in images different from a Poissonian distribution, and so the `SExtractor` uncertainties no longer accurate. For CLASH the situation is expected to be even worse, since these images are also affected by this additional GB signal, which is both wavelength- and position-dependent and shows small- and large-scale structure. In the light of this contradiction, we decided to empirically measure the photometric uncertainties taking place on the CLASH images and compared them to those reported by `SExtractor`.

We followed a similar approach as that introduced in Section 4.3.1, comparing how the magnitudes from a sample of galaxies from the $UDF/F775W$ will change when observed through different

background conditions. At this point, it is worth stressing that theses reported differences between input and output magnitudes, represent an empirical quantification of the real photometric uncertainties undertaken in the images. Therefore, we used the previously derived photometric catalogues where original $UDF/F775W$ magnitudes were compared to those measured from the *Poisson* and the $MACS1206$ images (see Section 4.3.1).

Initially, we validated that `SExtractor` uncertainties were accurate for images with a background well-described by a Poisson distribution. To do so, we compared the photometric bias induced by the *Poisson* images with the uncertainties reported by `SExtractor`. As seen in Fig.4.13, we found a remarkable good agreement between the `SExtractor` (dashed black line) and the empirical (grey solid line) uncertainties. Then, we repeated the same exercise but using the photometric catalogues derived from the $MACS1206$ image; i.e., when galaxies are observed through the CLASH massive clusters. Since the GB contribution is expected to worsen the photometric bias, we compared the results for the cases of applying both a low- and a high-resolution background subtraction treatment. As seen in Fig.4.13, the photometric bias induced by real images was much larger than the predicted by `SExtractor`. Although the aggressive background subtraction (red line) served to quantitatively improve the photometric bias than that obtained when using a standard background subtraction (blue line) treatment, in any case, the `SExtractor` uncertainties were always underestimated. This result proved that reported uncertainties from `SExtractor` were not realistic at all for the CLASH images, and so the application of more refined methodologies becomes mandatory. It is worth emphasizing that the underestimation of real photometric uncertainties may critically affect either the photometric-depth estimation for any given survey (its limiting magnitude), as worsen the photometric redshift accuracy.

Finally, in order to retrieve more realistic photometric uncertainties for the CLASH data, it was necessary to rely on an empirical approach similar to those followed by Casertano et al. (2000), Labbé et al. (2003), Benítez et al. (2004), Gawiser et al. (2006), Quadri et al. (2007), Molino et al. (2013). As expected, it can be seen in Fig.4.14 how the CLASH images are accurately described by a Poisson distribution only on small scales. However, as photometric apertures (i.e., galaxy sizes) become larger, the RMS distribution (black line) starts to depart from the `SExtractor` expectations (red line), indicating the presence of large-scale correlations among pixels. In such as cases, the background distribution has to be described according to the following relation:

$$\sigma(A) = \frac{\sigma_1 \sqrt{N}(C_1 + C_2\sqrt{N})}{\sqrt{w_N}} \tag{4.4}$$

where coefficient C_1 indicates the Poisson contribution (dominant on small scales), C_2 the correlated contribution among pixels (dominant on large scales), w_N corresponds to the weight factor (from *weight* images) and σ_1 represents the 1-pixel aperture background value.

4.4.4.1 Aperture correction for bright sources

Finally, to verify the robustness of the so-derived empiric photometric uncertainties, we made use again of the UDF-16. As discussed before, since the original magnitudes from the UDF16 galaxies

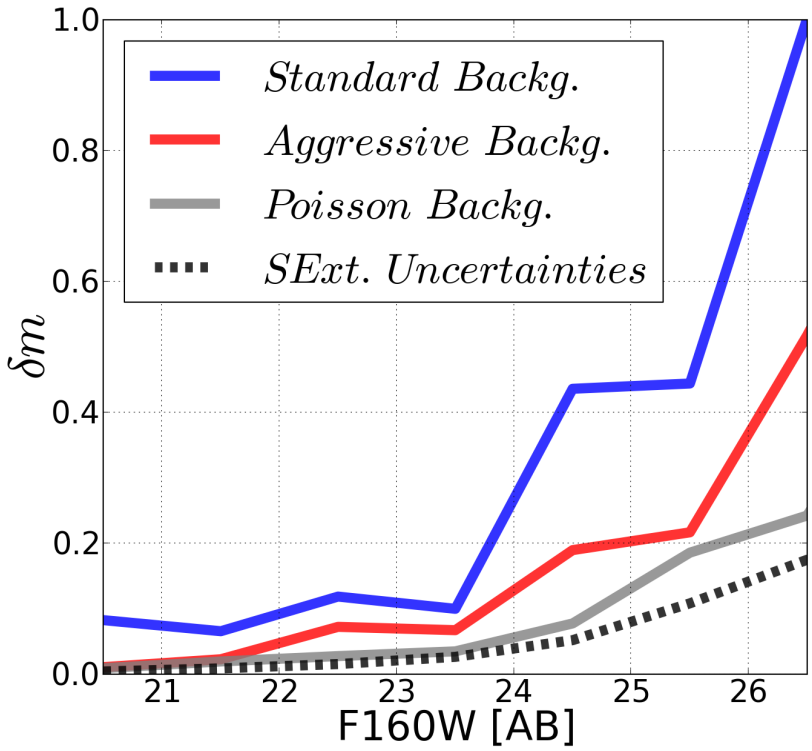

Figure 4.13 We studied the goodness of `SExtractor` reporting photometric uncertainties. Following a similar approach as that from Section 4.3.1, we compared how much the original magnitudes from the $UDF/F775W$ galaxies changed when observed through different background conditions. Understanding that the difference between the input and the output magnitudes, yielded an empirical quantification of the photometric uncertainties, we used of the photometric catalogues derived when comparing the original $UDF/F775W$ magnitudes with those from the *Poisson* and the $MACS1206$ images. Initially, we validated that `SExtractor` uncertainties were accurate for images with a background described by a Poisson distribution. In this case, it was found a remarkable good agreement between the `SExtractor` (dashed black line) and the empirical (grey solid line) uncertainties. Later on, the same exercise was repeated for the catalogues from the $MACS1206$ image, where the results for the cases of applying both a low- and a high-resolution background subtraction treatment were considered separatelly. For real images, the photometric bias induced was much larger than the predicted by `SExtractor`. Although the aggressive background subtraction (red line) served to quantitatively improve the photometric bias than that obtained when using a standard background subtraction (blue line) treatment, in any case, the `SExtractor` uncertainties were always underestimated. The latter result proved that reported uncertainties from `SExtractor` were not realistic at all for the CLASH images, and a more refined methodologies was mandatory.

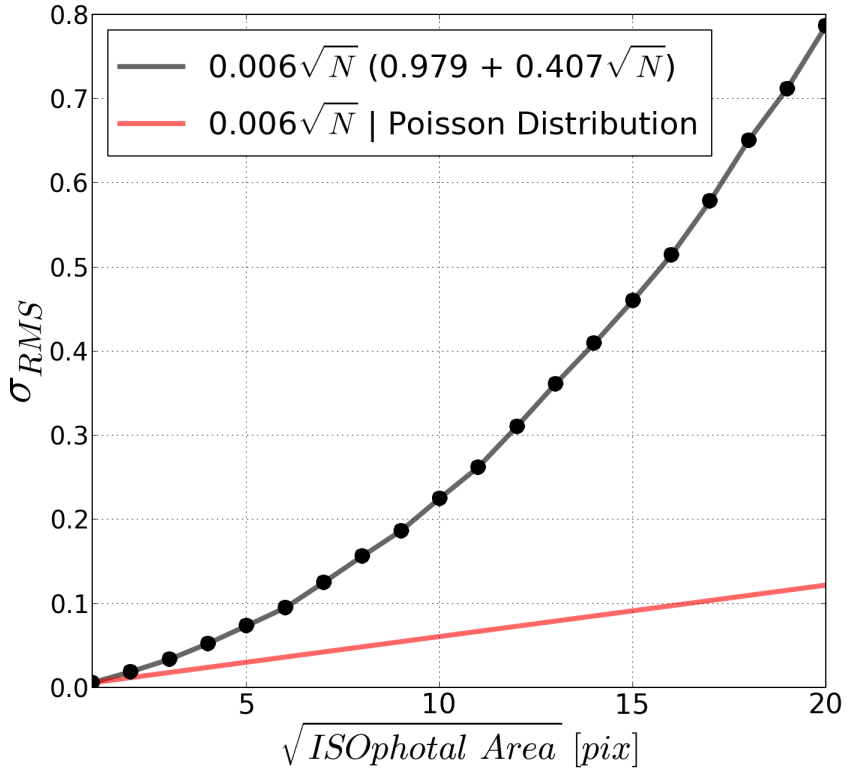

Figure 4.14 The figure represents an example about the empirical estimation of the CLASH photometric uncertainties. To retrieve more realistic photometric uncertainties for the CLASH data, it was necessary to rely on a similar approximation to that followed by Casertano et al. (2000), Labbé et al. (2003), Benítez et al. (2004), Gawiser et al. (2006), Quadri et al. (2007), Molino et al. (2013). As expected, the CLASH images are accurately described by a Poisson distribution only on small scales. However, as photometric apertures (i.e., galaxy sizes) become larger, the RMS distribution (black line) starts to depart from the `SExtractor` expectations (red line), indicating the presence of large-scale correlations among pixels.

were known before injecting them within the CLASH images, we figured out either the reported uncertainties were now proportional to the real variations in the magnitudes (δ_m) due to the noisy background. To do so, we defined the *uncertainty ratio* (Δm) according to the following equation:

$$\Delta m_i = \frac{|m_{out}^{i,j} - m_{in}^{i,j}|}{dm^{i,j}} \tag{4.5}$$

where for the i^{th} galaxy, observed through the j^{th} passband, m_{in} represents the original magnitude and m_{out} the final magnitude as measured after inserting the galaxy within the background-subtracted *Cluster* image. If photometric uncertainties were indeed well-calibrated, the *uncertainty ratio* had to be equal to the unicity for all galaxies.

To calculate this ratio, for each cluster, we ran `SExtractor` twice. First, we ran `SExtractor` on the original UDF16 images. For each galaxy (on each passband), the information regarding magnitudes and area were saved. Then, we ran `SExtractor` on the UDF16+CLASH images, using the optimal background configuration. Once the catalogues were ready, common detections were matched up to derived the *uncertainty ratio*. However, as seeing in Fig 4.15 (red solid line), we rapidly realized that systematically `SExtractor` was largely underestimating the photometric uncertainties for the brightest (and largest) galaxies. Since for high signal-to-noise sources, `SExtractor` uncertainties mainly depend on the inverse root squared of the integrated flux ($1/\sqrt{F}$, as described in the equation 4.6), we realized that so underestimated photometric uncertainties had to be related with a signal excess.

$$dm^{bright} = C \times \sqrt{\frac{\sigma^2 \times Area}{Flux^2} + \frac{1}{Gain \times Flux}} \propto \frac{1}{\sqrt{Flux}} \tag{4.6}$$

As shown in the inner panel of Fig. 4.15, we observed that `SExtractor` was indeed overestimating the photometric apertures for bright galaxies. Although counter-intutive, it came out that original *ISOphotal* apertures were smaller than those measured on the final images. Therefore, artificially enlarged apertures were leading to an excess in the integrated signal which was artificially biasing the photometric uncertainties. Likewise, it is worth mentioning that this aperture-bias effect is hard to be noticed when estimating a source magnitude, since the flux dependence with the aperture grows much slower with the aperture-size than it does the uncertainties.

In the light of this finding, it was necessary to also include an aperture-correction for bright sources and re-calculate the corresponding photometric uncertainties. As seen in Fig. 4.15, once the new bias was included in the analysis, the *uncertainty ratio* was neatly improved, assuring the so-derived photometric uncertainties now represent a much loyal estimation of the real uncertainties in the our images.

4.4.5 Empirical estimations for upper limits.

Accurate upper limits are extremely important for photometric redshifts estimations, whenever galaxies become fainter and start to not be observable in the shallowest filters. These limiting magnitudes serve to exclude unfeasible solutions and so, help constraining the color-redshift parameter space when photometric information becomes scarce. In the light of what was discussed in previous sections, we

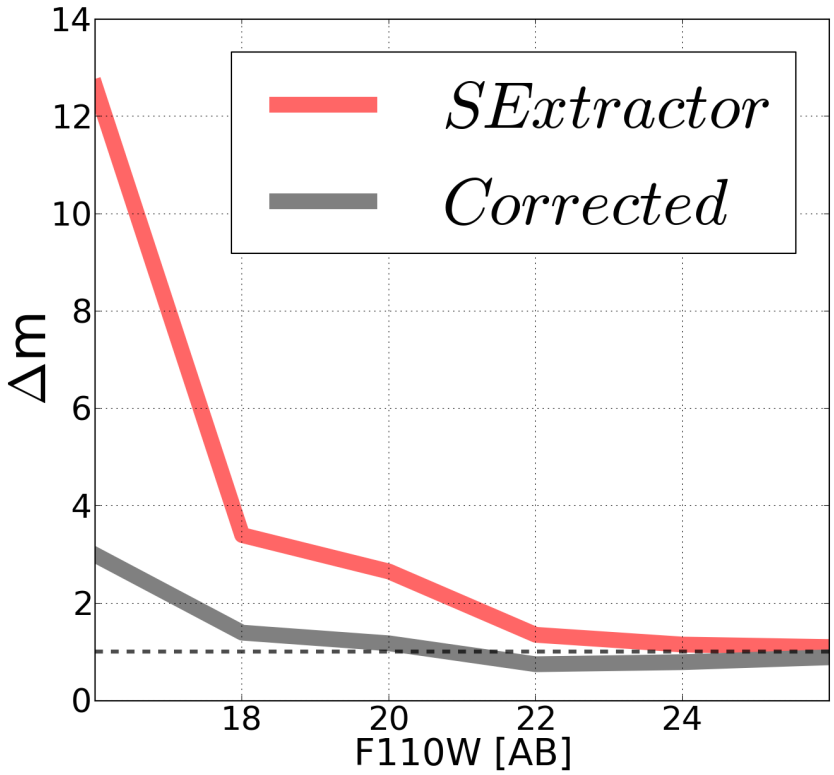

Figure 4.15 Aperture Correction for extended Sources (1). To verify the robustness of the new (empiric) photometric uncertainties, it was defined the *uncertainty ratio* (Δm) (see eq. 4.5). This usefulness parameter represents a comparison between the real variations in the magnitudes (due to the background) and the reported uncertainties. If photometric uncertainties are well-calibrated *uncertainty ratio* has to be equal to the unicity for all magnitude ranges (dashed black line). To calculate this ratio, we initially ran `SExtractor` on the original UDF16 images and then on the UDF16+CLASH images, using the optimal background configuration for each cluster. As seen in the Figure, where the *uncertainty ratio* is plot as a function of the WFC3/F110W magnitude, `SExtractor` was systematically underestimating the photometric uncertainties for the brightest (and largest) galaxies. The reason was that `SExtractor` was overestimating the sizes for the brightest sources. This aperture-bias effect was leading to an excess in the integrated signal which was artificially biasing the photometric uncertainties (solid red line). Once this new bias was included in the analysis, the *uncertainty ratio* was neatly improved (solid grey line) assuring the so-derived photometric uncertainties now to represent a much loyal estimation of the real uncertainties in the images.

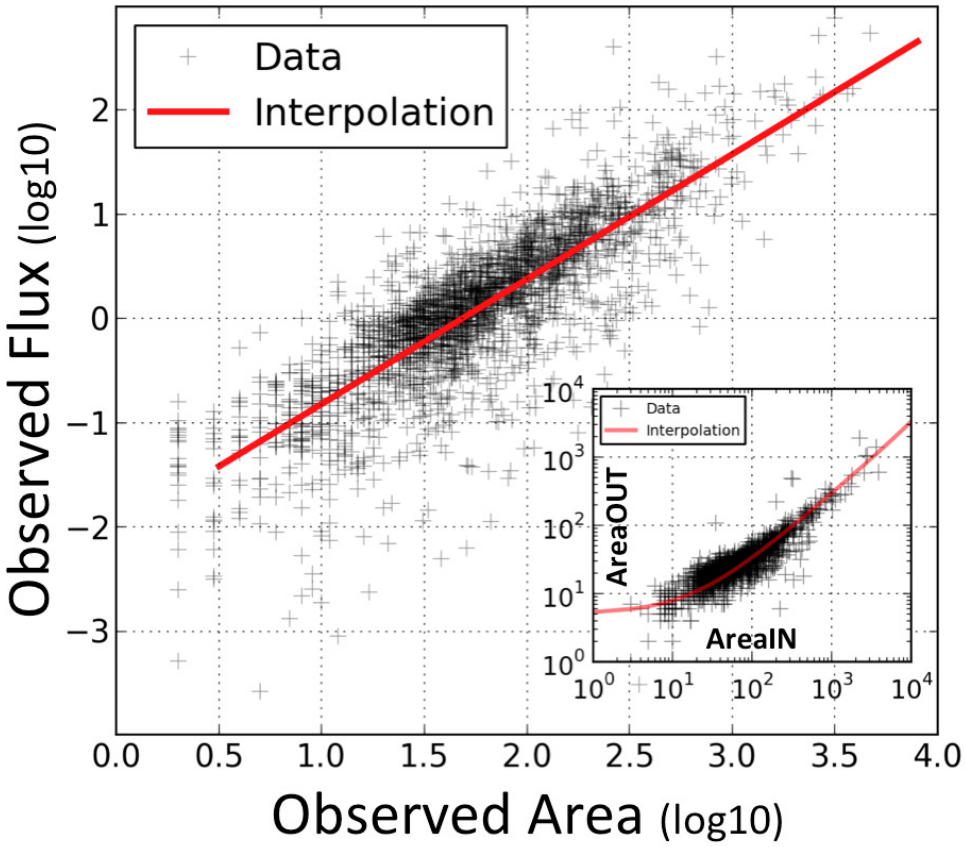

Figure 4.16 Aperture Correction for extended Sources (2). To calculate the *uncertainty ratio*, we initially ran `SExtractor` on the original UDF16 images and then on the UDF16+CLASH images, using the optimal background configuration for each cluster. As seen in the inner panel, where the original (UDF16) versus the final (UDF16+CLASH) *ISOphotal* apertures are shown, `SExtractor` was overestimating the galaxy sizes. Since `SExtractor` uncertainties mainly depend on the inverse root squared of the integrated flux ($\propto 1/\sqrt{F}$) for bright detections (main panel), an artificially enlarged aperture might lead to a signal excess and so to a underestimation of the photometric uncertainties.

explored how underestimated photometric uncertainties may bias photometric upper-limits. To do so, we employed the aforementioned empirical relations between the background signal (σ_{rms}) and the aperture sizes (Fig.4.14, Section 4.4.4), per every image. With this relation at hand, the limiting magnitudes can be easily computed as follows:

$$mag_{upp}^{1\sigma} = -2.5 \times log(rms) + ZP\,, \;\; where\ the\ rms = rms(area) \tag{4.7}$$

As can be seen from Fig.4.17, underestimated uncertainties like those provided by `SExtractor` (red line), make the upper limits to be artificially deeper (gray line). This bias is directly translated into the photometric redshift estimations since artificially deeper upper limits force `BPZ` to exclude solutions with brighter magnitudes in those bands. In other words, overestimated upper limits tell `BPZ` that galaxies are much fainter (than what they really are), and so artificially favor high redshift solutions. This effect can easily be seen as an artificial peak (at z>>2.5) in the galaxy redshift distributions $n(z)$, which is related to the well-known Balmer-to-Lyman break degeneracy. When more accurate upper limits (like those computed empirically) are used to derive photometric redshifts, the artificial peak vanishes.

4.5 A new tailored photometry for the CLASH data.

Once the optimal configurations were found and the tools for the photometric uncertainty estimations sharpen, we proceeded to test these improvements on real data. Unlike for the case of the UDF-16, for the CLASH data it was necessary to perform an accurate PSF-corrected photometry across filters. To do so, we relied on an updated version of `ColorPro` (Coe et al. 2006, Molino et al. 2013), since the software is capable to deal with images of varied PSF without degrading the whole dataset to the worst seeing condition. The only major assumption made by the code is that a single model has to represent the PSF of an image. To assure this condition could be met, we created and quantified the expected variability among PSF-models.

4.5.1 PSF-models for *HST* images.

All the 25 clusters were carefully scanned seeking for potential stars and ∼200 candidates were visually selected. Then, each star was double-checked to assure that it was not photometrically saturated and it had been observed in all the 16 filters. Additionally, stars with neighbors within a square box of 25 pixels (i.e., the PSF-model grid size) were also discarded. Finally, the remaining sample of stars (∼70) was combined and normalized to have a total integrated flux equal to unity. Figure D.1 shows the so-generated PSF-models for the *HST* images.

Although a certain spatial and temporal PSF variability is expected for the *HST* images, since `ColorPro` can only handle a model per image, we opted for building "averaged" models, combining stars from different positions (always within the HST/WFC3 field-of-view) and from different epochs. The final mean PSF values and the corresponding scatter (measured in pixels), is shown in table D.1. We observed twice as large dispersion for the ACS images as for the WFC3/NIR. Although WFC3/NIR PSF is broader than ACS.

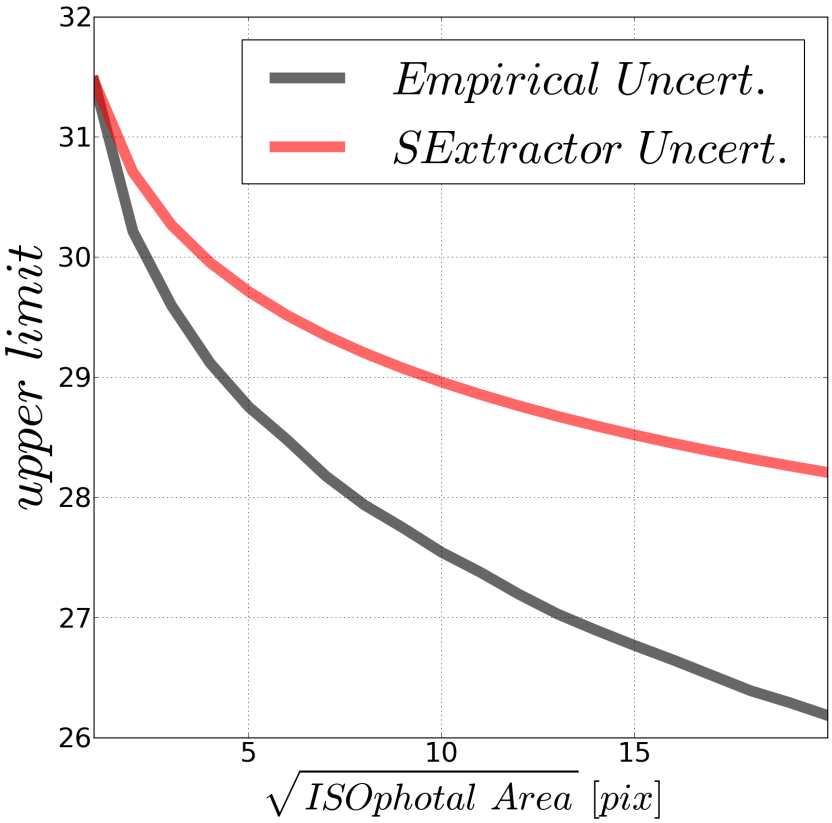

Figure 4.17 The figure shows how underestimated uncertainties like those provided by `SExtractor` (red line), make the upper limits to be artificially deeper (gray line). This bias directly translates into the photometric redshift values since upper limits force the codes to exclude solutions with brighter magnitudes. This effect makes the galaxy redshift distributions $n(z)$ to show an artificial peak at z>>2.5, which is related with the Balmer-to-Lyman break degeneracy. When more accurate upper limits (like those derived empirically) are used to derive photometric redshifts, the artificial peak vanishes.

Although these PSF-models were not intended for lensing analysis, we wanted to quantify the maximum photometric bias that the assumption of a single model per image could be introduced in our estimations. To do so, we selected two stars from the MACS1206/F814W image with the largest dispersion. In other words, the two stars with the narrowest and the broadest PSF value for that image. We used the light-curve of growth, from both stars, to compare the photometric bias as a function of the aperture size. To do so, we ran `SExtractor` on the ACS/F814W image but using circular apertures of multiple radius, to track their stellar light growth. Both curves were normalized to a maximum radii of 30 pixels where the signal was merely composed by background signal. The bias effect was defined as follows:

$$m_{star1} - m_{star2} = -2.5 \times log(\frac{F_{star1}}{F_{star2}}) + (\delta ZP_{12}) \tag{4.8}$$

where the logarithmic term corresponds to the fraction of light enclosed by each FWHM per aperture size, and the second term just accounts for the differences in the calibration to pass from fluxes to magnitudes. As can be seen in Fig.4.5.1, the differential flux was computed as a function of the aperture size, indicating biases <1% for the smallest detection on the image. This result assured the viability of using a single PSF-model per image.

Likewise, we quantified the expected photometric bias if PSF-correction are not considered among images. To do so, it was followed a similar approach where a well-isolated galaxy (with no neighbors) was selected from the MACS1206 ACS/F475W and MACS1206 WFC3/F125W images. Then `SExtractor` was run on both images using circular apertures of multiple radius. This time both growth curves were normalized to a maximum radii of 40 pixels where the signal faded into the background. Making use of the bias factor defined in equation 4.8, it was found that differences in flux as large as 15% might affect detections with sizes smaller than 20 pixels. This result reinforces the necessity of accounting for such as large corrections if accurate photometric redshifts are demanded.

4.5.2 Optimal Apertures for Cluster Members.

Spite of the fact that background-subtracted images served to improve the accuracy for photometric redshifts, it is worth noting that the so-retrieved magnitudes had not necessarily to be optimal for physical parameter studies of bright galaxies (such as metallicities, masses, ages,...) since most of their light had previously removed. In order to avoid biases when inferring these physical parameters, we studied the possibility of performing an alternative photometry yielding more realistic total magnitudes.

As discussed in Section 4.3.3, the number of detected sources on a detection image is strongly dependent on the background setting. In order to perform an alternative non-background-subtracted photometry for all the sources[3], without relying on any coordinate matching algorithm, we explored the possibility of using the same (background-free) detection image to derive total magnitudes. This very fact may assure the number of detections in both catalogues to be exactly the same, making its posterior combination much cleaner. However, since most of the light from the bright galaxies had

[3]All the sources detected on the background-free detection image.

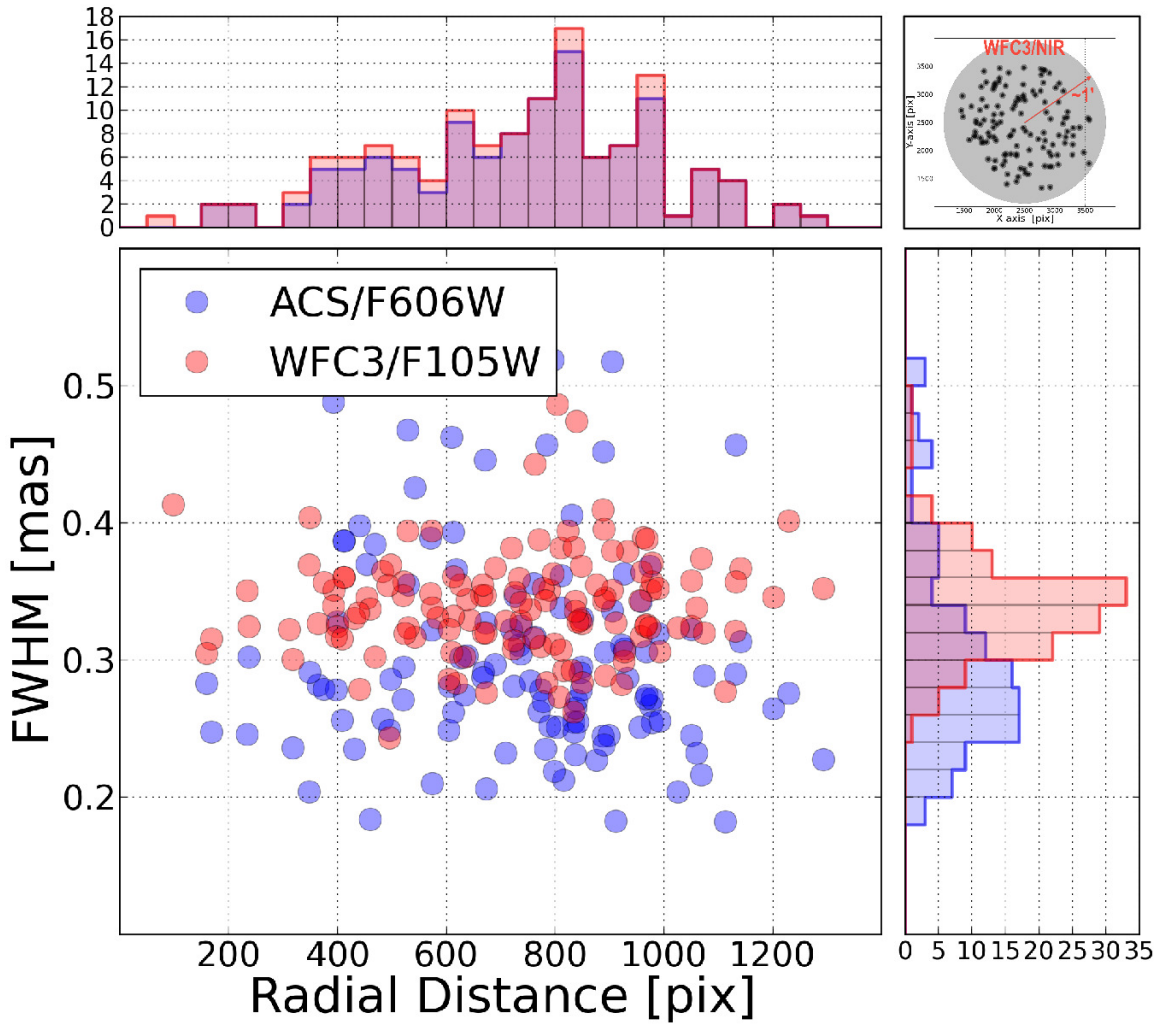

Figure 4.18 Left: Example of the selected stars used to derive empirical PSF-models. Gray circle indicates the internal region (∼1 arcmin) allowed for selections. Right:

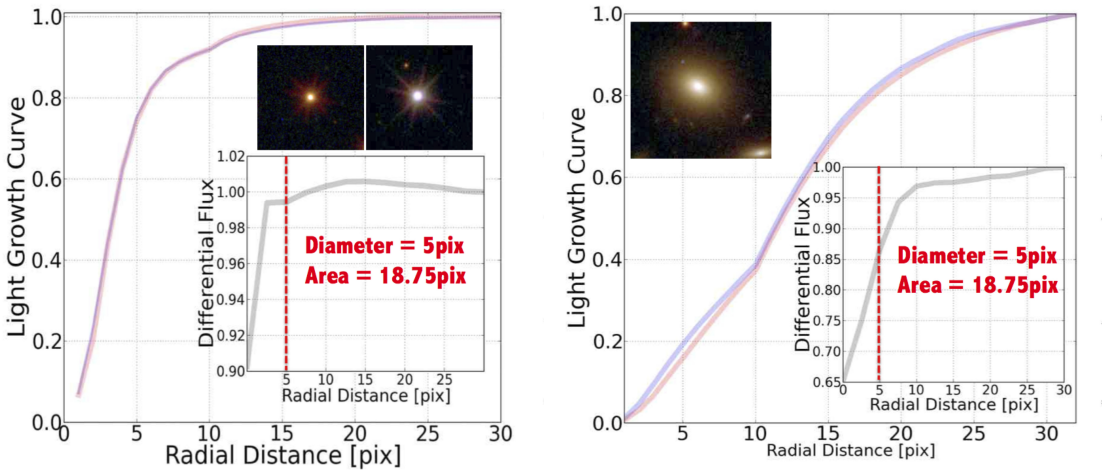

Figure 4.19 Left: We used the light-curve of growth to compare the photometric bias. We ran `SExtractor` on the ACS/F814W image using circular apertures of multiple radius. Both curves were normalized to a maximum radii of 30 pixels where the signal was merely composed by background signal. The differential flux was computed as a function of the aperture size, indicating biases $<<1\%$ across the image. This result assured the viability of using a single PSF-model per image. Right: Following a similar approach, a well-isolated galaxy (with no neighbors) was selected from the MACS1206 ACS/F475W and MACS1206 WFC3/F125W images. Again `SExtractor` was run on both images using circular apertures of multiple radius. Groth curves were normalized this time to a radii of 40 pixels. Differences in flux as large as 15% were observed for detections with sizes smaller than 20 pixels. The result reinforces the necessity of accounting for such as large corrections if accurate photometric redshifts are demanded.

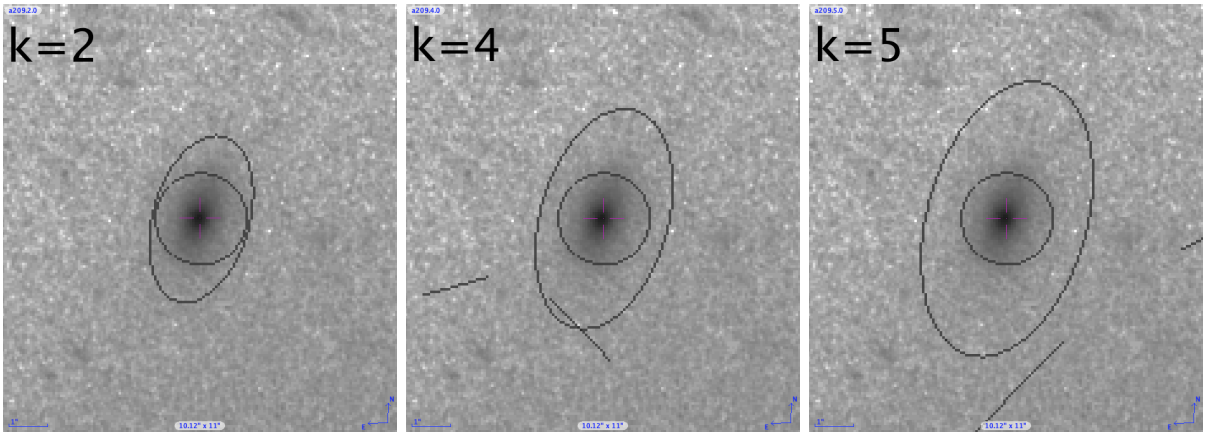

Figure 4.20 The figure illustrates the aperture optimization process. To identify the optimal configuration for `SExtractor` to retrieve total apertures (based on the observed sizes in the detection images), we systematically compared the magnitudes derived using different combinations of the (k_i, R_j) parameters with those `SExtractor_AUTO` magnitudes retrieved from the original individual images. From left to right, the figure shows how the photometric aperture increases as it varies the $Kron$ radius (k).

already been removed in these detection images (see Fig. 4.12), the following aperture definitions may lead to a serious miss underestimation of the real signal. To cope with this drawback, we explored the possibility of finding an optimal photometric aperture (defined on the background-subtracted detection image) capable to retrieve close magnitudes to those derived on the original (non background-subtracted) images.

To do so, we employed the `SExtractor` $PHOT\_AUTOPARAMS$ which regulates the definition of an elliptical aperture around every detection. To identify which might be the optimal configuration, we systematically varied the scale factor of the elliptical aperture (k) and the minimum radius (R_{min}) and compared the resulting magnitudes with those `SExtractor_AUTO` magnitudes retrieved from the original individual images, as illustrated in Fig.4.5.2 This magnitude variation δ_m was defined as follows:

$$\delta_m = m(k_i, R_i)^{det} - m^{ind}_{AUTO} \tag{4.9}$$

where $m(k_i, R_i)^{det}$ corresponds to the magnitude derived using the parameter (k,R) to define the photometric aperture, and m^{ind}_{AUTO} the magnitude when defining the aperture directly on the individual image. As seen in Fig. 4.5.2, where the averaged results for the 24 clusters are presented, the $(k = 4, R = 1)$ solution seems to be an optimal configuration for most of clusters. Therefore, these parameters were adopted when performing total non GB-corrected magnitudes.

4.5.3 Morphological Variation in Background-free Images.

It is well-known that ISOphotal represent the most convenient magnitudes when estimating photometric redshifts, since they yield robust colors using the innermost part of a galaxy where the signal-to-noise is maximum. Although the subtraction of a background-map improved the photometry for small

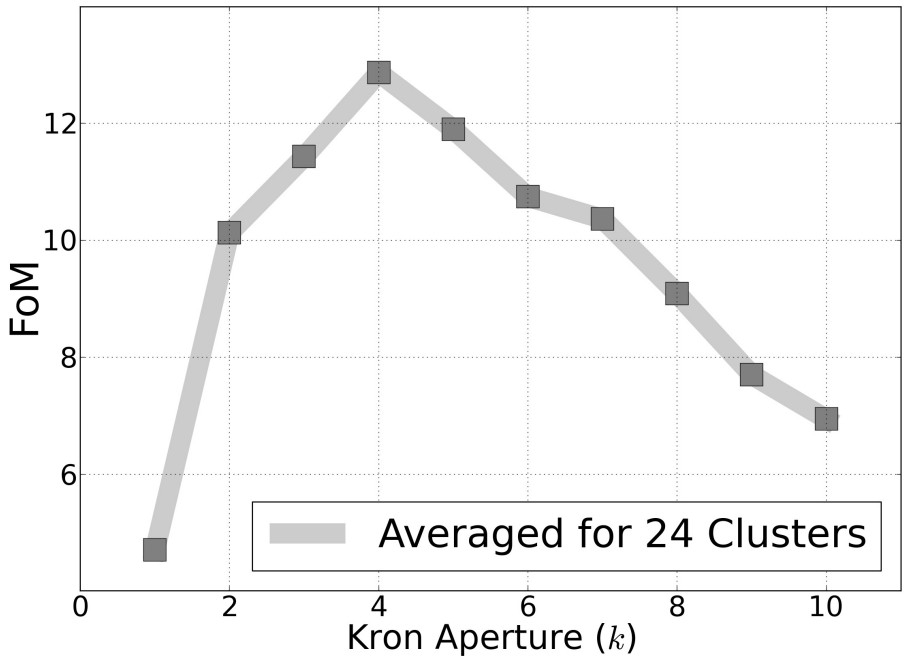

Figure 4.21 The figure illustrates the aperture optimization process. To identify the optimal configuration for `SExtractor` to retrieve total apertures (based on the sizes observed in the detection images), we systematically compared the magnitudes derived using different combinations of the (k_i, R_j) parameters with those `SExtractor_AUTO` magnitudes retrieved from the original individual images. From left to right, the figure shows how the photometric aperture increases as it varies the $Kron$ radius (k). As seen in the figure, where the solid grey line corresponds to the averaged results for the 24 clusters, the $k = 4, R = 1$ solution seems to be an optimal configuration for most of the clusters.

and faint galaxies, they also removed (part of the) light from the (largest) galaxies themselves. To assure this effect may not affect the estimation of ISOphotal colors for bright and extended galaxies, we studied the radial light profile variations for several cluster members before and after subtracting the background-maps.

Initially, we visually selected several well-isolated galaxies across the field [4]. Then, we derived the light growth curves since in the original detection image as in its corresponding background-free image. As seen in Fig. 4.22, while the background subtraction clearly removed light from the galaxy wings, the internal regions remained almost unaffected. i.e., precisely the regions utilized to derive ISOphotal colors. This simple test proved the robustness of photometric estimations performed on background-free detection images.

4.6 Enhanced Photometric Redshifts.

Finally, photometric redshifts for real galaxies in the CLASH fields were derived using BPZ. To do so, multi-wavelength photometric catalogues were previously generated, where all the aforementioned steps were taking into account; i.e., a cluster-by-cluster optimal background subtraction, a PSF-correction among bands, an empirical correction for the photometric uncertainties and a careful derivation of the upper limits.

To quantify the final performance of our photometric redshifts, a small sample of ∼160 spectroscopic redshift galaxies, drawn from four different clusters. As seen in Fig. 4.23, based on this sample all galaxies reached an accuracy better $\delta_z/(1+z_s) < 0.03$, where 80% of them reached an accuracy $\delta_z/(1+z_s) < 0.025$ and 60% an accuracy $\delta_z/(1+z_s) < 0.020$. The results was remarkably good since only 13 filters were used, due to the scarce signal of the first three UVIS/WFC3 filters. Unlike what happened with a non background-corrected photometry (Jouvel et al. 2013), this time the *Odds* parameter was capable to successfully isolate galaxies with accurate and secure redshift. This aspect represents a major breakthrough since now it becomes possible to safety use photometric redshift to build mass-models.

Meanwhile, it was carefully tested the quality of the selected photometry on lensed galaxies. In order to enhance as much as possible the photometric S/N of these faint multiple systems, magnitudes for all its individual images were converted to fluxes and then regrouped. This is worth noting that, by regrouping magnitudes, on the one hand it was possible to pass from (individual) magnitudes of F814W∼25-27 AB to (regrouped) of F814W∼19-22 AB. On the other hand regrouping different images, spread over different position within the image, makes possible to better average remaining photometric biases due to the incomplete background subtraction.

The approach described in this paper not only served to successfully improved the accuracy of our photometric redshift to their expected level, but also to shed new light on how perform accurate photometry on complex scenarios as the ones provided by massive cluster galaxies.

[4] Although it is not stated explicitly in the text, the analysis was systematically repeated for several clusters.

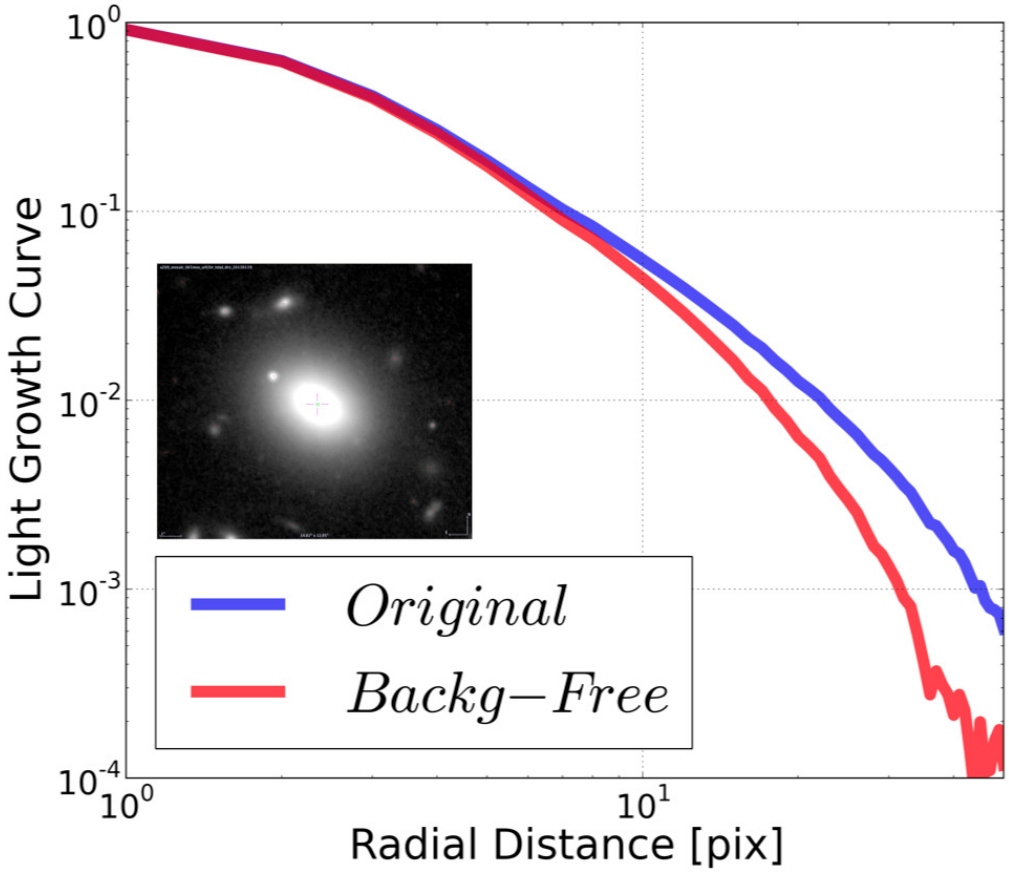

Figure 4.22 To assure the background subtraction may not affect the estimation of ISOphotal colors for bright and extended galaxies, we studied the radial light profile variations for several cluster members before and after subtracting the background-maps. First, several well-isolated galaxies across the field were selected and then the light growth curves, since in the original detection image (solid blue line) as in its corresponding background-free image (solid red line), were derived. While this effect clearly removed light from the galaxy wings, the internal regions remained almost unaffected. The result assured the robustness of measuring ISOphotal colors on background-free detection images.

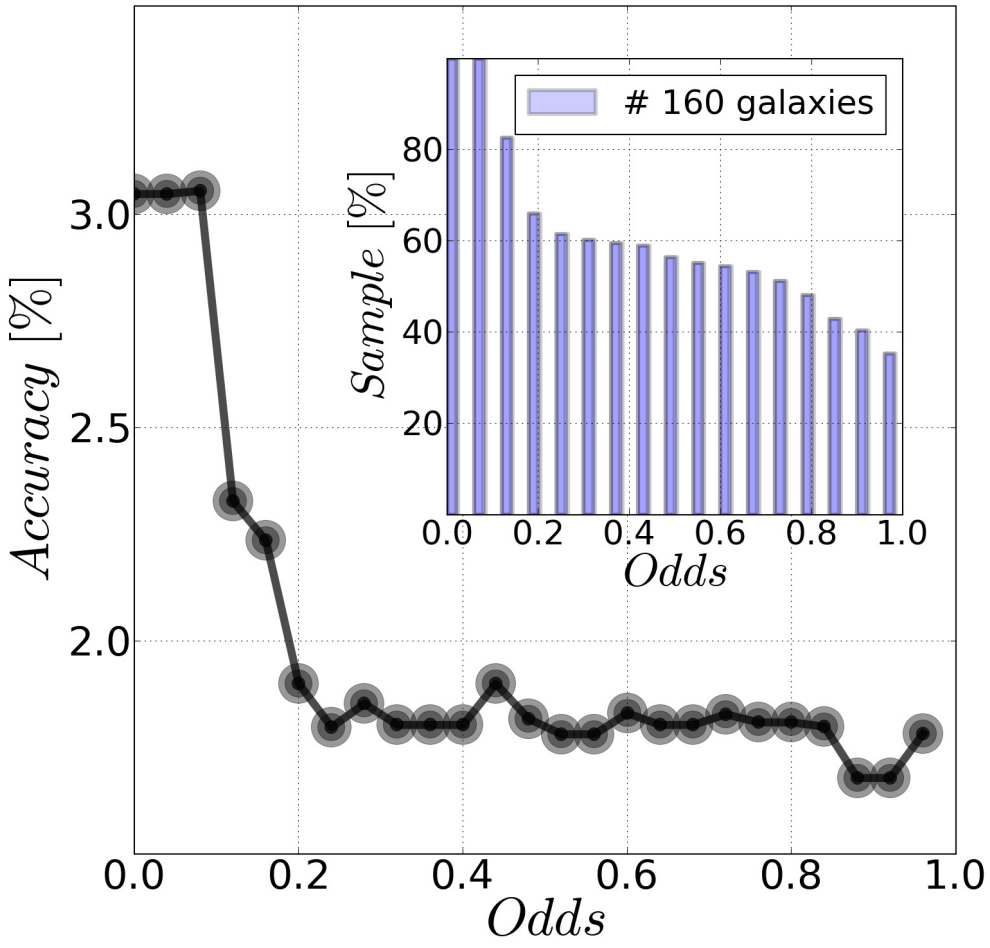

Figure 4.23 The figure shows an example of the final expected accuracy for the CLASH data after 1. background-subtraction, 2. PSF-correction and 3. photometric uncertainty restimation. Using a sample of 160 galaxies with secure spectroscopic redshifts, an accuracy of $\delta_z/(1+z_s) < 0.02$ for galaxies with $Odds > 0.2$ (secure photo-z) is retrieved.

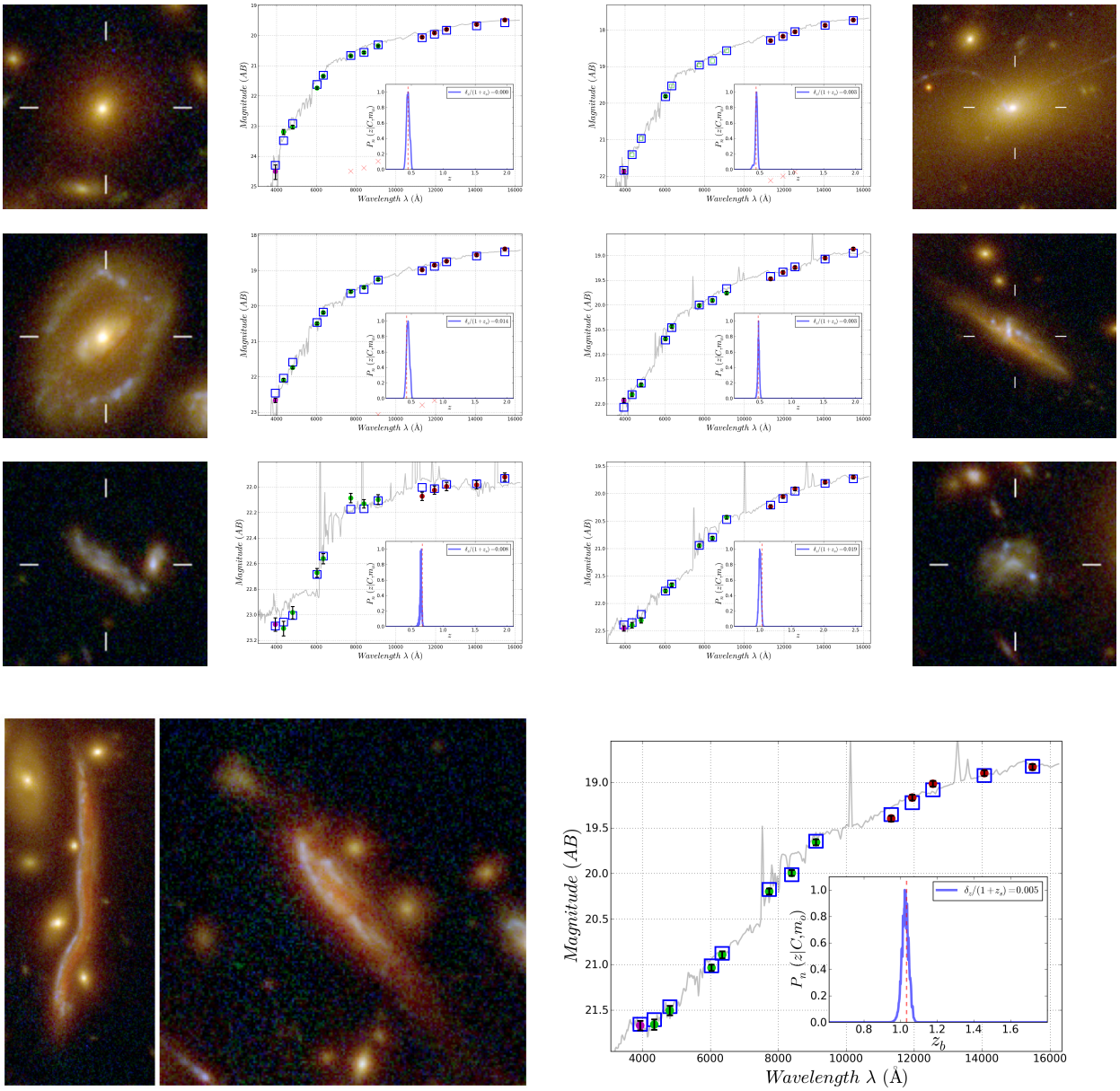

Figure 4.24 Top: Example of 6 galaxies from the spectroscopic-z sample. It encompasses different spectral-types (from early-to-late) and redshift ranges. In all 6 cases the final accuracy was always better than 2%. Bottom: The figure shows a lensed system considered for this analysis (left-hand side) and their final photometric redshift performances (right-hand side). In order to enhance the photometric S/N ratio, magnitudes for all individual images were regrouped and its photometric redshift recomputed. The system finally reached an accuracy $\delta_z/(1+z_s) < 0.01$.

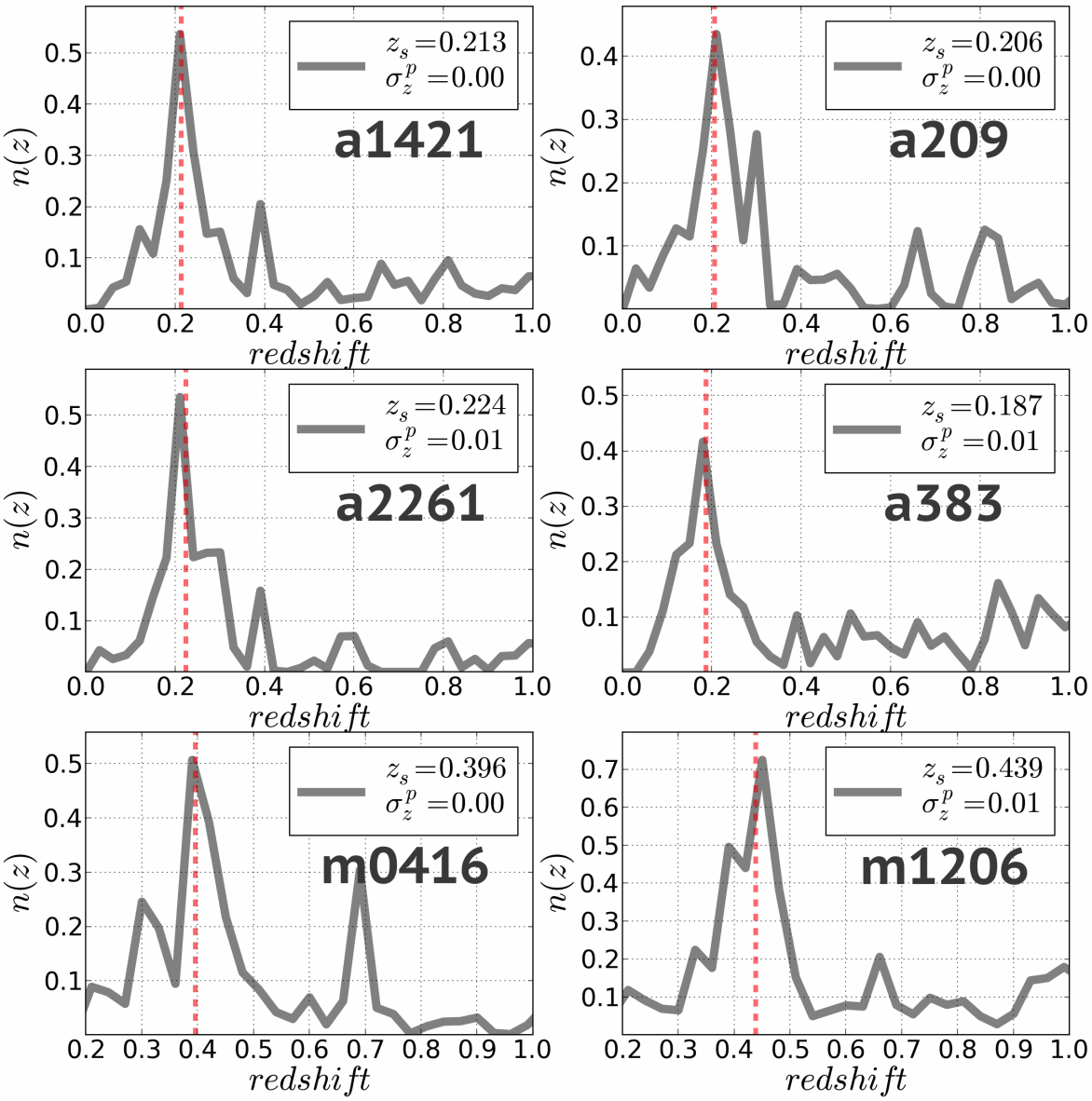

Figure 4.25 The figure shows an example of the redshift probability distribution function ($n(z)$) for the galaxy clusters $a1423$, $a209$, $a2261$, $a383$, $m0416$ & $m1206$, using the improved PSF-corrected, background-subtracted, reliable photometric uncertainties and galaxies with $Odds \geq 0.9$. As indicated by the dashed red lines, the redshift distributions clearly show a prominent peak at the clusters redshift with a typical deviation $\delta_z/(1+z) \leq 2\%$.

5

High-z Universe

5.1 The reonization epoch.

Observational cosmology has established that the age of the Universe is 13.7 billion years, and the reionization of the vast intergalactic medium (IGM) started around redshift $z \sim 11$ (Komatsu et al. 2011), as a result of radiation from the first generation of stars. The task of probing the most distant Universe is progressively challenging: While more than 10^5 quasars have been found, only one is at $z > 7$ (Mortlock et al. 2011); while thousands of gamma-ray burst events have been recorded, only one (Tanvir et al. 2009) is confirmed at $z \sim 6$, only one has been reported at $z \sim 10$ (Bouwens et al. 2011), which is based on a single-band detection. Galaxies at $z \sim 10$ are expected to be at a magnitude of ~ 29 (in the AB system; Bouwens et al. 2011, Oesch et al. 2012), near the detection limits of the deepest fields observed by *Hubble Space Telescope (HST)*, and beyond the spectroscopic capability of even the next generation of large telescopes.

Gravitational lensing by galaxy clusters enables the detection of high-redshift galaxies that are fainter than what otherwise could be found in the deepest images of the sky. The Cluster Lensing And Supernova with Hubble (CLASH) is a *HST* Multi-Cycle Treasury program that acquires images in 16 broad band between 0.2-1.7μm for 25 clusters. MACSJ1149.6+2223 is a massive cluster at redshift z=0.544, selected from a group of X-ray luminous clusters. The mass models for this cluster (Zitrin et al. 2009, Smith et al. 2009) suggest a relatively flat mass distribution profile and a large area of high magnification, making it one of the most powerful cosmic lenses known.

In Wei et al. 2012, we reported the discovery of an object found in the multi-band observations of the cluster MACSJ1149+22 that has a high probability of being a gravitationally magnified object from the early universe, whose most likely redshift is $z \sim 9.6$.

5.1.1 MACSJ1149-JD1.

The CLASH observations of MACS J1149.6+2223 were made between December 2010 and March 2011. The *HST* data were processed in two independent pipelines, combining, aligning and resampling the images with a common pixel scale of 65 mas. We used the combination of all WFC3/IR images as a detection image, and ran SExtractor (Bertin & Arnouts 1996) in dual image mode in every filter band.

As seen in Fig. 5.1, the source MACSJ1149-JD1 was firmly detected with a significance of 22σ in the two reddest bands of $HST/WFC3$, and not detected below 1.2μm, matching the characteristics of z$\sim$9 objects.

In addition, *Spitzer*/IRAC images of MACS J1149.6+2223 were retrieved from archive, with a total exposure time of 33.6 ksec in total, and 16.8 ksec on target for both channels. The candidate was not visually detected at 3.6μm in the total stack, with a 1σ upper limit of magnitude 26.1. The IRAC photometry at 4.5μm was carried out in several ways. We constructed simulated point sources convolved with the IRAC PSF profile and normalized to magnitudes of 24.0, 24.5 and 25.0, respectively. We placed these simulated sources in the vicinity of MACS1149-JD1, and ran *GALFIT* with different fitting windows, until the expected magnitude of each simulated source is recovered. We proceeded to fit the flux of MACS1149-JD1 using the fitting window and the background level on the image that recovered the brightness of the simulated sources most accurately. To account for the uncertainties in estimating the background at different positions around MACS1149-JD1, we chose their mean value of 24.77$\pm$0.3 as the source magnitude in the 4.5μm band. The final photometric measurements are those indicated in table 5.1.1.

F814W	F850LP	F105W	F110W	F125W	F140W	F160W	3.6μm	4.5μm
$> 29.4^a$	$> 27.9^a$	$> 28.2^a$	27.5 ± 0.3	26.8 ± 0.2	25.92 ± 0.08	25.70 ± 0.07	$> 26.1^a$	24.8 ± 0.3

[a] 1σ detection limit.

Using confirmed multiply-lensed images, strong-lensing (SL) models (Zitrin et al. 2009, Zitrin et al. 2011) allowed us to derive the mass distribution of DM in the cluster, which led to an amplification map for background sources. With 23 multiply-lensed images of seven sources, the best-fit model was derived in which the critical curve (of high magnification) of $z \sim 10$ extends to the vicinity of MACS1149-JD1, resulting in a magnification factor of $\mu = 14.5^{+4.2}_{-1.0}$. The results were in rough agreement with a second, independent model (Jullo et al. 2007), which yields a best-fit magnification with large error bars, $26.6^{+20.8}_{-7.7}$. From this it follows that MACS1149-JD1 is approximately 15$\times$ brighter than it would be in an unlensed field.

5.1.2 Redshift Probability Distribution Function.

We derived a robust photometric redshift of z=9.6$\pm$0.2, corresponding to a cosmic age of 490$\pm$15Myr (*i.e.*, 3.6% of the age of the Universe). To do so, we relied on two different algorithms for the redshift estimation: Le Phare (LPZ; Arnouts et al. 1999, Ilbert et al. 2006) and Bayesian Photometric Redshifts (BPZ; Benítez 2000, Coe et al. 2006). LPZ photometric redshifts are based on a template fitting procedure with a maximum likelihood (χ^2) estimate. We used the template library of the COSMOS survey (Koekemoer et al. 2007), including galaxy templates of three elliptical galaxies, seven spirals (Polletta et al. 2007) and 12 common templates (Bruzual & Charlot 2013), with starburst ages ranging from 30 Myr to 3 Gyr (billion year) to better reproduce the bluest galaxies. The LPZ solution from the marginalized posterior is z=9.60 $^{+0.20}_{-0.28}$ (at 68% confidence level), and the best-fit model is a starburst galaxy. BPZ multiplies the likelihood by the prior probability of a galaxy with an apparent magnitude m_0 of having a redshift z and spectral type T. We run BPZ using a new library

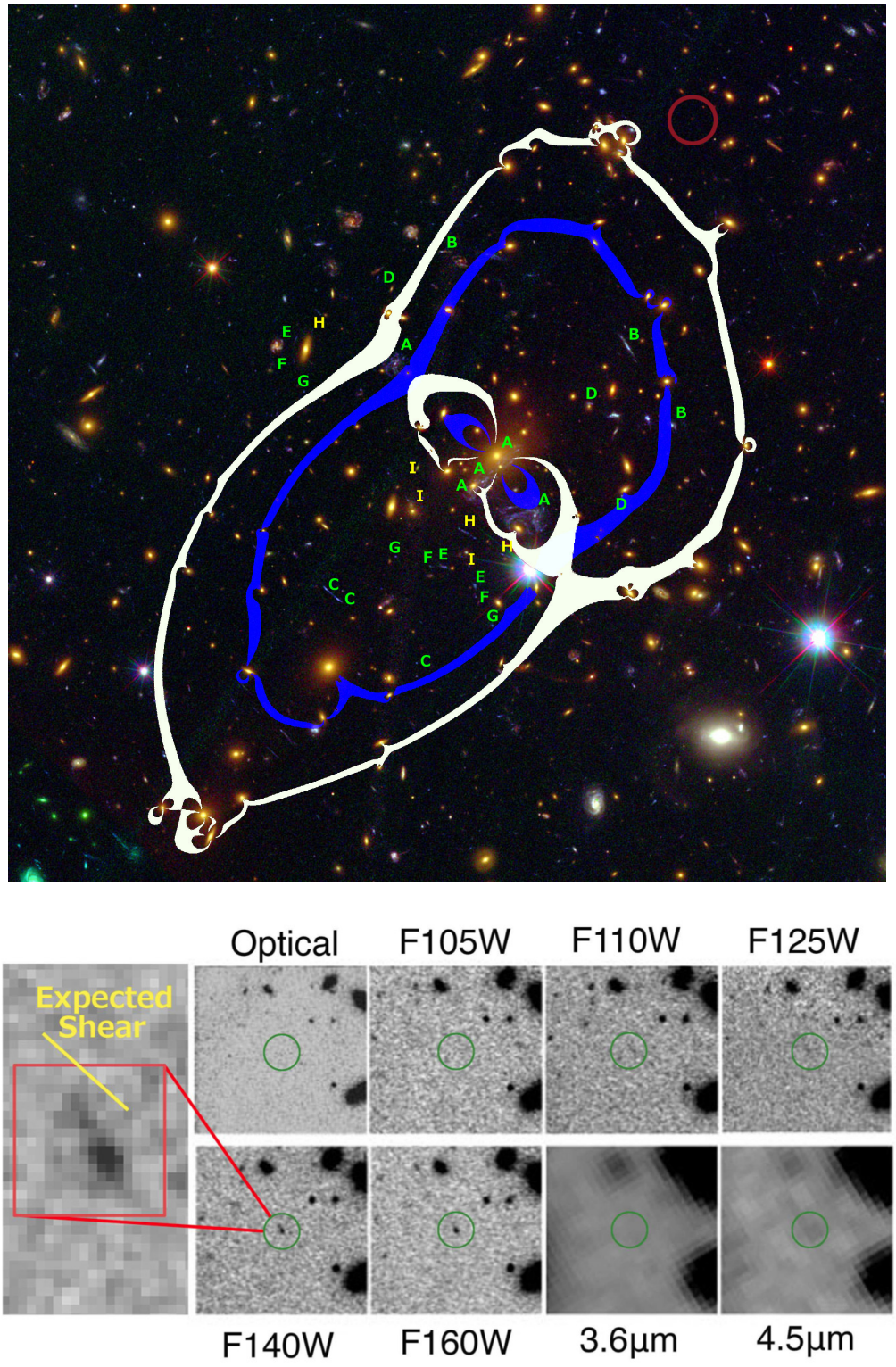

Figure 5.1 Top: composite color image of cluster MACS J1149.6+2223. The location of MACS1149-JD1 is marked with a red circle, at RA=$11^h49^d33^s.584$ and Dec=$+22\frac{1}{4}24'45".78$ (J2000). The z=9.6 critical curve for the best-fit lensing model is overplotted in white. Green letters correspond to the multiple images of seven sources that were used in the strong-lensing model. The FoV is 2.2 arcmin on each side. The z=9.6 critical curve Bottom: Catout images of MACS1149-JD1 in the optical (ACS, summed), near-infrared (WFC3) and infrared (IRAC) bands. Each image is 10ön one side. The source, located at the center of each image, is firmly detected in the F140W (1400 nm) and F160W bands and weakly detected in the F1110W, F125W and 4.5μm bands.

composed of 11 SED templates originally drawn from PEGASE (Fioc & Rocca-Volmerange 1997) but recalibrated using the FIREWORKS photometry and spectroscopic redshifts (Wuyts et al. 2008) to optimize its performance. This galaxy library includes five templates for ellipticals, two for spirals, and four for starbursts. The most likely BPZ solution is a starburst galaxy at z=$9.61^{+0.14}_{-0.13}$ (1σ).

As seen in Fig.5.2, while our most probable and robust photometric redshift estimations yield the high-redshift solution, we further studied alternative solutions when the IRAC data are not used in the fitting. Intermediate-redshift solutions were found at low probability when we ran LPZ and BPZ with only the four WFC3/IR bands where the source was detected. However, these intermediate redshift solutions all had considerably higher χ^2 values than the best fit solution at $z = 9.6$. For each model used, we calculated the χ^2 value from the estimations. LPZ yielded a best-fit model for a starburst galaxy at $z = 9.63 \pm 0.25$ with a low χ^2=0.37. We found a secondary solution for an elliptical galaxy at $z \sim$5.92 with a χ^2= 1.74. While this second solution was within 1σ from the best-fit value, it required a model with an old stellar population – an unlikely scenario at $z \sim 6$. Bottom panel from Fig.5.2 shows the χ^2 values as a function of redshifts and the types of galaxy templates as the LPZ output. Intermediate-redshift solutions yielded considerably higher χ^2 values and were hence considered unlikely.

Therefore, MACS1149-JD1 is the first z >9 candidate that is bright enough for detailed spectroscopic studies with $JamesWebbSpaceTelescope(JWST)$, demonstrating the unique potential of galaxy cluster fields for finding highly magnified, intrinsically faint galaxies at highest redshifts.

5.1.3 Analysis of the Stellar Population.

This significant magnification by cluster lensing (a factor of ∼15) allowed us to analyze the object's ultra-violet and optical luminosity in its rest-frame, thus enabling us to constrain on its stellar mass, star-formation rate and age. Because our data covered a broad range in the object's rest-frame, we were able to estimate some key properties for the source using the Bayesian SED-fitting code `iSEDfit` (Moustakas et al. 2011) coupled to state-of-the-art population synthesis models (Conroy et al. 2010) and based on the Chabrier (Chabrier 2003) initial mass function from $0.1 - 100\ M_\odot$ (solar mass). We considered a wide range of parameterized star formation histories and stellar metallicities and assumed no dust attenuation, as previous studies (Labbé et al. 2010, Bouwens et al. 2010) found no evidence for dust in galaxies at the highest redshifts. Fig.5.3 shows the results of our population synthesis modeling, adopting $z = 9.6$ as the source redshift.

Based on the median of the posterior probability distributions, our analysis suggested a stellar mass of $\sim 1.5 \times 10^8\ (\mu/15)^{-1}\ M_\odot$ and a star-formation rate (SFR) of $\sim 1.2\ (\mu/15)^{-1}\ M_\odot\ yr^{-1}$. Given the uncertainties in the IRAC photometry, we were unable to measure the age of the galaxy precisely; however, we did can constrain its SFR-weighted age, or the age at which most of the stars formed, to $\langle t \rangle_{SFR} < 200$ Myr (95% confidence level), suggesting a likely formation redshift z_f <14.2. Given that the source was brighter at 4.5μ than at 3.6μ, the presence of a Balmer break was likely, suggesting that MACS1149-JD1 may not be too young. This age implied a formation redshift of no earlier than $z_f \sim 11.3$, generally consistent with the estimated ages (>∼ 100 Myr) of galaxies at slightly lower redshifts, $z \sim 7 - 8$. (Labbé et al.2010)

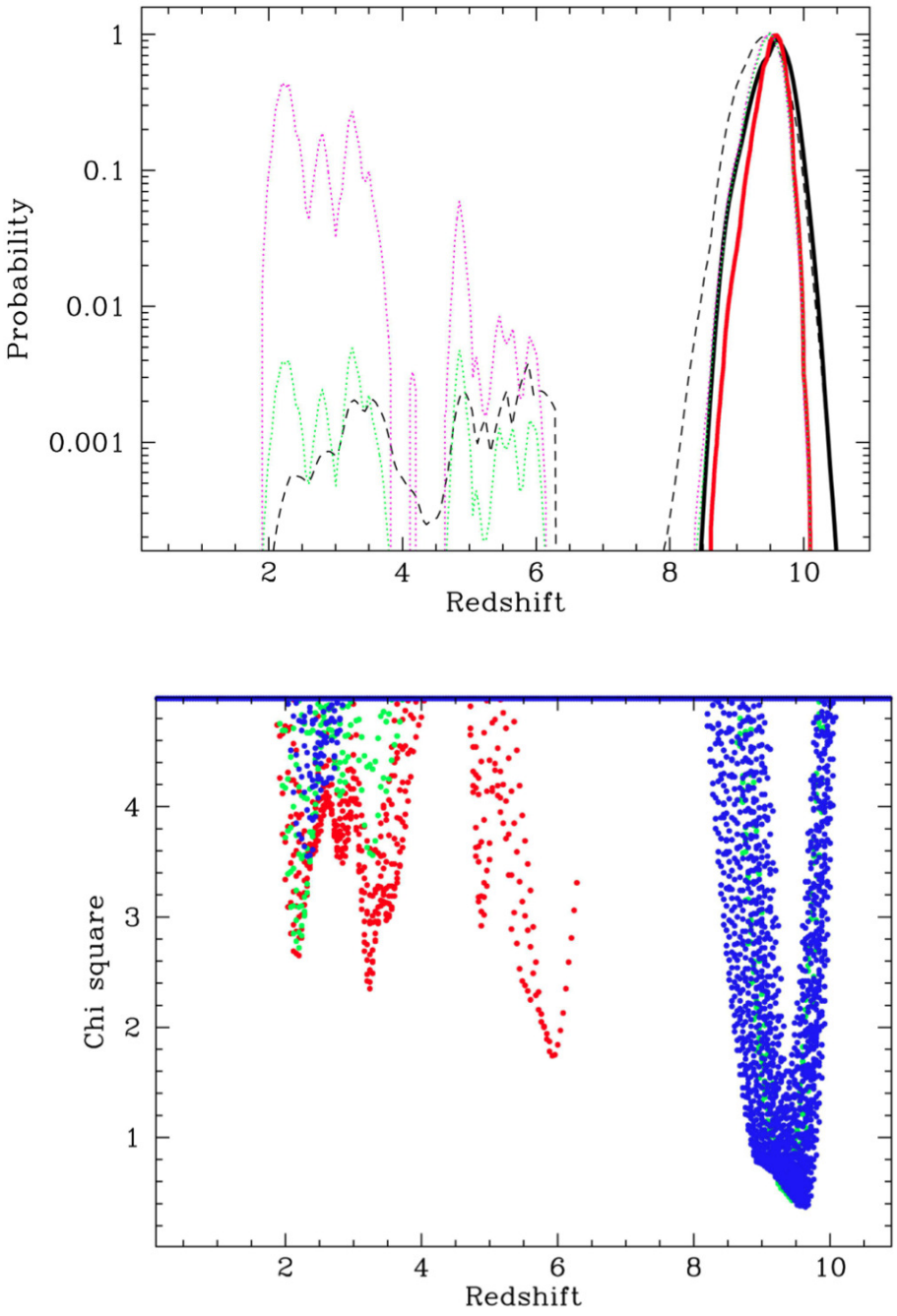

Figure 5.2 Top: Probability Distribution of photometric redshift estimation. All curves are normalized to their peak probability. Solid black curves correspond to LPZ, using all the HST and Spitzer data; Solid red curves correspond to BPZ with and without Priors, using all data. Only the high-redshift solutions are confirmed with high confidence ($>4\sigma$). Dashed black curves corresponds to LPZ using HST data only. Dotted green curves correspond to BPZ w/o Priors, using the HST data only. In these two cases, intermediate-redshift solutions are present at low probability ($<1\%$). Dotted magenta curves correspond to BPZ with priors, using the HST data only. Only in this case intermediate-redshift solutions become significant. Bottom: Likelihood distribution of photometric redshifts. We fit only the four HST bands where the source is detected, and the plot the χ^2 values at different fitted redshifts for each template. χ^2 values higher than 5 are truncated. Green points: elliptical galaxies; red point: spiral galaxies; blue points: starburst galaxies, some of which yield the lowest χ^2 values. Intermediate-redshift solutions yield considerably higher χ^2 values than the high-redshift solutions.

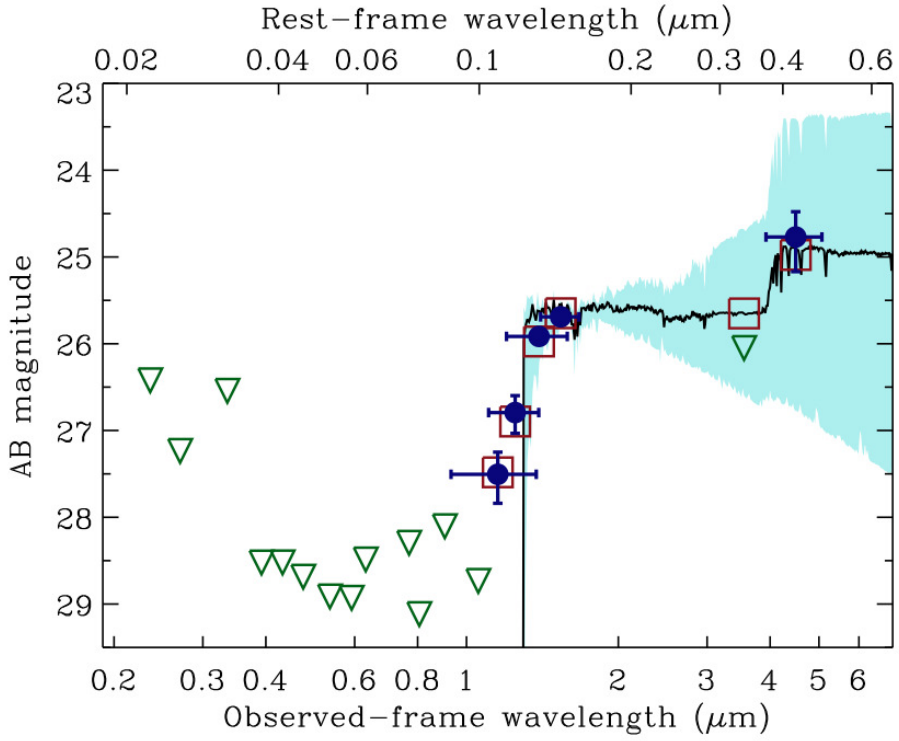

Figure 5.3 Stellar Population Synthesis Modeling results for MACS1149-JD1. The filled blue points mark bands in which the object is detected, while green triangles indicate 1σ upper limits. The errors in the F140W and F160W bands are small (<0.1 magnitude) and hence not visible. The black spectrum is the best-fit model, and the open red squares show the photometry of this model convolved with the WFC3, ACS and IRAC filter response functions. The light blue shading shows the range of 100 additional models drawn from the posterior probability distribution that are also statistically acceptable fits to the data.

6

The Accelerated expansion of the Universe.

6.1 The Dark Energy Equation of State and SNe Evolution.

The biggest cosmological surprise in decades came from observations of high-redshift type-Ia supernovae (SNe Ia), providing the first evidence that the expansion of the Universe now appears to be accelerating (Riess et al. 98, Perlmutter et al. 99), and indicating the Universe is dominated by "dark energy." The presence of dark energy has galvanized cosmologists as they seek to understand it. Observations of high-redshift SNe Ia have continued to lead the way in measuring the properties of dark energy (Riess et al. 11). The goal for cosmologists now is to measure the equation of state of dark energy, $w = P/(\rho c^2)$, and its time variation in the hope of discriminating between viable explanations. A departure of the present equation of state, w_0, from -1 or a detection of its variation, $\partial w/\partial z$, would invalidate an innate vacuum energy (i.e., the cosmological constant) as the source of dark energy and would point towards a present epoch of "weak inflation." A difference between the expansion history and the growth history of structure expected for $w(z)$ would point towards a breakdown in General Relativity as the cosmic scale factor approaches unity.

HST paired with *ACS* is a unique tool in this investigation, providing the only means to collect SNe Ia at $1 < z < 1.5$, which, in turn, provide the only constraints we have to date on the time variation of w. From the 23 SNe Ia at $z > 1$ with *HST* data (Riess et al. 04, Riess et al. 07) we have learned: 1) that cosmic expansion was once decelerating before it recently began accelerating, 2) that dark energy, i.e., an energy density with $w < 0$, was already present during this prior decelerating phase, 3) that SNe Ia at a look-back time of 10 Gyr appear both spectroscopically and photometrically similar to those seen locally and 4) no rapid change is seen in $w(z)$ and thus no departure is yet seen from the cosmological constant, though the constraint on the time variation remains an order of magnitude worse than on the w_0.

6.1.1 SNIa Rates

Although Type-Ia supernovae (SNe Ia) have been used to measure extragalactic distances and thus reveal the accelerating expansion of the Universe (Riess et al. 1998, Perlmutter et al. 1999), the nature

of the stellar system that leads to these explosions remains unclear. The current consensus is that the progenitor is a carbon-oxygen white dwarf (CO WD) that accretes matter from a binary companion until the pressure or temperature somewhere in the WD become high enough to ignite the carbon and lead to a thermonuclear explosion of the WD (Leibundgut 2000). Different scenarios have been proposed to explain the nature of the binary companion and the process of mass accretion. The leading scenarios are the single-degenerate scenario (SD; Whelan et al. 1973), in which the binary companion is either a main-sequence star, a subgiant just leaving the main sequence, a red giant, or a stripped "He star," and the WD accretes mass from the secondary through Roche-lobe overflow or a stellar wind. In the double-degenerate scenario (DD; Iben et al. 1984, Webbink 1984), the companion is a second CO WD and the two WDs merge due to loss of energy and angular momentum to gravitational waves.

Each of these scenarios predicts a different form of the distribution of times that elapse between a short burst of star formation and any subsequent SN Ia events, known as the delay-time distribution (DTD). The DTD can be thought of as a transfer function connecting the star-formation history (SFH) of a specific stellar environment and that environment's SN Ia rate. Thus, by measuring the SN Ia rate and comparing it to the SFH, one might reconstruct the DTD. The SN Ia DTD has been recovered using several techniques applied to different SN samples collected from different types of stellar environments. The emerging picture is that of a power-law DTD with an index of ~ -1, a form that arises naturally from the DD scenario, although combinations of DTDs from a DD channel and a SD channel cannot be ruled out. One method to recover the DTD, $\Psi(t)$, is to measure the SN Ia rate, $R_{\rm Ia}(t)$, as a function of cosmic time t in field galaxies, and compare them to the cosmic SFH, $S(t)$:

$$R_{\rm Ia}(t) = \int_0^t S(t-\tau)\Psi(\tau)d\tau. \tag{6.1}$$

Whereas measurements of the volumetric SN Ia rates (i.e., the SN Ia rates per unit volume) in field galaxies consistently agree out to $z \approx 1$, volumetric SN Ia rate measurements at $z > 1$ are more uncertain since they are dominated by small-number statistics. Although the GOODS (Giavalisco et al. 2004, Riess et al. 2004) and the SUBARU Deep Field (SDF, Graur et al. 2011) $z > 1$ SN Ia rates are consistent, their interpretation differs between the two groups. Based on the GOODS data, (Dahlen et al. 2004, Dahlen et al. 2008) argued that the SN Ia rate declined at $z > 0.8$. Fitting this declining SN Ia rate evolution, (Strolger et al. 2004, Strolger et al. 2010) surmised that the DTD is confined to delay times of 3–4 Gyr. In contrast, based on the SDF data, G11 found that the SN Ia rate evolution does not decline at high redshifts, but rather levels off, as would be expected of a power-law DTD.

Two new SN surveys are attempting to resolve this conflict. These surveys are components of two three-year *HST* Multi-Cycle Treasury programs that use the Advanced Camera for Surveys (ACS) and the new Wide Field Camera 3 (WFC3). Results from the Cosmic Assembly Near-infrared Deep Extragalactic Legacy Survey (CANDELS; (Grogin et al. 2011, Koekemoer et al. 2011) will be reported by Rodney et al. (in prep.). Here, we describe results from the Cluster Lensing And Supernova survey

with Hubble (CLASH; Postman et al. 2012). CLASH imaged 25 galaxy clusters in 16 broad-band filters from the near-ultraviolet (NUV) to the near-infrared (NIR) with the ACS and WFC3 cameras working in parallel mode. While one camera was pointed at the galaxy cluster, the other one was used to observe a parallel field far enough from the galaxy cluster so as not to be significantly affected by strong lensing. Our SN survey was conducted in both the primary and the parallel fields.

6.1.2 Observations

The orientation of *HST* and the cadence between succeeding visits to the galaxy cluster ("prime") field were chosen so that two ACS and two WFC3 parallel fields would each be observed on four separate occasions, with a median cadence of 18 days. Each visit to a WFC3 parallel field consisted of one orbit comprising two F160W filter exposures and one exposure in filters F125W and F350LP each (filter+system central wavelengths $\lambda_0 \approx$ 15,369, 12,486, and 5846 Å, respectively). Visits to the ACS parallel fields consisted of one orbit when the prime field was imaged with either the ACS or WFC3-IR cameras and two orbits when the prime field was imaged with the WFC3-UVIS camera. During single-orbit visits, the parallel ACS orbit comprised four F850LP filter exposures and one F775W filter exposure (filter+system central wavelengths $\lambda_0 \approx$ 9445 and 7764 Å, respectively). When the ACS parallel fields were imaged over two orbits, they consisted of six F850LP and two F775W exposures. These filters, the reddest in each camera, were chosen to detect high-redshift SNe. The F350LP band was added to the WFC3 observations for additional color information to aid in the classification of any SNe discovered in those fields.

6.2 Supernova Sample

A total of 20 brightening and 7 declining SNe were discovered in the parallel fields of the 25 CLASH clusters. Of these, 18 were discovered in the ACS and 9 in the WFC3 fields. 19 (or 70%) of the SN host galaxies have spectroscopic redshifts. We classified slightly less than half of this sample as SNe Ia, four of which are at $z > 1.2$. We discovered 12 additional SN candidates in the prime fields. However, as the effects of gravitational lensing must be taken into account to properly classify any SNe discovered behind the galaxy clusters, we left their treatment to a future paper. The complete photometry of all 39 SNe in our sample will appear in a future paper by Graur et al. (in prep.).

6.2.1 Host-galaxy Redshifts.

Our classification method, as with most SN classification techniques, relies on a good knowledge of the redshift of either the SN or its host galaxy. As part of our survey strategy, we have endeavored to obtain spec-z measurements of the host galaxies of all the SNe in our sample, mostly with ground-based observatories. Some of the SN host galaxies suspected of being at $z > 1.2$ were also followed up with *HST* slitless spectroscopy using the ACS G800L grism. At this time, we have acquired and reduced the spectra of 19 of the 27 SN host galaxies in our sample. For the remaining eight SN host galaxies, we rely on photo-z measurements. A complete description of our photo-z technique appears in Jouvel et al. (2013) and Molino et al. (2014, in prep.).

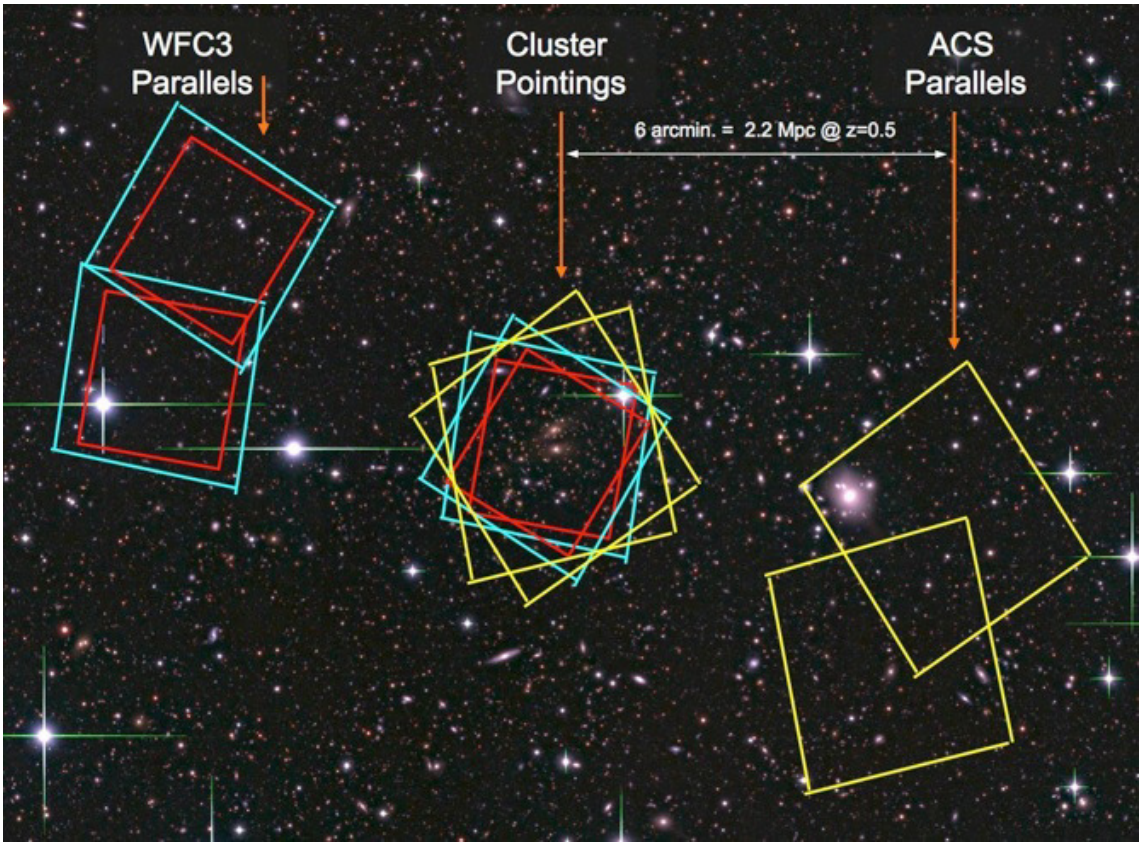

Figure 6.1 The CLASH survey uses *ACS* in parallel with the cluster program to continue the discovery of SNe Ia at $1 < z < 1.5$, the objects which tell us about the variation in w. With *WFC3* in parallel, CLASH will yield SNe Ia at $1.5 < z < 2.5$ (Rodney et al. 11). Because the SNe Ia are detected when these cameras are in parallel, they are far from the cluster core (~ 2 Mpc at the median cluster redshift of $z = 0.4$) and, hence, the effects of lensing are small (and correctable), making the SNe usable for improving the limits on the redshift variation of the dark energy equation of state. At $z < 1$, SN Ia distance measurements are most sensitive to the static component of dark energy, w_0. At $1 < z < 1.5$, the measurements are most sensitive to the dynamic component, w_a. By $z > 1.5$, the measurements are most sensitive to evolution if present (e.g., the changing C/O ratio of the donor star), providing the means to diagnose and calibrate the degree of SN Ia evolution in dark energy measurements.

Here, we give only a brief description of this technique. The spec-z and photo-z values of the SNe in our sample are shown in Figure 6.2. We estimated the redshift and spectral type of all SN host galaxies with photometry obtained from deep Subaru images (in the B, V, R_c, I_c, and z' bands) and the Bayesian Photometric Redshift code (BPZ; Benitez et al. 2000). For the host galaxies of SNe that were discovered in the WFC3 parallel fields, we also added galaxy photometry in the F125W and F160W bands. Some host galaxies were previously imaged by the Sloan Digital Sky Survey (SDSS; York et al. 2000), allowing us to include photometry in the u', g, r', i', and z' bands as well.

For each galaxy, BPZ calculates a likelihood, $L(z, T)$, as a function of redshift, z, and spectral type, T, comparing the observed colors of the galaxies with the template library, and then multiplies it by an empirical prior, $p(z, T|m)$, which depends on the galaxy magnitude in some reference band, m, yielding a full probability, $p(z, T)$, for each galaxy. The new version of BPZ (Benítez, in prep.) includes a new template library comprising six SED templates originally from PEGASE (Fioc & Rocca-Volmerange 1997) and four early-type templates from Polletta et al. (2007). The PEGASE templates were recalibrated using the FIREWORKS photometry and spectroscopic redshifts (Wuyts et al. 2008) to optimize its performance together with the new early-type galaxy templates. In total, we use five templates for early-type galaxies, two for intermediate galaxies, and four for starburst galaxies. The prior was calibrated using the GOODS-MUSIC (Grazian et al. 2006), UDF (Coe et al. 2006), and COSMOS (Ilbert et al. 2009) samples. As a result of the high-quality HST imaging used for its calibration and using an approach similar to that developed by Coe et al. (2006), the representation of typical galaxy colors provided by this library can be used to calibrate ground-based photometry to an accuracy of $\sim 2\%$ (Molino et al., in prep.).

6.2.2 Supernova Classification

We classified our SNe into SNe Ia, SNe Ib/c, or SNe II by fitting light curves to their multi-band photometry using a Bayesian approach first introduced by Jones et al. (2013), where it was used to classify the CANDELS SN UDS10Wil. The full description of this classification technique, named the Supernova Taxonomy And Redshift Determination Using $SNANA$ Templates ($STARDUST$), along with a detailed examination of any systematic biases it might introduce, will appear in a future paper by Rodney et al. (in prep.). Briefly, for each SN we calculate the probability that it is a SN Ia, P(Ia), by comparing the observed fluxes (in all available bands and epochs) to light-curve models generated using the $SNANA$ simulation package. We computed the likelihood that a given model matches the observable data, multiply it by priors of the model parameters, then marginalize over all models to derive the final posterior classification probability. We classify a SN as a SN Ia if $P(\text{Ia}) \geq 0.5$.

6.2.3 The Type-Ia Supernova Rate

We use the aforementioned SN Ia sample, along with the detection efficiencies as a function of redshift and their classification probabilities, to measure the rates of SNe Ia as a function of redshift, or lookback time. So as not to bias our results, we use the SN classification without the assumption of the SN-fraction prior. The SNe Ia in our sample can be divided among three categories, according to when they reached maximum light: before, during, or after the monitored interval of time spent on

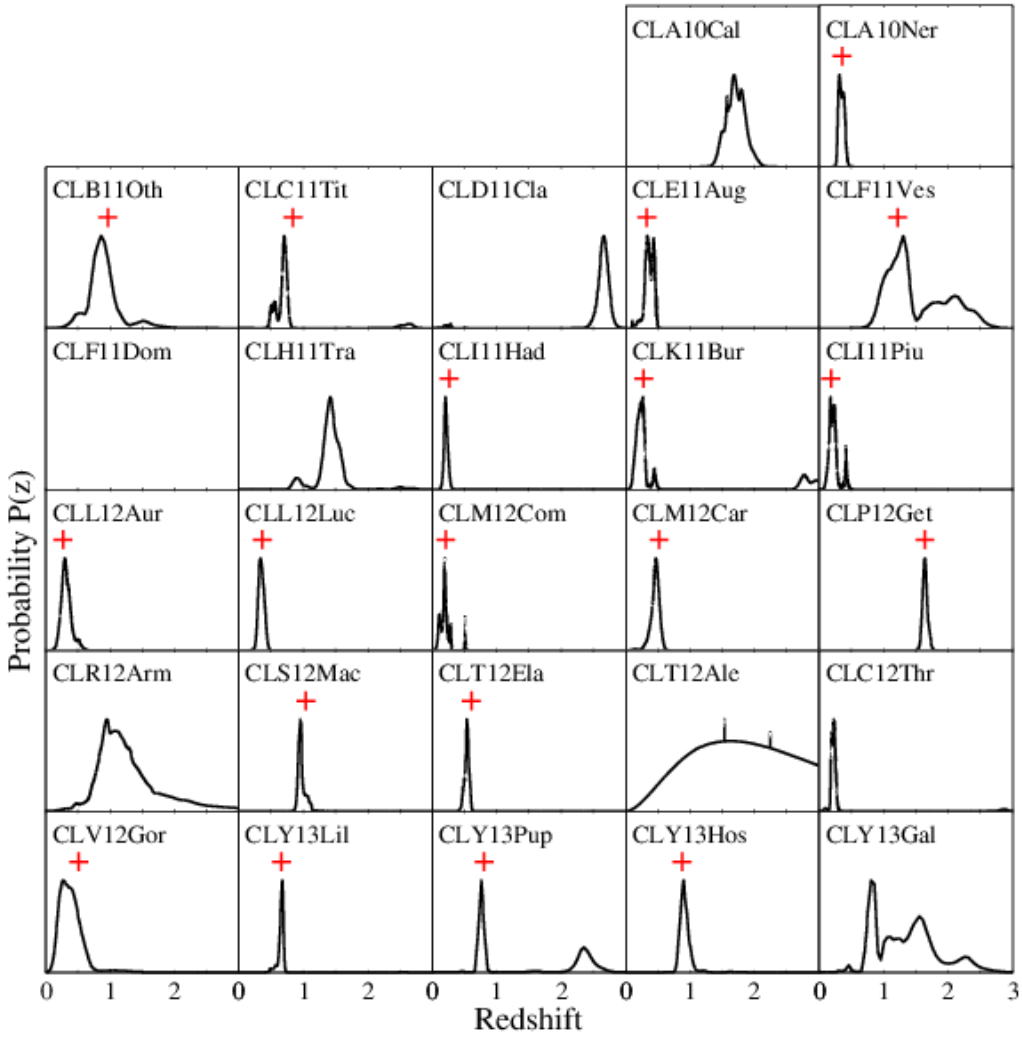

Figure 6.2 BPZ z-PDFs of the SN host galaxies. The z-PDFs are the solid curves and the spectroscopic redshifts, where available, are marked by red crosses. The designation of each SN appears in the upper left corner of each panel. All z-PDFs have been normalized so that $\int P(z)dz = 1$. We estimated the redshift and spectral type of all SN host galaxies with photometry obtained from deep Subaru images (in the B, V , Rc, Ic, and z' bands) and the Bayesian Photometric Redshift code (BPZ). For the host galaxies of SNe that were discovered in the WFC3 parallel fields, we also added galaxy photometry in the F125W and F160W bands. Some host galaxies were previously imaged by the Sloan Digital Sky Survey (SDSS; York et al. 2000), allowing us to include photometry in the u', g, r', i', and z' bands as well.

each field. Each category will have a distinct detection efficiency as a function of redshift.

The date of maximum light can occur up to 40 days before and 20 days after the duration of the survey. These values were chosen according to the approximate time when the SNe Ia in our sample reached their peak, relative to the survey times in the fields where they were discovered, based on preliminary light-curve fits. Accordingly, the visibility time of our survey is defined as the sum of the times each parallel field in each cluster was monitored (i.e., the time between the first and last epoch of that field), with the addition of 40 days before and 20 days after the observation period, in order to account for the SNe Ia in our sample that were caught either in decline or on the rise.

6.3 Results

We reported a sample of 27 SNe discovered in the parallel fields. Of these SNe, $\sim$13 were classified as SN Ia candidates, including four SN Ia candidates at redshifts $z>1.2$. We measured volumetric SN Ia rates to redshift 1.8 and add the first upper limit on the SN Ia rate in the range $1.8<z<2.4$. The results were consistent with the rates measured by the HST/GOODS and Subaru Deep Field SN surveys.

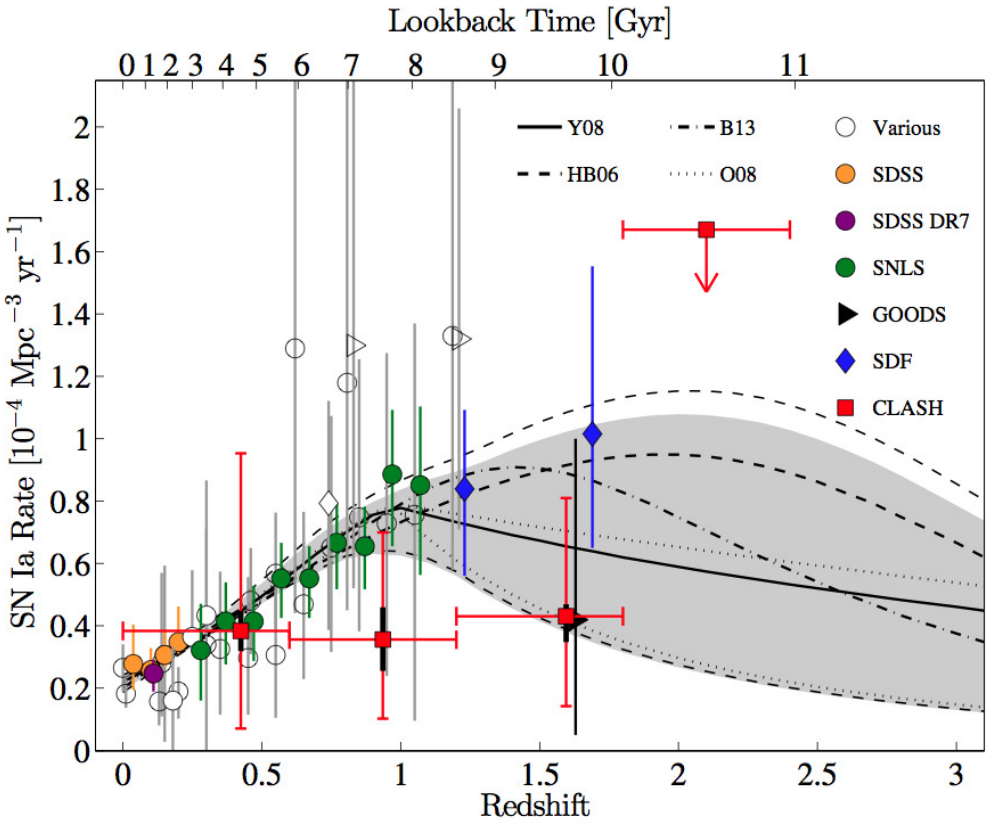

Figure 6.3 SN Ia rates from CLASH (filled, red squares) compared to rates from the literature and best-fitting SN Ia rate evolutions derived by convolving a power-law DTD with different SFHs. Circles denote data from surveys with measurements out to $z \approx 1$ from Cappellaro et al. 1999, Hardin et al. 2000, Pain et al. 2002, Tonry et al. 2003, Blanc et al. 2004, Botticella et al. 2008, Horesh et al. 2008, Rodney & Tonry 2010, Li et al. 2011, Barbary et al. 2012 & Melinder et al. 2012. Filled circles denote the most accurate and precise measurements at $z < 1$ and are from the SDSS Stripe 82 survey (Dilday et al. 2010, orange), SNLS (Perrett et al. 2012), and SDSS DR7 (Graur & Maoz 2013, purple). The GOODS rates from Dahlen et al. 2008 are shown as downturned triangles and the SDF rates from Graur et al. 2011 are shown as diamonds. The z>1.5 rates from these two surveys are colored in black and blue, respectively. The thick curves are convolutions of several SFHs (dashed, Hopkins & Beacom 2006; solid, Yuksel et al. 2008; dotted, Oda et al. 2008; dot-dashed, Behroozi et al. 2012) with the best-fitting power-law DTDs. The shaded area is the confidence region resulting from the combined 68% statistical uncertainties in the values of the power-law index fit with the above SFHs. The thin dashed lines indicate the 68% statistical uncertainty region obtained without the new CLASH measurements. All vertical error bars are sums of the statistical and systematic uncertainties. The CLASH vertical error bars are composed of the systematic uncertainty, shown as black thick lines, and the statistical uncertainty, shown as red thin lines. The horizontal error bars delineate the CLASH redshift bins. The Perrett et al. 2012 and z>1.5 Dahlen et al. 2008 SN Ia rates have been shifted by $\Delta z = +0.02$ to disentangle them from other results.

7

Conclussions

In this section, the main results obtained during this PhD thesis are listed and discussed. Before entering into the details, it is worth stressing that the work described in this manuscript leaves behind two legacy datasets which, might lead to an ongoing (or incoming) scientific exploitation. By itself, the participation in these two cosmological surveys has provided a good learning about the fundamental problems and challenges when deriving accurate photometric redshift estimations. Likewise, these PhD thesis yields several new analytical tools which will surely be applied to the (incoming) new generation of photometric surveys.

Since very different cosmological scenarios (such as field galaxies, galaxy clusters, supernovae or primordial high-z galaxies) were faced, the relevance and feasibility of nowadays photometric redshift surveys, to explore and attain the open questions in modern cosmology, was clearly manifested. Likewise, during this thesis there were identified several potential limitations for photometric surveys when retrieving accurate and unbiased pictures of the Universe. In particular, as discussed in the following section, it was identified a way to self-calibrate medium to narrow-band survey using emission line galaxies. This fact will make feasible to consistently calibrate the new generation of full-sky narrow-band photometric redshift surveys like JPAS.

7.1 ALHAMBRA survey

- Probably, a third of the time required to perform accurate PSF-corrected photometry was invested on the careful selection of point sources on each individual image. By means of the generation of star-mosaics containing hundredths of well-isolated and good photometric stars, it was possible to assure the fidelity of the PSF-models and, therefore, retrieve an accurate seeing homogenization across filters. Although this step yielded robust photometric measurements, this semi-manual procedure took too long, being impractical for new generation of full-sky photometric surveys. A fully automatize procedure to detect, select good stars and build PSF-models needs to be implemented.

- The software we relied on to perform PSF-corrected photometry (`ColorPro`), had to be updated

during the time of this thesis, to meet the observational conditions for the ALHAMBRA-survey. In particular, since the software was originally developed to cope with space-based data (from *HST*) which have particularly low background signal, the photometric error treatment was untreatable for ground-based images. It was necessary to develop and proceed with an empirical treatment of the photometric uncertainties. Meanwhile, `ColorPro` was designed to assume that the detection image had to have the best seeing condition for PSF-correction purposes. Since in ALHAMBRA it was frequent to find individual bands that had a better seeing that the synthetic F814W detection image, it was necessary to update `ColorPro` and make it able to deal with that reversal problem.

- It was developed a new approach to generate broad-band images as a combination of individual bands using transformation equations derived from galaxy colors. This served for ALHAMBRA to create synthetic HST/ACS F814W detection images, and so define a constant and homogeneous window for all the ALHAMBRA fields. These images served not only to improve the quality of the photometric detections (with enhanced signal-to-noise) but also to carry out systematic comparisons with the COSMOS-survey. Considering the robustness of this technique, future generation of photometric may take advantage of this initiative an generate their own broad-band images and so derive systematic comparison with other survey datasets. This procedure might be easily implemented on other photometric surveys pipelines.

- To assure the accuracy of `ColorPro` retrieving precise photometry across images with varied PSF, it was necessary to design a set of simulations. We degraded ACS/HST images (from COSMOS) to the typical condition of ALHAMBRA (in terms of PSF and background noise) and run `ColorPro` on it expecting retrieve null colors (equal magnitudes) for a sample of galaxies when observed under different PSFs. We found that the simulated colors showed a dispersion of $\sigma\sim0.03$ for sources brighter than magnitude F814W=23.0 and a $\sigma<0.05$ for sources with magnitudes in between 23<F814W<24, with negligible biases. We also used the simulations to study the expected photometric completeness for the ALHAMBRA fields. So, we derived the statistical probability of detecting a sample of faint galaxies when observed through the typical ALHAMBRA observational conditions. These testing simulations, which had never been reported before by any user of `ColorPro`, served to convince ourselves about the virtue of `ColorPro` retrieving accurate PSF-corrected photometry, making the software an excellent choice for multi-wavelength photometric analysis.

- Although one of the criteria imposed when selecting the ALHAMBRA fields was the presence of none bright sources, since the ALHAMBRA observations reached a total exposure time of ∼700hrs, several faint stars appeared and unfortunately saturated the final science images. In order to improve both the source detection efficiency and the background subtraction, it was developed a new approach to mask out saturated star, stellar spikes, ghosts or damaged areas. Basically, this method detected and combined all compromised pixels in both image sizes, and replaced them with a similar background noise to avoid fake detections on the edges of areas with no signal. Therefore, this approach served to improved the scientific quality of the ALHAMBRA

images, and might be easily implemented on other photometric surveys pipelines.

- To decontaminate extragalactic sources from field stars, it was developed a statistical classification method where every detection was classified in terms of the probability of being a star or a galaxy, given its apparent geometry, F814W magnitude, optical F489W-F814W and NIR J-Ks colors. We tested the goodness of our statistical classification by comparing the density of finding stars against that predicted by the `Trilegal` software (Girardi 2002, 2005). We found a very good agreement between both samples. When this statistical criteria is applied to the complete catalogue, we observed that stars dominate the sample down to a magnitude F814W<19. For fainter magnitudes, the fraction of stars from galaxies rapidly declines with a contribution of $\sim$1% for magnitudes F814W=22.5. We retrieve an averaged stellar density in the galactic halo of $\sim$7000 stars per deg^2 ($\sim$450 stars per CCD) for sources brighter than F814W=22.5. This procedure might be easily implemented on other photometric surveys pipelines.

- Quite a few time was spent dealing with the photometric zeropoint calibration issue. We refined photometric zeropoints derived using standard stellar-based calibration techniques, by comparing the observed colors of galaxies (for which spectroscopic redshifts were available) with those expected by the BPZ library of templates. We found that the so-derived corrections improved not only improved the photometric redshifts accuracy but also reduced the fraction of catastrophic outliers. Considering the possibility of a systematic effect during the data reduction, we represented globally the zeropoint corrections for the all the individual images as a function of the AIRMASS, the Stellar Symmetry, the FWHM Scatter, differences between PSFs-models and stars, magnitude ranges, redshift ranges or aperture sizes. No clear correlations were observed with typical fluctuations smaller than 3%.

  These analysis served to conclude that the zeropoint offsets did not depend on the photometric treatment and represented real differences between the calibration obtained from traditional color transformations based on stars and the average colors of galaxies as defined by the BPZ template set, calibrated with HST observations. Therefore, emphasizing the importance of undertake these kind of calibration steps on every (extragalactic) photometric redshift survey.

- During this thesis, it was developed a new methodology capable to calibrate the photometric zeropoint estimations based on our own photometric redshift estimations, for all those fields without spectroscopic coverage. Essentially, we realized that the photometric redshifts obtained for emission line galaxies were quite robust to changes in the zeropoint calibration and therefore could be treated as spectroscopic for calibration purposes, obtaining an automatic and self-contained zeropoint correction for all our fields. In other words, this methodology not only successfully improved the photometric redshifts accuracy (almost up to the level provided by the spectroscopic sample), but also dramatically reduced the fraction of catastrophic outliers, avoiding serious problem of inhomogeneity among fields. This method solved a potential limitation for photometric redshift surveys, since a spectroscopic sample of redshift galaxies is always needed for both calibration and verification.

- Since the redshift probability distribution function p(z) usually becomes multimodal and com-

pletely asymmetric for most faint galaxies (which represents the largest fraction of galaxies in ALHAMBRA), we made use of the complete information yielded by the P (z, T|C). We ran BPZ on the photometric catalogue used by Ilbert et al. (2009) to derive the $P(z)$ for the COSMOS field and so consistently compare its redshift probability distribution with ALHAMBRA. When comparing the $P(z)$ derived from ALHAMBRA-04 and that from COSMOS, we observed that both distributions consistently reproduced a double peak at redshifts z$\sim$0.3 and z$\sim$0.9. However, the global P(z) derived averaging the seven ALHAMBRA fields showed a mean redshift $\langle z\rangle$=0.56 for F814W<22.5 and $\langle z\rangle$ = 0.85 for F814W<25.5, indicates that the COSMOS field has a rather peculiar redshift distribution which mimics a significant redshift density evolution effect. Therefore, we found out that the well-known bimodal distribution in the COSMOS field was not systematically observed along the other fields, emphasizing the usefulness of the ALHAMBRA data disentangling cosmic variance and, so the relevance of this dataset on galaxy evolution studies.

- We compiled a sample of $\sim$7200 galaxies with secure spectroscopic redshifts, to both calibrate our photometric zero points and to estimate the precision for our photometric redshift estimations. Based on this spectroscopic sample, our we reached a precision of $\delta_z/(1+z_s)$=1% for galaxies brighter than I<22.5 and $\delta_z/(1+z_s)$=1.4% for 22.5<F814W<24.5. These results were remarkable since they clearly surpassed the theoretical expectations for ALHAMBRA filter system which was estimated to be $\delta_z/(1+z_s)$=1.5%. In particular, it is worth mentioning that precisions of $\delta_z/(1+z_s)<$ 0.5 % were reached for the brightest and more secure ($Odds$ >0.9) galaxies, probing the potential of medium/narrow-band photometric surveys to attain cosmological studies which demand extremely precise photometric redshift estimations.

- We discovered a new methodology to identify potential AGN candidates using BPZ. When plotting the Odds distribution as a function of F814W magnitude for all galaxies, we found an unexpected locus at magnitudes in between 18<F814W<23 and 0.0<Odds<0.1. When plotting the logarithmic χ^2 distribution over the former $Odds$ vs magnitude diagram, it revealed those detections to have the highest χ^2 values and so the worst SED-fitting results to the galaxy templates. After purging the sample for photometrically flagged detections, remaining galaxies within that locus were classified in two different groups: 1. unresolved stellar pairs with clearly asymmetric morphologies (spite of its photometric colors) and 2. very strong broad emission-line objects, AGNs or variable sources. All galaxy types not included in the BPZ library of templates.

7.2 CLASH survey

7.2.1 Massive Galaxy Clusters

- This thesis served to disentangle a new and unexpected problem when deriving photometric redshifts in massive galaxy clusters. An additional background signal from the Brightest Cluster Galaxies (BCGs) and the Intra-Cluster-Light (ICL), disrupted the galaxy colors as much as to completely deteriorate the photometric redshift estimations. This background signal was typically inhomogeneous (related to the cluster geometry), position-dependent (varying across

the cluster), wavelength-dependent (becoming stronger for the reddest filters) and showing both small- and large-scale structure, and so making its treatment a real challenge. Therefore, since this nuisance signal was closely tied to the properties of each cluster, an one-by-one analysis had to be done.

- The quantification of the photometric bias induced by this effect, was carried out using the galaxies from the HST/UDF. By observing these galaxies through different background conditions, it turned out possible to quantify how much their magnitudes had varied. In particular, two scenarios were recreated. On the one hand, the $UDF/F775W$ image was background-scaled to the level of the CLASH observations using Poisson signal, to show the impact of observing the galaxies in a much shallower (noisier) image. On the other hand, the $UDF/775W$ image was combined with the CLASH/F160W image (from one of the CLASH clusters), to quantify the impact of observing the galaxies through a massive galaxy cluster. As a result, when comparing the input and the output magnitudes, it was found that whereas for the first scenario a well-behaved symmetric distribution (progressively noisier as sources got fainter) was retrieved, an unexpected asymmetric distribution with a photometric scatter as large as two magnitude for galaxies as faint as 26AB magnitudes, was observed for the second scenario. The latter distorting effect could not be explained by means of a gaussian signal and, therefore it was not included in any previous simulation.

- It was proved that with a more aggressive background subtraction, the photometric bias induced by the ICL might be partially mitigated. To do so, `SExtractor` was utilized since it could automatically compute (and subtract) background-maps derived from the images themselves. To figure out the importance of this process, two opposed (a standard "smoothy" & a discouraged "aggressive") background-configuration files were employed. `SExtractor` was run on the aforementioned combined (UDF+$CLASH$) image. After comparing the resulting photometric colors (m^{UDF} - $m^{UDF+CLASH}$) for both configurations, it was found that the "aggressive" background parametrization indeed improved the photometry, retrieving colors closer that the originals (m^{UDF}).

- It was demonstrated that photometric redshifts could be used to calibrate the CLASH photometry, since they are very sensitive algorithms to the quality of the inputed data and mostly exhaustive representing the colors of the galaxies in the Universe. Based on that assumption, the possibility of using photometric redshifts as tracers to identify which background configuration would properly retrieve the original galaxy colors, was explored.

- To overcome the problem of an insufficient spectroscopic redshift sample for photometric redshift testing, it was developed and implemented a new approach in which a synthetic sample of galaxies was created. Based on the UDF photometric catalogue (Coe et al. 2006), and the new BPZ library of galaxy templates, it was extended the UDF from its 4 original bands to the 16 constituting the CLASH filter system. We called it the UDF-16. The injection of this synthetic dataset (composed by ∼1.000 regular galaxies with known redshifts, spectral-types and (input)

magnitudes) within the clusters, served to emulate the same sort of photometric biases expected for the real galaxies.

- A set of simulations were designed spanning ∼500 different background configurations. Per each cluster, it was first generated its synthetic CLASH+UDF16 dataset over which perform the photometric measurements and the photometric redshift estimations. To identify the most convenient background parametrization for each cluster, a figure-of-merit was defined taking into account not only the retrieved photometric redshift accuracy (according to the UDF16 spectroscopic sample), but also including the fraction of extracted sources, the mean photometric zeropoint offsets and the mean photometric zeropoint scatter.

- It was discovered that the detectability of faint galaxies was also strongly background-dependent. This fact reemphasized the importance of undertake proper background subtractions, not only for very high-z (faint) galaxy identifications within the innermost part of the clusters, but also to avoid biased analysis on the (incoming) luminosity and mass function studies.

- CLASH/HST PSF-models were built for each image in order to perform PSF-corrected photometry. Around ∼200 potential stars were visually selected from the 25 clusters. Each star was double-checked to assure either its photometric quality, to be observed in all the 16 filters and not having close neighbors. The remaining sample (∼70 stars) was combined and normalized to generate the models. The PSF stability across images was also explored, using the light-curve of growth for two wisely selected stars. The expected photometric bias turned out to be smaller than $<<1\%$. Likewise, the expected photometric bias if PSF-corrections may not be considered was also quantified, indicating that differences in flux as large as 15% might affect all detections with sizes smaller than 20 pixels.

- It was confirmed that the photometric uncertainties reported by `SExtractor` were highly underestimating the real photometric uncertainties taking place in the CLASH images. To cope with this problem, a more realistic approach was adopted and implemented, where the empirical dependence between the background signal and the photometric apertures was systematically estimated per every image. The results confirmed that CLASH images were only accurately described by a Poisson distribution on small scales, indicating the presence of large-scale correlations among pixels.

- To verify the robustness of the new empirically derived photometric uncertainties, the information provided by the UDF16 galaxies was used again to figured out either the reported uncertainties were now proportional to the real variations in the magnitudes (δ_m) due to the noisy background. Surprisingly, it was noticed that `SExtractor` was enormously underestimating the photometric uncertainties for the brightest sources. After exploring the source of this effect, it was found out that `SExtractor` was overestimating the photometric apertures for the brightest galaxies. These artificially enlarged apertures were leading to an excessed integrated signal which artificially biased the photometric uncertainties. Once this new bias was calculated per each cluster and image and included in the analysis, the new photometric uncertainties showed a remarkable agreement with the expected scatter for the UDF16 magnitudes.

- Even though background-subtracted images served to neatly improve the accuracy for photometric redshifts, since most light from the brightest galaxies had been removed as background signal, the resulting magnitudes did not represented optimal fluxes for the estimation of physical parameters for the galaxies. Therefore, it was explored the possibility of performing an alternative photometry based on the background-subtracted detection images (to preserve the number of detections) capable to retrieve similar magnitudes to those that might be obtained on a non background-subtracted image. To do so, the `SExtractor` $PHOT\_AUTOPARAMS$ (which regulates the definition of an elliptical aperture around every detection) was employed to figure out if there may exist an optimal photometric aperture per each cluster. Finally, it was found that indeed there exist an optimal aperture ($k = 4$) which minimized the photometric differences between images. The so-derived photometric apertures were used to include an additional photometry the catalogues.

- To assure the background subtraction process may not affect the estimation of ISOphotal colors for bright and extended galaxies, we studied the radial light profile variations for several cluster members, as much in the original as in the corresponding background-free images. Fortunately, it was confirmed that while the background subtraction was clearly removing a large fraction of light from galaxy wings, the innermost regions remained almost unaffected. This result assured the feasibility of measuring accurate ISOphotal colors on background-free detection images.

- Accurate upper limits were computed per every image, using the empirically estimated photometric uncertainties. It was demonstrated that by using the photometric uncertainties reported by `SExtractor`, the photometric upper limits became strongly overestimated. This bias had a direct impact on photometric redshift estimations forcing BPZ to artificially favor higher redshift solutions, and so making the galaxy redshift distributions $n(z)$ to show an "false" peak at z>>2.5, directly related with the Balmer-to-Lyman break degeneracy. When the empirical upper limits were used, the artificial peak vanishes.

- Multi-wavelength PSF-corrected photometric catalogues were derived for all the 25 clusters using the `ColorPro2.0` software. These catalogues included all the aforementioned improvements; i.e., an optimized background subtraction, empirical PSF-models, recomputed photometric uncertainties and realistic upper limits. Then, BPZ2.0 was run on all the before mentioned catalogues to derived their photometric redshift estimations.

- When compared to a real sample of ∼160 spectroscopic redshift galaxies, the so-derived photometric redshifts showed an accuracy better than 3% for the complete sample, 2.5% accuracy was retrieved for ∼80% of the galaxies and 2.0% accuracy for ∼60%. The results were in good agreement with those expected from simulations, considering that the first three UVIS/WFC3 filters were not included in the analysis. In other words, photometric redshifts were finally computed using 13 instead 16 filters, due to the scarce signal-to-noise from those filters.

- With the so-enhanced photometric redshifts, the Odds (BPZ) parameter was now capable to retrieve secure and precise photometric redshift samples. This remarkable fact made possible for

CLASH to retrieve improved mass model estimations than those obtained with the preliminary versions of the photometric redshifts catalogues.

7.2.2 High-z Galaxies

- The discovery of the first z>9 galaxy in the Universe, served not only to confirm the potentiality of using massive galaxy clusters to explore the re-ionization era, but also to develop an optimize set of analytical tools for the CLASH fields.
- All the tailored photometric measurements performed on the IRAC/Spitzer data, served not only to assure the z∼10 nature of MACS1149-JD, but to explore its older stellar populations content. This fact made possible to asses, with 95% confidence level, that the galaxy was formed less than 200 million years after the Big Bang (z ∼14.0).
- The strong agreement between BPZ and LePhare photometric redshift codes, served to downsize the possibility for MACS1149-JD to be an interloper at redshift z<2.
- When the small sky area surveyed in this discovery is taken into account, it leads to the conclusion that faint galaxies might be abundant at such a cosmic age, and so suggesting that they may be the dominant source for the early re-ionization of the intergalactic medium.

7.2.3 SN Ia

- The CLASH SN Ia program represented a three-year long work where the analysis of every solid candidate was immediately explored in terms of its photometry and photometric redshift.
- Whenever the photometric redshift probability distribution function (P(z)) for the host galaxy was compatible with a SN type Ia, the viability of triggering a follow-up spectroscopy was immediately discussed. i.e., meaning that photometric redshift analysis were decisive in multiple occasions.
- For those SN host galaxies for which a spectroscopy follow-up was triggered, it was systematically confirmed that photometric redshift estimations were in perfect agreement within the error intervals. This very fact proves once again the usefulness of relying on photometric redshift estimations for target selections.
- Although several host galaxies were observed since in the HST/ACS parallel fields as in the wide-field SUBARU images, the missing of an appropriate photometric pipeline made, in most cases, the combination of all that information often impractical and inaccurate.

7.3 Personal Conclussions.

Personally, I would say that the most important conclusion from this thesis might be the following. In spite of this seven-year long work (with uncountable weekends working at home and an interesting amount of deadlines) to have weaken my strength, today I feel the same enthusiasm for learning

cosmology and astrophysics that once brought me to here. At this early point of my personal carrier, while typing these very words, I have the impression that willing to stay on the same road might indicate, in somehow, that I am in my right track.

8

Future Work

In this section, the main lines of research to be approached during the next years are briefly outlined.

8.1 The ALHAMBRA survey.

- After the production of the ALHAMBRA photometric redshift catalogue, the next step forward will be the derivation of the Mass and Luminosity Functions. Since the ALHAMBRA sample covers seven, well-separated regions of the sky, it represents an ideal dataset to the study and quantify the impact of cosmic variance in galaxy evolution studies.

- The ALHAMBRA-survey was designed to observe 4 squared degrees in the sky. However, as discussed in this work, only 3 squared degrees were available at the time of this thesis. As new observational campaigns have already been scheduled, in the near future a new dataset of ∼370 images will be available for reduction and process. These new fields will represent (approximately) ∼160.000 more galaxies whose photometric properties and redshift have to be estimated.

- Since the ALHAMBRA observations were spread over days, weeks, months and years, there is already an ongoing-work initiative aiming at studying the variability of all the sources observed in the ALHAMBRA fields. This valuable new catalogue will unveil hundredths of variable stars in the galactic halo, along with variable QSO or AGN galaxies.

- Finally, another on-going project we are already work in is the compilation of a Stellar catalogue in the Galactic Halo. To do so, the PSF-corrected photometry and the Star/Galaxy Classification criteria discussed in this manuscript will be used. At the time, there is a sample of $\sim$ 20.000 sources classified as secure "Stellar Objects".

8.2 The CLASH survey.

The first step in CLASH was the design of a new photometric pipeline capable to deal with the extremely complicated scenario described during this thesis. However, once the photometry and the photometric redshifts catalogues for the 25 clusters, are generated and validated, it is time to start exploding its potential science. Among other, there is a list of interesting goal which might be approached:

- Based on the analysis of the individual redshift distribution function for each galaxy P(Z), it might be possible to derive secure samples of background galaxies. i.e., galaxies behind the galaxy clusters and so in no physical contact with them. Since these massive clusters are capable to highly magnify faint galaxies in the source plane, a derivation of the faint-end of the luminosity and mass function will be faced. Having 24 lines-of-sight will provide an interesting estimation of the importance of the cosmic variance.

- Apart from the "standard" CLASH dataset, the Hubble Space Telescope Frontier Fields (HSTFF) will provide a new set of much deeper observations. With the methodology developed in this work, a precise treatment of those images should provide an interesting "step-forward" in the estimation of the faint-end luminosity function.

- As expected, the HSTFF program will bring many new very high-z candidates and (hopefully) the discovery of some high-z SNIa. These candidates will have to be (promptly) analyzed. An on-going work in these two lines of research is expected.

8.3 The JPAS survey.

- Most of the improvements and implementations developed during this thesis, when deriving accurate photometry and photometric redshifts for ALHAMBRA and CLASH, will be immediately applied to the next generation of full-sky narrow-band photometric redshift surveys, like JPAS. Therefore, one of the incoming "future" work will be to adapt all these analytical tools to the format of the new datasets.

- One of the most crucial steps for JPAS will be to retrieve the so-expected extremely accurate photometric redshifts, if the Baryonic Acoustic Oscillations (BAO) excess signal is intended to be detected at the significance posed by the simulations. This goal would be achieve only if a robust multi-band photometry is performed and if precise absolute and relative photometric zero-point calibrations are properly done. While the former point will be marked by the success of correcting the PSF variability across filters in a quick and smart way, the latter will depend on how well the internal photometric calibration is reached using emission-line galaxies. These two task will surely represent major efforts in the short-term.

A

Appendix Chapter 1

A.1 The Equations of State

The table A.1 summarizes the different equation of states and its dependencies with a.

A.2 The Deceleration Parameter.

A.3 Cosmic Evolution of the Energy Density.

A.4 Cosmological Parameters.

The cosmological parameters serve to 1. describe the global dynamics of the Universe (such as its expansion rate and curvature), 2. explain how the matter content of the Universe is built up from its constituents (baryons, photons, neutrinos, dark matter and dark energy) and 3. to describe the physical state of the Universe as a function of cosmic time. Therefore, the cosmological parameters allow us to track the history of the Universe back in time, at least until an epoch where interactions allow interchanges between the densities of the different species. A short list with the most relevant cosmological parameters (values provided by the Planck Collaboration (2013)), used to describe the

Table A.1 The different equations of state...

ω	$\rho(a)$	Kind of Energy Density
+1	$\propto a^{-6}$	Scalar fields w/o mass, stationary state
+1/3	$\propto a^{-4}$	Relativistic Matter and radiation
0	$\propto a^{-3}$	Non-relativistic matter
-1/3	$\propto a^{-2}$	Energy of curvature, cosmic strings
-2/3	$\propto a^{-1}$	Walls
-1/3> ω >-1	$\propto a^{-3(1+\omega)}$	Quintaessence
-1	$\propto a^{0}$	Cosmological Constant or Energy of emptiness
<-1	$\propto a^{n}$	Ghost Energy

Table A.2 Possible scenarios for the Deceleration parameter

ϵ	Ω	$\omega = 1/3$	$\omega = 0$	ω = -1/3	ω = -2/3	ω = -1
+1	>1	q > 1	q > 1/2	q = 0	q < -1/2	q < -1
0	1	q = 1	q = 1/2	q = 0	q = -1/2	q = -1
-1	<1	q < 1	q < 1/2	q = 0	q > -1/2	q > -1

Table A.3 Energy density parameters as a function of Cosmic Time:

z	w	Dominant Ω
$z >>$3000	ϵ=0, w=1/3	Ω_r
0.33 << z <3000	ϵ=0, w= 0	Ω_m
0< z <1	ϵ=0, w=0 & w=1	Ω_r & Ω_Λ
-1< z <0	ϵ=0, w=-1	Ω_Λ

ΛCDM model, are presented in the following table A.4:

Table A.4 Cosmological Parameter Values for the ΛCDM model:

Parameter	Value	Definition
$\Omega_b h^2$	0.022±0.001	Baryon Density Today
$\Omega_c h^2$	0.119±0.002	Cold Dark Matter Density Today
$100\Omega_K$	-0.10±0.60	Curvature Parameter Today
Ω_m	0.308±0.010	Matter Density
Ω_Λ	0.692±0.010	Dark Energy Density
ω	-1.13±0.25	Dark Energy Equation State
H_0	67.80±0.77	Current expansion rate ($kms^{-1}Mpc^{-1}$)
T_0	2.7255±0.0006	Photon Temperature Today (K)
n_s	0.961±0.005	Scalar spectrum power-law index
t_o	13.798±0.037	Age of the Universe today (Gyr)
σ_8	0.826±0.012	RMS matter fluctuations ($8h^{-1}$Mpc)
τ	0.092±0.013	Thomson Scatt. Optical Depth (reionization)

B

Appendix Chapter 2

B.1 Cosmological Surveys in the last decades.

Here we list the main cosmological surveys undertaken in the last decades, classified in three main groups according to the technique utilized to infer the redshift.

1. **Photometric Broad-band surveys**:

   - 2MASS, http://pegasus.phast.umass.edu/
   - SDSS, http://www.sdss.org/
   - UKIDSS(LAS), http://www.ukidss.org/
   - CFHTLS (wide shallow), http://www.cfht.hawaii.edu/Science/CFHLS/
   - CFHTLS (wide synoptic), http://www.cfht.hawaii.edu/Science/CFHLS/
   - UKIDSS (DXS), http://www.ukidss.org/
   - Deep Lens Survey, http://www.dls.bell.labs.com/
   - NOAO Deep WideField Survey, http://www.noao.edu/noao/noaodeep/
   - CFHT12k/ESO (VIRMOS), http://www.astrspmrs.fr/virmos/
   - CFHTLS (deep synoptic), http://www.cfht.hawaii.edu/Science/CFHLS/
   - EIS, http://www.astro.caltech.edu/cosmos/
   - COSMOS, http://www.cosmos.astro.caltech.edu/
   - LCIRS, http://www.ociw.edu/lcirs/lcir.html
   - MUSYC, http://www.astro.yale.edu/MUSYC/
   - UKIDSS (UDS), http://www.ukidss.org/
   - MUNICS, http://www.capella.usm.uni-muenchen.de/ drory/munics/munics.html
   - GEMS (COMBO-17), http://www.mpia.de/GEMS/gems.htm
   - SUBARU Deep Survey, http://www.subarutelescope.org/Science/SubaruProject/SDS/

- EIS Deep, http://www.eso.org/science/eis/
- GOODS, http://www.stsci.edu/science/goods/
- FIRES, http://www.strw.leidenuniv.nl/ fires/
- UDF, http://www.stsci.edu/hst/udf
- HDF, http://www.stsci.edu/ftp/science/hdf/hdf.html
- HDFS, http://www.stsci.edu/ftp/science/hdfsouth/hdfs.html
- **CLASH, http://www.stsci.edu/ postman/CLASH/Home.html**
- UltraVISTA, http://home.strw.leidenuniv.nl/ ultravista/

2. **Photometric Medium-band to Narrow-band surveys**:

- JPAS, http://j-pas.org
- **ALHAMBRA, http://alhambrasurvey.com**
- SHARDS, http://guaix.fis.ucm.es/ pgperez/SHARDS/
- MUSYC, http://www.astro.yale.edu/MUSYC/
- COMBO17, http://www.mpiahd.mpg.de/COMBO/combo_index.html
- CADIS, http://www.mpiahd.mpg.de/GALAXIES/CADIS/welcome.html

3. **Spectroscopic Redshift Surveys**:

- LBG-z3, http://www.ctio.noao.edu/noao/content/Luminous-Z3-Lyman-Break-Galaxies-Deep-and-Wide-Field-Surveys
- VVDS-deep, http://cesam.oamp.fr/vvdsproject/vvds.htm
- CNOC2, http://www.astro.utoronto.ca/ cnoc/cnoc2.html
- zCOSMOS, http://www.exp-astro.phys.ethz.ch/zCOSMOS/index.html
- Autofib, http://www.ucolick.org/ simard/phd/root/node12.html
- H-AAO, http://www.aao.gov.au/ukst/halpha.html
- AGES, http://www.astro.cardiff.ac.uk/research/astro/egalactic/surveys/?page=AGES
- VVDS-wide, http://cesam.oamp.fr/vvds/
- MGC, http://www.eso.org/ jliske/mgc/plots/survey.html
- GAMA, http://www.gama-survey.org
- 2SLAQ-lrg, http://www.2slaq.info
- SDSS-s82, http://www.sdss.org/legacy/stripe82.html
- LCRS, http://www.astro.ucla.edu/ wright/lcrs.html
- WiggleZ, http://wigglez.swin.edu.au/site/
- SSRS2, http://www.sao.ru/cats/doc/SSRS2.html

Table B.1 Photometric Redshift Surveys. For narrow/medium -band photometric survey (*), the photometric redshift accuracy is strongly dependent on the signal-to-noise. For the brightest sources, both surveys reach a performance similar to COSMOS's or MUSYC's ($\delta_z/(1+z) < 0.01$).

survey	Reference	Bands	$\delta_z/(1+z)$
HDF	Sawicki (1997)	4	0.080
SDSS/DR6	Csabai (2003)	5	0.035
SWIRE	Rowan-Robinson (2008)	5	0.035
HUDF	Coe (2006)	6	0.040
HDF	Fernández-Soto (1999)	7	0.060
CFHTLS	Ilbert (2006)	9	0.030
GOODS	Dahlen (2010)	12	0.040
CLASH	Molino (2014, prep.)	16	0.025
COMBO-17*	Wolf (2008)	17	0.020
ALHAMBRA*	Molino (this work)	23	0.013
COSMOS	Ilbert (2009)	30	0.007
MUSYC	Cardamone (2010)	32	0.007
JPAS	Benítez (2009a, 2014 prep.)	59	0.003

- 6dFGS, http://www.aao.gov.au/6dFGS/
- CfA2, https://www.cfa.harvard.edu/ dfabricant/huchra/zcat/
- PSCz, http://wwwik.fzk.de/ katrin/liebenzell/ccd_data/hamilton/pscz.html
- 2MRS, https://www.cfa.harvard.edu/ dfabricant/huchra/2mass/
- SDSS-lrg, http://www.sdss.org/
- SDSS-mgs, http://www.sdss.org/
- 2dFGRS, http://www.mso.anu.edu.au/2dFGRS/
- VIRMOS, http://www.astrspmrs.fr/virmos/
- DEEP2, http://www.deep.berkeley.edu/
- CFRS, http://www.astro.utoronto.ca/ lily/CFRS/
- TKSurvey, http://www2.keck.hawaii.edu/science/tksurvey/
- Hawaii, http://www.ifa.hawaii.edu/ cowie/hhdf/acs.html
- GDDS, http://www.ociw.edu/lcirs/gdds.html
- K20, http://www.arcetri.astro.it/ k20/

B.2 Evolution of Photometric Redshift Surveys

B.3 Photometric Redshift Codes.

In this section, the main photometric photometric redshift codes are listed.

1. **TEMPLATE-FITTING METHODS**:

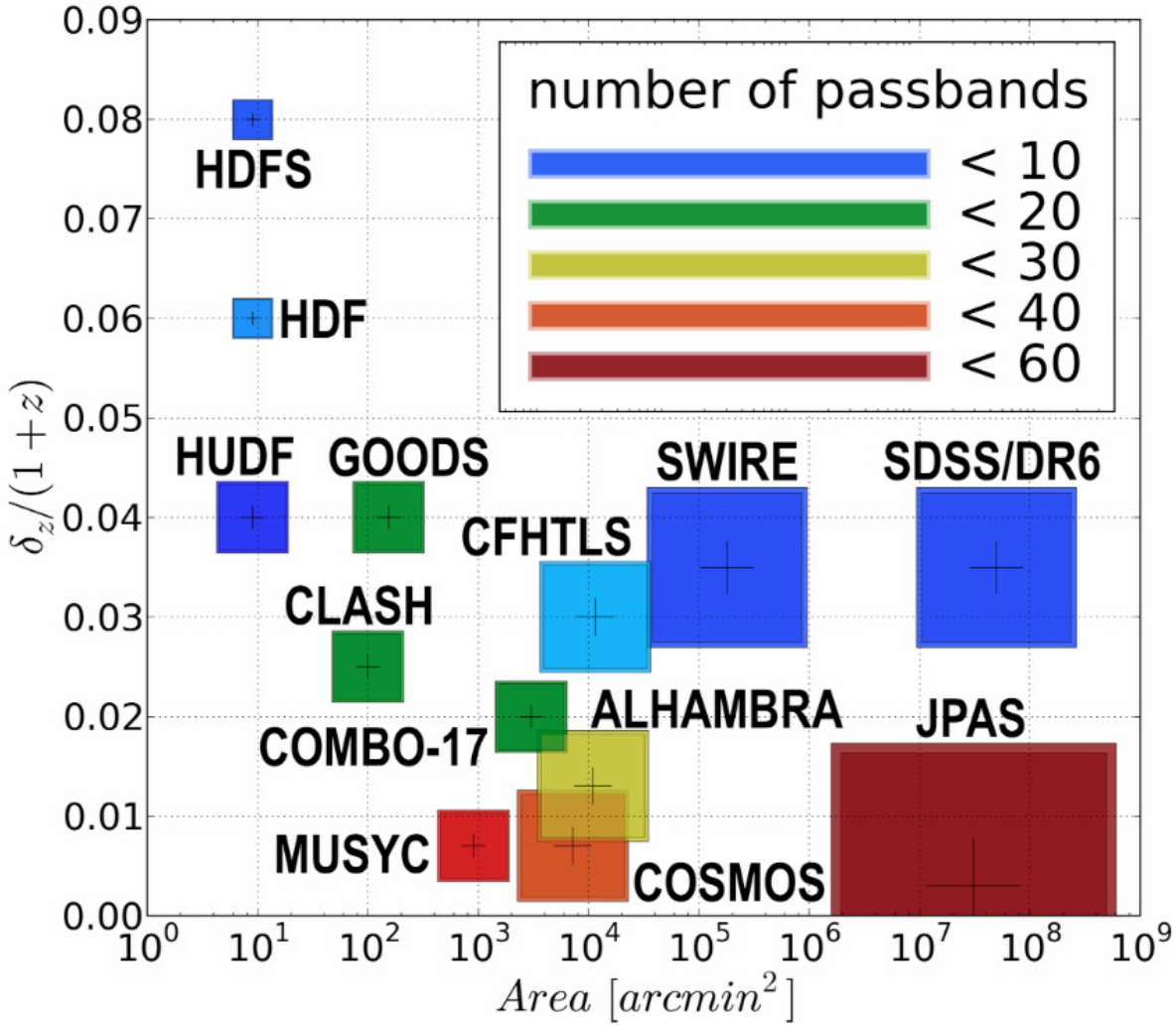

Figure B.1 Photometric redshift surveys comparison. The figure represents the photometric redshift accuracy versus the covered area for several surveys (see Table B.1). The number of photometric passbands is color-coded as described in the top-right panel. While the marker-size represents logarithmically the number of detections, the position of the internal plus sign indicates to its photometric redshift accuracy.

- BPZ (Benítez 2000)
- Hyperz (Bolzonella et al. 2000)
- Le Phare (Arnouts et al. 2002; Ilbert et al. 2006)
- IMPZ (Babbedge et al. 2004)
- ZEBRA (Feldmann et al. 2006)
- EAZY (Brammer et al. 2008)
- GAZELLE (Kotulla & Fritze 2009)
- GOODZ (Dahlen et al. 2010)
- LRT (Assef et al. 2008, 2010)

2. **EMPIRICAL METHODS**:

- Polynomial Regression (Connolly et al. 1995, Hsieh et al. 2005, Li et al. 2008, Wang et al. 2008a)
- Nearest Neighbor algorithms (Ball et al. 2008, Wang et al. 2010a, Wang et al. 2010b)
- Kernel Regression (Wang et al. 2007, Wang et al. 2008, Wolf 2009)
- Decision Tree (Carliles et al. 2010, Gerdes et al. 2010)
- Gaussian Processes (Bonfield et al. 2010, Way et al. 2006, Way et al. 2009, Way 2011)
- Mathematical Solution (Budavaári 2009)
- Artificial Neural Networks (Firth et al. 2003, Vanzella et al. 2004, Collister et al. 2004, Zhang et al. 2009, Abdalla et al. 2011)
- Support Vector Machines (Wadadekar 2005, Wang et al. 2008b)
- Weak Gated Experts (Laurino et al. 2011)
- Spectral Connectivity Analysis (Freeman et al. 2009)

C

Appendix Chapter 3

C.1 Photometric Redshift Catalogues description.

In this appendix we include the description of the photometric redshift catalogues content in more detail.

C.2 SExtractor configuration files

In this appendix we present an example of the SExtractor configuration used to derive the F814W detections.

C.3 Effective area for the ALHAMBRA survey fields.

Along with this, we also includes several tables containing statistical information concerning the observations. The definition of the effective area is provided in section 3.12.

Table C.1 The ALHAMBRA Photometric Redshift Catalogs Content. Part I

COLUMN	PARAMETER	DESCRIPTION
1	ID_ColorPro	Object ID Number
2	Field	ALHAMBRA field
3	Pointing	Pointing within the field
4	CCD	Detector within the pointing
5	RA	Right Ascension in decimal degrees [J2000]
6	DEC	Declination in decimal degrees [J2000]
7	XX	x pixel coordinate
8	YY	y pixel coordinate
9	AREA	Isophotal aperture area (pixels)
10	FWHM	Full width at half maximum (arcsec)
11	STELL	SExtractor 'stellarity' (1 = star; 0 = galaxy)
12	ELL	Ellipticity = 1 - B/A
13	a	Profile RMS along major axis (pixels)
14	b	Profile RMS along minor axis (pixels)
15	THETA	Position Angle (CCW/x)
16	RK	Kron apertures in units of A or B (pixels)
17	RF	Fraction-of-light radii (pixels)
18	S/N	Signal to Noise (SExt_FLUX_AUTO/SExt_FLUXERR_AUTO)
19	PhotoFlag	SExtractor Photometric Flag
20,21	F365W, dF365W	F365W total magnitude & uncertainty
22,23	F396W, dF396W	F396W total magnitude & uncertainty
24,25	F427W, dF427W	F427W total magnitude & uncertainty
26,27	F458W, dF458W	F458W total magnitude & uncertainty
28,29	F489W, dF489W	F489W total magnitude & uncertainty
30,31	F520W, dF520W	F520W total magnitude & uncertainty
32,33	F551W, dF551W	F551W total magnitude & uncertainty
34,35	F582W, dF582W	F582W total magnitude & uncertainty
36,37	F613W, dF613W	F613W total magnitude & uncertainty
38,39	F644W, dF644W	F644W total magnitude & uncertainty
40,41	F675W, dF675W	F675W total magnitude & uncertainty
42,43	F706W, dF706W	F706W total magnitude & uncertainty
44,45	F737W, dF737W	F737W total magnitude & uncertainty
46,47	F768W, dF768W	F768W total magnitude & uncertainty
48,49	F799W, dF799W	F799W total magnitude & uncertainty
50,51	F830W, dF830W	F830W total magnitude & uncertainty
52,53	F861W, dF861W	F861W total magnitude & uncertainty
54,55	F892W, dF892W	F892W total magnitude & uncertainty
56,57	F923W, dF923W	F923W total magnitude & uncertainty
58,59	F954W, dF954W	F954W total magnitude & uncertainty
60,61	J, dJ	NIR-J total magnitude & uncertainty
62,63	H, dH	NIR-H total magnitude & uncertainty
64,65	KS, dKS	NIR-KS total magnitude & uncertainty
66,67	F814W, dF814W	F814W total magnitude & uncertainty
68	F814W_3arcs	3arcsec Circular Aperture magnitude [AB]
69	dF814W_3arcs	3arcsec Circular Aperture magnitude uncertainty [AB]
70	F814W_3arcs_corr	Corrected 3arcsec Circular Aperture Magnitude [AB]
71	nfd	Number Filters Detected (out of 24)
72	xray	X-Ray Source [0:NO,1:YES] (2XMM;Watson et al. 2009)
73	PercW	Percentual Photometric Weight (on detection image).
74	Satur_Flag	Saturation-Flag [0:Good Detection, 1:Saturated Detection]
75	Stellar_Flag	STAR/GALAXY Discriminator [0:Galaxy,0.5:Unknown,1:Star]
76	DupliDet_Flag	Duplicated Detection Flag [0:Unique, 1:Duplicated]

Table C.2 Photometric Redshift Catalogs Content. Part II

COLUMN	PARAMETER	DESCRIPTION
77	zb	BPZ most likely redshift
78	zb_min	Lower limit (95p confidence)
79	zb_max	Upper limit (95p confidence)
80	tb	BPZ most likely spectral type
81	Odds	P(z) contained within zb +/- 2*0.01*(1+z)
82	z_ml	Maximum Likelihood most likely redshift
83	t_ml	Maximum Likelihood most likely spectral type
84	Chi2	Poorness of BPZ fit: observed vs. model fluxes
85	Stell_Mass	Stellar Mass (log10($M_{\odot}$))
86	M_ABS	Absolute Magnitude [AB] (B_JOHNSON)
87	MagPrior	Magnitude Used for the Prior (F814W)
88	irms_F365W	Percentual Weight on F365W 1/RMS image (within ISOphotal Area).
89	irms_F396W	Percentual Weight on F396W 1/RMS image (within ISOphotal Area).
90	irms_F427W	Percentual Weight on F427W 1/RMS image (within ISOphotal Area).
91	irms_F458W	Percentual Weight on F458W 1/RMS image (within ISOphotal Area).
92	irms_F489W	Percentual Weight on F489W 1/RMS image (within ISOphotal Area).
93	irms_F520W	Percentual Weight on F520W 1/RMS image (within ISOphotal Area).
94	irms_F551W	Percentual Weight on F551W 1/RMS image (within ISOphotal Area).
95	irms_F582W	Percentual Weight on F582W 1/RMS image (within ISOphotal Area).
96	irms_F613W	Percentual Weight on F613W 1/RMS image (within ISOphotal Area).
97	irms_F644W	Percentual Weight on F644W 1/RMS image (within ISOphotal Area).
98	irms_F675W	Percentual Weight on F675W 1/RMS image (within ISOphotal Area).
99	irms_F706W	Percentual Weight on F706W 1/RMS image (within ISOphotal Area).
100	irms_F737W	Percentual Weight on F737W 1/RMS image (within ISOphotal Area).
101	irms_F768W	Percentual Weight on F768W 1/RMS image (within ISOphotal Area).
102	irms_F799W	Percentual Weight on F799W 1/RMS image (within ISOphotal Area).
Ê 103	irms_F830W	Percentual Weight on F830W 1/RMS image (within ISOphotal Area).
104	irms_F861W	Percentual Weight on F861W 1/RMS image (within ISOphotal Area).
105	irms_F892W	Percentual Weight on F892W 1/RMS image (within ISOphotal Area).
106	irms_F923W	Percentual Weight on F923W 1/RMS image (within ISOphotal Area).
107	irms_F954W	Percentual Weight on F954W 1/RMS image (within ISOphotal Area).
108	irms_J	Percentual Weight on J 1/RMS image (within ISOphotal Area).
109	irms_H	Percentual Weight on H 1/RMS image (within ISOphotal Area).
110	irms_KS	Percentual Weight on KS 1/RMS image (within ISOphotal Area).
111	irms_F814W	Percentual Weight on F814W 1/RMS image (within ISOphotal Area).
112	irms_OPT_Flag	Optical-Quality-Flag. Number of Optical Filters with PercW < 0.8
113	irms_NIR_Flag	NIR-Quality-Flag. Number of NIR Filters with PercW < 0.8

Table C.3 Example of the typical SExtractor configuration used to derive the ALHAMBRA photometric catalogs. Asterisked parameters may vary among CCDs.

PARAMETER	SETTING	COMMENT
ANALYSIS_THRESH	1.3*	Limit for isophotal analysis σ
BACK_SIZE	256	Background mesh in pixels
BACK_FILTERSIZE	5	Background filter
BACKPHOTO_THICK	102	Thickness of the background LOCAL annulus
BACKPHOTO_TYPE	LOCAL	Photometry background subtraction type
CATALOG_NAME	STDOUT	Output to pipe instead of file
CATALOG_TYPE	ASCII	Output type
CLEAN	Y	Clean spurious detections
CLEAN_PARAM	1	Cleaning efficiency
CHECKIMAGE_TYPE	SEGMENTATION	Output Image Type
DETECT_MINAREA	8*	Minimum number of pixels above threshold
DEBLEND_MINCONT	0.0002	Minimum contrast parameter for deblending
DEBLEND_NTHRESH	64	Number of deblending sub-thresholds
DETECT_THRESH	1.35*	Detection Threshold in σ
DETECT_TYPE	CCD	Detector type
FILTER	Y	Use filtering
FILTER_NAME	tophat_3.0_3x3.conv	Filter for detection image
GAIN	57.68*	Gain is 1 for absolute RMS map
MAG_GAMMA	4.0	Gamma of emulsion
MAG_ZEROPOINT	0.*	Magnitude zero-point
MEMORY_PIXSTACK	2600000	Number of pixels in stack
MEMORY_BUFSIZE	4600	Number of lines in buffer
MEMORY_OBJSTACK	15000	Size of the buffer containing objects
MASK_TYPE	CORRECT	Correct flux for blended objects
PARAMETERS_NAME	ColorPro.param	Fields to be included in output catalog
PHOT_APERTURES	14.0	MAG_APER aperture diameter(s) in pixels
PHOT_AUTOPARAMS	2.5,3.5	MAG_AUTO parameters: <Kron_fact>,<min_radius>
PIXEL_SCALE	0.221	Size of pixel in arcseconds
SATUR_LEVEL	50000	Level of saturation
SEEING_FWHM	0.86*	Stellar FWHM in arcseconds
STARNNW_NAME	default.nnw	Neural-Network_Weight table filename
WEIGHT_TYPE	MAP_WEIGHT	Set Weight image type

Table C.4 Effective Surveyed Area.

Field Name	Eff. Area [deg^2]	Field Name	Eff. Area [deg^2]
ALHAMBRA_F02P01C01	0.0580	ALHAMBRA_F06P01C01	0.0593
ALHAMBRA_F02P01C02	0.0584	ALHAMBRA_F06P01C02	0.0583
ALHAMBRA_F02P01C03	0.0540	ALHAMBRA_F06P01C03	0.0585
ALHAMBRA_F02P01C04	0.0582	ALHAMBRA_F06P01C04	0.0582
ALHAMBRA_F02P02C01	0.0596	ALHAMBRA_F06P02C01	0.0587
ALHAMBRA_F02P02C02	0.0506	ALHAMBRA_F06P02C02	0.0587
ALHAMBRA_F02P02C03	0.0538	ALHAMBRA_F06P02C03	0.0572
ALHAMBRA_F02P02C04	0.0586	ALHAMBRA_F06P02C04	0.0589
ALHAMBRA_F03P01C01	0.0586	ALHAMBRA_F07P03C01	0.0587
ALHAMBRA_F03P01C02	0.0589	ALHAMBRA_F07P03C02	0.0590
ALHAMBRA_F03P01C03	0.0578	ALHAMBRA_F07P03C03	0.0576
ALHAMBRA_F03P01C04	0.0592	ALHAMBRA_F07P03C04	0.0587
ALHAMBRA_F03P02C01	0.0592	ALHAMBRA_F07P04C01	0.0589
ALHAMBRA_F03P02C02	0.0577	ALHAMBRA_F07P04C02	0.0566
ALHAMBRA_F03P02C03	0.0569	ALHAMBRA_F07P04C03	0.0580
ALHAMBRA_F03P02C04	0.0590	ALHAMBRA_F07P04C04	0.0590
ALHAMBRA_F04P01C01	0.0589	ALHAMBRA_F08P01C01	0.0588
ALHAMBRA_F04P01C02	0.0590	ALHAMBRA_F08P01C02	0.0590
ALHAMBRA_F04P01C03	0.0569	ALHAMBRA_F08P01C03	0.0577
ALHAMBRA_F04P01C04	0.0589	ALHAMBRA_F08P01C04	0.0587
ALHAMBRA_F05P01C01	0.0595	ALHAMBRA_F08P02C01	0.0585
ALHAMBRA_F05P01C02	0.0594	ALHAMBRA_F08P02C02	0.0583
ALHAMBRA_F05P01C03	0.0588	ALHAMBRA_F08P02C03	0.0558
ALHAMBRA_F05P01C04	0.0594	ALHAMBRA_F08P02C04	0.0576

D

Appendix Chapter 4

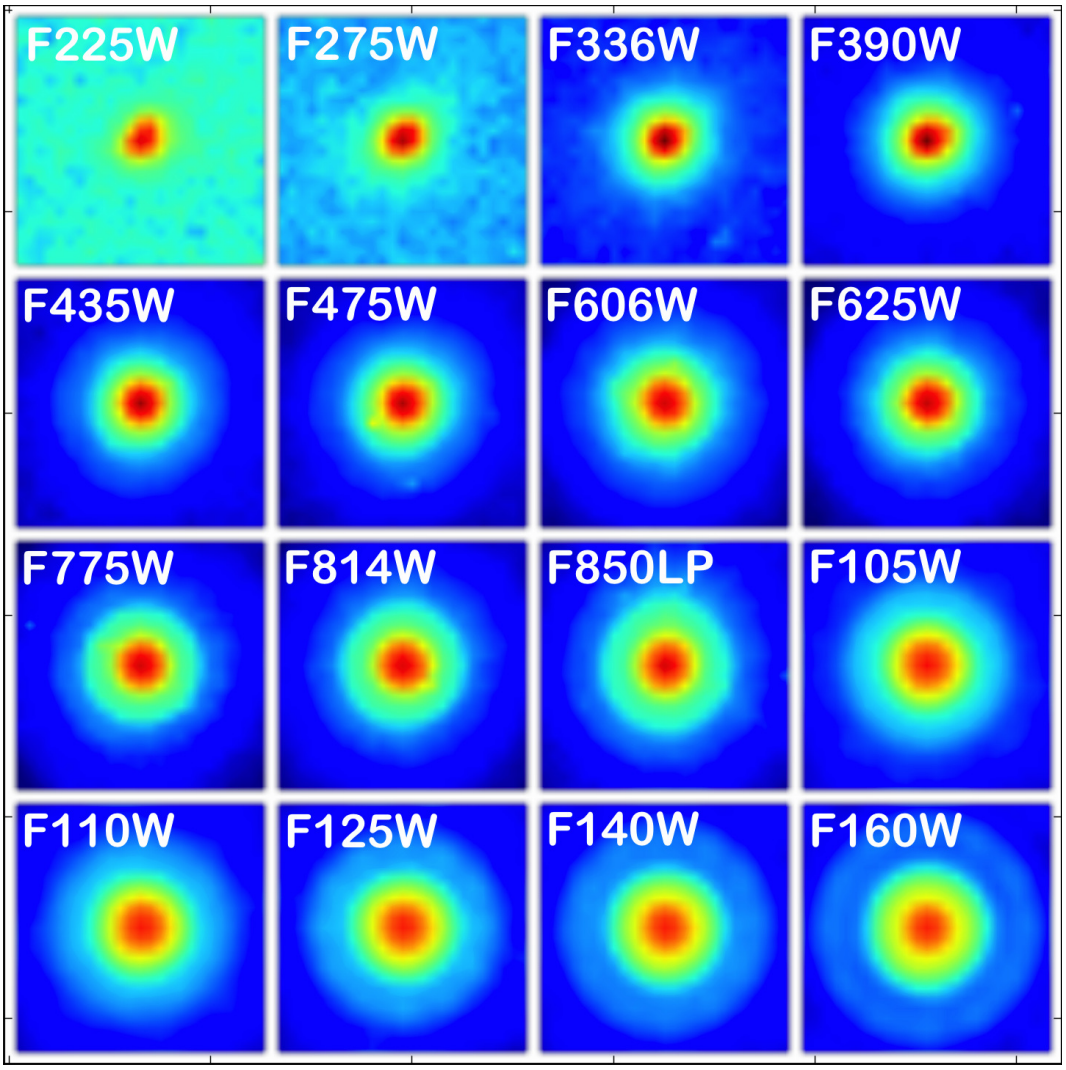

Figure D.1 Around ∼200 star candidates were visually selected across the 25 CLASH clusters. Each stars was double-checked to assure its photometric quality along with had been observed in all the 16 filters. Stars with neighbors were also discarded. The remaining sample of stars (∼70) was combined and normalized to have a total integrated flux equal to unity

Table D.1 The table shows the empirically estimated internal PSF for each filter and its intrinsic scatter. The stars were selecting within the innermost part of the WFC3 covering a FoV of ∼1'.

FILTER	CAMERA	<FWHM> [pix] / [mas]	δ_{FWHM} [pix] / [mas]
F225W/UV	WFC3	4.83 / 0.31	2.08 / 0.13
F275W/UV	WFC3	4.60 / 0.30	1.90 / 0.12
F336W/UV	WFC3	4.67 / 0.30	1.78 / 0.12
F390W/UV	WFC3	4.58 / 0.30	1.36 / 0.09
F435W/OPT	ACS	4.44 / 0.29	0.74 / 0.05
F475W/OPT	ACS	4.60 / 0.30	0.70 / 0.05
F606W/OPT	ACS	4.65 / 0.30	0.84 / 0.05
F625W/OPT	ACS	4.64 / 0.30	0.93 / 0.06
F775W/OPT	ACS	4.47 / 0.29	0.99 / 0.06
F814W/OPT	ACS	4.63 / 0.30	1.00 / 0.06
F850LP/OPT	ACS	4.43 / 0.29	0.82 / 0.05
F105W/NIR	WFC3	5.32 / 0.34	0.47 / 0.03
F110W/NIR	WFC3	5.19 / 0.34	0.46 / 0.03
F125W/NIR	WFC3	5.35 / 0.35	0.56 / 0.04
F140W/NIR	WFC3	5.22 / 0.34	0.40 / 0.03
F160W/NIR	WFC3	5.08 / 0.33	0.33 / 0.02

E

Appendix Chapter 6

E.1 SNe discovered in the CLASH parallel fields.

The *HST* reduction and image-subtraction pipeline was carried out as follows. Raw *HST* images were first calibrated using the STSDAS calibration tools. The calibrations include bias correction, dark subtraction, and flat fielding. In the case of WFC3-IR images, "up-the-ramp" fitting was used to remove cosmic ray events (CRs). Next, the subexposures in each filter were combined using MULTIDRIZZLE (Koekemoer et al. 2003). This stage also removed the geometrical distortion of the *HST* focal plane. For each filter, it was created "template" images comprised of all previous observations in the same filter. Finally, it was subtracted the template images from the drizzled "target" images to produce the difference images that were then searched for SNe. Owing to the stable point-spread-function (PSF) of *HST*, it was not need to degrade the PSF of either the target or template images to match the PSF of the images, as done in ground-based SN surveys.

E.2 Definition of the SN rate

The rate, $R_{\rm Ia}$, was defined in a redshift bin bound by redshifts z_1 and z_2, as follows:

$$R_{\rm Ia}(z_1 < z < z_2) = \frac{\sum\limits_i N_i(z)/\eta_i(z)}{\sum\limits_j t_j A_j \int_{z_1}^{z_2} \frac{1}{(1+z)} \frac{dV}{dz} dz}, \tag{E.1}$$

where N_i is the number of SNe Ia; η_i is that category's detection efficiency at the redshift, z, of each SN; t_j is the visibility time, composed of the time between the first and last epoch of observation of a field j, plus 40 days before the start of the survey and 20 days after its end; A_j is the solid angle of the searchable area of field j, divided by 4π steradians; dV are thin volume elements behind each searchable area; and the $(1 + z)$ factor converts the rates from the observer frame to the rest frame. Although we classified a SN as a SN Ia if $P(\rm Ia) \geq 0.5$, we defined N_i as the sum of $P(\rm Ia)_{np}$ values of all the SNe in each subcategory (before, during, or after the monitored interval). This is based on our treatment of $P(\rm Ia)$ as a measure of the probability of a SN being a SN Ia. This approach allows us to

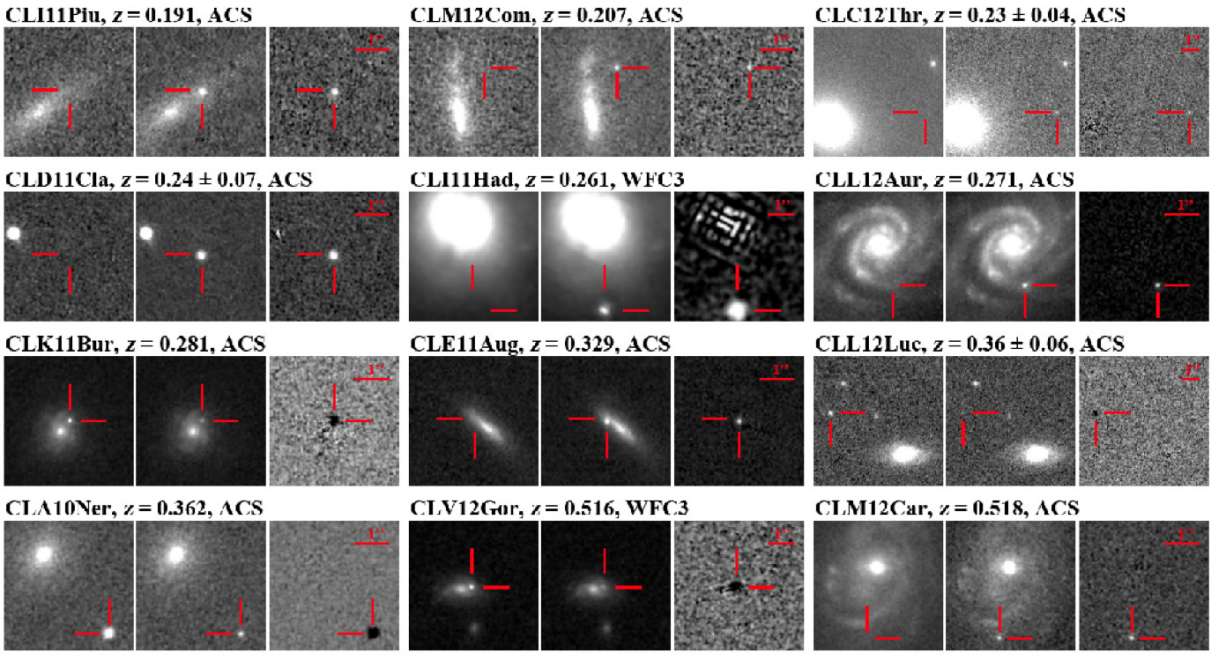

Figure E.1 SNe discovered in the parallel fields of the CLASH clusters. North is up and east is left. In the triplet of tiles for each event, the left-hand tiles show the SN host galaxies without any SN light, whereas the center tiles display the SN host galaxy as imaged when the SN was first discovered. For the declining SNe CLK11Bur, CLL12Luc, CLA10Ner, CLV12Gor, CLF11Dom, CLT12Ela, and CLY13Gal, the left-hand and center tiles show the SN and host galaxy on the first and last visits to the field, respectively. The right-hand tiles show the subtraction in the F850LP or F160W bands for SNe discovered in the ACS or WFC3 parallel fields, respectively. The stretch of the images and the location of the SN differ from panel to panel in order to highlight host-galaxy properties. The header of each panel gives the designation of the SN along with its redshift and camera. Spectroscopic redshifts (cases with no uncertainties in z noted) are given to three significant digits. Photometric redshifts are shown with their uncertainty; in cases where the photometric redshift is not well constrained, we note the approximate peak of the probability density function.

take into account the uncertainty of our classifications, especially for SNe with sparse data.

F

Publications

The following list of scientific publications represents the different contributions done during the period this thesis lasted.

1. **Type-Ia Supernova Rates to Redshift 2.4 from CLASH: the Cluster Lensing And Supernova survey with Hubble**: Graur et al. 2014, ApJ, 783, 28

2. **CLASH: z∼6 young galaxy candidate quintuply lensed by the frontier field cluster RXC J2248.7-4431**: Monna, A., Seitz, S., Greisel, N., et al. 2014, MNRAS, 438, 1417

3. **CLASH: Photometric redshifts with 16 HST bands in galaxy cluster fields**: Jouvel, S., Host, O., Lahav, O., et al. 2014, A&A, 562, A86

4. **The ALHAMBRA survey: an empirical estimation of the cosmic variance for merger fraction studies based on close pairs**: López-Sanjuan et al., 2014, arXiv:1401.4993

5. **Photometric type Ia supernova surveys in narrow band filters**: Xavier, Henrique et al. 2014, arXiv:1312.5706

6. **Three Gravitationally Lensed Supernovae Behind CLASH Galaxy Clusters**: Brandon et al. 2014, arXiv:1312.0943

7. **The ALHAMBRA survey: reliable morphological catalogue of 22 051 early- and late-type galaxies**: Pović, M., Huertas-Company, M., Aguerri, J. A. L., et al. 2013, MNRAS, 435, 3444

8. **The ALHAMBRA survey: evolution of galaxy clustering since** $z \sim 1$: Arnalte et al. 2013, arXiv:1311.3280

9. **CLASH: Complete Lensing Analysis of the Largest Cosmic Lens MACS J0717.5+3745 and Surrounding Structures**: Medezinski, E., Umetsu, K., Nonino, M., et al. 2013, ApJ, 777, 43

10. **CLASH-VLT: spectroscopic confirmation of a z = 6.11 quintuply lensed galaxy in the Frontier Fields cluster RXC J2248.7-4431**: Balestra et al. 2013, A&A, 559, L9

11. **Lyman Break and ultraviolet-selected galaxies at z ∼1 - II. PACS 100 ?m/160 ?m FIR detections**: Oteo, I., Magdis, G., Bongiovanni, Á., et al. 2013, MNRAS, 435, 158

12. **The Contribution of Halos with Different Mass Ratios to the Overall Growth of Cluster-sized Halos**: Lemze, D., Postman, M., Genel, S., et al. 2013, ApJ, 776, 91

13. **Galaxy Halo Truncation and Giant Arc Surface Brightness Reconstruction in the Cluster MACSJ1206.2-0847**: Eichner, T., Seitz, S., Suyu, S. H., et al. 2013, ApJ, 774, 124

14. **The ALHAMBRA survey: Discovery of a faint QSO at z = 5.41**: Matute, I., Masegosa, J., Márquez, I., et al. 2013, A&A, 557, A78

15. **Lyman break and ultraviolet-selected galaxies at z∼1 - I. Stellar populations from the ALHAMBRA survey**: Oteo, I., Bongiovanni, Á., Cepa, J., et al. 2013, MNRAS, 433, 2706

16. **CLASH: A Census of Magnified Star-Forming Galaxies at z ∼ 6-8**: Bradley, L. D., Zitrin, A., Coe, D., et al. 2013, arXiv:1308.1692

17. **Evidence for Ubiquitous, High-EW Nebular Emission in z∼7 Galaxies: Towards a Clean Measurement of the Specific Star Formation Rate using a Sample of Bright, Magnified Galaxies**: Smit, R., Bouwens, R. J., Labbe, I., et al. 2013, arXiv:1307.5847

18. **The ALHAMBRA Survey: Bayesian Photometric Redshifts with 23 bands for 3 squared degrees**: Molino, A., Benítez, N., Moles, M., et al. 2013, arXiv:1306.4968

19. **Joint SZ/X-Ray Deprojections and Nonthermal Pressure Ratio Profiles of the Bolocam Cluster Sample**: Shitanishi, J., Pierpaoli, E., Ameglio, S., et al. 2013, American Astronomical Society Meeting Abstracts, 221, #226.08

20. **Properties of a Young Galaxy at z=9.6 as Viewed through a Cosmic Lens**: Zheng, W., Postman, M., Zitrin, A., et al. 2013, American Astronomical Society Meeting Abstracts, 221, #207.08

21. **A Census of Star-Forming Galaxies in the z∼9-10 Universe based on HST+Spitzer Observations Over 19 CLASH clusters: Three Candidate z∼9-10 Galaxies and Improved Constraints on the Star Formation Rate Density at z∼9.2**: Bouwens, R., Bradley, L., Zitrin, A., et al. 2012, arXiv:1211.2230

22. **A magnified young galaxy from about 500 million years after the Big Bang**: Zheng, W., Postman, M., Zitrin, A., et al. 2012, Nature, 489, 406

23. **CLASH: Precise New Constraints on the Mass Profile of the Galaxy Cluster A2261**: Coe, D., Umetsu, K., Zitrin, A., et al. 2012, ApJ, 757, 22

24. **CLASH: Mass Distribution in and around MACS J1206.2-0847 from a Full Cluster Lensing Analysis**: Umetsu, K., Medezinski, E., Nonino, M., et al. 2012, ApJ, 755, 56

25. **CLASH sources for MACS1149.6+2223 (Postman+, 2012)**: Postman, M., Coe, D., Benitez, N., et al. 2012, VizieR Online Data Catalog, 219, 90025

26. **Quasi-stellar objects in the ALHAMBRA survey. I. Photometric redshift accuracy based on 23 optical-NIR filter photometry**: Matute, I., Márquez, I., Masegosa, J., et al. 2012, A&A, 542, A20

27. **Joint SZ/X-Ray Deprojections and Nonthermal Pressure Profiles of Galaxy Clusters Using Bolocam**: Shitanishi, J., Pierpaoli, E., Ameglio, S., et al. 2012, American Astronomical Society Meeting Abstracts #220, 220, #507.02

28. **The Cluster Lensing and Supernova Survey with Hubble: An Overview**: Postman, M., Coe, D., Benítez, N., et al. 2012, ApJS, 199, 25

29. **CLASH: New Multiple Images Constraining the Inner Mass Profile of MACS J1206.2-0847**: Zitrin, A., Rosati, P., Nonino, M., et al. 2012, ApJ, 749, 97

30. **CLASH: Discovery of a Bright z ∼= 6.2 Dwarf Galaxy Quadruply Lensed by MACS J0329.6-0211**: Zitrin, A., Moustakas, J., Bradley, L., et al. 2012, ApJ, 747, L9

31. **Cluster-cluster lensing and the case of Abell 383**: Zitrin, A., Rephaeli, Y., Sadeh, S., et al. 2012, MNRAS, 420, 1621

32. **The Cluster Lensing and Supernova Survey with Hubble (CLASH): Strong-lensing Analysis of A383 from 16-band HST/WFC3/ACS Imaging**: Zitrin, A., Broadhurst, T., Coe, D., et al. 2011, ApJ, 742, 117

33. **Herschel FIR counterparts of selected Ly? emitters at z∼2.2. Fast evolution since z∼3 or missed obscured AGNs?**: Bongiovanni, A., Oteo, I., Cepa, J., et al. 2010, A&A, 519, L4

Bibliography

Abdalla, F. B., Banerji, M., Lahav, O., & Rashkov, V. 2011, MNRAS, 417, 1891

Abrahamse, A., Knox, L., Schmidt, S., et al. 2011, ApJ, 734, 36

Aparicio Villegas, T., Alfaro, E. J., Cabrera-Caño, J., et al. 2010, AJ, 139, 1242

Appenzeller, I., Fricke, K., Fürtig, W., et al. 1998, The Messenger, 94, 1

Arnouts, S., Cristiani, S., Moscardini, L., et al. 1999, MNRAS, 310, 540

Arnouts, S., Moscardini, L., Vanzella, E., et al. 2002, MNRAS, 329, 355

Assef, R. J., Kochanek, C. S., Brodwin, M., et al. 2008, ApJ, 676, 286

Babbedge, T. S. R., Rowan-Robinson, M., Gonzalez-Solares, E., et al. 2004, MNRAS, 353, 654

Ball, N. M., Brunner, R. J., & Myers, A. D. 2008, Astronomical Data Analysis Software and Systems XVII, 394, 201

Barger, A. J.; Cowie, L. L.; Wang, W.-H. 2008, ApJ, 689, 687

Baum, W. A. 1962, IAU Symp. 15: Problems of Extra-Galactic Research, 15, 390

Beckwith, S. V. W., Stiavelli, M., Koekemoer, A. M., et al. 2006, AJ, 132, 1729

Behroozi, P. S., Wechsler, R. H., & Conroy, C. 2013, ApJ, 770, 57

Bell, E. F., & de Jong, R. S. 2001, ApJ, 550, 212

Bell, E. F., McIntosh, D. H., Katz, N., & Weinberg, M. D. 2003, ApJS, 149, 289

Bennett, C. L., Smoot, G. F., Hinshaw, G., et al. 1992, ApJL, 396, L7

Benítez, N. 2000, ApJ, 536, 571

Benítez N., Ford, H., Bouwens, R., et al. 2004, ApJ, 150, 1

Benítez, N., Gaztañaga, E., Miquel, R., et al. 2009, ApJ, 691, 241

Benítez N., et al., 2009, ApJ, 692L 5B

Bernardi, M., Shankar, F., Hyde, J. B., et al. 2010, MNRAS, 404, 2087

Bertin, E. & Arnouts, S. 1996, A&A, 117, 393

Bertin, E., Mellier, Y., Radovich, M., et al. 2002, Astronomical Data Analysis Software and Systems XI, 281, 228

Bohlin, R. C. 2007, The Future of Photometric, Spectrophotometric and Polarimetric Standardization, 364, 315

Bolzonella, M., Miralles, J.-M., & Pelló, R. 2000, A&A, 363, 476

Bonfield, D. G., Sun, Y., Davey, N., et al. 2010, MNRAS, 405, 987

Bongiovanni, A., Oteo, I., Cepa, J., et al. 2010, A&A, 519, L4

Bordoloi, R., Lilly, S. J., & Amara, A. 2010, MNRAS, 406, 881

Bouwens, R. J., Illingworth, G. D., Oesch, P. A., et al. 2010, ApJL, 708, L69

Bouwens, R. J., Illingworth, G. D., Labbe, I., et al. 2011, NATURE, 469, 504

Bouwens, R., Bradley, L., Zitrin, A., et al. 2012, arXiv:1211.2230

Bouwens, R. J., Oesch, P. A., Illingworth, G. D., et al. 2013, ApJL, 765, L16

Bradley, L. D., Zitrin, A., Coe, D., et al. 2013, arXiv:1308.1692

Brammer, G. B., van Dokkum, P. G., & Coppi, P. 2008, ApJ, 686, 1503

Broadhurst, T., Benítez, N., Coe, D., et al. 2005, ApJ, 621, 53

Broadhurst, T. J., & Barkana, R. 2008, MNRAS, 390, 1647

Brunner, R. J., Connolly, A. J., Szalay, A. S., & Bershady, M. A. 1997, ApJL, 482, L21

Bruzual, G., & Charlot, S. 2003, MNRAS, 344, 1000

Budavári, T. 2009, ApJ, 695, 747

Bundy, K., Ellis, R. S., Conselice, C. J., et al. 2006, ApJ, 651, 120

Capak et al., 2007, ApJS,172,99

Cardamone et al., 2010, ApJS,189,270

Carliles, S., Budavári, T., Heinis, S., Priebe, C., & Szalay, A. S. 2010, ApJ, 712, 511

Casertano, S., de Mello, D., Dickinson, M., et al. 2000, AJ, 120, 2747

Chabrier, G. 2003, PASP, 115, 763

Clowe, D., Bradač, M., Gonzalez, A. H., et al. 2006, ApJL, 648, L109

Coe, D., Benítez, N., Sánchez, S. F., et al. 2006, AJ, 132, 926. & Brunner, R. J. 1997, ApJ, 486, L11

Coe, D., Benítez, N., Broadhurst, T., & Moustakas, L. A. 2010, ApJ, 723, 1678

Coe, D., Zitrin, A., Carrasco, M., et al. 2013, ApJ, 762, 32

Cole, S., Norberg, P., Baugh, C. M., et al. 2001, MNRAS, 326, 255

Coleman, G. D., Wu, C.-C., & Weedman, D. W. 1980, ApJS, 43, 393

Collister, A. A., & Lahav, O. 2004, PASP, 116, 345

Connolly, A. J., Csabai, I., Szalay, A. S., et al. 1995, AJ, 110, 2655

Connolly, A. J., Szalay, A. S., Dickinson, M., Subbarao, M. U., & Brunner, R. J. 1997, ApJL, 486, L11

Connolly, A. J., Szalay, A. S., & Brunner, R. J. 1998, ApJL, 499, L125

Conroy, C., & Gunn, J. E. 2010, ApJ, 712, 833

Cristóbal-Hornillos, D., Aguerri, J. A. L., Moles, M., et al. 2009, ApJ, 696, 1554

Csabai, I.,Budavári, T., Connolly, A. J., et al. 2003, AJ, 125, 580

Cunha, C. E., Lima, M., Oyaizu, H., Frieman, J., & Lin, H. 2009, MNRAS, 396, 2379

Cutri, R. M., Skrutskie, M. F., van Dyk, S., et al. 2003, "The IRSA 2MASS All-Sky Point Source Catalog, NASA/IPAC Infrared Science Archive.

Daddi, E., Cimatti, A., Renzini, A., et al. 2004, ApJ, 617, 746

Dahlen, T., Strolger, L.-G., Riess, A. G., et al. 2004, ApJ, 613, 189

Dahlen, T., Strolger, L.-G., & Riess, A. G. 2008, ApJ, 681, 462

Dahlen, T., Mobasher, B., Dickinson, M., et al. 2010, ApJ, 724, 425

de Santis, C., Grazian, A., Fontana, A., & Santini, P., New Astron. 2007, 12, 271

Einasto, J. 1965, Trudy Astrofizicheskogo Instituta Alma-Ata, 5, 87

Eisenhardt, P. R. M., Brodwin, M., Gonzalez, A. H., et al. 2008, ApJ, 684, 905

Faber, S. M., Phillips, A. C., Kibrick, R. I., et al. 2003, PROCSPIE, 4841, 165

Feldmann, R., Carollo, C. M., Porciani, C., et al. 2006, MNRAS, 372, 565

Fernández-Soto, A., Lanzetta, K. M., & Yahil, A. 1999, ApJ, 513, 34

Fernández-Soto, A., Lanzetta, K. M., Chen, H.-W., Pascarelle, S. M., & Yahata, N. 2001, ApJs, 135, 41

Fioc, M., & Rocca-Volmerange, B. 1997, A&A, 326, 950

Firth, A. E., Lahav, O., & Somerville, R. S. 2003, MNRAS, 339, 1195

Foley, R. J., Andersson, K., Bazin, G., et al. 2011, ApJ, 731, 86

Freeman, P. E., Newman, J. A., Lee, A. B., Richards, J. W., & Schafer, C. M. 2009, MNRAS, 398, 2012

Gawiser, E., van Dokkum, P. G., Herrera, D., et al. 2006, ApJs, 162, 1

Giavalisco, M., Dickinson, M., Ferguson, H. C., et al. 2004, ApJL, 600, L103

Girardi, L., Bertelli, G., Bressan, A., et al. 2002, A&A, 391, 195

Girardi,L.,Groenewegen,M. A. T.,Hatziminaoglou,E.,& da Costa,L. 2005,A&A,436,895

Gerdes, D. W., Sypniewski, A. J., McKay, T. A., et al. 2010, ApJ, 715, 823

Graur, O., Poznanski, D., Maoz, D., et al. 2011, MNRAS, 417, 916

Graur, O., Rodney, S. A., Maoz, D., et al. 2014, ApJ, 783, 28

Grazian, A., Fontana, A., de Santis, C., et al. 2006, A&A, 449, 951

Gregg, M. D., et al. 2004, Bulletin of the American Astronomical Society, 36, 1496

Grogin, N. A., Kocevski, D. D., Faber, S. M., et al. 2011, ApJS, 197, 35

Gwyn, S. D. J., & Hartwick, F. D. A. 1996, ApJL, 468, L77

Hickson, P., Gibson, B. K., & Callaghan, K. A. S. 1994, MNRAS, 267, 911

Hennawi, J. F., Dalal, N., Bode, P., & Ostriker, J. P. 2007, ApJ, 654, 714

Hickson, P. & Mulrooney, M.K. 1998, Astrophys. J. (Suppl.), 115,35-42

Hildebrandt, H., Wolf, C., & Benítez, N. 2008, A&A, 480, 703

Hook, I., Allington-Smith, J. R., Beard, S. M., et al. 2003, PROCSPIE, 4841, 1645

Hopkins, A. M., & Beacom, J. F. 2006, ApJ, 651, 142

Hsieh, B. C., Yee, H. K. C., Lin, H., & Gladders, M. D. 2005, ApJS, 158, 161

Iben, I., Jr., & Tutukov, A. V. 1984, ApJS, 54, 335

Ilbert, O., Arnouts, S., McCracken, H. J., et al. 2006, A&A, 457, 841

Ilbert, O., Capak, P., Salvato, M., et al. 2009, ApJ, 690, 1236

Jee, M. J., Rosati, P., Ford, H. C., et al. 2009, ApJ, 704, 672

Johnson, H. L., & Morgan, W. W. 1953, ApJ, 117, 313

Jones, D. O., Rodney, S. A., Riess, A. G., et al. 2013, ApJ, 768, 166

Jouvel, S., Host, O., Lahav, O., et al. 2013, arXiv:1308.0063

Jullo, E., Kneib, J.-P., Limousin, M., et al. 2007, New Journal of Physics, 9, 447

Jungman, G., Kamionkowski, M., Kosowsky, A., & Spergel, D. N. 1996, Phys. Rev., 54, 1332

Kashikawa, N., Shimasaku, K., Yasuda, N., et al. 2004, PASJ, 56, 1011

Koekemoer, A. M., Fruchter, A. S., Hook, R. N., & Hack, W. 2003, HST Calibration Workshop : Hubble after the Installation of the ACS and the NICMOS Cooling System, 337

Koekemoer, A. M., Aussel, H., Calzetti, D., et al. 2007, ApJS, 172, 196

Koekemoer, A. M., Faber, S. M., Ferguson, H. C., et al. 2011, ApJS, 197, 36

Komatsu, E., Smith, K. M., Dunkley, J., et al. 2011, ApJS, 192, 18

Koo, D. C. 1985, AJ, 90, 418

Kotulla, R., & Fritze, U. 2009, MNRAS, 393, L55

Kuijken, K. 2008, A&A, 482, 1053

Labbé, I., Franx, M., Rudnick, G., et al. 2003, AJ, 125, 1107

Labbé, I., González, V., Bouwens, R. J., et al. 2010, ApJL, 708, L26

Labbé, I., González, V., Bouwens, R. J., et al. 2010, ApJL, 716, L103

Laidler, V. G., Grogin, N., Clubb, K., et al. 2006, Astronomical Data Analysis Software and Systems XV, 351, 228

Lanzetta, K.M., Yahil, A.& Fernández-Soto, A. 1996, Nature, 381, 759

Laurino, O., D'Abrusco, R., Longo, G., & Riccio, G. 2011, MNRAS, 418, 2165

Le Fèvre, O., Saisse, M., Mancini, D., et al. 2003, PROCSPIE, 4841, 1670

Leibundgut, B. 2000, A&A Rev., 10, 179

Li, I. H., & Yee, H. K. C. 2008, AJ, 135, 809

Limousin, M., Richard, J., Jullo, E., et al. 2007, ApJ, 668, 643

Loh, E. D., & Spillar, E. J. 1986, ApJ, 303, 154

Madau, P. 1995, QSO Absorption Lines, 377

Madau, P. 1998, Origins, 148, 88

Mandelbaum, R., Seljak, U., Hirata, C. M., et al. 2008, MNRAS, 386, 781

Massey, P., & Gronwall, C. 1990, ApJ, 358, 344

Matute, I., Márquez, I., Masegosa, J., et al. 2012, A&A, 542, A20

Matute, I., Masegosa, J., Márquez, I., et al. 2013, A&A, 557, A78

Meneghetti, M., Fedeli, C., Pace, F., Gottlöber, S., & Yepes, G. 2010, A&A, 519, A90

Meneghetti, M., Fedeli, C., Zitrin, A., et al. 2011, A&A, 530, A17

Merson, A. I., Baugh, C. M., Helly, J. C., et al. 2013, MNRAS, 429, 556

Miralles, J. M., & Pello, R. 1998, arXiv:astro-ph/9801062

Mitchell, P. D., Lacey, C. G., Baugh, C. M., & Cole, S. 2013, arXiv:1303.7228

Miyazaki, S., Komiyama, Y., Sekiguchi, M., et al. 2002, PASJ, 54, 833

Mobasher, B., Rowan-Robinson, M., Georgakakis, A., & Eaton, N. 1996, MNRAS, 282, L7

Moles, M., et al. 2008, AJ, 136, 1325

Mortlock, D. J., Warren, S. J., Venemans, B. P., et al. 2011, NATURE, 474, 616

Moustakas, J., Zaritsky, D., Brown, M., et al. 2011, arXiv:1112.3300

Navarro, J. F., Frenk, C. S., & White, S. D. M. 1996, ApJ, 462, 563

Navarro, J. F., Frenk, C. S., & White, S. D. M. 1997, ApJ, 490, 493

Navarro, J. F., Hayashi, E., Power, C., et al. 2004, MNRAS, 349, 1039

Navarro, J. F., Ludlow, A., Springel, V., et al. 2010, MNRAS, 402, 21

Nonino, M., Dickinson, M., Rosati, P., et al. 2009, ApJS, 183, 244

Oda, T., Totani, T., Yasuda, N., et al. 2008, PASJ, 60, 169

Oesch, P. A., Bouwens, R. J., Illingworth, G. D., et al. 2012, ApJ, 745, 110

Oguri, M., & Blandford, R. D. 2009, MNRAS, 392, 930

Oke, J. B., & Gunn, J. E. 1983, AJ, 266, 713

Oke, J. B. 1990, AJ, 99, 1621

Oke, J. B., Cohen, J. G., Carr, M., et al. 1995, PASP, 107, 375

Papovich, C., Momcheva, I., Willmer, C. N. A., et al. 2010, ApJ, 716, 1503

Pérez-González, P. G., Cava, A., Barro, G., et al. 2013, ApJ, 762, 46

Perlmutter, S., Aldering, G., Goldhaber, G., et al. 1999, ApJ, 517, 565

Planck Collaboration, Ade, P. A. R., Aghanim, N., et al. 2011, A&A, 536, A1

Planck Collaboration, Ade, P. A. R., Aghanim, N., et al. 2013, arXiv:1303.5062

Pogge, R. W., Atwood, B., Brewer, D. F., et al. 2010, PROCSPIE, 7735,

Polletta, M., Tajer, M., Maraschi, L., et al. 2007, ApJ, 663, 81

Postman, M., Coe, D., Benítez, N., et al. 2012, ApJS,199, 25

Quadri, R., Marchesini, D., van Dokkum, P., et al. 2007, AJ, 134, 1103

Riess, A. G., Filippenko, A. V., Challis, P., et al. 1998, ApJ, 116, 1009

Riess, A. G., Strolger, L.-G., Tonry, J., et al. 2004, ApJ, 607, 665

Riess, A. G., Macri, L., Casertano, S., et al. 2011, ApJ, 730, 119

Rowan-Robinson, M., Babbedge, T., Oliver, S., et al. 2008, MNRAS, 386, 697

Saha, P., & Read, J. I. 2009, ApJ, 690, 154

Salpeter, E. E. 1955, ApJ, 121, 161

Santini, P., Fontana, A., Grazian, A., et al. 2009, VizieR Online Data Catalog, 350, 40751

Sawicki, M. J., Lin, H., & Yee, H. K. C. 1997, AJ, 113, 1

Schlegel, D.J., Finkbeiner, D.P., Davis, M., 1998, ApJ, 500 525

Schwope, A. D., Lamer, G., de Hoon, A., et al. 2010, A&A, 513, L10

Scoville, N., Abraham, R. G., Aussel, H., et al. 2007, ApJS, 172, 38

Sereno, M., Jetzer, P., & Lubini, M. 2010, MNRAS, 403, 2077

Sérsic, J. L. 1963, Boletin de la Asociacion Argentina de Astronomia La Plata Argentina, 6, 41

Sheldon, E. S., Cunha, C. E., Mandelbaum, R., Brinkmann, J., & Weaver, B. A. 2012, ApJS, 201, 32

Smith, G. P., Ebeling, H., Limousin, M., et al. 2009, ApJL, 707, L163

Stanford, S. A., Romer, A. K., Sabirli, K., et al. 2006, ApJL, 646, L13

Stabenau H. F., Connolly A., Jain B., 2008, MNRAS, 387, 1215

Stetson, P. B. 1987, PASP, 99, 191

Stone, R. P. S.1996, ApJS, 107, 423

Strolger, L.-G., Riess, A. G., Dahlen, T., et al. 2004, ApJ, 613, 200

Strolger, L.-G., Dahlen, T., & Riess, A. G. 2010, ApJ, 713, 32

Subbarao, M. U., Connolly, A. J., Szalay, A. S., & Koo, D. C. 1996, AJ, 112, 929

Taniguchi, Y. 2004, Studies of Galaxies in the Young Universe with New Generation Telescope, 107

Tanvir, N. R., Fox, D. B., Levan, A. J., et al. 2009, NATURE, 461, 1254

Taylor, E. N., Hopkins, A. M., Baldry, I. K., et al. 2011, MNRAS, 418, 1587

Tucker, D. L., Smith, J. A., & Brinkmann, J. 2001, The New Era of Wide Field Astronomy, 232, 13

Umetsu, K., Medezinski, E., Broadhurst, T., et al. 2010, ApJ, 714, 1470

van Dokkum, P. G., Labbé, I., Marchesini, D., et al. 2009, PASP, 121, 2

Vanzella, E., Cristiani, S., Fontana, A., et al. 2004, A&A, 423, 761

Vernet, J., Dekker, H., D'Odorico, S., et al. 2011, A&A, 536, A105

Wadadekar, Y. 2005, PASP, 117, 79

Wang, Y., Bahcall, N., & Turner, E. L. 1998, AJ, 116, 2081

Wang, Y., Bahcall, N., & Turner, E. L. 1999, Photometric Redshifts and the Detection of High Redshift Galaxies, 191, 25

Wang, D., Zhang, Y. X., Liu, C., & Zhao, Y. H. 2007, MNRAS, 382, 1601

Wang, D., Zhang, Y.-x., & Zhao, Y.-h. 2008, Proc. of SPIE, 7019,

Wang, D., Zhang, Y., & Zhao, Y. 2008, Astronomical Data Analysis Software and Systems XVII, 394, 509

Wang, D., Zhang, Y.-X., Liu, C., & Zhao, Y.-H. 2008, ChJAA, 8, 119

Wang, D., Zhang, Y., & Zhao, Y. 2010, Proc. of SPIE, 7740,

Wang, D., Zhang, Y.-X., & Zhao, Y.-H. 2010, Proc. of SPIE, 7740,

Watson, M. G., Schröder, A. C., Fyfe, D., et al. 2009, A&A, 493, 339

Way, M. J., & Srivastava, A. N. 2006, ApJ, 647, 102

Way, M. J., Foster, L. V., Gazis, P. R., & Srivastava, A. N. 2009, ApJ, 706, 623

Way, M. J. 2011, ApJL, 734, L9

Webbink, R. F. 1984, ApJ, 277, 355

Whelan, J., & Iben, I., Jr. 1973, ApJ, 186, 1007

Williams, R. E., Blacker, B., Dickinson, M., et al. 1996, AJ, 112, 1335

Wittman, D. 2009, ApJ, 700, L174

Wolf, C., Meisenheimer, K., Roser, H.-J. 2001, A&A, 365, 660

Wolf, C. et al. 2001a, A&A, 365, 681

Wolf, C., Meisenheimer, K., Kleinheinrich, M., et al. 2004, A&A, 421, 913

Wolf, C., Hildebrandt, H., Taylor, E. N., & Meisenheimer, K. 2008, A&A, 492, 933

Wolf, C. 2009, MNRAS, 397, 520

Wuyts et al. 2008, ApJ, 682, 985

Yee, H. K. C. 1998, arXiv:astro-ph/9809347

York, D. G., Adelman, J., Anderson, J. E., Jr., et al. 2000, AJ, 120, 1579

Yüksel, H., Kistler, M. D., Beacom, J. F., & Hopkins, A. M. 2008, ApJL, 683, L5

Zhang, Y., Li, L., & Zhao, Y. 2009, MNRAS, 392, 233

Zheng, W., Postman, M., Zitrin, A., et al. 2012, NATURE, 489, 406

Zitrin, A., & Broadhurst, T. 2009, ApJL, 703, L132

Zitrin, A., Broadhurst, T., Barkana, R., Rephaeli, Y., & Benítez, N. 2011, MNRAS, 410, 1939